Modelling barium isotopes in metal-poor stars

— Andrew James Gallagher —

Centre for Astrophysics Research
Science and Technology Research Institute
— University of Hertfordshire —

Submitted to the University of Hertfordshire in partial fulfilment of the requirements of the degree of Ph.D.

Principal Supervisor: Prof. Sean G. Ryan

— July 2012 —

Declaration

This Ph.D. thesis consists of six chapters. Chapters 3 and 4 are unedited journal publications produced from research conducted during the course of the Ph.D. In addition, a conference proceeding was written following a talk given at the 11^{th} Nuclei in the Cosmos symposium held in Heidelberg on the $19^{\text{th}} - 23^{\text{rd}}$ July 2010. The bulk of the conference proceeding consisted of early stages of research for the first journal publication in Chapter 3 and as such is not included in the work presented here.

The NLTE calculations used for work presented in §4.4 were computed by Adam Hosford for publication in Gallagher, Ryan, Hosford, García Pérez, Aoki, & Honda (2012), which was published in Astronomy & Astrophysics. The CO^{5}BOLD model atmospheres used in Chapter 5 were computed by Hans-Günter Ludwig (Heidelberg) with whom I am collaborating.

With the exception of the contributions just stated, I certify that the rest of the content presented in this thesis is my own work. Any results, diagrams and tables used from other published works have been properly cited.

Andrew J. Gallagher

Acknowledgements

I would like to thank Prof. Sean Ryan. His guidance has been invaluable over these last three and a half years. He always had time to help me with my work and discuss (numerous) new ideas that led to a very interesting topic of research, regardless of his busy schedule. He was always enthusiastic about the work and encouraged me to work more independently as my experience grew. His motivation and passion for the work was the driving force behind this successful start to my career, and I will never forget that. Most importantly though, this thesis would not have been possible without his hard work. Thank you Sean.

My thanks also go to Dr Ana Elia García Pérez, who assumed the role of my second supervisor. She gave me access to her χ^2 code, written for her work with Li, which I adapted and used throughout my analyses. Unfortunately, her brief time at the institute after my arrival meant that we didn't work on as much together as I would have hoped. Maybe in the future Ana!

I would like to thank Dr Adam Hosford for his work on the NLTE project. His hard work on this project became part of an interesting second paper.

My thanks to Dr Wako Aoki, Dr Satoshi Honda and Dr Ana Elia García Pérez, who supplied me with all of the reduced stellar data I use in this thesis. Wako also invited me to the Subaru Telescope for an observing run in December 2011. Poor weather conditions cut our run short, but thanks to Wako, I was able to visit an observatory at least once during my Ph.D.

I would like to thank Dr Hans-Gunter Ludwig (and Ana for the introduction via email!). Together, we began work on an ongoing project on 3D model atmospheres that promises to yield interesting results. His guidance and input to this work was invaluable and his patience has been very much appreciated.

I would also like to take this opportunity to thank Dr James Jenkins for our lengthy

discussions on ‘planet hunting’ using the latest observational techniques. Admittedly, such an acknowledgement should have been included with my second publication as it was there that I began to think about the possible implications that such techniques would have on my work. However, it would appear I was rather absent minded when I submitted the final copy to the publishers. Sorry James, I hope this makes up for it!

I would like to take this opportunity to thank my friends and family for supporting me during the last three and a half years. Unfortunately there are too many people to name, but to all of them I say thanks. I would particularly like to thank my parents Ann and Stephen for putting a roof over my head during the last month of the write-up (and beyond!) and for being so supportive, not only with my pursuit of this Ph.D., but also with the decisions I have made in my life that have lead me to this point. I would also like to thank James Frith and Simon Weston for their discussions about work in the office and their contributions to several hangovers outside the office – but mostly for making life bearable in the office. My thanks also to James and Maria Frith for their regular hospitality and friendship.

Last, but by no means least, I would like to thank Simon Miller and Lydia Golby. They both gave me a home away from home which regularly allowed me to escape the stresses of work with home cooked meals and good company. Most recently they were there to offer me a place to stay during the couple of days I returned to Hertfordshire to submit and again during my examination – my thanks to both of you.

Abstract

The principal theory concerning the origin of the elements heavier than the Fe-peak, such as Ba, strongly suggest that for old, metal-poor environments, the rapid (r-) process is the most likely path taken in their synthesis, while the slow (s-) process becomes more substantial in younger, more metal-rich stellar populations.

In this work I test this theory by evaluating the isotope ratios of Ba. It is understood that Ba consists of seven stable isotopes, five of which are synthesised by the two neutron-capture processes. The two odd isotopes, ^{135,137}Ba, as well as ^{138}Ba are synthesised via both the r- and s-processes while two of the even isotopes, ^{134,136}Ba are synthesised via the s-process only. The relative contribution of the r- and s-process to these isotopes can be understood via nucleosynthesis calculations and is described using the parameter $f_{\rm odd}$, where $f_{\rm odd} = [N(^{135}\mathrm{Ba}) + N(^{137}\mathrm{Ba})]/N(\mathrm{Ba})$. Low values of $f_{\rm odd}$ (~ 0.11) indicate an s-process regime, while high values of $f_{\rm odd}$ (~ 0.46) indicate an r-process regime.

In the Ba II 4554 Å line the even isotopes lie close to the line centre, while the odd isotopes, which are hyperfine split because of their non-zero nuclear spin, lie in the wings of the line. From an analysis of the line profile shape, one can determine whether Ba has been synthesised primarily through the r-process or s-process; a broad, asymmetric line would indicate a high r-process contribution, while a line with a deeper core and shallower wings would indicate a high s-process contribution.

Using the radiative transfer code ATLAS, which assumes local thermodynamic equilibrium (LTE) and employs 1-dimensional (1D) KURUCZ06 model atmospheres, I synthesised line profiles for six metal-poor stars: HD 140283, HD 122563, HD 88609, HD 84937, BD-04° 3208 and BD$+26^\circ$ 3578 - for a range of isotope ratios. All six are of sufficiently low metallicity that Ba was expected to have an r-process origin. These were fit to high resolution ($R \equiv \lambda/\Delta\lambda = 90\,000 - 95\,000$), high signal-to-noise

($S/N = 550 - 1100$) observed stellar spectra using a χ^2 code. It was found that the Ba isotopic ratios were extremely sensitive to a star's macroturbulent velocity, which is a measure of the velocity distributions in the gas of a star's atmosphere. So that the star's macroturbulence could be measured independently of the Ba line, I fit synthetic Fe lines to a few dozen observed Fe lines for each star adopting a Gaussian macroturbulent profile. Through fitting fully-resolved synthetic Ba profiles to the observed stellar spectra, I found that the Ba II line profiles indicated an s-process signature, which disagrees with current theoretical expectations.

As a confirmation of the isotopic ratio derived from the Ba II 4554 Å line, the Ba II 4934 Å line was examined for one star. However, blends with other lines made it difficult to accurately determine the isotopic ratio. Nevertheless, it seemed to confirm the isotope ratio derived from the 4554 Å line, but with a significant increase in uncertainty.

Two further types of symmetric profiles were examined to model the stellar macroscopic broadening, in addition to the Gaussian profiles already used. It was found that fitting the observed lines with synthetic lines broadened by $v \sin i$ profiles, which are used to model the effect of rotation on line broadening, produced poorer fits than the Gaussian macroturbulent broadening profiles. The third profile used to model stellar macroturbulence was a radial-tangential ($\zeta_{\rm RT}$) broadening profile. Improvements to the statistical fits (as measured by their χ^2 minima) were seen when compared to the Gaussian profiles.

However, it was found that using a 1D LTE radiative transfer code and 1D model atmospheres produced poor fits to the observed spectra, regardless of the type of profile used to model the stellar macroturbulence. In particular, the observed Fe profiles showed greater absorption in the red wing than in the blue wing, particularly ~ 140 mÅ redward of the line centre. It was suspected that this could be attributed to the simplistic assumptions that 1D atmospheres and radiative transfer codes make when synthesising synthetic spectra, leaving them unable to model asymmetries caused by convection, which are visible in the high quality stellar spectra used in this thesis.

In an attempt to fit these lines better, two different techniques were examined using the Fe lines. The tests used Fe lines as they are relatively simple to model, compared

to the Ba II 4554 Å line which has multiple components. In the first test, synthetic spectra were computed using the non local thermodynamic equilibrium (NLTE) radiative transfer code MULTI. The synthetic line profiles were fit to a number of lines in HD 140283. Although this technique might have improved the fit in the line core, it was found that such a treatment did not improve upon fitting errors associated with the best fit 1D LTE synthetic profiles.

The second test used a 3-dimensional (3D) radiative transfer code (LINFOR3D) that employed 3D, time-dependent atmospheres produced with CO^{5}BOLD. The 3D synthetic profiles were fit to a selection of Fe lines and improvements over the poor fits produced by the 1D LTE synthesis were seen. It was found that the 3D synthesis could almost completely reproduce the line asymmetries seen in the observed stellar spectrum. This result suggests that further work to refine the 3D calculations and synthesis code would be valuable.

Contents

List of Figures

List of Tables

List of Symbols and Units

a_o	Bohr radius (5.292×10^{-9} cm)
B_ν	Planck function
c	speed of light (2.998×10^5 km s^{-1})
e	electron
eV	electron volt (1.602×10^{-26} erg)
$f_{\rm odd}$	ratio of odd-to-even isotopes in a Ba spectral line
$f_{{\rm odd},r}$	$f_{\rm odd}$ for a purely rapid-process Ba isotope mixture
$f_{{\rm odd},s}$	$f_{\rm odd}$ for a purely slow-process Ba isotope mixture
G	gravitational constant (currently measured to be 6.673×10^{-8} cm^3 g^{-1} s^{-2})
Gyr	10^9 years
gf	product of the oscillator strength and statistical weight of an atomic or ionic species
h	Planck's constant (6.626×10^{-27} erg s)
$\hbar$	Planck's constant divided by two pi ($\hbar = h/2\pi = 1.055 \times 10^{-27}$ erg s)
H_2	molecular hydrogen
I_2	molecular iodine
I_ν	specific stellar intensity
k	Boltzmann constant (1.381×10^{-16} erg K^{-1})
keV	10^3 eV
$L_\odot$	solar luminosity (3.827×10^{33} erg s^{-1})
L_*	stellar luminosity calculated as $L_* = 4\pi R_*^2 \sigma T_{\rm eff}^4$
$\log g$	logarithm (base 10) of the surface gravity of a star (usually quoted in cgs units)
$\log gf$	logarithm of the gf value

$M_\odot$	solar mass (1.989×10^{33} g)
mb	millibarn (10^{-27} cm^2)
MeV	10^6 eV
Mm	10^6 m
Myr	10^6 years
n	neutron
n_n	neutron density
p	proton
P_T	total pressure in a stellar atmosphere
P_g	gas pressure in a stellar atmosphere
P_e	electron pressure in a stellar atmosphere
P_{rad}	radiation pressure in a stellar atmosphere
ps	picosecond (10^{-12} s)
R	spectral resolution defined as $\lambda/\Delta\lambda$ where $\Delta\lambda$ is the wavelength interval per resolution element
R_*	stellar radius
S_ν	source function
T_{eff}	effective temperature of a star
t_{ff}	free-fall time-scale
t_{KH}	Kelvin-Helmholtz time-scale
t_n	neutron-capture time scale, typically measured in seconds
v_{conv}	velocity-space full-width at half-maxima of the broadening function applied to intrinsic stellar spectral lines
$v_{Doppler}$	velocity-space full-width at half-maxima Doppler broadening
$v_{natural}$	velocity-space full-width at half-maxima natural broadening
$v_{thermal}$	velocity-space full-width at half-maxima thermal broadening
v_Γ	velocity-space full-width at half-maxima macroturbulence
v_{obs}	velocity-space full-width at half-maxima of observed spectral lines
v_ξ	velocity-space full-width at half-maxima microturbulence

$v \sin i$	projected equatorial rotational velocity of a star whose rotation is inclined i degrees to the line of site
W	equivalent width of the spectral feature
$\mathrm{Z}_{\odot}$	solar metallicity by mass (0.02)
yr	year
α	helium-4 nucleus
ζ_{rt}	radial-tangential macroturbulent velocity
κ_{ROSS}	Rosseland mean absorption coefficient
κ_{ν}	absorption coefficient in ν space
κ_0	absorption coefficient at $\lambda = 5000\,\text{Å}$
ξ	microturbulent velocity
σ	Stefan-Boltzmann constant ($5.671 \times 10^{-5}\,\mathrm{erg\,cm^{-2}\,K^{-4}}$)
τ_{ROSS}	Rosseland mean optical depth
τ_{ν}	optical depth in ν space
τ_0	optical depth at $\lambda = 5000\,\text{Å}$
τ_{n}	free neutron decay time, typically measured in seconds
χ	line transition excitation energy (usually quoted in eV)

List of common Abbreviations

1D	1 dimensional
3D	3 dimensional
AGB	asymptotic giant branch
BBN	big bang nucleosynthesis
BSG	blue supergiant
CNO	carbon-nitrogen-oxygen
E-AGB	early asymptotic giant branch
e-process	equilibrium process
$FWHM$	full-width at half-maximum
HB	horizontal branch
H-R	Hertzsprung-Russell
HDS	High Dispersion Spectrograph
hfs	hyperfine structure
HST	Hubble Space Telescope
IMF	initial mass function
ISM	interstellar medium
LBV	luminous blue variable
LTE	local thermodynamic equilibrium
Myr	10^6 years
NLTE	non local thermodynamic equilibrium
OLS	ordinary least square
p-process	proton-capture process
PI	pair instability
PN	planetary nebula
r-process	rapid neutron-capture process

RGB	red giant branch
RMS	root-mean-square
RSG	red supergiant
s-process	slow neutron-capture process
S/N	signal-to-noise ratio
SGB	subgiant branch star
SN	supernova
SNe	supernovae
TP-AGB	thermal pulsing asymptotic giant branch
WC	carbon rich Wolf-Rayet star
WN	nitrogen rich Wolf-Rayet star
WO	oxygen rich Wolf-Rayet star
WR	Wolf-Rayet star
ZAMS	zero age main-sequence

Chapter 1: Introduction

Heavy element production via the two neutron-capture processes, the rapid (r-) and slow (s-) process, has been of long standing interest in nuclear astrophysics, particularly the consideration of the sites in which they occur. It is fairly well established that the majority of the s-process occurs in evolved, low- to intermediate-mass stars via sub-reactions during advanced burning stages (Burbidge et al., 1957; Iben, 1983; Smith & Lambert, 1989; Busso et al., 1999, etc.). A sub-class of the s-process, which is responsible for the majority of the heavy elements between Fe and Sr ($60 \lesssim A \lesssim 90$), takes place in more massive stars (Prantzos et al., 1990; Raiteri et al., 1991; Pignatari et al., 2010, etc.). These are known as the main and weak s-process respectively. The exact physics behind the various mixing processes that must precede s-process nucleosynthesis are still not fully understood. Details of these two s-processes are discussed in §1.3.1. The r-process site(s), however, has never been observed directly and debates are on going as to where they may occur (Wanajo & Ishimaru, 2006).

Clues to the origin of the r-process site(s) can be studied through observations of r- and s-process elements in metal-poor stars. In extremely metal-poor stars, the overabundance of r-process nuclei relative to s-process nuclei would support the most favoured hypothesis that the r-process occurs in supernova (SN) events of massive, short lived, progenitor stars (details on this are presented in §1.3.2). In the early Universe, as the first stars form, it is believed that the metal-free environments would preferentially form massive stars (see formation in §1.2).

These stars would not have the ability to synthesise heavy elements via the weak s-process as that requires the presence of Fe seed nuclei, which cannot be synthesised in early stages of massive star evolution. However supernovae (SNe) events would have the ability to produce Fe and free neutrons in large quantities via runaway nuclear fusion processes (see advanced burning stages in §1.1.2). High contributions by the r-process in metal-poor stars would strengthen current theories on the formation of the first stars in the Universe, which are believed to have induced the epoch of reionisation (Haiman & Loeb, 1997; Sokasian et al., 2004).

In this scenario the r-process should dominate over the s-process at early times, an hypothesis established by Truran (1981). Results published in Spite & Spite (1978) were particularly influential in developing this postulate. See §3.1 for further details on these two studies. The question of whether this hypothesis is upheld observationally in the Ba isotope ratio is the main motivation for the research presented in this thesis.

By examining the isotope ratios of Ba in metal-poor stars we can probe the contribution of the r- and s-process to them. Ideally, one would conduct such an analysis for several different heavy elements to construct a clear picture of the r- and s-process contributions in the metal-poor star. Currently this is not possible to a high enough degree of accuracy, as Roederer et al. (2008) demonstrated. They studied the isotopic fractions of Eu, Sm and Nd for two metal-poor stars, using high signal-to-noise ($S/N \sim 160 - 1000$), high resolution ($R \equiv \Delta\lambda/\lambda \sim 120\,000$) spectra. Despite the high quality of their data and their analysis, the results were tainted by large uncertainties, particularly for their analysis of Nd. The large uncertainties were due to the insufficient quality of the data so that accurate detections of the extremely minute changes in the isotope configurations could not be achieved, even though the resolution and S/N of the data was amongst the highest possible with current instrumentation.

For Ba, which has five stable isotopes that form via the two neutron-capture processes, two of the isotopes (^{134,136}Ba) are produced exclusively by the s-process, whilst the other three isotopes (^{135,137,138}Ba) can form via both processes. Also, the Ba 4554 Å absorption line's hyperfine structure (hfs) is such that the even isotopes, the major fraction of which is synthesised via the s-process, form close to the centre of the line whilst the odd isotopes, the major fraction of which is synthesised via the r-process, form towards the wings of the line. As such, the relative contributions of the isotopes are distinct enough in this line to allow for much more accurate detections of the r- and s-process contributions relative to those heavy elements just discussed. However, one must still employ the highest quality data. I will discuss details of the isotope structure of Ba and the hyperfine structure of its absorption lines in Chapter 2. Although using one atomic species in this manner to explore the r- and s-process contributions is not ideal, it represents the sum of what is possible with the current generation of

telescopes and, as we'll see throughout this study, the most popular spectrum synthesis codes currently employed.

In this chapter I give a brief overview of the physics evolved in stellar evolution and the nuclear fusion processes associated with each particular phase in the context of chemical evolution. In the first section I shall describe the processes involved in stellar evolution for two stellar mass ranges; low- to intermediate-mass stars and high-mass stars. This should not only show the distinctions in their evolution, but also the difference in their evolution from the first stars in the Universe, which is described in §1.2. It should also explain how chemical processes taking place throughout their lifetimes allow for the r- and s-processes to occur. Finally, in §1.3, I discuss the r- and s-processes in detail, particularly the locations of their sites.

1.1 Stellar evolution

Stars with initial mass $M < 0.5\,\mathrm{M}_{\odot}$ do not evolve through different branches on the Hertzsprung-Russell (H-R) diagram. They will continually replenish their supply of H in the core and mix freshly synthesised He into the envelope and atmosphere. This is because these stars are fully convective. As such when their source of H is depleted they will evolve off the main-sequence to become a He white dwarf. Also they will never chemically enrich the Galaxy as their atmospheres will not detach and pollute the ISM, due to the low luminosities associated with these stars. The same fate applies to more massive progenitor stars that experience significant mass loss on the red giant branch (RGB) so that the star's mass falls below the $0.5\,\mathrm{M}_{\odot}$ limit before the onset of He core burning. This can be achieved through binary interaction, which has been well documented (Serenelli et al., 2002; Steinfadt et al., 2010; Parsons et al., 2011).

During a more massive ($M > 0.5\,\mathrm{M}_{\odot}$) star's lifetime it evolves through several phases of evolution, which are driven by the relationship between gravitational collapse and nuclear fusion. In this section I briefly discuss these phases of evolution for a further two scenarios: low- to intermediate-mass stars of mass $0.5\,\mathrm{M}_{\odot} \leq M \leq 10\,\mathrm{M}_{\odot}$, and massive stars ($M > 10\mathrm{M}_{\odot}$), and the various nuclear processes that work to halt

the star's collapse. The evolution of the two types of star differ in the later stages of their evolution. In §1.1.1 I discuss the evolution of low- to intermediate-mass stars as they evolve along the H-R diagram (Fig. 1.1) and in §1.1.2 I discuss the evolution of massive stars as they evolve along their part of the H-R diagram.

1.1.1 Low- to intermediate-mass stars

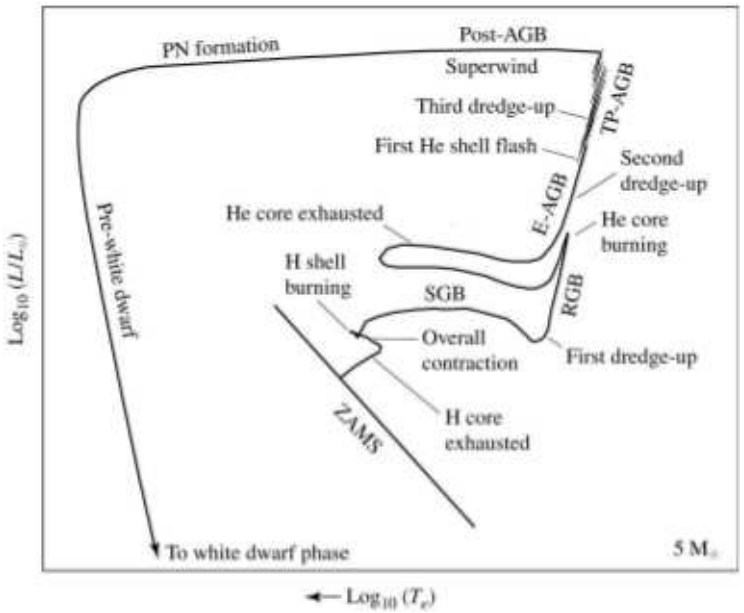

Fig. 1.1: A H-R diagram schematic for a solar-metallicity intermediate-mass ($M = 5\,\mathrm{M}_\odot$) star. Image from Carroll & Ostlie (2006).

Formation and the main-sequence

Stars are formed out of molecular gas clouds that collapse under their own gravity. As a gas cloud collapses, initially on a free-fall time-scale

$$t_{\mathrm{ff}} = \left(\frac{3\pi}{32 G \rho_0}\right)^{\frac{1}{2}}, \tag{1.1}$$

where ρ_0 is the initial density of the molecular gas cloud, interactions between particles cause the temperature of the system to increase. The protostar slowly contracts in hydrostatic equilibrium on a thermal (Kelvin-Helmholtz) time-scale

$$t_{\mathrm{KH}} = \frac{3}{10}\frac{G M_*^2}{R_* L_*}, \tag{1.2}$$

where L_* R_* and M_* are the luminosity, radius and mass of the protostar respectively. The heat generated from its collapse eventually ignites fusion at the centre. The energy it releases effectively halts any further collapse. The outward gas pressure is almost in equilibrium with the force of gravity which drives the star's collapse. At this stage of its life, the star is said to be a main-sequence star. A main-sequence star's radiated energy comes from fusion of H to He. There are two processes by which this is achieved, which I will now discuss.

The pp-chain

A main-sequence star can fuse H to produce He as part of a chain known as the pp-chain, which can be split into three separate branches (see Fig. 1.2). The first reaction in the main chain, $\mathrm{p}\,(\mathrm{p}, \mathrm{e}^+\,\nu_\mathrm{e})\,\mathrm{d}$, operates via the weak force through β-decay, $\mathrm{p} \rightarrow \mathrm{n}$. As such it is an extremely slow reaction; roughly $10^{10}\,\mathrm{yr}$ per proton pair in low- to intermediate-mass stars (Pagel, 1997). The second reaction is much faster, with a typical reaction time of 1.6 s.

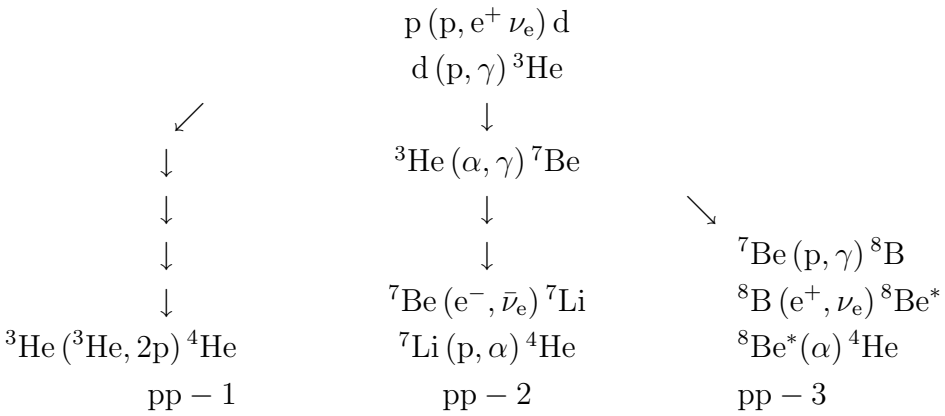

Fig. 1.2: The three branches of the pp-chain.

Each branch in the chain operates simultaneously, but have different contributions to the total energy production rate, of 86%, 14% and 0.02% for the pp-1, pp-2 and pp-3 in the Sun respectively (Prialnik, 2000). Whereas pp-1 only loses 2.0% of the total energy output ($Q_\mathrm{pp} = 26.73\,\mathrm{MeV}$) through neutrino production, pp-2 and pp-3 lose 4.0% and 28.3% through neutrino loses respectively (Rolfs & Rodney, 1988). However,

the relative importance of each branch to the total energy production of the pp-chain increases with increasing temperature (Prialnik, 2000).

The pp-chain requires the lowest temperature to initialise ($\sim 4 \times 10^6$ K) and has the smallest temperature sensitivity, T^4, of all the thermonuclear processes. However, it releases the largest energy per complete reaction, which is measured as the difference in mass between four protons and one He nucleus, $Q_{\mathrm{p-p}} = 4\Delta M(\mathrm{p}) - \Delta M(\alpha) = 26.73\,\mathrm{MeV}$ (Prialnik, 2000).

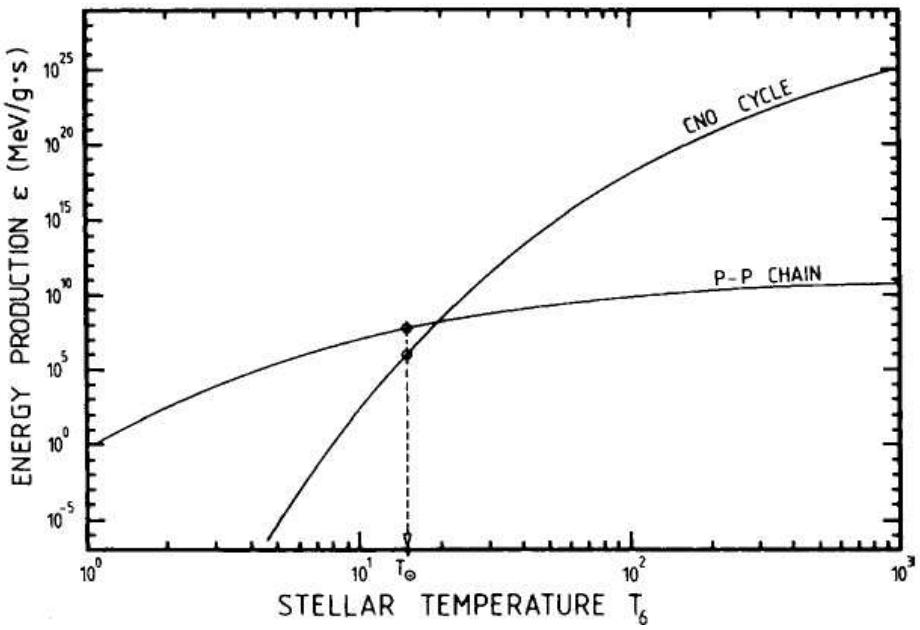

Fig. 1.3: The temperature dependence on the pp-chain and CNO-cycle. The dashed arrow indicates the solar temperature. It is shown that for the Sun the pp-chain would be the dominant form of energy production. Image from Pagel (1997).

The CNO-cycle

A main-sequence, metal-abundant star, with core temperatures higher than those in the Sun, would also use the CNO-cycle to burn hydrogen, see Fig. 1.3. This process uses C, N and O like catalysts; the total abundance of C+N+O remains unchanged, however there is some modification to the isotope ratios of C, N and O due to the different reaction rates. In fact most of the C, and at higher temperatures most of the O, in the burning zones will be converted over the main-sequence lifetime to ^{14}N (Pagel, 1997).

Like the pp-chain, the CNO-cycle can be further divided into a bi-cycle (Fig. 1.4).

The main part of the cycle, the CN-cycle, is responsible for the majority of the energy production whilst the second cycle, the ON-cycle, contributes little energy to the total output. However the ON-cycle will begin to contribute a larger proportion of the total energy as temperatures increase.

$^{12}\mathrm{C}\,(\mathrm{p},\gamma)\,^{13}\mathrm{N}$	$^{14}\mathrm{N}\,(\mathrm{p},\gamma)\,^{15}\mathrm{O}$
$^{13}\mathrm{N}\,(,\mathrm{e}^{+}\nu_{\mathrm{e}})\,^{13}\mathrm{C}$	$^{15}\mathrm{O}\,(,\mathrm{e}^{+}\nu_{\mathrm{e}})\,^{15}\mathrm{N}$
$^{13}\mathrm{C}\,(\mathrm{p},\gamma)\,^{14}\mathrm{N}$	$^{15}\mathrm{N}\,(\mathrm{p},\gamma)\,^{16}\mathrm{O}$
$^{14}\mathrm{N}\,(\mathrm{p},\gamma)\,^{15}\mathrm{O}$	$^{16}\mathrm{O}\,(\mathrm{p},\gamma)^{17}\mathrm{F}$
$^{15}\mathrm{O}\,(,\mathrm{e}^{+}\nu_{\mathrm{e}})\,^{15}\mathrm{N}$	$^{17}\mathrm{F}\,(,\mathrm{e}^{+}\nu_{\mathrm{e}})\,^{17}\mathrm{O}$
$^{15}\mathrm{N}\,(\mathrm{p},{}^{12}\mathrm{C})\,^{4}\mathrm{He}$	$^{17}\mathrm{O}\,(\mathrm{p},{}^{14}\mathrm{N})\,^{4}\mathrm{He}$
$\mathrm{CN}-\mathrm{cycle}$	$\mathrm{ON}-\mathrm{cycle}$

Fig. 1.4: The CNO bi-cycle.

The CN-cycle is highly temperature dependent, as Fig. 1.3 shows, due to the high Coulomb barriers. The energy production rate for the CNO-cycle, for stars with masses large enough for core temperatures to increase beyond $\sim 1.5 \times 10^{7}\,\mathrm{K}$, is much higher due to this larger temperature dependence (Prialnik, 2000). As such, when the core temperatures in a star are hotter than this, the CNO-cycle becomes the dominant source of nuclear fusion (Fig. 1.3).

First ascent red giant stars

The evolution of low-mass ($M \leq 1\,\mathrm{M}_{\odot}$) stars off the main-sequence varies slightly to the intermediate-mass ($M > 1\,\mathrm{M}_{\odot}$) case. For low-mass stars that have depleted their H in the core, there is an almost immediate activation of H burning in the shell that surrounds the He core. The core begins to contract, which increases the temperature of the surrounding burning shell, increasing its energy production rate, which increases its luminosity. This causes the effective temperature (T_{eff}) of the star to decrease as the surrounding layers and the stellar envelope expand slightly.

For intermediate mass stars, the scenario is slightly different. Unlike the low-mass case, the shell of H surrounding the core does not switch on immediately following core

burning extinction, rather the whole star begins to contract slightly under gravity over a Kelvin-Helmholtz time-scale. The contraction of the star forces the luminosity and effective temperature to increase. Once the temperature in the H shell, surrounding the core reaches high enough, H burning begins. The surrounding layers of the star absorb some of the energy generated by the burning shell, which causes them to expand outward slightly, which drops the effective temperature and luminosity slightly. These processes have an effect on the path of the star's evolution on the H-R diagram, which can be seen in Fig. 1.1 after the zero age main-sequence (ZAMS) and before the subgiant branch (SGB).

In both types of star described here, this evolutionary phase is known as the main-sequence turn-off. The freshly synthesised He from the H burning shell is steadily deposited on to the He core, increasing its mass. This increases the rate of core contraction, increasing its temperature which causes further expansion of the stellar envelope, further decreasing $T_{\rm eff}$. At this point the star is said to be a SGB star. As the star evolves along the SGB, further increases to the mass of the He core causes more contraction and its temperature to rise. The H burning shell increases its energy production rate.

The increasing outward pressure forces the stellar envelope to expand further, which causes the effective temperature to reduce. A large convection zone develops near the surface and descends through the stellar atmosphere. The star begins to ascend the RGB as continued core contraction causes the H shell's luminosity to increase. This increase in luminosity and moderate decrease in $T_{\rm eff}$ means that RGB stars ascend near the so-called Hayashi limit (Hayashi, 1961), on tracks similar to the one seen in Fig. 1.1 labelled RGB. These tracks are characteristic of RGB and asymptotic giant branch (AGB) evolution along the H-R diagram. The zone to the right of the track is forbidden as the conditions for hydrostatic equilibrium are no longer fulfilled; stars are fully convective at the limit so there is no adequate energy transport mechanism that can transport the luminosity out of the star at lower values of $T_{\rm eff}$. During this stage of evolution the convective zone of its atmosphere becomes important to its chemical enrichment. Because stars at the Hayashi limit would be fully convective the envelope

of an RGB star is convectively unstable.

As the developing convective zone reaches down to layers of the star where nuclear fusion has taken place, convection causes mixing of initially present isotopes[1] with new material synthesised via nuclear reactions. This can be detected at the stellar surface when comparing two stars of equal mass and metallicity at different phases of evolution, e.g. an RGB and main-sequence star. This mixing event is known as first dredge-up and is discussed further in the next section.

As a star evolves, its rotation reduces. It is believed that this is due to magnetic winds that remove mass from the star, reducing the star's angular momentum (Washimi & Shibata, 1993). Magnetic breaking has little to no effect in massive stars. This is because such stars are short lived, whereas the breaking effect caused by magnetic fields is very gradual. As such only older, less massive stars lose angular momentum via this process. The exact physics behind this are beyond the scope of this work, however, observations show that evolved low-mass giant stars show very little rotation (Gray, 1989).

First dredge-up

Dredge-up is an important chemical mixing event in stars. It involves the mixing of material that has been synthesised or depleted by thermonuclear fusion into the outer convection zone of stars. Dredge-up occurs at the end of a dominant nuclear fusion event (e.g. when H and He core burning ceases) and the stellar envelope expands and cools while the core contracts and heats up (Herwig, 2005). As mixing is poorly modelled, the exact physics behind dredge-up events are still relatively unknown.

First dredge-up occurs in early-type[2] RGB stars after H core burning ends (parts D to E, Fig. 1.5). As the star evolves along the RGB, the stellar envelope is continuously expanding whilst the He core is contracting and heating up. Standard theory states that the convective envelope extends inwards and reaches the He core, where material processed by the CNO-cycle and pp-chain are dredged-up through the convective zone

[1] Present during the star's formation.

[2] Newly evolved RGB stars that are approaching the Hayashi limit on the H-R diagram are sometimes referred to as early-type RGB stars.

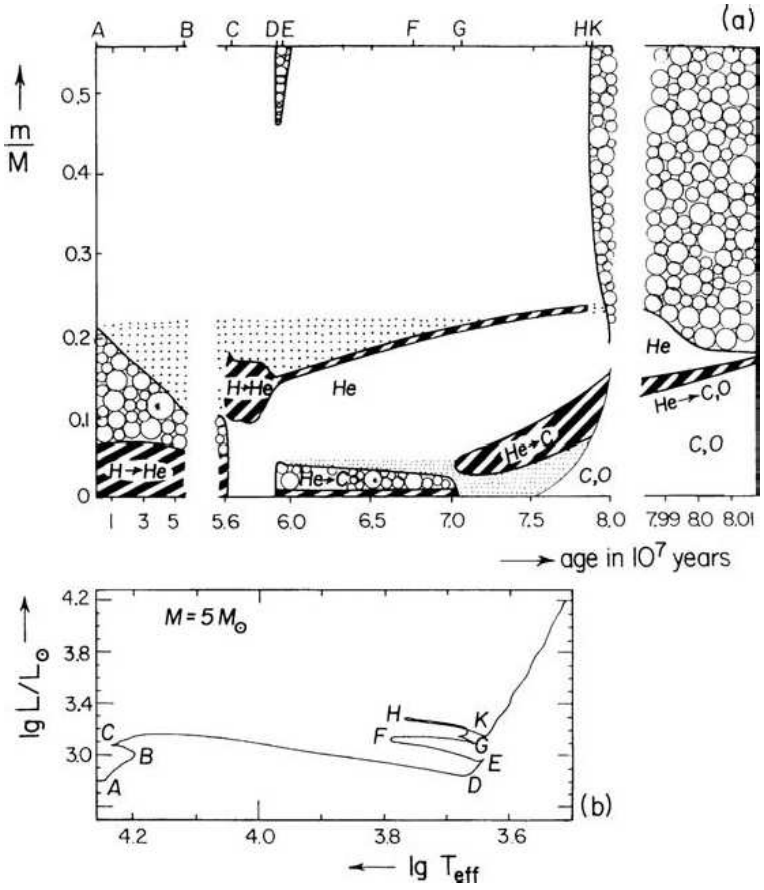

Fig. 1.5: The evolution of a $5\,M_\odot$ star from the ZAMS to the thermal pulsing asymptotic giant branch (TP-AGB). **(a)**: The structure of the star as a function of time of units 10 Myr. It shows the various burning regions (*thick horizontal stripes*), regions of variable chemical composition (*dots*), and convection zones (*circles*). **(b)**: The corresponding H-R diagram for the evolution of the star. Each part (A to K) represents a particular part on the top panel (top axis). Image from Kippenhahn & Weigert (1990).

to the stellar atmosphere. In Fig. 1.5(a), the convective envelope reaches maximum depth at point *E*, but does not reach all the way down to the H-burnt core, and so no first dredge-up occurs in this model. In particular ^{7}Li and ^{3}He abundances increase whilst the ^{12}C/^{13}C ratio decreases (Charbonnel, 1995). However, observational comparisons between SGB and RGB stars in globular clusters suggest that the ^{12}C/^{13}C ratio continues to decrease after the completion of the first dredge-up event (Gilroy & Brown, 1991). In addition, the standard model predicts that ^{3}He abundances would remain constant until ejection from the star at the end of its lifetime (Olive et al., 1995), however, observations do not support this as ^{3}He/H ratios in the ISM remain much lower than are predicted (Rood et al., 1998).

Charbonnel (1995) suggests a non-standard model that corrects for the observed

^{3}He abundance in the ISM and accounts for the decreasing $^{12}C/^{13}C$ ratio in RGB stars by introducing extra mixing on the RGB, the efficiency of which is dependent on the composition of the H burning shell as well as the initial stellar mass. Boothroyd et al. (1995) referred to this as cool bottom processing. Higher-mass stars ($M > 1.8\,M_\odot$), that do not experience a He core flash (discussed in detail below), will not initiate cool bottom processing as they evolve off the RGB before it can take place (Boothroyd & Sackmann, 1999). As you can see, the exact cause and effect of this dredge-up event is still in debate.

Helium core burning phase

The conditions at the point of ignition of the He core are dependent on initial mass (Herwig, 2005). For low-mass stars, $0.5\,M_\odot < M < 1.8\,M_\odot$[3], He core burning starts violently with a He core flash. This is because in this mass range, the inert He core of the RGB becomes electron-degenerate. As such, the temperature and pressure are largely independent of one another. When the conditions become hot enough for He burning through the triple-α process, the initial energy release is nearly explosive. In contrast, the He cores of the more massive stars, $M > 1.8\,M_\odot$, are not electron degenerate and there is no He core flash when temperatures are high enough for the triple-α to occur.

Horizontal giant branch (HB) and clump stars are fuelled by He core and H shell burning (parts E to G on Fig. 1.5). The difference between these stars has to do with their mass and metallicity. Low-mass, metal-poor stars are found on the HB part of the H-R diagram, otherwise stars evolving through this phase are found in a clump on the H-R diagram. This phase of evolution is far shorter than the main-sequence as He burning releases roughly a tenth of the energy that H burning does, and the luminosity of such stars are much higher than when they were on the main-sequence (Prialnik, 2000).

The high temperature dependence of the triple-α process means that the core is convective (Prialnik, 2000). In fact, He burning takes place at the very centre of the

[3]Remember that stars with $M < 0.5\,M_\odot$ do not evolve through the giant branch.

core, where the temperatures are hottest, and the convection in the core means that He is continuously replenished, and newly synthesised C and O transported outwards. After a relatively short time, the He core is depleted after converting He into C and O. In fact this phase would be even shorter, except that H shell burning contributes to the total energy output of the star, which slightly decreases the rate at which He is needed to be burnt in order to maintain hydrostatic equilibrium.

The triple-α process

As temperatures reach $\sim 1 \times 10^8$ K, He can be fused into C and O. This is a known as the triple-α process. The various reactions that make up the triple-α process are listed in Fig. 1.6.

$$^4\mathrm{He}\,(\alpha)\,{}^8\mathrm{Be}^*$$
$$^8\mathrm{Be}^*\,(\alpha,\gamma)\,{}^{12}\mathrm{C}$$

And as ^{12}C densities increase:

$$^{12}\mathrm{C}\,(\alpha,\gamma)\,{}^{16}\mathrm{O}$$

Fig. 1.6: The triple-α process.

This process is extremely sensitive to the time-scales for the reaction $^8\mathrm{Be}^*\,(\alpha,\gamma)\,{}^{12}\mathrm{C}$ as the lifetime of ^{8}Be* is only 2.6×10^{-16} s. However, in 1952 Edwin Salpeter found that the scattering time of an α particle at $T \geq 10^8$ K is less than the Be lifetime. This being true, the relative Be abundance at any one time is $\sim$ one in 10^9 particles (Prialnik, 2000). The solution to this came shortly after when Fred Hoyle realised that the probability of an $^8\mathrm{Be}^*(\alpha)$ reaction would be increased if the C nucleus had a nuclear energy level close to the $^8\mathrm{Be}^* + \alpha$ energies, which we now know it does. This is known as a resonant reaction.

Second dredge-up

In the final stages of HB evolution, the star will have a He burning core surrounded by unprocessed He, which will accumulate below the H burning shell. As He in the

core is depleted, it will contract. This will cause temperatures to rise until He shell burning is ignited around the CO core, which causes expansion of the He burning shell and overlaying layers, temporarily switching off the H burning shell. Second dredge-up occurs at this stage (part K, Fig. 1.5), when the convective envelope descends into layers where material synthesised via the triple-α reaction is found.

In low-mass stars, the convective envelope is incapable of descending this far into the star. Only stars with mass $M \gtrsim 4\,\mathrm{M}_{\odot}$ are able to go through second dredge-up (Boothroyd & Sackmann, 1999). The ^{4}He and ^{14}N[4] abundances are enhanced relative to H at the stellar surface, and small changes to the C and O isotopic ratios are found (Boothroyd & Sackmann, 1999; Karakas, 2003).

A lot of work has been published on the second dredge-up in metal-poor populations such as globular clusters (Lau et al., 2008; Pumo et al., 2008; Decressin et al., 2009, and references therein). Models published by Decressin et al. (2009) predict that the second dredge-up for a $5\,\mathrm{M}_{\odot}$, non-rotating star at metallicities $Z = 0.001$, 0.0005, 0.0001 and 0.00001[5] sees the sum of the CNO abundances (^{12}C, ^{16}O and ^{14}N) remain constant throughout dredge-up, whilst the abundance of ^{14}N increases on the stellar surface, which agrees well with Karakas (2003). In rotating models, with initial ZAMS surface rotation assumed to be $300\,\mathrm{km\,s^{-1}}$ for the same mass and metallicities they find that the chemical structure is modified compared to the non-rotating case. The total sum of CNO abundances still remain constant and ^{14}N is still enhanced whilst ^{12}C and ^{16}O decreases at the surface, however, the abundance gradients are smoothed out, which allows for easier diffusion between layers in the star (see Decressin et al., 2009, their Fig. 1 for further details). As metallicity decreases, remaining rotation of the star (calculated from the ZAMS rotation) increases, increasing the mixing between layers in the star.

[4] An important isotope for s-processing via the weak path, which is discussed in §1.3.1.
[5] [Fe/H]≈ -1.3, -1.6, -2.3 and -3.3 respectively, where [Fe/H]$\approx \log Z/\mathrm{Z}_{\odot}$.

Asymptotic giant branch stars

During second dredge-up the convection zone descends through the star reaching the He burning shell. As well as dredging up He- and N-rich material, H is mixed with deeper layers in the star. This allows the H burning shell to ignite. An AGB star is fuelled by dual shell burning; the inert CO core is surrounded by a He burning shell, which is surrounded by a dormant He rich shell, surrounded by a H burning shell. A basic schematic of an AGB star is shown in Fig. 1.7. During the early asymptotic giant branch (E-AGB) the major source of the energy comes from the He burning shell. At this stage the H burning shell is mostly inactive.

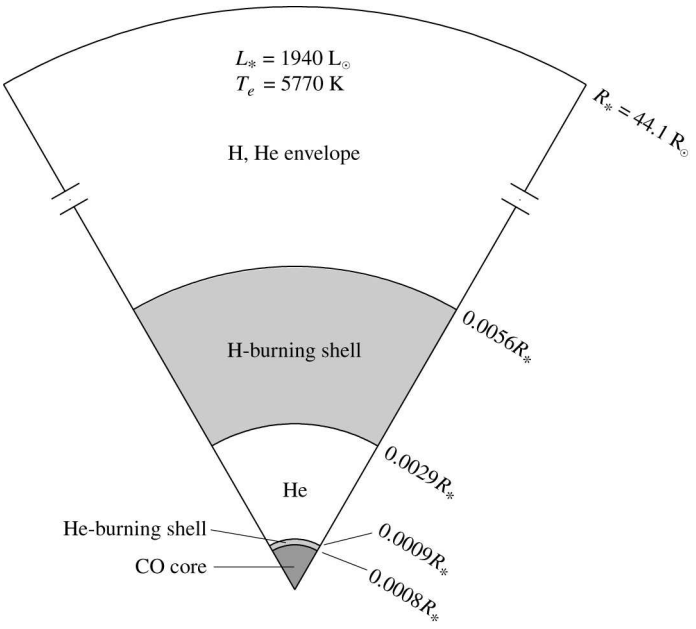

Fig. 1.7: A basic schematic of the interior layers of a $5\,M_\odot$, solar-metallicity AGB star designed to give some understanding as to the scales of the various layers with the overall radius of the star. Image from Carroll & Ostlie (2006).

The increasing luminosities brought about from He shell burning causes the AGB star's envelope to extend further and the star to evolve near the Hayashi limit on the H-R diagram. The freshly synthesised He from the H burning shell falls to the He rich layer, causing its density to increase and for it to become degenerate. The pressure and heat in the He shell causes the He to ignite periodically in a violent He shell flash. The effect of the flash pushes the H burning shell further out (in terms of its radius coordinate relative to the core), which cools the shell and causes it to extinguish.

The He shell will begin to contract again until the H shell is once again ignited. This process acts periodically ($\sim 10^4$ yr, Karakas, 2003) and is known as the thermal pulsing asymptotic giant branch (TP-AGB) phase, which is discussed below.

Low- to intermediate-mass stars that are on the AGB experience severe mass loss through stellar winds. The theoretical understanding of AGB mass loss is still incomplete. An extensive review on current mass loss theory is presented in Willson (2000) and more recent theoretical models are presented in Mattsson & Höfner (2011) and Ventura et al. (2012). For the purposes of this short review, the mechanisms for mass loss are not important. By means of these stellar wind mechanisms, coupled with high luminosities and stellar pulsations brought upon by flash episodes, material that has been through dredge-up can be ejected into space during this phase where it will enrich the ISM.

Thermal pulsing and third dredge-up

Third dredge-up occurs during a star's AGB phase over a period of instability where the star experiences several thermal pulses. The star is gravitationally supported by H and He shell burning where thermal instabilities in the He shell cause it to ignite violently and flash roughly every 10^4 yr (Karakas, 2003).

A He flash increases the energy output of the He burning shell. This causes a convection zone between the H and He burning shells in the He shell (see Fig. 1.5). The convection zone in the envelope deepens with the He shell flashes. After the first thermal pulse the AGB star is said to be a TP-AGB star. These flashes may cause the convective regions in the AGB star to descend into the regions where He burning has taken place, mixing freshly synthesised material with the stellar atmosphere. It can cause the star to become C-rich (C/O ratios greater than 1) and is known as third dredge-up. However, for intermediate-mass stars, $M \gtrsim 4\,\mathrm{M}_\odot$ (Ventura & D'Antona, 2011), during the periods in between thermal pulsing, CNO-cycle burning at the base of the convective envelope via hot bottom burning can convert the majority of ^{12}C, dredged-up by third dredge-up, into ^{14}N, impeding the formation of a C-rich star (Renzini & Voli, 1981)

Third dredge-up is an important mixing event for the purposes of this thesis as it is the mechanism by which the products of s-process nucleosynthesis are brought to the surface. Details on the s-process site are discussed in detail in §1.3.1.

Post AGB and planetary nebulae

For more massive stars ($M \geq 10\,\mathrm{M}_{\odot}$) the fusion processes continue onto C, O and Si burning. However, for low- to intermediate-mass stars fusion ceases after He and H shell burning. As the degenerate CO core cools through neutrino losses, the outward pressure it exerts will decrease. This means that the surrounding layers will begin to contract. As mentioned above, AGB stars experience high mass loss rates[6]. As the stellar wind begins to deplete the H envelope, the star will evolve toward the bluer side of the H-R diagram (top of Fig. 1.1). The severe mass-loss and increase in luminosity is typical of a star that has evolved to be a post-AGB (Kwok, 2000).

When the central star is hot enough ($T \sim 30\,000\,\mathrm{K}$) it will ionise the ejecta from mass loss. As the gas from the detached envelope expands ever outward, ultraviolet light emitted from the central star can be absorbed by the gas. The excited electrons re-emit photons in the visible wavelength range, causing it to glow. This object is known as a planetary nebular (PN). This period is relatively short lived as specific conditions for nebula emission are only fulfilled over a short period of time. The gas from the PN will dissipate, enriching the ISM. Eventually the chemically rich gas will become part of a new collapsing gas cloud system where new, more metal-rich stars are formed. The electron degenerate central star enters the white dwarf cooling sequence and will remain structurally unchanged and cool down for the rest of time.

1.1.2 Massive stars

The evolution of a massive stars differs from low- to intermediate-mass stars on the H-R diagram, as Fig. 1.8 shows. As will be discussed in the later parts of §1.2, SN progenitors ($M \geq 10\,\mathrm{M}_{\odot}$) evolve from massive stars. Conti (1976) proposed a scheme,

[6]This is dependent on metallicity; high metallicity increases mass loss efficiency due to high opacities in the atmosphere. Low metallicity stars retain more of their envelope as opacity driven winds are less efficient.

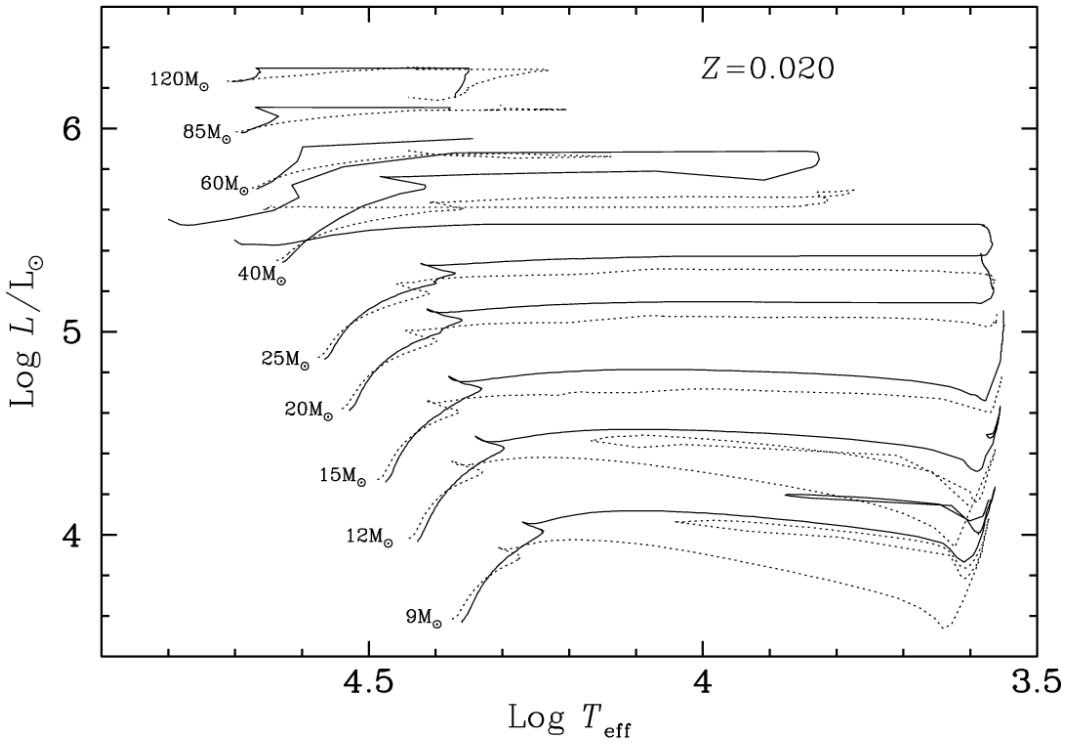

Fig. 1.8: A H-R diagram schematic for massive solar-metallicity stars with an initial rotation of $300\,\mathrm{km\,s^{-1}}$ (*solid lines*) and without rotation (*dotted lines*). Image from Meynet & Maeder (2003).

the so-called Conti Scenario, for massive star evolution that included the existence of Wolf-Rayet (WR) stars discovered by C. Wolf and G. Rayet in 1876, which I shall discuss shortly. In the Conti Scenario massive O-type stars evolve through different phases of evolution, which are dependent on the star's initial mass.

The Conti Scenario is outlined in Fig. 1.9. It must be stated that this is a purely theoretical scenario, but it does illustrate diversity of massive star evolution if true. However the mass limits shown would be a function of the star's metallicity (Massey, 2003). The best known super-massive star in the Milky Way is η-Carinae. Mass determinations of this star are variable, but current mass limits set this star between 80 and $120\,\mathrm{M}_\odot$ (Davidson & Humphreys, 1997; Hillier et al., 2001), which makes it the most massive star known in our galaxy. It is also an ideal example of a luminous blue variable (LBV) star. Similarly, a well known red supergiant (RSG) star is Betelgeuse. These stars are also very good examples of massive star mass-loss. Present estimates show the current mass-loss rate of η-Carinae $\dot{M} \gtrsim 10^{-4}\,\mathrm{M}_\odot\,\mathrm{yr}^{-1}$ (Davidson & Humphreys, 1997), whilst Betelgeuse has a mass loss $\dot{M} \approx 10^{-6}\,\mathrm{M}_\odot\,\mathrm{yr}^{-1}$ (Mauron & Josselin, 2011).

$$
\begin{aligned}
M > 85\,\mathrm{M}_{\odot} &: \text{MS} \longrightarrow \text{LBV} \longrightarrow \text{WN} \longrightarrow \text{WC} \longrightarrow \text{SN} \\
40\,\mathrm{M}_{\odot} \leq M \leq 85\,\mathrm{M}_{\odot} &: \text{MS} \longrightarrow \text{WN} \longrightarrow \text{WC} \longrightarrow \text{SN} \\
25\,\mathrm{M}_{\odot} \leq M \leq 40\,\mathrm{M}_{\odot} &: \text{MS} \longrightarrow \text{RSG} \longrightarrow \text{WN} \longrightarrow \text{WC} \longrightarrow \text{SN} \\
20\,\mathrm{M}_{\odot} \leq M \leq 25\,\mathrm{M}_{\odot} &: \text{MS} \longrightarrow \text{RSG} \longrightarrow \text{WN} \longrightarrow \text{SN} \\
10\,\mathrm{M}_{\odot} \leq M \leq 20\,\mathrm{M}_{\odot} &: \text{MS} \longrightarrow \text{RSG} \longrightarrow \text{BSG} \longrightarrow \text{SN}
\end{aligned}
$$

Fig. 1.9: The Conti Scenario for massive star evolution.

Massive stars on the main-sequence

The main-sequence phase of a massive star will consist of similar processes to those we observe in low- to intermediate-mass stars; fusion of H to He via the CNO-cycles. The effective temperatures of these stars are $\sim 30\,000 - 50\,000\,\mathrm{K}$ (Massey, 2003). During their lifetime on the main-sequence, their effective temperatures will begin to decrease whilst their bolometric[7] luminosities remain relatively unchanged. This is because most of the bolometric luminosity is radiated at wavelengths beyond the visible region of the spectrum, e.g. ultraviolet. When the temperature decreases, there is a shift in wavelength from which the majority of the luminosity is radiated, in accordance with Wien's law, meaning that more of the luminosity is radiated in the visible part of the spectrum; the star will get brighter as it evolves. Therefore it is difficult to classify these stars as, e.g. a zero-age $60\,\mathrm{M}_{\odot}$ star has an almost identical spectral type as an older $85\,\mathrm{M}_{\odot}$ star (Massey, 2003).

During the main-sequence and subsequent evolutionary phases, their high luminosities and strong stellar winds have a large impact on the surrounding ISM. They effectively drive the evolution of galaxies. In fact Brott et al. (2011a) say that one can think of massive stars as cosmic engines. Whether they drive (Koo et al., 2008) or disrupt (Massey, 1998) further star formation is still very much in debate. Issues surrounding mixing and mass-loss massive star evolutionary models have long been a problem (Chiosi & Maeder, 1986), and are still being perfected today (Brott et al., 2011a,b).

[7] The total energy radiated by a star at all wavelengths.

Red supergiant stars

Current theory suggests that stars, such as Betelgeuse, with $M \lesssim 40\,\mathrm{M}_{\odot}$ evolve off the main-sequence through the RSG branch (Massey, 2003). Problems between observations and models are prominent for this transition as current evolution codes cannot evolve a massive main-sequence star to the RSG branch because they cannot cool the main-sequence atmospheres sufficiently to produce RSGs. It is believed that this has to do with how mixing in the stellar atmosphere is dealt with (Maeder & Meynet, 1987). Metallicity appears to have a large impact on RSG production. As the metallicity is increased, it would appear that the length of time a star spends as a RSG decreases as mass-loss rates increase with increasing metallicity (Massey, 2003).

Luminous blue variable stars

LBV stars (Conti, 1984) have extremely variable mass-loss rates that can be as high as $10^{-1}\,\mathrm{M}_{\odot}\,\mathrm{yr}^{-1}$ (Massey, 2003), coupled with increases in visual magnitude ($> 1-2\,\mathrm{dex}$) leading to large alterations in spectral type (Conti, 1997). These outbursts can happen on time-scales of the order of $10^{1} - 10^{2}\,\mathrm{yr}$ (Massey, 2003) making them difficult to classify but when they are experiencing one of these events, they are amongst the brightest resolved stellar objects in the Universe. The mechanism(s) behind these periods of extreme variability is not yet understood as detection of these objects is difficult due to long periods without change (relative to human lifetimes) in their spectral classification (Davidson & Humphreys, 1997; Massey, 2003).

As stated, η-Carinae's mass-loss is currently measured at $\dot{M} \gtrsim 10^{-4}\,\mathrm{M}_{\odot}\,\mathrm{yr}^{-1}$, however during the 1840's there was a very large increase in its apparent magnitude and mass-loss rate (Hillier et al., 2001). It is still unclear what the mechanisms that drove this transformation were and evidence would suggest that this was not an isolated event. Proper motion studies conducted by Walborn et al. (1978) seem to suggest that another similar event occurred in the 15^{th} century. If one chooses to accept the Conti Scenario (Fig. 1.9), η-Carinae is in the early stages of massive star evolution as a LBV.

Wolf-Rayet stars

Another type of star that experiences heavy mass-loss is a WR star, with mass-loss rates $\dot{M} > 10^{-4}\,\mathrm{M_{\odot}yr^{-1}}$, which can be seen through their strong emission lines (Nugis et al., 1998). They are known via chemical analysis of their atmospheres to have evolved stellar surfaces. In the early stages of the WR phase the star's spectrum will most likely include strong N emission lines, which is in good agreement with the products of the CNO-cycle, as N is overproduced relative to C and O in massive stars during CNO cycling (Maeder, 1983). Such a star is known as a WN type WR star.

Strong winds will eventually blow away this N layer and its spectrum will change to show almost no N but strong C lines with a little O. These are known as WC or WO type WR stars. WO stars are very rare and depend upon the products of the triple-α process. In general C will be more abundant than O (Maeder, 1983).

According to theory only the most massive stars, with metallicities approaching solar or beyond, will achieve sufficient mass-loss to evolve through to the WC or WO phase (see Fig. 1.9). WR stars are progenitors to Type Ib/c SNe, which have a similar core collapse mechanism to the more common Type II SNe but H lines are absent. The basic distinction between Type Ib and Type Ic SNe comes from the presence or absence of strong He lines respectively. It is therefore quite clear that these stars would have significant impact on the chemistry of the Galaxy. However, the existence of WR stars would only emerge once the metallicity of the Galaxy was high enough. This is discussed further in §1.2.

Further burning stages

Early burning phases of massive stars would include H burning and He burning via the CNO-cycle, pp-chain and the triple-α processes, like those found in low- to intermediate-mass stars. The high central temperatures in massive stars would mean that these processes would have increased burning rates when compared to lower-mass stars, which would lead to shorter time-scales on the main-sequence and early giant phases. However, for massive stars thermonuclear fusion will not cease with the termination of the

triple-α process.

As temperatures rise to $T > 6 \times 10^8$ K, C begins to fuse with itself. There are many variations on the end product of C–C burning that are energetically allowable, unlike the previous reactions discussed in §1.1.1.

Fig. 1.10 shows the various paths C–C burning can take. Experiments conducted in the laboratory show the $^{12}\mathrm{C}(^{12}\mathrm{C},\mathrm{p})^{23}\mathrm{Na}$ and $^{12}\mathrm{C}(^{12}\mathrm{C},\alpha)^{20}\mathrm{Ne}$ reactions have nearly equal probability of occurring, whereas $^{12}\mathrm{C}\,(^{12}\mathrm{C},\gamma)\,^{24}\mathrm{Mg}$ and $^{12}\mathrm{C}\,(^{12}\mathrm{C},2\alpha)\,^{16}\mathrm{O}$ reactions have a low probability of occurring. Therefore it can be expected that the products of the C burning process are dominated by ^{23}Na, ^{20}Ne, protons and α-particles (Clayton, 1984). There is a significant network of secondary reactions that occur alongside C burning. The protons and α-particles will quickly be captured by other isotopes at these high temperatures as their Coulomb barriers are so low.

$^{12}\mathrm{C}\,(^{12}\mathrm{C},\gamma)\,^{24}\mathrm{Mg}$	$^{16}\mathrm{O}\,(^{16}\mathrm{O},\gamma)\,^{32}\mathrm{S}$
$^{12}\mathrm{C}\,(^{12}\mathrm{C},\mathrm{n})\,^{23}\mathrm{Mg}$	$^{16}\mathrm{O}\,(^{16}\mathrm{O},\mathrm{p})\,^{31}\mathrm{p}$
$^{12}\mathrm{C}\,(^{12}\mathrm{C},\mathrm{p})\,^{23}\mathrm{Na}$	$^{16}\mathrm{O}\,(^{16}\mathrm{O},\mathrm{n})\,^{31}\mathrm{S}$
$^{12}\mathrm{C}\,(^{12}\mathrm{C},\alpha)\,^{20}\mathrm{Ne}$	$^{16}\mathrm{O}\,(^{16}\mathrm{O},\alpha)\,^{28}\mathrm{Si}$
$^{12}\mathrm{C}\,(^{12}\mathrm{C},2\alpha)\,^{16}\mathrm{O}$	$^{16}\mathrm{O}\,(^{16}\mathrm{O},2\alpha)\,^{24}\mathrm{Mg}$

Fig. 1.10: The C–C and O–O burning paths.

At temperatures high enough for C burning the Coulomb barrier is still large enough so that the $^{12}\mathrm{C} + {}^{16}\mathrm{O}$ reaction is too slow to contribute significantly. Then, as the star contracts and temperatures sufficiently rise for it to occur, C is all but depleted. Therefore the next set of reactions to significantly affect stellar abundances are ^{16}O burning, which like C burning has several energetically allowable routes, see Fig. 1.10.

This channel of reactions has a slightly larger set of secondary reactions than C burning. Also the isotopes involved can be heavier, as the temperature ($T > 1 \times 10^9$ K) helps overcome the Coulomb barrier. Also, like C burning there is a higher probability route that O burning takes; the most abundant final isotope from the primary set of reactions is ^{28}Si.

At $T > 3 \times 10^9$ K, Si burning can take place to produce nuclei around the Fe-peak.

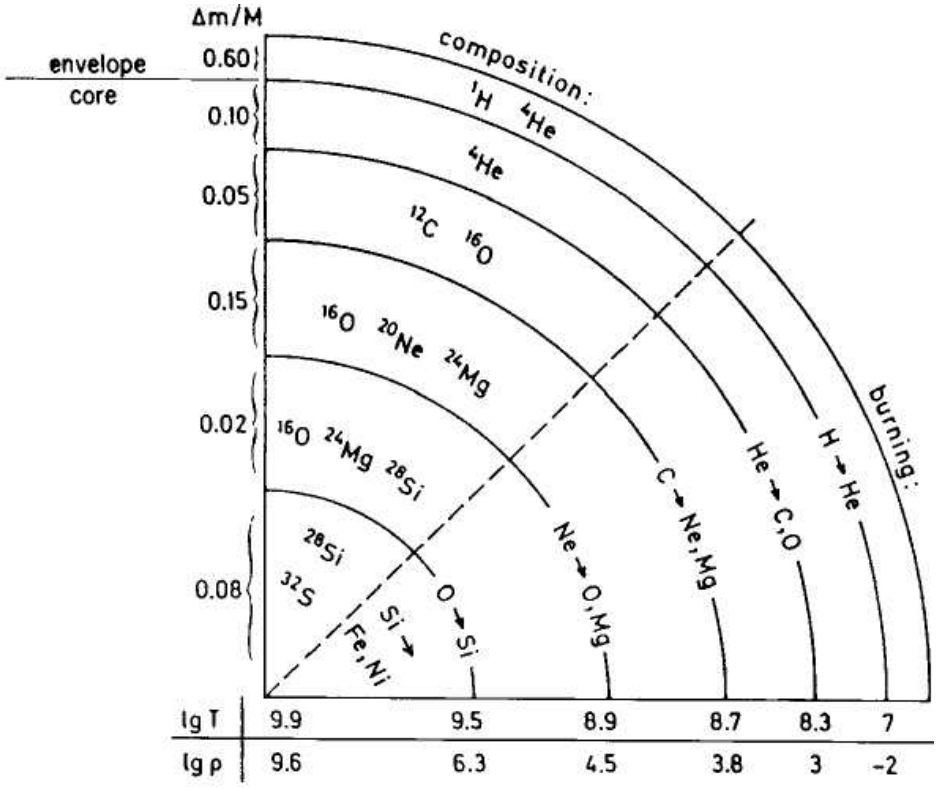

Fig. 1.11: A schematic layout of a SNe progenitor, in this case a well evolved $25\,M_\odot$ star, showing the different layers of nucleosynthesis events (not to scale). This is for illustration purposes only. Image from Kippenhahn & Weigert (1990).

However, at these temperatures nuclides can be broken down into lighter species. This occurrence, called photodisintegration, is similar to photoionisation of atoms but this time the reaction is nuclear, not atomic. Photodisintegration of a species usually occurs at temperatures roughly 10^6 times higher than its photoionisation since ionisation energies are of order 8 eV whereas nuclear binding energies (per nucleon) are around 8 MeV. During the Si burning phase (which is extremely short-lived if it occurs at all) nuclides are continuously being fused together and broken down. In fact one of the first major disintegrations, which is initialised before O–O burning is ^{20}Ne via the reaction $^{20}\mathrm{Ne}(\gamma,\alpha)^{16}\mathrm{O}$ (Clayton, 1984).

Chief among the isotopes produced during Si burning is Fe. This is one of the most stable of the elements as it has almost the highest nuclear binding energy per nucleon. Fig. 1.11 shows how the various advanced burning stages could influence the interior of a massive star (in this example $M = 25\,M_\odot$). It shows an almost "onion skin" structure.

After this short-lived phase, the core will collapse under its own gravity. This generates a thermal runaway, triggered by electron capture and photodisintegration, on dynamical time-scales of $\sim 1\,\mathrm{ms}$ (Prialnik, 2000). Details of SNe events can be found at the end of §1.2. This is believed to be a critical time for heavy element production, particularly for r-process nucleosynthesis, which I will discuss in §1.3.2. I now move on to discuss how the first stars in the Universe formed, evolved and died.

1.2 The first stars

Moments after the big bang, $t \approx 2\,\mathrm{s}$, protons and neutrons began to combine to form d, He and trace amounts of Li. This was known as big bang nucleosynthesis (BBN). The whole process lasted only a few minutes. After the Universe was roughly ten minutes old, temperatures and densities required for nuclear fusion were too low and nucleosynthesis stopped. Throughout, free neutrons, which are unstable ($\tau_\mathrm{n} = 890\,\mathrm{s}$), decayed into protons via the reaction $\mathrm{n} \left(\mathrm{e}^- \bar{\nu}_\mathrm{e}\right) \mathrm{p}$ (Wagoner et al., 1967).

After the Universe had cooled sufficiently ($t \approx 3 \times 10^5\,\mathrm{yr}$), protons began to combine with electrons to form atoms. This was known as the epoch of recombination. Up until this stage the Universe was opaque, as free electrons caused photons to scatter. Recombination caused photons to decouple from matter and the Universe became transparent for the first time. The first stars that formed in the Universe induced photoionisation in the surrounding areas of gas, causing them to ionise. This was known as the epoch of reionisation and occurred roughly 30 Myr after the big bang, or at redshift, $z \approx 65$ (Naoz et al., 2006).

Formation

The first stars are believed to have formed in dark matter halos from pristine gas, i.e. gas composed of the remnants of BBN. These primordial, metal-free stars are known as population III stars. Although never observed, population III stars are thought to be super-massive, $M > 100\,\mathrm{M}_\odot$, due to a top-heavy initial mass function (IMF), brought upon by the lack of effective gas cloud cooling during star formation (Abel

et al., 2002; O'Shea & Norman, 2007). In the current epoch of star formation, the most effective gas cloud cooling is through interactions between high velocity particles and metals, which would ionise the metals, decrease the particles' velocities, and thus cool down the gas. Energy escapes the system via line radiation when the ionised gas de-excites. As pristine gas is free of metals, molecular hydrogen (H_2), which is less efficient at cooling than metals is the primary cooling mechanism. This means that higher temperatures are required in order to excite the rotational and vibrational energy states of H_2 (Tegmark et al., 1997).

Nakamura & Umemura (2001) propose that the IMF could in fact be bimodal with peaks about $1\,M_\odot$ and $100\,M_\odot$. They state that the initial mass of the star would depend on the density of the primordial gas cloud. For higher mass gas clouds, where H_2 cooling is more effective, the fragmentation mass is lowered to $1\,M_\odot$, but their models do predict that the majority of the mass fraction falls at $100\,M_\odot$. Contrary to this however, the latest 3D simulations of population III star formation show that protostellar cores do not fracture when the gas becomes fully molecular into several, less massive cores viz. several stars, but rather collapse to form one super-massive star (Abel et al., 2002). Typically then only a single population III star would form in any one dark matter halo.

Evolution

The lack of empirical evidence makes it difficult to predict the evolution of population III stars; their evolution could differ from other stars studied in the Galaxy because of their chemical composition. Magnetic fields would certainly be less significant to population III evolution as field strengths would be minute in comparison to population I (metal-rich) stars due to the lack of ionised metals, which are responsible for a significant portion of a stellar magnetic field. Population III stars would certainly form with a much smaller initial magnetic field (O'Shea & Norman, 2007).

Another large departure between metal-rich and metal-free evolution would be the nuclear processes occurring in the core during the main-sequence. It is well understood that the CNO-cycle acts as the dominant nuclear process in more massive stars on the

main-sequence. However, metal-free stars would not initially have the necessary nuclei for the CNO-cycle to occur. Rather, a population III star would have to rely on the p-p chain for its energy generation. The p-p chain is less efficient compared to the CNO-cycle, which means that extremely high temperatures must be reached in the stellar core to sustain surface radiation losses (Marigo et al., 2001). It is therefore plausible that C, N and O could form via the triple-α process, in the core of a metal-free star during its main-sequence phase (Cassisi & Castellani, 1993), which would imply that the p-p chain and triple-α processes could occur at the same time. This would mean that during a star's lifetime on the main-sequence a switch from the p-p chain to the CNO-cycle as the primary energy source could occur, which could affect the stellar structure (Marigo et al., 2001).

Theoretical simulations of metal-free star evolution seem to suggest their evolution for a given mass would not differ much from the evolution of a metal-rich star of the same mass. According to Marigo et al. (2001) population III stars with low- to intermediate mass would have a main-sequence, RGB and AGB phase in their evolution, and stars with high-mass would continue through C, N, O and Si burning, like a massive metal-rich star. However, unlike metal-rich populations, massive population III stars would not develop high opacity-driven super-winds, which otherwise would blow away large amounts of their atmospheres and cause severe mass loss. This means that population III stars would not evolve through the WR phase of evolution like massive metal-rich stars (discussed in §1.1.2). Chemical enrichment of their atmospheres through dredge-up phases also seem to occur in these models. Dredge-up is discussed in §1.1.1 in the context of low- to intermediate-mass stellar evolution. However, models by Lau et al. (2008) find that He core luminosities are too low during an AGB thermal pulse for third dredge-up to occur in metal-free regimes in $5\,M_\odot$ and $7\,M_\odot$ stars.

Another possible difference between present epoch and population III evolution could be due to the higher rotational speeds in low metallicity stars achieved by less efficient mechanisms that would otherwise reduce the angular momentum in the system, such as magnetic winds (discussed briefly in §1.1.2). Rotation has effects on both the evolution of the star and chemical mixing processes that occur, and the SN event at

the end of the star's life (Meynet et al., 2006; Chiappini et al., 2006; Heger & Woosley, 2010)

Death

It is well studied and understood that massive stars are short lived. We can quantify their lifetimes using equations found in Romano et al. (2005). The typical lifetimes of $8\,M_\odot$, $140\,M_\odot$, and $260\,M_\odot$ stars are ~ 36.5, 0.2, and 0.07 Myr respectively.

At the end of a massive star's life, if there has not been sufficient mass loss, the star becomes highly unstable as all its thermonuclear fusion processes cease. When this occurs it has long been understood that the star will explode as a SN (Baade & Zwicky, 1934) depending on the size of the star (Heger et al., 2003). Run away nuclear processes can lead to the quick production of heavy elements via the e-, p- and r-processes. The r-process is discussed in detail in §1.3.2.

The e-process involves a series of (γ, α), (γ, n), (γ, p), (α, γ), (p, γ), (n, γ), (p, n) reactions with elements close to the Fe-peak that will convert them from one element, e.g. Fe, to another, such as V, Cr and Mn (Hoyle, 1946, 1954; Hainebach et al., 1974). The p-process involves a series of proton-captures that lead to a small abundance of heavy elements not synthesised via either of the two neutron-captures (Burbidge et al., 1957; Glorius et al., 2011). For either of these two processes to occur conditions leading to very high temperatures ($T > 10^9\,\mathrm{K}$) must be satisfied. Both processes are beyond the scope of the work discussed in this thesis, but references supplied here give detailed accounts to both of them.

The most common and most understood of the three types of SNe discussed here is a core-collapse SN. This occurs in stars with a SN progenitor mass range $10\,M_\odot \leq M \leq 140\,M_\odot$ (Anderson & James, 2008) but is also reported to occur in stars with masses down to $8\,M_\odot$ (Smartt, 2009). However, this mass range may also depend on metallicity (Cassisi & Castellani, 1993). The top panel of Fig. 1.12 illustrates the mass threshold of each core-collapse SN as a function of metallicity. As the thermonuclear processes cease, the core undergoes rapid contraction. The outer layers of the star, which are primary candidates as sites for the r-process (Wheeler et al., 1998; Kajino

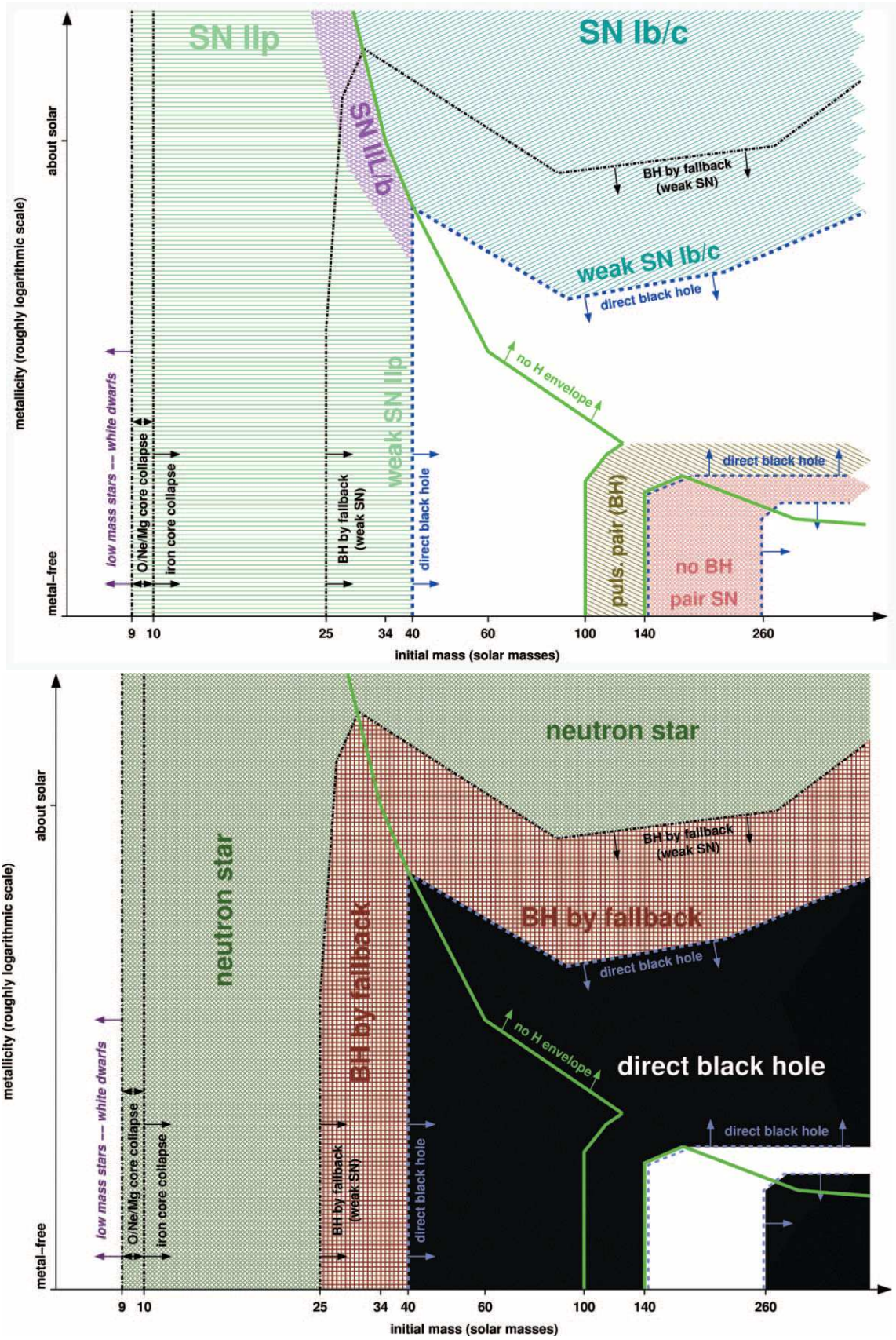

Fig. 1.12: *Top*: The mass/metallicity relationship for a given type of SN event. The two white regions represent complete collapse of the star with no SN explosion. *Bottom*: SN remnants for a given initial mass as a function of metallicity. Both figures are the product of evolution models for non-rotating single stars with mass ranges $9 - 300\,M_{\odot}$. Mass loss is also taken into account in the evolution models used to generate the two figures, which are taken from Heger et al. (2003).

et al., 2002), are explosively ejected into the ISM. In this type of SN explosion, a core remnant is left behind.

The core-collapse SN can be split into three distinct categories; Type II, Type Ib, and Type Ic. Type Ib/c SNe have a similar core collapse mechanism to Type II SNe but their spectra are devoid of H lines, and are distinct from each other through the presence or absence of strong He lines respectively.

In solar metallicity regimes Type Ib/c SNe cover the high end of the mass range ($M > 34\,\mathrm{M}_\odot$, Heger et al., 2003), removing the possibility of pair instability (PI) SN or direct collapse (discussed below). This is not entirely surprising as Type Ib/c SN progenitors experience high mass loss (Heger et al., 2003) and super-winds as they evolve through the WR phase. WR stars and Type Ib/c SNe are briefly discussed in §1.1.2. In metal-free and metal-poor stars, a Type II SN is expected for the lower mass range of progenitors ($M < 40\,\mathrm{M}_\odot$).

The bottom panel of Fig. 1.12 shows that for the progenitor mass range of $9-25\,\mathrm{M}_\odot$ in metal-free populations, a neutron star is produced[8]. As the core collapses, temperatures and pressures increase dramatically. The increase of pressure and temperature create the necessary conditions for electron capture, $\mathrm{p}\,(\mathrm{e}, \bar{\nu}_\mathrm{e})\,\mathrm{n}$, on very short timescales. Neutrons, like electrons, are fermions, which are subject to the Pauli exclusion principle. This leaves an extremely dense, neutron-degenerate remnant which is left to cool for eternity. Between the masses of $25 - 40\,\mathrm{M}_\odot$ (Fig. 1.12 bottom panel) a black hole by fall back is produced. This occurs when the core collapses into a massive neutron star and the gravity it produces causes some of the SN ejecta to fall back in to the remnant, which increases its mass. The degenerate neutron pressure is no longer able to balance the enormous gravitational force of the structure and the star undergoes further collapse into a singularity, or black hole. Finally between the masses of $40 - 140\,\mathrm{M}_\odot$ the stellar core will directly collapse under its own gravity to a black hole (Heger et al., 2003).

In extremely high-mass stars of mass range $140\,\mathrm{M}_\odot < M < 260\,\mathrm{M}_\odot$, in low metallic-

[8]For high metallicity stars, $Z \geq \mathrm{Z}_\odot$, with $M > 34\,\mathrm{M}_\odot$ the remnant is extremely metallicity dependent as the bottom panel of Fig. 1.12 illustrates.

ity regimes, PI SNe occur. Here, high temperatures and the onset of the pair-production (e^-/e^+) instability, brought on by $\gamma(\gamma, e^+)e^-$ reduces thermal pressure inside the star and produces a thermonuclear runaway. This reverses the gravitational collapse and ejects the entire star into the ISM with a highly energetic explosion ($E \leq 10^{53}$ erg), which leaves no remnant behind (Kasen et al., 2011). The SN event can be long lasting; expectations from simulations indicate a PI SN flash could last up to 300 days. As metal-free stars would experience very little mass loss throughout their lifetime as the lack of metals would drive down opacities, PI SNe may have been fairly common in the early Universe and may have contributed a high fraction to the chemical enrichment in metal-free/poor regimes. In the present epoch of star formation, models such as those presented in Fig. 1.12 would seem to suggest that high metal content would prevent stars exploding as PI SN, however, evidence presented in Gal-Yam et al. (2009) suggest that SN2007bi may in fact have been a PI SN.

Stars with $M > 260\,M_\odot$ in metal-poor regimes are thought to go through total collapse (Fig. 1.12, bottom panel). This means that the star would collapse with no ejecta into a black hole with no SN (Fryer et al., 2001). Therefore the super-massive star would not enrich the ISM with newly synthesised material. However, if the IMF at early times is as described in Nakamura & Umemura (2001) then these stars would still be quite rare.

After the SN event, for SN projector masses $M < 260\,M_\odot$, chemically rich material will be ejected into the ISM, polluting the metal-free environment. New stars will begin to form from gas enriched by the SNe remnants of the population III stars. The higher metal content will help in gas cloud cooling and less massive, metal-poor stars will emerge. With the understanding of massive star lifetimes and the violent nature of SN events, it would be plausible to believe that the population III epoch would have been very short lived, relative to the lifetimes of low-mass stars we observe in the metal-rich environment of the present Universe.

With the onset of SNe events of population III stars, the heavy elements that are synthesised via the r-process path should begin to pollute the ISM, but those produced via the s-process should not. This is because the s-process, which occurs in earlier

stages of massive star evolution, requires Fe seed nuclei to be present. As metal-free stars do not have any initial metal content, there will be no Fe available for the s-process to take place, as Fe is only produced in the much later stages of nuclear burning in massive stars. I shall now move on and discuss the neutron-capture processes in detail. I clarify the distinction between the two processes and the locations of where they occur.

1.3 The neutron-capture processes

In §1.1 we considered the various thermonuclear fusion processes that occur in a star as it evolves along the H-R diagram. After a star's death, the products of those reactions will be expelled from the star and enrich the ISM. However the products of the processes discussed so far only account for the first 26 known elements of the periodic table. The majority of the heavier isotopes are synthesised via a series of neutron-captures by seed nuclei, typically assumed to be ^{56}Fe.

Proton-captures contribute a very small fraction to the heavy element abundances. Like thermonuclear fusion, proton-captures have to overcome the Coulomb barrier. For lighter isotopes in high temperature environments, such as SNe sites, this isn't particularly difficult. However, when overcoming the Coulomb barrier of heavy elements proton captures become rare. As such, proton-captures do not contribute much to the heavy element abundance. As this thesis is not centred around proton-captures, they will not be discussed any further.

There are two types of neutron-capture, the slow (s-) process and the rapid (r-) process. The s-process neutron-capture rate is much slower than the β-decay rate of the unstable isotope, whereas neutron-captures for the r-process occur on time-scales much shorter than β-decay rates. This is due to the neutron fluxes in the environments where the r- and s-processes occur, which will be discussed in §1.3.1 & §1.3.2.

For the s-process, which takes place during evolutionary states prior to the formation of Fe, the Fe seed nuclei must be present during the star's formation for it to occur. The Fe content remains constant from formation up until the s-process initialises. The

r-process, which is believed to occur in SNe, does not require any Fe in the progenitor star, as massive stars can fuse up to the Fe-peak. Even during the SNe event, freshly synthesised Fe is still being produced, see further burning stages in §1.1.2. Also we know that massive stars are short lived relative to lower mass stars. This would imply that the r-process would occur shortly after the formation of the first stars, which means that in metal-free and metal-poor environments the majority of the elements beyond the Fe-peak must have formed via the r-process (Truran, 1981).

1.3.1 The s-process

The s-process is defined as the path taken by neutron-capture that runs along the valley of β stability (Burbidge et al., 1957). This is represented by the thick black line on Fig. 1.13. In other words the flux of neutrons is low, which allows for β-decay of an unstable nucleus, e.g. $(A+1, Z)$, where A and Z are the baryon number and atomic number respectively, to the point of stability, $(A+1, Z+1)$, before another neutron is captured. As such the s-process path is fixed to follow the path of stability.

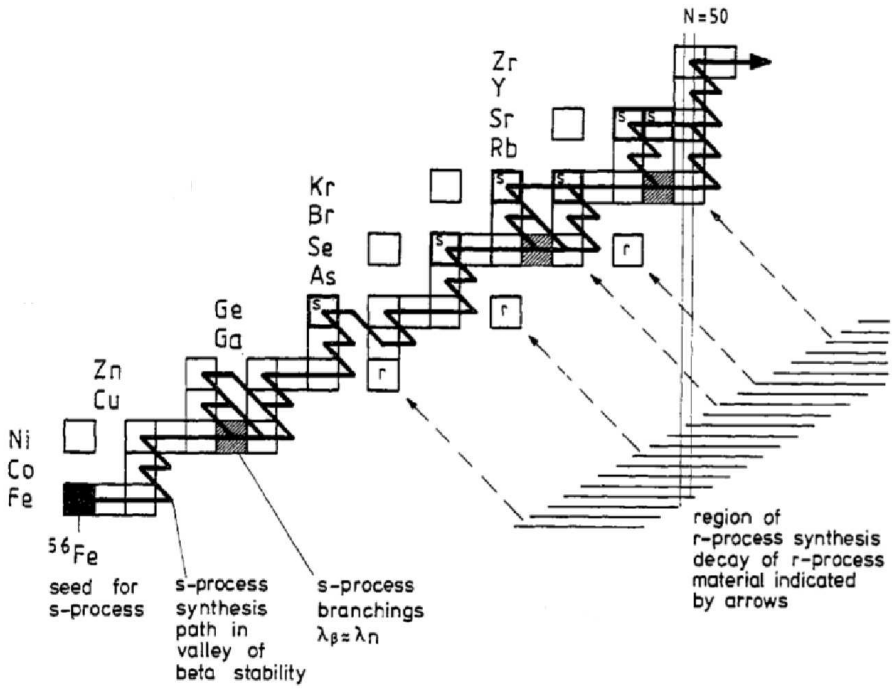

Fig. 1.13: A section of the chart of nuclides showing the stable nuclides and path that the s-process takes (thick black line) along the valley of β stability from Fe to Zr. The dashed diagonal lines show the β-decay of extremely unstable isotopes, which were populated by the r-process. The image also shows the r- and s-process-only isotopes which are created by shielding. Image adapted from Kappeler et al. (1989).

The main s-process

The third dredge-up plays a crucial role in main s-process nucleosynthesis. As discussed in §1.1.1, a star that is on the TP-AGB and is experiencing third dredge-up events is extremely likely to be s-processing as well.

Mixing of C rich material with overlying H and He during third dredge-up events allows for the thermonuclear reaction $^{12}\mathrm{C}(\mathrm{p},\gamma)^{13}\mathrm{N}(\beta^{+})^{13}\mathrm{C}(\alpha,\mathrm{n})^{16}\mathrm{O}$, which releases free neutrons in low- to intermediate-mass stars ($1\,\mathrm{M}_{\odot} \leq M \leq 10\,\mathrm{M}_{\odot}$, Busso et al., 1999). This reaction produces the neutron flux for the s-process to occur and is responsible for the main s-process.

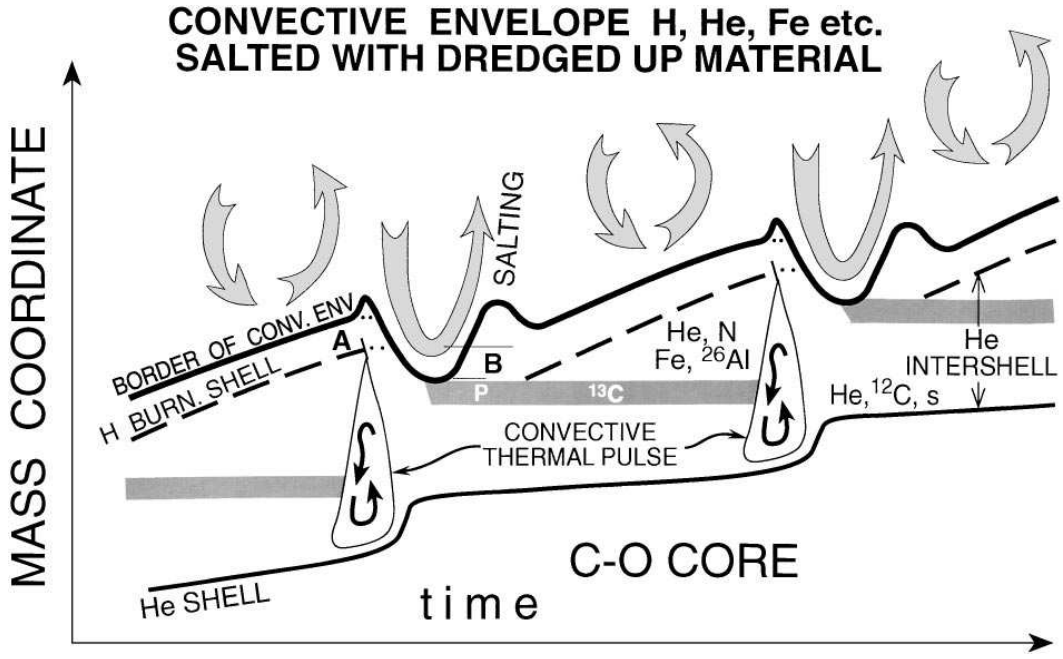

Fig. 1.14: A schematic of chemical mixing during and after a third dredge-up event with respect to the mass coordinate over time. Image from Busso et al. (1999).

Fig. 1.14 shows the third dredge-up events induced by thermal pulses, and how they mix the various layers of the AGB star. When the He shell pulses, the outer layers of the star expand outward. This cools these layers and switches the H burning shell off, which allows for the convective zones in the stellar envelope and the He shell to mix materials (shown as triangular shapes in Fig. 1.14). Some unknown event allows protons to mix down into regions of the star containing C to produce $^{13}\mathrm{C}$, which is represented by the grey regions in Fig. 1.14. Regions *A* (the H burning shell) and *B* (the He shell between the H and He burning shells) in the schematic mix with the

convective envelope which becomes polluted with freshly synthesised material as well as s-process material (Busso et al., 1999).

The main s-process can be observed by measurable Tc abundances in the star's atmosphere. Tc isotopes, which are synthesised by the s-process, are unstable. The ^{98}Tc and ^{99}Tc isotopes have the largest β-decay half-lives, which are very close to the TP-AGB lifetime of a $1\,M_\odot$ star, $\sim 1 - 1.5\,$Myr (Iben, 1983). Studies such as Smith & Lambert (1989) measured abundances of Tc I in TP-AGB stars as a tracer of active s-process sites.

The weak s-process

The weak s-process is responsible for most of the s-process isotopes between Fe and Sr found in solar type stars. It does not have the ability to produce the heavier elements due to the low neutron fluences that are involved in the process (Boothroyd & Sackmann, 1988; Blöcker, 1995). The neutrons are supplied via the reaction $^{22}\mathrm{Ne}\,(\alpha, \mathrm{n})\,^{25}\mathrm{Mg}$, which requires higher temperatures than can be managed in low- to intermediate-mass TP-AGB stars as such more massive stars are required, $M > 8\,M_\odot$ (Pignatari et al., 2010), for the reaction to take place.

The s-process in this case takes place at the end of convective He core burning (Prantzos et al., 1990) and again at the end of convective C shell burning (Raiteri et al., 1991). It will also most likely occur during C core burning, however material synthesised via the s-process path during this time will not contribute significantly to the weak s-process abundance; it is likely any s-process material will collapse with the core during the subsequent SN event before any substantial mixing takes place (Pignatari et al., 2010).

As previously stated (§1.1.1), ^{14}N abundances are important for weak s-processing. The ^{22}Ne abundance originates from the initial ^{14}N abundance, which is converted to ^{22}Ne via the reaction $^{14}\mathrm{N}(\alpha,\gamma)^{18}\mathrm{F}(\beta\nu_\mathrm{e})^{18}\mathrm{O}(\alpha,\gamma)^{22}\mathrm{Ne}$ during He burning. Finally, s-processing takes place once the He core reaches temperatures beyond $2.5 \times 10^8\,$K. However, the supply of ^{22}Ne is not depleted at He core exhaustion and s-processing can continue during C burning once sufficient quantities of α-particles are released via

the reaction $^{12}\mathrm{C}(^{12}\mathrm{C},\alpha)^{20}\mathrm{Ne}$ (Prantzos et al., 1990).

1.3.2 The r-process

For the r-process, neutron-capture occurs on time-scales much faster than subsequent β-decays. While the s-process path is limited to the path of stability (see Fig. 1.13), the r-process path is limited by the neutron drip-line, where the neutron binding energy becomes effectively 0 eV, meaning that neutrons can no longer be added. Unlike the s-process, the r-process path can take many different neutron-capture paths, which is determined by neutron density, n_n, and temperature (Pagel, 1997). The r-process path is not expected to follow the neutron drip-line however, rather the drip-line is an absolute limit on the number of neutrons, N, that a given species, Z, can contain. The drip-line is far from well understood empirically as it has only been completed as far as $Z = 9$ (^{29}F), and according to Woods & Davids (1997) this is not expected to progress too much further in the foreseeable future.

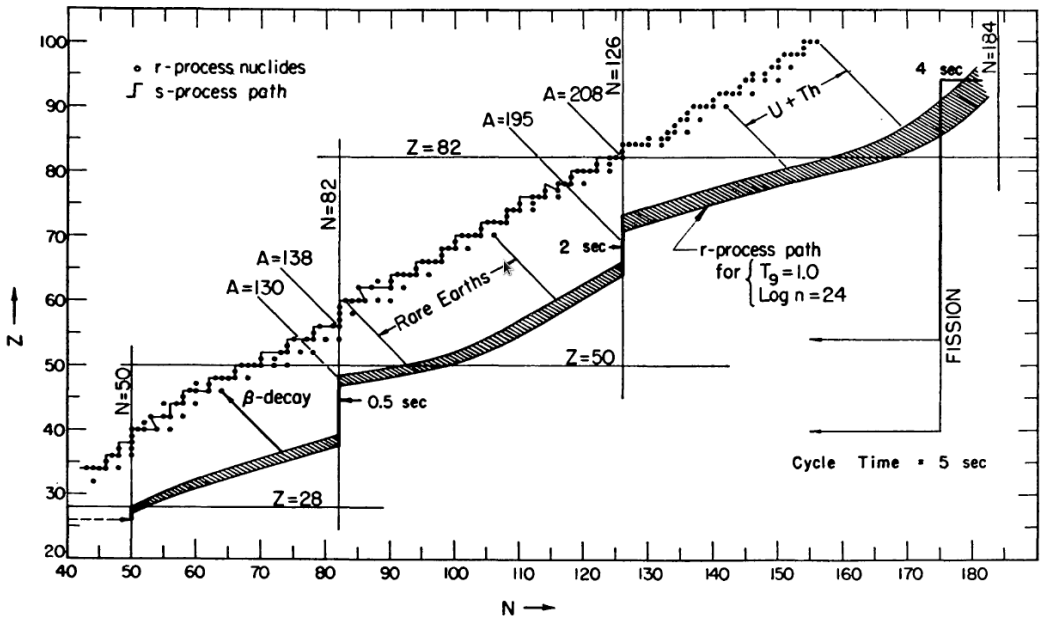

Fig. 1.15: The table of nuclides that demonstrates a range of r-process paths (shaded area) for a temperature range, $0.8\times10^9 \leq T\ (\mathrm{K}) \leq 1.2\times10^9$ and neutron density range, $10^{22} \leq n_\mathrm{n}\ (\mathrm{cm}^{-3}) \leq 10^{26}$. It can be seen that at the magic neutron numbers (28, 50, 126) the neutron-capture rates are halted temporarily until sufficient β-decay has brought the isotope closer to the path of stability, where neutron-capture cross-sections are larger. Image from Seeger et al. (1965).

Fig. 1.15 shows another example of the table of nuclides. Unlike Fig. 1.13, however, it shows a possible route that the r-process could take along the table of nuclides for a

given neutron density and temperature, which was calculated by Seeger et al. (1965). It can be seen at the magic neutron numbers ($N = 50$, 82, 126 etc.) the neutron-capture rate slows down to allow β-decay of extremely unstable isotopes. This is not because the neutron flux is reduced but rather that the isotope cross section is much smaller; isotopes at the magic neutron numbers are statistically unlikely to capture another neutron until the neutron binding energy is large enough, which increases the closer to the valley of stability the unstable isotopes are.

Whereas the s-process can synthesise isotopes up to Bi, with the majority of s-process synthesis ending at Pb, the nature of the r-process path allows heavier, less stable nuclei to form, such as all of the actinides, e.g. Th, U and Pu.

Unlike the s-process, the r-process site is still not established observationally. It is well understood however that the r-process requires environments where nuclear physics allows the production of many many free neutrons and extremely unstable nuclei. Over the years there have been several suggestions for the r-process site, not that there must only be one. These include the "neutrino wind" scenario, where neutrino heated ejecta from high mass SNe allow for r-processing (Meyer et al., 1992; Woosley et al., 1994); neutron star mergers (Freiburghaus et al., 1999; Goriely et al., 2005); a "prompt explosion" of a lower mass ($8\,\mathrm{M}_\odot \leq M \leq 11\,\mathrm{M}_\odot$) SN (Sumiyoshi et al., 2001; Wanajo et al., 2003); and "collapsars" or failed SN explosions, where the core collapse of a star fails to produce a SN explosion and instead collapses to become a low-mass ($2-3\,\mathrm{M}_\odot$) black hole (MacFadyen & Woosley, 1999; Pruet et al., 2004).

All of these scenarios have yet to fully theoretically explain the r-process (Wanajo & Ishimaru, 2006), although the most agreed upon site for the r-process is a SN event. The collapsar and neutron star merger events would be extremely rare relative even to SN explosions.

I shall now move on to Chapter 2 and discuss how I make use of the hyperfine splitting patterns in Ba absorption lines to detect r- and s-process fractions in metal-poor stars. This will include details about spectrum synthesis using a 1-dimensional (1D) local thermodynamic equilibrium (LTE) radiative transfer.

References

Abel, T., Bryan, G. L., & Norman, M. L. 2002, Science, 295, 93 [ADS]

Anderson, J. P. & James, P. A. 2008, MNRAS, 390, 1527 [ADS]

Baade, W. & Zwicky, F. 1934, Physical Review, 46, 76 [ADS]

Blöcker, T. 1995, A&A, 297, 727 [ADS]

Boothroyd, A. I. & Sackmann, I.-J. 1988, ApJ, 328, 653 [ADS]

—. 1999, ApJ, 510, 232 [ADS]

Boothroyd, A. I., Sackmann, I.-J., & Wasserburg, G. J. 1995, ApJ, 442, L21 [ADS]

Brott, I., de Mink, S. E., Cantiello, M., Langer, N., de Koter, A., Evans, C. J., Hunter, I., Trundle, C., & Vink, J. S. 2011a, A&A, 530, A115 [ADS]

Brott, I., Evans, C. J., Hunter, I., de Koter, A., Langer, N., Dufton, P. L., Cantiello, M., Trundle, C., Lennon, D. J., de Mink, S. E., Yoon, S.-C., & Anders, P. 2011b, A&A, 530, A116 [ADS]

Burbidge, E. M., Burbidge, G. R., Fowler, W. A., & Hoyle, F. 1957, Reviews of Modern Physics, 29, 547 [ADS]

Busso, M., Gallino, R., & Wasserburg, G. J. 1999, ARA&A, 37, 239 [ADS]

Carroll, B. W. & Ostlie, D. A. 2006, An introduction to modern astrophysics and cosmology [ADS]

Cassisi, S. & Castellani, V. 1993, ApJS, 88, 509 [ADS]

Charbonnel, C. 1995, ApJ, 453, L41 [ADS]

Chiappini, C., Hirschi, R., Meynet, G., Ekström, S., Maeder, A., & Matteucci, F. 2006, A&A, 449, L27 [ADS]

Chiosi, C. & Maeder, A. 1986, ARA&A, 24, 329 [ADS]

Clayton, D. D. 1984, Principles of stellar evolution and nucleosynthesis. [ADS]

Conti, P. S. 1976, Memoires of the Societe Royale des Sciences de Liege, 9, 193 [ADS]

Conti, P. S. 1984, in IAU Symposium, Vol. 105, Observational Tests of the Stellar Evolution Theory, 233 [ADS]

Conti, P. S. 1997, in Astronomical Society of the Pacific Conference Series, Vol. 120, Luminous Blue Variables: Massive Stars in Transition, 387 [ADS]

Davidson, K. & Humphreys, R. M. 1997, ARA&A, 35, 1 [ADS]

Decressin, T., Charbonnel, C., Siess, L., Palacios, A., Meynet, G., & Georgy, C. 2009, A&A, 505, 727 [ADS]

Freiburghaus, C., Rosswog, S., & Thielemann, F.-K. 1999, ApJ, 525, L121 [ADS]

Fryer, C. L., Woosley, S. E., & Heger, A. 2001, ApJ, 550, 372 [ADS]

Gal-Yam, A., Mazzali, P., Ofek, E. O., Nugent, P. E., Kulkarni, S. R., Kasliwal, M. M., Quimby, R. M., Filippenko, A. V., Cenko, S. B., Chornock, R., Waldman, R., Kasen, D., Sullivan, M., Beshore, E. C., Drake, A. J., Thomas, R. C., Bloom, J. S., Poznanski, D., Miller, A. A., Foley, R. J., Silverman, J. M., Arcavi, I., Ellis, R. S., & Deng, J. 2009, Nature, 462, 624 [ADS]

Gilroy, K. K. & Brown, J. A. 1991, ApJ, 371, 578 [ADS]

Glorius, J., Knörzer, M., Müller, S., Pietralla, N., Sauerwein, A., Sonnabend, K., Wälzlein, C., & Wiescher, M. 2011, Progress in Particle and Nuclear Physics, 66, 379 [ADS]

Goriely, S., Demetriou, P., Janka, H.-T., Pearson, J. M., & Samyn, M. 2005, Nuclear Physics A, 758, 587 [ADS]

Gray, D. F. 1989, ApJ, 347, 1021 [ADS]

Haiman, Z. & Loeb, A. 1997, ApJ, 483, 21 [ADS]

Hainebach, K. L., Clayton, D. D., Arnett, W. D., & Woosley, S. E. 1974, ApJ, 193, 157 [ADS]

Hayashi, C. 1961, PASJ, 13, 450 [ADS]

Heger, A., Fryer, C. L., Woosley, S. E., Langer, N., & Hartmann, D. H. 2003, ApJ, 591, 288 [ADS]

Heger, A. & Woosley, S. E. 2010, ApJ, 724, 341 [ADS]

Herwig, F. 2005, ARA&A, 43, 435 [ADS]

Hillier, D. J., Davidson, K., Ishibashi, K., & Gull, T. 2001, ApJ, 553, 837 [ADS]

Hoyle, F. 1946, MNRAS, 106, 343 [ADS]

—. 1954, ApJS, 1, 121 [ADS]

Iben, Jr., I. 1983, ApJ, 275, L65 [ADS]

Kajino, T., Wanajo, S., & Mathews, G. J. 2002, Nuclear Physics A, 704, 165 [ADS]

Kappeler, F., Beer, H., & Wisshak, K. 1989, Reports on Progress in Physics, 52, 945 [ADS]

Karakas, A. I. 2003, PhD thesis, School of Mathematics and Statistics, Monash University, Australia. [LINK]

Kasen, D., Woosley, S. E., & Heger, A. 2011, ApJ, 734, 102 [ADS]

Kippenhahn, R. & Weigert, A. 1990, Stellar Structure and Evolution [ADS]

Koo, B.-C., McKee, C. F., Lee, J.-J., Lee, H.-G., Lee, J.-E., Moon, D.-S., Hong, S. S., Kaneda, H., & Onaka, T. 2008, ApJ, 673, L147 [ADS]

Kwok, S. 2000, The Origin and Evolution of Planetary Nebulae [ADS]

Lau, H. H. B., Stancliffe, R. J., & Tout, C. A. 2008, MNRAS, 385, 301 [ADS]

MacFadyen, A. I. & Woosley, S. E. 1999, ApJ, 524, 262 [ADS]

Maeder, A. 1983, A&A, 120, 113 [ADS]

Maeder, A. & Meynet, G. 1987, A&A, 182, 243 [ADS]

Marigo, P., Girardi, L., Chiosi, C., & Wood, P. R. 2001, A&A, 371, 152 [ADS]

Massey, P. 1998, in Astronomical Society of the Pacific Conference Series, Vol. 142, The Stellar Initial Mass Function (38th Herstmonceux Conference), 17 [ADS]

Massey, P. 2003, ARA&A, 41, 15 [ADS]

Mattsson, L. & Höfner, S. 2011, A&A, 533, A42 [ADS]

Mauron, N. & Josselin, E. 2011, A&A, 526, A156 [ADS]

Meyer, B. S., Mathews, G. J., Howard, W. M., Woosley, S. E., & Hoffman, R. D. 1992, ApJ, 399, 656 [ADS]

Meynet, G., Hirschi, R., Ekström, S., & Maeder, A. 2006, in Astronomical Society of the Pacific Conference Series, Vol. 353, Stellar Evolution at Low Metallicity: Mass Loss, Explosions, Cosmology, 49 [ADS]

Meynet, G. & Maeder, A. 2003, A&A, 404, 975 [ADS]

Nakamura, F. & Umemura, M. 2001, ApJ, 548, 19 [ADS]

Naoz, S., Noter, S., & Barkana, R. 2006, MNRAS, 373, L98 [ADS]

Nugis, T., Crowther, P. A., & Willis, A. J. 1998, A&A, 333, 956 [ADS]

Olive, K. A., Rood, R. T., Schramm, D. N., Truran, J., & Vangioni-Flam, E. 1995, ApJ, 444, 680 [ADS]

O'Shea, B. W. & Norman, M. L. 2007, ApJ, 654, 66 [ADS]

Pagel, B. E. J. 1997, Nucleosynthesis and Chemical Evolution of Galaxies [ADS]

Parsons, S. G., Marsh, T. R., Gänsicke, B. T., Drake, A. J., & Koester, D. 2011, ApJ, 735, L30 [ADS]

Pignatari, M., Gallino, R., Heil, M., Wiescher, M., Käppeler, F., Herwig, F., & Bisterzo, S. 2010, ApJ, 710, 1557 [ADS]

Prantzos, N., Hashimoto, M., & Nomoto, K. 1990, A&A, 234, 211 [ADS]

Prialnik, D. 2000, An Introduction to the Theory of Stellar Structure and Evolution [ADS]

Pruet, J., Thompson, T. A., & Hoffman, R. D. 2004, ApJ, 606, 1006 [ADS]

Pumo, M. L., D'Antona, F., & Ventura, P. 2008, ApJ, 672, L25 [ADS]

Raiteri, C. M., Busso, M., Picchio, G., & Gallino, R. 1991, ApJ, 371, 665 [ADS]

Renzini, A. & Voli, M. 1981, A&A, 94, 175 [ADS]

Roederer, I. U., Lawler, J. E., Sneden, C., Cowan, J. J., Sobeck, J. S., & Pilachowski, C. A. 2008, ApJ, 675, 723 [ADS]

Rolfs, C. E. & Rodney, W. S. 1988, Cauldrons in the cosmos: Nuclear astrophysics [ADS]

Romano, D., Chiappini, C., Matteucci, F., & Tosi, M. 2005, A&A, 430, 491 [ADS]

Rood, R. T., Bania, T. M., Balser, D. S., & Wilson, T. L. 1998, Space Sci. Rev., 84, 185 [ADS]

Seeger, P. A., Fowler, W. A., & Clayton, D. D. 1965, ApJS, 11, 121 [ADS]

Serenelli, A. M., Althaus, L. G., Rohrmann, R. D., & Benvenuto, O. G. 2002, MNRAS, 337, 1091 [ADS]

Smartt, S. J. 2009, ARA&A, 47, 63 [ADS]

Smith, V. V. & Lambert, D. L. 1989, ApJ, 345, L75 [ADS]

Sokasian, A., Yoshida, N., Abel, T., Hernquist, L., & Springel, V. 2004, MNRAS, 350, 47 [ADS]

Spite, M. & Spite, F. 1978, A&A, 67, 23 [ADS]

Steinfadt, J. D. R., Bildsten, L., & Arras, P. 2010, ApJ, 718, 441 [ADS]

Sumiyoshi, K., Terasawa, M., Mathews, G. J., Kajino, T., Yamada, S., & Suzuki, H. 2001, ApJ, 562, 880 [ADS]

Tegmark, M., Silk, J., Rees, M. J., Blanchard, A., Abel, T., & Palla, F. 1997, ApJ, 474, 1 [ADS]

Truran, J. W. 1981, A&A, 97, 391 [ADS]

Ventura, P., Criscienzo, M. D., Schneider, R., Carini, R., Valiante, R., D'Antona, F., Gallerani, S., Maiolino, R., & Tornambé, A. 2012, MNRAS, 424, 2345 [ADS]

Ventura, P. & D'Antona, F. 2011, MNRAS, 410, 2760 [ADS]

Wagoner, R. V., Fowler, W. A., & Hoyle, F. 1967, ApJ, 148, 3 [ADS]

Walborn, N. R., Blanco, B. M., & Thackeray, A. D. 1978, ApJ, 219, 498 [ADS]

Wanajo, S. & Ishimaru, Y. 2006, Nuclear Physics A, 777, 676 [ADS]

Wanajo, S., Tamamura, M., Itoh, N., Nomoto, K., Ishimaru, Y., Beers, T. C., & Nozawa, S. 2003, ApJ, 593, 968 [ADS]

Washimi, H. & Shibata, S. 1993, MNRAS, 262, 936 [ADS]

Wheeler, J. C., Cowan, J. J., & Hillebrandt, W. 1998, ApJ, 493, L101 [ADS]

Willson, L. A. 2000, ARA&A, 38, 573 [ADS]

Woods, P. J. & Davids, C. N. 1997, Annual Review of Nuclear and Particle Science, 47, 541 [ADS]

Woosley, S. E., Wilson, J. R., Mathews, G. J., Hoffman, R. D., & Meyer, B. S. 1994, ApJ, 433, 229 [ADS]

Chapter 2: Modelling a stellar spectrum in 1-dimension

The delay in the development of modern stellar atmosphere models impeded the pursuit of obtaining a clear picture of the chemical history of the Galaxy through the study of elemental abundances in stars. This was mainly because of the limitations in computer power, up until approximately ten years ago. Before this, the most basic atmospheres and radiative transfer codes were slow in modelling a star's spectrum for analysis, which would have to be repeated several times for different parameter sets because, as we shall see over the course of this thesis, the use of just one synthetic spectrum cannot tell you a great deal about a stellar atmosphere. Over the last ten years or so there has been an increase in the number of abundance publications that utilise faster, more powerful computers, that have been responsible for quicker spectrum analysis, through abilities such as parallel processing synthesis and subsequent χ^2 fitting. They have also been extremely important in the development of newer, more precise stellar atmospheres and radiative transfer codes.

The implementation of codes, such as MULTI (Carlsson, 1986), that use non-local thermodynamic equilibrium (NLTE) radiation fields to compute the radiative transfer calculations of stellar atmospheres, which we briefly explore in §4.4, is now fairly commonplace. Such a treatment of an atmosphere is important when modelling very hot or low-gravity stars, such as massive main-sequence stars, hot white dwarfs and giant stars. However, to employ NLTE for a simple abundance analysis of a single element in a star, requires the construction of a detailed model atom. This means that a list of (ideally) all transitions to and from each energy level is required, which is time consuming to construct (see Thévenin & Idiart, 1999, their Fig. 1 for a graphical representation of the number of transitions mapped for Fe I and Fe II) and which suffer from incomplete and/or inaccurate data. More complex atoms, such as Ba, are currently difficult to calculate due to the added complication of isotope blends and hyperfine structure (hfs) effects.

Other codes that are able to compute time-dependent radiative transfer calculations for a star in 3-dimensions, and include effects caused by phenomena such as stellar granulation and convection, referred to as 3D hydrodynamics, are currently being developed and tested (Stein & Nordlund, 1998; Steffen, 2007; Freytag et al., 2010). These codes are extremely complex, so the completion of the radiative transfer calculations is currently extremely time consuming. Nevertheless, I explore this new approach in Chapter 5.

Eventually, the development and coalescence of these totally separate treatments should lead to the implementation of time-dependent, fully 3-dimensional, non-local thermodynamic equilibrium atmospheres to solve the radiative transfer equations, which will replace more basic codes currently in use. There have already been investigations that employ both these treatments to the line synthesis (Asplund et al., 2003; Kromer et al., 2009), however, it would seem that there is still much to be learnt from simpler 1-dimensional (1D) local thermodynamic equilibrium (LTE) codes. They have the advantage of providing a more standard result that can be replicated easily by other investigators, and can be computed much faster (discussed in Chapter 5) allowing for finer sampling of atmospheric parameter space. In this work, I use 1D codes (LTE and NLTE) in Chapters 3 and 4, and utilise a 3D code in Chapter 5. In the present chapter, I introduce the radiative transfer theory on which these codes, especially the 1D code, are based.

2.1 Basic assumptions

For my early studies I used a radiative transfer code that assumes LTE and employs model stellar atmospheres that infer a 1D geometry. As the majority of my stars are not giants subject to extreme NLTE effects and large amounts of convection, it seemed like a sensible approximation to start with. When working in 1D LTE, the following six basic assumptions are taken into consideration when constructing model atmospheres (Rutten, 2003):

1. Only one spatial coordinate (1D) is considered when solving the equations of

radiative transfer.

2. The atmosphere is in a state of local thermodynamic equilibrium; free electrons obey the Maxwell-Boltzmann distribution[1].

3. There is no noticeable collapse or expansion of the star and no significant mass-loss that would affect gravity, implying changes to the density of the star at a given optical depth in the atmosphere; the star is in a state of hydrostatic equilibrium.

4. The effect of stellar granulation, starspots and other such structures that would affect continuum opacities are negligible and as such are ignored.

5. Magnetic fields are ignored in the photosphere as it is assumed that the majority of magnetic activity occurs in the chromosphere, which is also ignored.

6. Convective mixing of the elements in a star's model atmosphere that affect local temperatures is approximated by a parameter called the mixing-length.

The 1D LTE analysis discussed in Chapters 3 and 4 was completed using the radiative transfer spectrum synthesis code ATLAS (Cottrell & Norris, 1978) with KURUCZ06 model atmospheres[2], which are an improved grid of atmospheres, based upon the Kurucz (1979) model atmosphere grids.

In the first section of this Chapter, I discuss the various steps required to create a 1D LTE model atmosphere. I then move on to discuss the basics of radiative transfer, which ATLAS uses to produce a synthetic spectrum. Next I briefly discuss the Fe lines, which were used to determine a star's macroturbulent broadening and then I discuss the synthesis of the Ba lines in detail. Finally I discuss details of the acquisition of the observed stellar spectra used in Chapters 3 to 5.

[1]The Maxwell-Boltzmann distribution describes the speed of a particle within a gas of a given temperature.

[2]downloadable at `kurucz.harvard.edu/grids.html`.

2.2 Modelling a stellar atmosphere in 1-dimension

A 1D LTE model atmosphere is characterised by three basic input parameters; its effective temperature ($T_{\rm eff}$)[3], metallicity (parametrised by [Fe/H]), and surface gravity ($g_{\rm s}$), which is usually quoted as a logarithm ($\log g$). The Kurucz atmosphere is simply a list of physical quantities, based on these three parameters, which are calculated using the six assumptions tabulated above for 35 layers of the photosphere[4]. An example of a KURUCZ06 model atmosphere is given in Appendix A.1. The six quantities used to describe the atmosphere are:

RHOX The line-of-sight integral of the density within each layer multiplied by the thickness of the layer or the integral of $\rho {\rm d}z$ measured in $\mathrm{g\,cm^{-2}}$, i.e. a column mass.

P The total pressure ($P_{\rm T}$) within each layer, measured in dyne $\mathrm{cm^{-2}}$.

T The temperature within each layer, measured in K.

XNE The number density of free electrons ($N_{\rm e}$) within each layer, measured in $\mathrm{cm^{-3}}$.

ABROSS The Rosseland mean opacity ($\kappa_{\rm ROSS}$) for a given layer.

PRAD The radiation pressure ($P_{\rm rad}$) for a given layer, measured in dyne $\mathrm{cm^{-2}}$.

RHO The total density, measured in $\mathrm{g\,cm^{-3}}$.

2.2.1 Basic input physics

The 35 layers in the atmosphere are evaluated over a mean optical depth ($\bar{\tau}_\nu$) range $0.00 \leq \bar{\tau}_\nu \leq 10.00$ for all quantities tabulated, thus $\bar{\tau}_\nu$ is not tabulated itself. Each layer is almost equidistant in $\mathrm{d}\log\bar{\tau}_\nu$ space. The precise manner in which the Kurucz atmospheres are constructed are beyond the scope of work presented here. For concise

[3] The effective temperature of a star is a relationship that describes the temperature which a black body would need to have if it were to radiate the same amount of energy per $\mathrm{cm^2\,s}$ as the star; $\mathfrak{F} = \sigma T_{\rm eff}^4$.

[4] The KURUCZ06 atmospheres are capable of producing the same relationships for 72 layers, however, ATLAS requires that the layers be evaluated for only 35 layers.

instructions on how this is done see Kurucz (1970). However, in the next four parts of this section I briefly outline some of the assumptions involved in producing parts of a Kurucz atmosphere.

Temperature relationships

Empirical $T(\tau_\nu)$ relationships are based upon solar centre to limb observations. Fig. 2.1 illustrates the effect of limb darkening, which restricts us to observing higher, cooler and less bright layers in the photosphere for a given optical depth (τ_ν); $\tau_\nu = \tau_\nu^0 \cos\theta$, where $\tau_\nu = \tau_\nu^0$ at the solar centre and θ is the angle of the line-of-slight relative to the normal as shown in Fig. 2.1.

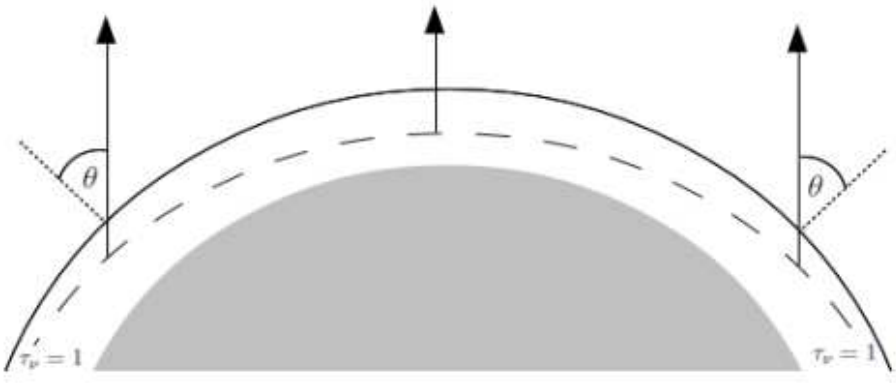

Fig. 2.1: The effects of limb darkening on observations of the photosphere (in white). The grey region represents layers beneath the photosphere.

As the intensity (I_ν) is dependent on τ_ν and, as a consequence of 1D LTE, the source function (S_ν) has the relationship

$$\frac{\mathrm{d}I_\nu}{\mathrm{d}\tau_\nu} = S_\nu - I_\nu \tag{2.1}$$

with I_ν. This is the general, differential equation of radiative transfer. Through manipulation of Eq. (2.1) that accounts for how S_ν varies with θ, and mapping the relative intensity (I_ν/I_ν^0) for different frequencies across the centre-to-limb in the Sun, the optical depth dependence of S_ν can be calculated. For a more detailed review of how this is achieved, I refer the reader to Gray (2008). S_ν is defined as the ratio of the emission

(j_ν) to absorption (κ_ν) at a given optical depth

$$S_\nu = \frac{j_\nu}{\kappa_\nu}. \tag{2.2}$$

If one assumes LTE, S_ν can be expressed by the Planck function ($S_\nu = B_\nu(T)$), which describes the behaviour of a black body

$$B_\nu(T) = \frac{2h\nu^3}{c^2}\frac{1}{\mathrm{e}^{h\nu/kT} - 1}, \tag{2.3}$$

then the S_ν depth dependence can be solved for T (Gray, 2008).

Opacity relationships

The opacity of a photosphere is highly dependent on the wavelength. For example, observing the solar photosphere at 1.6μm, allows us to see furthest into the Sun (Gray, 2008).

The procedure for calculating κ_ν is rather complex and the details are not needed here, however, I refer the reader to Kurucz (1970) for a full description on how the Kurucz atmospheres establish and calculate the various components that determine this. One must consider all sources of absorption (briefly discussed in §2.3.1) and calculate their dependence on wavelength, temperature and chemical structure. From these determinations κ_ν will be equal to the sum of the constituents for a given wavelength. However, to tabulate the opacity at each wavelength in every model atmosphere produced would be an extremely large undertaking. As such the Kurucz atmospheres tabulate the Rosseland mean opacity (κ_{ROSS}), which is a flux weighted opacity evaluated over all wavelengths

$$\frac{1}{\kappa_{\mathrm{ROSS}}} = \frac{\int_0^\infty (1/\kappa_\nu)\,(\mathrm{d}B_\nu/\mathrm{d}T)\,\mathrm{d}\nu}{\int_0^\infty (\mathrm{d}B_\nu/\mathrm{d}T)\,\mathrm{d}\nu}, \tag{2.4}$$

where B_ν is the Planck black body function and is defined in Eq. (2.3) and $\int_0^\infty (\mathrm{d}B_\nu/\mathrm{d}T)\,\mathrm{d}\nu$ is evaluated as $4\sigma T^3/\pi$ (Kurucz, 1970). This can be useful as it makes re-evaluating the temperature scale based upon a new T_{eff} value easier to resolve as it is assumed

that at large optical depths

$$T(\tau_{\rm ROSS})^{\rm new} = \frac{T_{\rm eff}^{\rm new}}{T_{\rm eff}^{\rm old}} T(\tau_{\rm ROSS})^{\rm old}, \tag{2.5}$$

where $\tau_{\rm ROSS}$ in the Kurucz atmospheres has values between 10^{-5} and 10 distributed over 35 layers. However, $B_\nu = S_\nu$ at large values of τ_ν. Therefore this relationship only holds at large optical depths.

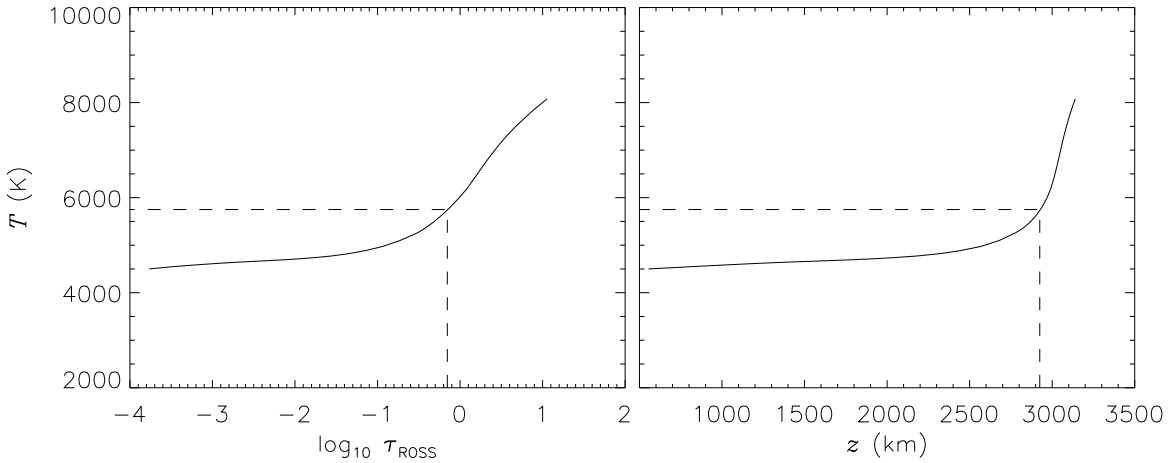

Fig. 2.2: *Left*: The temperature scale as a function of the Rosseland mean optical depth ($\tau_{\rm ROSS}$) taken as a logarithm for HD 140283's model atmosphere ($T_{\rm eff}/\log g/[{\rm Fe/H}] = 5750/3.7/-2.5$). The dashed lines indicate where $T = T_{\rm eff}$ at $\tau_{\rm ROSS} = \frac{2}{3}$. *Right*: The corresponding temperature scale as a function of geometrical depth (z). The dashed lines again indicate where $T = T_{\rm eff}$ at $\tau_{\rm ROSS} = \frac{2}{3}$. It is shown to occur at $z \approx 2900\,{\rm km}$ from the edge of the star.

Fig. 2.2 shows T as a function of both $\tau_{\rm ROSS}$ and geometrical depth (z) for HD 140283, a metal-poor subgiant star with Kurucz atmosphere parameters $T_{\rm eff}/\log g/[{\rm Fe/H}] = 5750/3.7/-2.5$. The atmosphere file used to create these plots is available in Appendix A.1. From Fig. 2.2 we can see that for the given atmosphere parameters, its geometrical thickness is 2500 km (in the range $10^{-4} \leq \tau_{\rm ROSS} \leq 1$) and at $z \approx 2900\,{\rm km}$ $T(\tau_{\rm ROSS}) = T_{\rm eff}$ ($\tau_{\rm ROSS} = \frac{2}{3}$). By comparison, the Sun's photosphere reaches $T(\tau_{\rm ROSS}) = T_{\rm eff} \approx 700\,{\rm km}$ (Gray, 2008). This is because the geometrical depth of a star at a given optical depth depends upon the opacity and density at that depth

$$\mathrm{d}\tau_\nu = \kappa_\nu \rho \, \mathrm{d}z. \tag{2.6}$$

where g_s and ρ are the surface gravity and density. Therefore because the Sun has a higher surface gravity ($\log g = 4.4$) than HD 140283 ($\log g = 3.7$), and hence a higher density, so that $T \longrightarrow T_{\rm eff}$ at a smaller value of z. In addition altering the metallicity of the star will affect the number of free electrons through ionisation. This means that the pressure resulting will be affected further affecting the opacity. Therefore once the pressure for a given temperature distribution is solved, the Kurucz models then determine the opacities at this time (Kurucz, 1970). The pressure determinations are discussed below.

Pressure relationships

We have established from the basic assumptions that the star can be treated as though it is in a state of hydrostatic equilibrium; the forces of gravity and all sources of outward pressure (gas, radiation, electron) are balanced. (Note that this assumption is dropped in the 3D models we will meet in Chapter 5, which are allowed to respond hydrodynamically.) The equation of hydrostatic equilibrium can be evaluated as

$$\mathrm{d}P = \rho g_s \, \mathrm{d}z. \tag{2.7}$$

The optical depth (τ_ν) at a given geometrical depth is given by Eq. (2.6). Substituting this into Eq. (2.7) we find

$$\frac{\mathrm{d}P}{\mathrm{d}\tau_\nu} = \frac{g_s}{\kappa_\nu}. \tag{2.8}$$

The majority of the total pressure (P_T) in Eq. (2.8) comes from the gas pressure P_g as a result of solving the equation (Gray, 2008; Böhm-Vitense, 1989). This is illustrated by Fig. 2.3 as it is difficult to differentiate the P_T from P_g. To solve Eq. (2.8) for the Kurucz optical depth range, the corresponding opacities must be known. The pressure from all other sources must also be considered.

The Saha equation calculates the ratio of the atomic species at any ionisation (N_i) to the number at the next ionisation (N_{i+1}), which is temperature dependent. By extension the number of free electrons (N_e) will vary according to the ratio N_{i+1}/N_i;

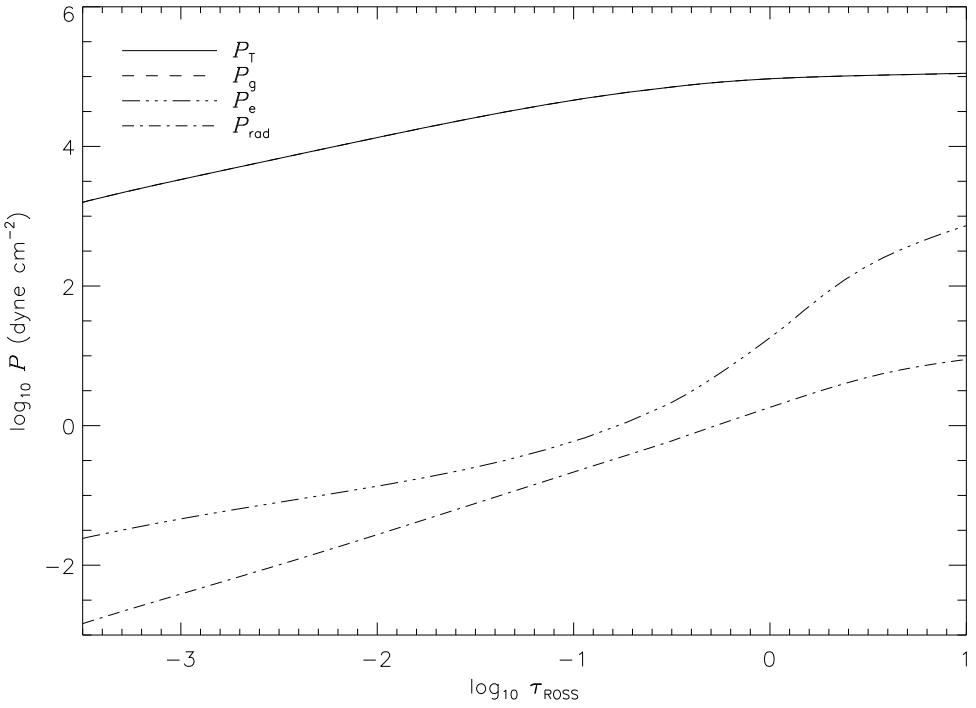

Fig. 2.3: Each source of pressure in HD 140283 as a function of the optical depth. The total pressure is taken as the sum of the three constituent pressures. The gas pressure has the largest contribution to the total pressure in the star; it is difficult to distinguish it from the total pressure.

a small ratio would imply fewer free electrons than a high ratio. These ratios are also sensitive to the chemical structure of the star. Fewer metals with low ionisation energies would result in fewer free electrons, particularly in cool stars where H is not ionised. The Kurucz models calculate $N_{\rm e}$ at each layer of the atmosphere. The electron pressure for a given layer is then $P_{\rm e} = N_{\rm e}kT$, where k is the Boltzmann constant.

Electromagnetic radiation, like particles of matter, has momentum determined by its energy divided by its speed (the speed of light). The pressure ($P_{\rm rad}$) exerted by these photons are computed and tabulated in the Kurucz atmosphere. This is related to the intensity of the radiation field I_ν and is temperature dependent. For hot stars $P_{\rm rad}$ becomes quite important, however, for my sample consisting of relatively cool stars it is less important than the gas and electron pressures.

Another source of pressure in real stars is that related to the magnetic field. The effect that magnetic fields have on pressure is not important outside of star spots. However, for 1D LTE atmospheres magnetic fields are ignored (assumption 5). The total pressure from all three pressure terms is tabulated for every layer in the Kurucz

model atmosphere.

Abundance determinations

The Kurucz atmosphere contains a list of elemental abundances adopted from the Anders & Grevesse (1989) solar abundance observations. An elemental abundance is often quoted as

$$A(\mathrm{X}) = \log_{10}\left(\frac{N(\mathrm{X})}{N(\mathrm{H})}\right) + 12. \tag{2.9}$$

However, Kurucz, like Anders & Grevesse (1989), tabulates $\log_{10}(N(\mathrm{X})/N(\mathrm{total}))$, which in effect ignores the addition of 12 and has an offset of 0.03 dex. Using the scaling factor included in the atmosphere, which scales the list of solar abundances to the metallicity of the atmosphere, one can determine the abundance of a particular element in a star. For example, the scaling factors for an [Fe/H] $= -2.0$ and -3.0 atmosphere would be 10^{-2} and 10^{-3} times the solar abundance, respectively, where

$$[\mathrm{X/Y}] = \log_{10}\left(\frac{N(\mathrm{X})}{N(\mathrm{Y})}\right)_{*} - \log_{10}\left(\frac{N(\mathrm{X})}{N(\mathrm{Y})}\right)_{\odot}. \tag{2.10}$$

As well as altering the elemental solar abundances used during the synthesis of a spectrum, the change in the metallicity will affect the temperature and density relationships with opacity. The star gets hotter (increasing its effective temperature, $T_{\mathrm{eff}} \approx T(\tau_\nu = 2/3)$) and more compact when the metallicity is decreased.

Convective mixing

Convective mixing is strictly a time-dependent phenomena; it requires a certain amount of time for a convection cell to rise or sink. However, time-independent approximations through iterative calculations that compensate for the rapid and nonlinear change in the opacity with temperature, which produces the convective instability, are used in most 1D LTE atmospheres, including the Kurucz atmospheres used in the present work. The convective mixing of the elements is dealt with using the local mixing-length theory (Böhm-Vitense, 1958; Kurucz, 1970) (Assumption 6).

Incorporating this theory into 1D models has three positive characteristics: firstly has a certain amount of plausibility which improves the accuracy of the model, it is a relatively simple concept, and it is relatively easy to program (Lester et al., 1982). Also, with today's computing power, this routine needs an unnoticeable amount of runtime to compute. In the mixing-length theory, convectively unstable levels in a star are pictured as rising hot elements and cooler elements that sink, this is known as the Schwarzschild criterion, which can be written as

$$\left(\frac{\mathrm{d}\log T}{\mathrm{d}\log P}\right)_{\text{average}} > 1 - \frac{1}{\gamma} + \frac{\mathrm{d}\log \mu}{\mathrm{d}\log P}, \tag{2.11}$$

where P is the total pressure, μ is the mean molecular weight, T is the temperature and γ is the ratio of specific heats. Through an iterative process, the averaged temperature is re-evaluated from the changing temperatures that are expected in convectively unstable gas and the convective flux contribution to the total flux is determined from this.

2.3 Synthesis of a stellar spectrum with ATLAS

In this section I discuss the procedures and basic input physics that are involved when synthesising a stellar spectrum using the radiative transfer code, ATLAS. The code requires several input parameters: a model atmosphere, a list of spectral features such as absorption line information to calculate line opacities, and stellar macroturbulent, microturbulent and instrumental broadening. My work required the analysis of Fe lines and Ba lines. The details of these line lists are discussed in §2.4 and §2.5.

2.3.1 Continuous and line opacity

The Kurucz model atmospheres considers sources of continuous opacity i.e. interactions between photons and absorbers, based on the star's chemical structure which shape the continuum of its spectrum. The flux weighted opacity is then tabulated for each of the 35 layers calculated, although this is not required until the synthesis of

a spectrum. Working in 1D LTE allows us to assume that the radiation field can be modelled as a black body, Eq. (2.3). The various sources of opacity then remove flux through absorption as the photons travel through the photosphere. There are three types of absorption mechanisms considered in a 1D LTE atmosphere, two of which are responsible for the continuous opacity and the other for the line opacity. All three are discussed below.

Continuous opacity

The continuous opacity in a 1D LTE atmosphere depends on processes such as bound-free and free-free transitions. However, when working in a crowded spectral region, overlapping spectral lines can behave much like the continuum opacity, but for this to occur, the user must tabulate these lines separately. The majority of the continuous opacity is due to H in the atmosphere as it is considerably more abundant than any other element. Neutral H is responsible for a series of continuous absorptions such as Lyman, Balmer and Paschen absorption. These are examples of bound-free absorptions.

Another state of H that contributes to the continuous opacity is H^-. This ion is extremely dependent on the amount of metals in the atmosphere, which ionise easily (relative to H or He) and their freed electrons are subsequently captured by H. It requires very little energy to ionise this, photons with $\lambda < 16\,421$ Å ionise H^- (Gray, 2008). This source of opacity only affects cooler stars, like the Sun, which implies that for most of my star sample, this would be a significant contribution to the overall continuous opacity. However, because the stars I work with are extremely metal-poor, the abundances of the electron donors, metals, is small relative to solar, reducing the overall contribution of the H^- ion to the continuum opacity, relative to solar metallicity.

As He is the second most abundant element, one would naively expect that this would have a large contribution to the overall opacity in a star. Certainly in extremely hot stars, such as O-type stars, this is true, but because of the amounts of energy required for excitation and ionisation of He, it has little affect in the Sun or my star sample in the infra red or visible wavelengths where the majority of the flux in these

stars is found.

Free electrons contribute to the continuous opacity at the same rate over all wavelengths and is an example of a free-free interaction. This is because electron-photon interaction (known as Thompson scattering) is wavelength independent. Like H^-, the amount that electron scatter contributes to the overall continuous opacity depends on the amount of electron donors. In metal-rich O- and B-type stars, this becomes very important as metals, H and, if temperatures are hot enough, He will donate electrons to the atmosphere, increasing the probability of scattering and hence opacity. For my metal-poor star sample, however, this source of opacity will be less significant but nevertheless must still be considered.

Metals in significant quantities will also contribute to continuous opacity through bound-free transitions. Like electron scattering, this becomes more significant in metal-rich regimes but must still be taken into consideration when synthesising a spectrum of a metal-poor star, particularly in the UV where photon energies are large enough to ionise significant quantities of metals (Bell et al., 2001). Kurucz calculates the opacities for C I, Mg I, Al I and Si I, which is not a complete opacity source list, but it is assumed that these are responsible for the majority of the opacity caused by metals (Kurucz, 1970).

Line opacity

So far I have discussed various sources of opacity that contribute to the overall profile of the continuum. ATLAS will calculate this based on the temperatures and densities tabulated in the KURUCZ06 atmosphere. In addition ATLAS will calculate line opacities of any spectral feature the user wishes to include. This requires the input of a line list that contains several key pieces of information on every spectral feature synthesised. Details of the line lists are discussed in §2.4. Bound-bound transitions are responsible for absorption in this case.

Unlike continuous opacity, the line opacity affects a specific wavelength in a spectrum. This is determined by the specific photon energy a spectral feature absorbs. The line opacities for a given atomic species also depend on the continuous opacity at this

wavelength. For example, at UV wavelengths the ionisation of metals, which contribute to the continuous opacity, remove absorbers that would otherwise contribute to line opacities thus removing absorption lines from the spectrum. Spectral lines are affected by several physical processes that broaden them. These processes are now discussed.

2.3.2 Broadening of spectral lines

To properly model the observed broadening of an absorption line ($\Delta\lambda_{\rm obs}$) several physical parameters must be resolved. The observed broadening of an absorption line represents the convolution of several parameters so that

$$\Delta\lambda_{\rm obs} = \Delta\lambda_{\rm natural} * \Delta\lambda_{\rm pressure} * \Delta\lambda_{\rm Doppler} * \Delta\lambda_{\rm inst}, \tag{2.12}$$

where $\Delta\lambda_{\rm natural}$, $\Delta\lambda_{\rm pressure}$, $\Delta\lambda_{\rm Doppler}$ and $\Delta\lambda_{\rm inst}$ represent the $FWHM$ of the natural, pressure, Doppler and instrumental broadening respectively. The $*$ symbol represents a convolution. Each term is individually discussed below. ATLAS convolves these parameters during or just after the spectrum synthesis. The Doppler term includes several parameters

$$\Delta\lambda_{\rm Doppler} = \Delta\lambda_{\rm thermal} * \Delta\lambda_{\xi} * \Delta\lambda_{\Gamma}, \tag{2.13}$$

where $\Delta\lambda_{\rm thermal}$, $\Delta\lambda_{\xi}$ and $\Delta\lambda_{\Gamma}$ are the $FWHM$ of the thermal, microturbulent and macroturbulent broadening respectively. If all these terms are represented by a Gaussian, which they usually are in 1D LTE, it is acceptable to calculate $\Delta\lambda_{\rm Doppler}$ by adding the separate terms in quadrature, i.e. $z^2 = x^2 + y^2$, where xyz are numbers representing the profile's $FWHM$. I often describe these parameters in terms of their velocity-space $FWHM$ (i.e. $v_{\rm obs}$, $v_{\rm Doppler}$, etc.) throughout the present work, which can be calculated by using $\Delta\lambda/\lambda = v/c$, where c is the speed of light and v is the velocity-space $FWHM$. I now briefly discuss each broadening component in turn.

2.3.3 Natural broadening

A parameter that is calculated by ATLAS during the synthesis of a spectrum is the natural broadening. It is calculated for all spectral features included in the synthesis. This is caused by the spontaneous de-excitation of electrons in excited states, which have typical lifetimes of $\sim 10^{-8}$ s. The limited lifetime of the higher energy levels implies an uncertainty in the energy of any transition from them according to the Heisenberg uncertainty principle

$$\Delta E \Delta t \geq \frac{\hbar}{2}. \tag{2.14}$$

As a result of the uncertainty, spectral lines broaden without any other external influence, e.g. pressure exerted by other particles.

2.3.4 Pressure broadening

The collisional effect of perturbing particles with the absorbing species in the atmosphere results in further broadening of the spectral feature. We call this pressure broadening. For metals such as Fe and Ba in the cool stars analysed in the present work, the strongest pressure effect is often treated as coming from the van der Waals interaction. In ATLAS this is calculated by the Unsöld approximation

$$C_6 = 3 \times 10^{-31} \left[\frac{1}{(I - \chi - \chi_\lambda)^2} - \frac{1}{(I - \chi)^2} \right], \tag{2.15}$$

where χ, χ_λ and I represents the excitation potential, the energy of the photon in the line and the ionisation potential respectively, and all are measured in units of eV. The energy of the photon, $\chi_\lambda = h\nu = 12398./\lambda$, with λ in Ångstroms (taken from Gray, 2008). The ionisation potential gives the energy required to ionise the atom or ion from its ground state, e.g. Fe I to Fe II requires 7.902 eV. Lists of the energies required to ionise several ionised stages of an atomic species can be found for reference in books like Gray (2008), his Appendix D. For a more complete listing see Allen (1976).

The broadening constant, C_6 is used in the following approximation to calculate

the broadening parameter γ_6 (Steffen et al., 2010)

$$\gamma_6 = 8.08\, C_6^{2/5}\, v_{\rm rel}^{3/5}\, N_{\rm H}, \tag{2.16}$$

where $v_{\rm rel}$ represents the relative velocity between the absorber and the perturber. For perturbing particles smaller than the absorber (i.e. H relative to Fe), which is mostly the case, $v_{\rm rel}^2 = 8kT/\pi m_{\rm H} = 2.105 \times 10^8\, T\ ({\rm cm\,s^{-1}})^2$ so that γ_6 can be expressed as (Steffen et al., 2010)

$$\log \frac{\gamma_6}{N_{\rm H}} = 3.404 + \frac{2}{5}\log C_6 + \frac{3}{10}\log T. \tag{2.17}$$

We shall see in §2.4 that the Unsöld/van der Waals approximation constantly underestimates γ_6, and I show how ATLAS compensates for this.

2.3.5 Doppler broadening

Thermal, rotational, macroscopic and microscopic motions of matter in the stellar photosphere result in further broadening of spectral lines

$$\frac{\Delta\lambda}{\lambda} = \frac{v_{\rm Doppler}}{c}, \tag{2.18}$$

where $v_{\rm Doppler}$ represents the velocity of the absorber due to the Doppler effect and $\Delta\lambda$ is the change in the wavelength λ of the photons that the absorber will absorb due to the velocity of the absorber $v_{\rm Doppler}$.

While ATLAS treats the thermal and microscopic (microturbulent) component during the synthesis, the rotational and macroscopic components are ignored as it assumes the star has a static, time-independent atmosphere. In reality we know this isn't the case. Using the Sun as an example, we know from observations that it rotates and that there are convective cells that move through the photosphere. Also, when we compare its spectrum to 1D LTE model spectra we see an excess in line broadening, which is not due to the effects discussed above or the thermal Doppler component discussed below.

The effect of the microscopic motions of matter to the broadening of spectral lines is not as large as those caused by macroscopic motions but are important to synthesise. Though they are treated separately during the synthesis, it is common to model both the macroturbulent and microturbulent profiles as a Gaussian. In this section I discuss how I (or for thermal broadening, ATLAS) take into account each of the Doppler effects when modelling a stellar spectrum, beginning with the thermal component.

Thermal broadening

All absorbers in the stellar atmosphere will have some component of thermal broadening. The thermal broadening redistributes the opacity of an absorption line over a wavelength range $\Delta\lambda$. The redistribution of the line opacity has a Gaussian distribution which is calculated as

$$\alpha_{\text{thermal}} = \frac{\pi^{1/2}\mathrm{e}^2 f\lambda^2}{\mathrm{m_A} c\Delta\lambda_{\mathrm{D}}}\,\mathrm{e}^{-(\Delta\lambda/\Delta\lambda_{\mathrm{D}})^2}, \tag{2.19}$$

where e is the charge of an electron, $\mathrm{m_A}$ is the mass of the absorber, f is the oscillator strength of the absorber and $\Delta\lambda_{\mathrm{D}}$ is the Doppler shift of the most probable velocity calculated as $\sqrt{2kT/\mathrm{m_A}}$, also known as standard deviation of the wavelength distribution (Gray, 2008, his Eq. 11.42). The standard deviation (σ) of the Gaussian distribution in Eq. (2.19) is calculated as

$$\Delta\lambda_{\mathrm{D}} = 4.301 \times 10^{-7}\lambda\sqrt{\frac{T}{A}}, \tag{2.20}$$

where A is the atomic weight in atomic mass units and T is the local temperature of the gas around the absorber. Therefore $\Delta\lambda_{\mathrm{D}} = \sigma$. The $FWHM$ of a Gaussian distribution is given as $FWHM = 2\sigma\ln 2$. The velocity component of the $FWHM$ is calculated by Eq. (2.18). Therefore Eq. (2.20) can be rewritten in velocity-space as

$$v_{\text{thermal}} = 1.788 \times 10^{-1}\sqrt{\frac{T}{A}}, \tag{2.21}$$

in units of $\mathrm{km\,s^{-1}}$.

In my star sample, this parameter is small relative to other Doppler effects discussed below, $v_{\rm thermal} \sim 1.0 - 2.0\,{\rm km\,s^{-1}}$. ATLAS calculates the thermal broadening component for each atomic species during the synthesis using these assumptions and equations.

Microturbulent broadening

We must consider the effect small scale motions of particles (i.e. motions of particles on scales smaller than the photon mean free path) have on the absorber. We call this the microturbulence (ξ). Traditionally, we model ξ as a Gaussian profile. This broadening value is usually small relative to the macroturbulent broadening.

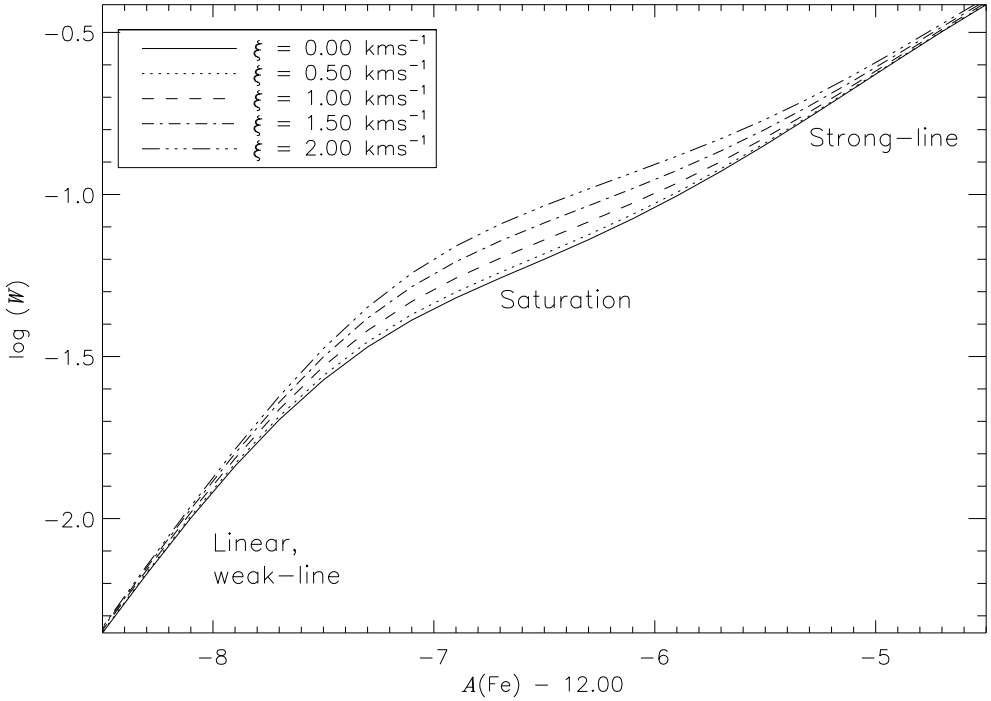

Fig. 2.4: Curve of growth computed using ATLAS for the synthetic Fe I 4282 Å line at $\xi = 0.00$, 0.50, 1.00, 1.50 and $2.00\,{\rm km\,s^{-1}}$ for the HD 140283 model atmosphere ($T_{\rm eff}/\log g/[{\rm Fe/H}] = 5750/3.7/-2.5$). The macroturbulence is set to $0.0\,{\rm km\,s^{-1}}$ but would have no effect on the structure of this plot. There are three distinct regions to the curve of growth. The linear part, where $W \propto A$, shows how weak lines behave. Here there is no saturation so that one can model the broadening of these lines through their Doppler motions without pressure effects dominating. The next part of the curve of growth shows how lines react under core saturation where $W \propto \ln A$. Here the core of the line begins to saturate. Increasing ξ increases the equivalent width at which this occurs. The final part of the curve of growth, where strong lines reside, shows the relationship between W and abundance change again. At this stage $W \propto \sqrt{A}$, as τ_ν in the wings becomes large relative to κ_ν (Gray, 2008).

Like the macroturbulence, ξ is another parameter that cannot be properly modelled by synthesis codes so is calculated separately from it. A synthetic curve of growth, like

Fig. 2.4 for $\xi = 0.0\,\mathrm{km\,s^{-1}}$, underestimates the point at which saturation of the line core occurs. The inclusion of $\xi > 0$ in the synthesis shifts the point at which saturation occurs to higher equivalent widths (W), which is a measurement of line strength

$$W = \int_0^\infty \frac{F_c - F_\lambda}{F_c}\,\mathrm{d}\lambda, \tag{2.22}$$

where F_c and F_λ are the fluxes at the continuum and at the line core respectively. Re-evaluating the synthesis to include ξ values that fit the observed spectral lines with consistent abundances allows one to constrain this parameter.

Macroturbulent broadening

If we observe how matter in the photosphere of the Sun behaves, we notice it moves in convection cells that rise to the surface and fall back into the deeper layers of the atmosphere. We can also see that the Sun rotates. A subroutine of ATLAS, called ATLAS_VELBROADEN, calculates three types of symmetric profile; a Gaussian, a radial-tangential (ζ_{RT}) and a $v \sin i$ profile. The macroturbulence of the star is modelled by either a Gaussian or ζ_{RT} profile, while the rotation is modelled using a $v \sin i$ profile. By convolving any of these profiles with the synthetic spectrum we can mimic and therefore measure this excess broadening of spectral features caused by the macroscopic turbulence and the rotation of the star. Fig. 2.5 demonstrates how the line profile of an absorption line is affected by each type of broadening.

Each convection cell in the Sun (or a star) has the effect of Doppler shifting photons that particles emit or absorb. Studying the Sun tells us that there are many convection cells with different velocities. Therefore when we take a spectrum of a star, we know that the light collected would have come from or been absorbed by many similar convective cells of varying Doppler shifted velocities (Gray, 2008).

When modelling the velocity distribution of the Doppler shifted convective cells it is common to treat its behaviour as Gaussian. A simple Gaussian profile of user input $FWHM$ is convolved with the synthetic spectrum, thereby broadening the profile of each absorption line in the spectrum. Grids of varying Gaussian broadening are then

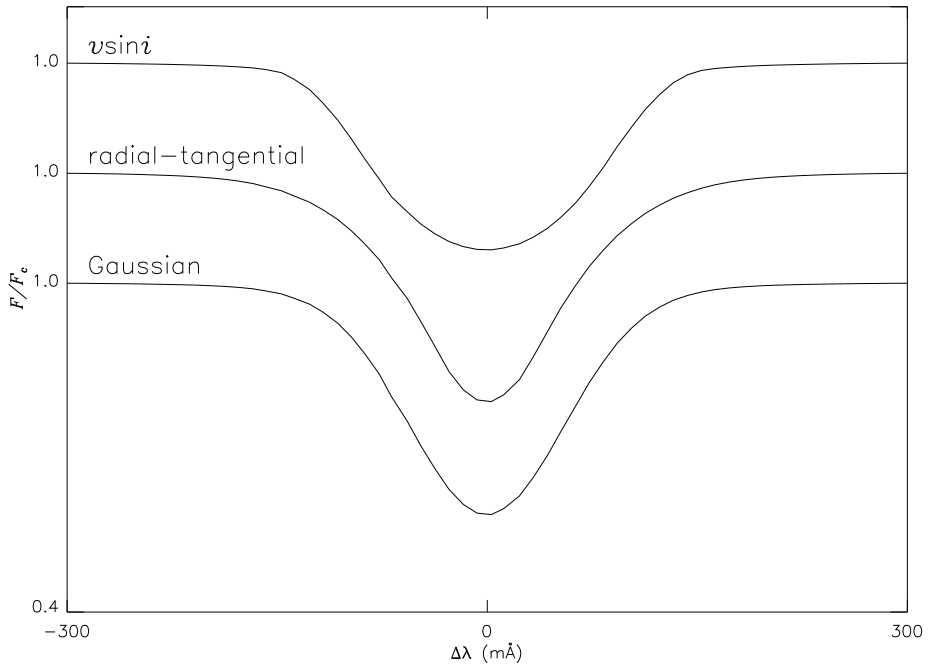

Fig. 2.5: The effect that each type of broadening has when convolved with the profile of an absorption line (Fe I 4282 Å). The profiles were synthesised using the HD 140283 model atmosphere ($T_{\rm eff}/\log g/[{\rm Fe/H}] = 5750/3.7/-2.5$). All profiles shown here include thermal, natural and pressure profiles as well as the excess macroturbulence. The velocities of all three profiles were set to $8.0\,{\rm km\,s^{-1}}$ and there was no microturbulence included.

compared to observed data to measure the macroturbulence.

However, it has been established for some time through solar observations that the velocity distributions of these convective cells are not distributed as a perfect Gaussian (Gray, 2008) and that spectral features are in fact asymmetric. In the past, however, quality of a solar spectrum was vastly superior to any stellar spectrum so asymmetric behaviours visible in a solar spectrum were obscured in stellar data. With more powerful telescopes and improvements in instrumentation, the quality of stellar data has improved enough so that asymmetries in stellar absorption lines caused by asymmetric velocity fields in the convection cells are now observable (Gallagher et al., 2010). This means that synthetic fits to stellar data worsen as 1D LTE codes are limited to calculating symmetric profiles.

I show later (Chapters 3 and 4) that a radial-tangential ($\zeta_{\rm RT}$) profile simulates line shapes better than a Gaussian (Gallagher et al., 2010, 2012). The profile is still symmetric so still not able to fully replicate the effects of true 3D convection, but unlike a simple Gaussian the $\zeta_{\rm RT}$ profile considers the Doppler broadening of absorbing and

emitting photons within convective cells separately in two directions; the radial or line-of-sight broadening and the direction tangential to this. A schematic diagram of the radial-tangential consideration can be found in Fig. 2.6 and the effect this parameter has on the absorption profile is shown in Fig. 2.5.

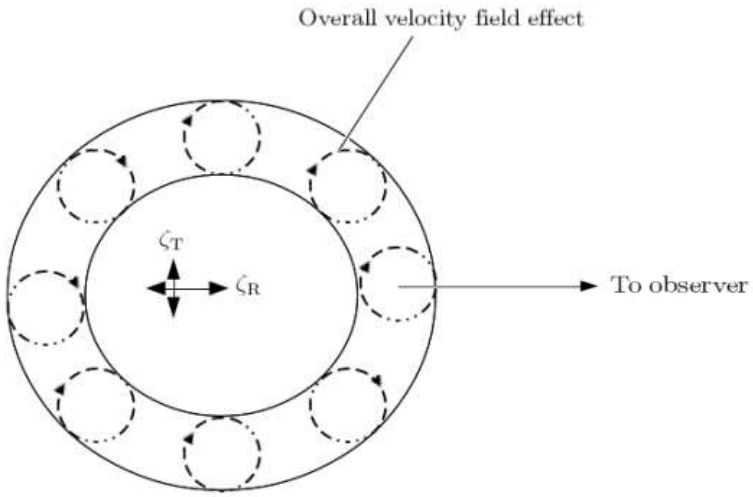

Fig. 2.6: The overall effect of the two velocity components in an ζ_{RT} broadening profile on the photosphere. Photons that are absorbed or emitted in these velocity cells are subject to broadening (Gray, 2008).

As is illustrated, the two components simulate the turbulent motions of the gas within a convective cell, which rises and falls through the photosphere, as it emits and absorbs light. From Gray (2008) the integrals that define these two components are evaluated as

$$\Delta\lambda_R = \frac{1}{\pi^{1/2}\zeta_R}\int_0^{\frac{\pi}{2}} e^{(-\Delta\lambda/\zeta_R\cos\theta)^2}\sin\theta\,d\theta \tag{2.23}$$

$$\Delta\lambda_T = \frac{1}{\pi^{1/2}\zeta_T}\int_0^{\frac{\pi}{2}} e^{(-\Delta\lambda/\zeta_R\sin\theta)^2}\cos\theta\,d\theta \tag{2.24}$$

where ζ_R and ζ_T are the radial and tangential velocity components respectively. The derivations of these components is beyond the scope of the work presented here. Usually, and in the present work, it is assumed that $\zeta_R = \zeta_T = \zeta_{RT}$, however, varying the ζ_R and ζ_T components could be considered when utilising ζ_{RT} in future works.

Rotational broadening

The rotation of a star Doppler shifts the light it emits; the light emitted from the star's edge with a negative velocity component will be blue shifted relative to the light emitted from the positive velocity component, which is red shifted. This is modelled by $v \sin i$ where v is the equatorial rotation speed of the star and i represents the inclination of the rotation axis to the line-of-sight. Fig. 2.5 shows how $v \sin i$ affects an absorption line profile.

The rotational component in metal-poor stars is usually negligible as they have usually spun down through the mechanisms discussed in §1.1.1. This is nicely illustrated in Chapter 3 where I determine HD 140283's maximum rotational value and again in Chapter 5 where I determine $v \sin i$ for several Fe lines using a 3D LTE modelling technique.

2.3.6 Instrumental broadening

As a direct result of the finite slit width and image characteristics of spectrographs, an additional broadening mechanism must be accounted for when synthesising a spectrum: the instrumental broadening. The mathematics that explain image quality goes beyond the scope of the work presented here. Suffice it to say that the spectral resolution of the spectrograph is quantified by measuring ThAr emission lines exposed before or after the stellar spectrum. Measuring the $FWHM$ of the ThAr lines can tell you two things: the resolution of the spectrograph's configuration

$$R \equiv \frac{\lambda}{\Delta\lambda}, \tag{2.25}$$

where $\Delta\lambda$ is the $FWHM$ of the ThAr emission lines, and the instrumental broadening contribution in velocity-space found by using Eq. (2.18).

In general, the instrumental profile is modelled using a Gaussian profile (Aoki et al., 2004). Similarly if the macroscopic Doppler broadening is modelled as a Gaussian, rather than modelling both these profiles separately and convolving them post synthesis, I simply add $v_{\rm inst}$ (in quadrature) to the velocity-space Doppler $FWHM$ contribu-

tion $v_{\rm Doppler}$, which I call $v_{\rm conv}$.

2.3.7 Chemical abundances

Changing the abundance parameters of the model atmosphere affects the number of absorbers in the atmosphere. An increase in absorbers (an increase in abundance) would increase line strength as photons have a higher probability of being absorbed (Fig. 2.4). This also has an effect on line profile. Fig. 2.7 shows how increasing the abundance affects the strength of the line and how it behaves under core saturation.

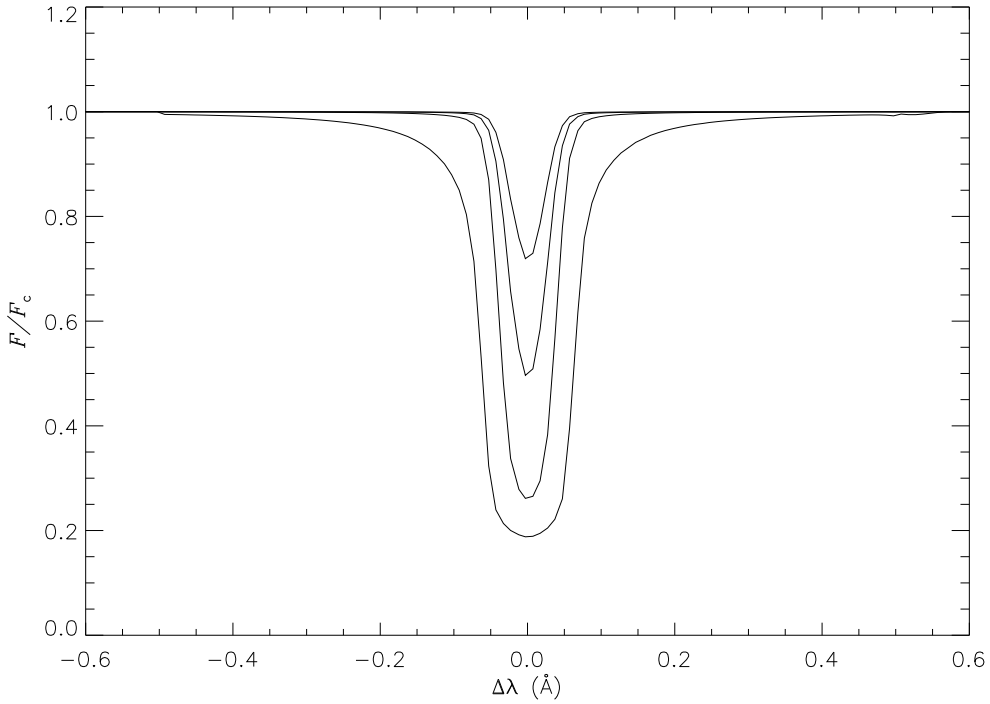

Fig. 2.7: The effect of changing A(Fe) on HD 140283's Fe I 4282 Å absorption line's equivalent width with A(Fe) = 4.10, 4.50, 5.10 and 6.30. As saturation occurs the wings of the line become significantly broadened.

As the abundances in the Kurucz model atmospheres are scaled to solar, it is easy to convert them to the standard abundance scale, defined in Eq. (2.9)

$$A(\mathrm{X})_* = A(\mathrm{X})_{\rm Kurucz} + [\mathrm{Fe/H}] + [\mathrm{X/Fe}], \tag{2.26}$$

where $A(\mathrm{X})_*$ is the abundance as defined by Eq. (2.9), $A(\mathrm{X})_{\rm Kurucz}$ is the Kurucz solar abundance scale (from Anders & Grevesse, 1989), [Fe/H] is the model atmosphere

metallicity, and [X/Fe] is the abundance scale set by the model atmosphere metallicity.

2.3.8 Running ATLAS

To run ATLAS, I wrote two tc-shell scripts so that grids of synthetic spectra could be produced relatively easily for either Fe or Ba lines. The script includes the option to run ATLAS for several different values of microturbulence, abundance and isotope ratio (for Ba only). The script then calls ATLAS_VELBROADEN once ATLAS has computed the intrinsic spectrum to compute and convolve macroturbulent or rotational broadening to it. An example of this script, which I used for synthesising grids of Fe lines, can be found in Appendix A.2.

The scripts also allowed me to set the wavelength spacing ($\Delta\lambda$) and the wavelength ranges of the spectra. Given that my observed data had resolutions of $\sim 90\,000-95\,000$, which equates to $\langle\Delta\lambda\rangle = 0.02$ Å averaged over the wavelength ranges of my spectra, it seemed satisfactory to run my synthetic grids with $\Delta\lambda$ set at 0.01 Å.

As I stated in the opening of this Chapter, faster, more powerful computers have meant that spectrum synthesis construction is incredibly fast. It takes roughly five seconds to synthesise one spectrum over a wavelength range $4100 \leq \lambda$ (Å) ≤ 6900 with a wavelength spacing $\Delta\lambda = 0.01$ Å (the wavelength sampling size and range used in the analysis of HD 140283). Therefore completing a typical grid of 680 spectra with various abundances and macroturbulences, used for the analysis in Chapter 3 (the specific details on the abundance and macrotrubulence are found there), takes roughly one hour of computation.

2.4 The Fe line data

For ATLAS to synthesise absorption lines, a list of lines must be input along with the atmosphere. This list must include several physical parameters, characteristic to each line to synthesised. They are the central wavelength (λ_c), the atomic number (Z), the atomic weight, the excitation potential (χ), $\log gf$ and the van der Waals γ_6 enhancement factor (E_γ). An example of the formatting of this file is shown in Fig. 2.8.

As shown, Z is not represented by an integer number, but rather by a real number, which represents the ionised state of the line, e.g Fe I and Fe II are represented by 26.00 and 26.01 respectively.

```
3659.519  26.00  55.85  2.453  0.0703072 2.2
3660.317  26.00  55.85  2.865  0.0000700 2.2
3660.401  26.00  55.85  2.609  0.0005649 2.2
3660.448  26.01  55.85  8.959  0.0000279 2.2
3660.900  26.01  55.85  8.801  0.0000255 2.2
```

Fig. 2.8: An example of the Fe line list input into ATLAS. From left to right the columns represent λ_c, Z, atomic weight, χ, gf and E_γ.

The excitation potential (χ) represents the energy of the lower-level transition, and in the present work is expressed in eV. For example the excitation potential for an $n = 2$ to $n = 4$ transition would be the energy at $n = 2$, where n represents the energy level, with $n = 1$ as the ground state level ($\chi = 0\,\mathrm{eV}$).

The input parameter gf represents the product of the statistical weight (g) of the lower-level transition and the oscillator strength (f), or rather gf represents the probability of a transition. ATLAS requires its input in this manner, although it is more usual to see gf values tabulated as a logarithm ($\log gf$). For hydrogen or hydrogenic ions[5], g can be calculated by $g = 2n^2$. However, g is calculated empirically for more complex atomic or ionic systems. The parameter f represents the quantum mechanical correction to the harmonic-oscillator line strength calculated using the classical approach and, like g, is also typically measured under laboratory conditions.

The parameter E_γ is not a mandatory parameter for ATLAS and can be set to 1.0. It represents an enhancement factor usually included when using the Unsöld approximation for C_6, Eq. (2.15), to calculate γ_6, Eq. (2.17). In §2.3.4 I stated that the Unsöld approximation for the van der Waals pressure broadening ($\gamma_{6,\mathrm{vdW}}$) constantly underestimates γ_6. Therefore E_γ is used to re-evaluate this term to a more realistic value. I set $E_\gamma = 2.2$ throughout the present work, unless stated otherwise (Ryan, 1998).

The Fe line data comes from several sources; the IRON PROJECT (which consists of several papers written over the last 20 years), Kurucz & Peytremann (1975), Blackwell

[5]Hydrogenic ions are atoms with only one electron, e.g. He II, Li III, etc.

et al. (1979), Blackwell et al. (1980), Blackwell et al. (1982), Fuhr et al. (1988), Bard et al. (1991), O'Brian et al. (1991), Bard & Kock (1994) and Nave et al. (1994).

2.5 The Ba lines

To accurately explain the heavy element chemical history in a star through interpretation of its observed spectrum, one must study the relative contributions of the s- and r-process for several atomic species for comparison to current nuclear theory. In the present work I have studied Ba in great detail, and Eu to a lesser degree (§3.6), rather than a series of heavy elements. This is for two reasons, which I now discuss.

Currently, analysis of the Ba isotopes requires the most precise stellar spectra with the highest levels of R and S/N even though, as we shall see over the rest of this chapter, Ba has a large differences in the isotope configurations between the s- and r-process limits, relative to other heavy element isotope configurations. However, Roederer et al. (2008) carried out an isotope analysis on Eu, Sm and Nd with precarious results.

The relative contributions by the s- and r-processes to isotopes in the solar system varies for different species. For example, Eu has two stable isotopes: ^{151}Eu has relative s- and r-process contributions 6.5% and 93.5% respectively and ^{153}Eu has relative s- and r-process contributions 5.1% and 94.9% respectively (Arlandini et al., 1999). To determine the relative contributions of this species, Roederer et al. (2008) used the relationship f_{151}, where:

$$f_{151} = \frac{N(^{151}\mathrm{Eu})}{N(\mathrm{Eu})}. \tag{2.27}$$

According to isotope information presented in Arlandini et al. (1999), $f_{151} = 0.54$ for an s-process-only isotope configuration and $f_{151} = 0.47$ for an r-process one. This means that an extremely sensitive analysis would be required to determine the precise s- and r-process contributions to the Eu line, which is beyond the capabilities of all 1D LTE codes due to the assumptions used to calculate them (§2.1).

In summary, new instrumentation is constantly improving and the data obtainable

via various techniques designed to improve upon how systematic errors associated with their reduction are treated (e.g. Butler et al., 1996) are also increasing the level of sensitivity. As such, individual isotopes in absorption lines are partially resolvable. The trade off however, is that real astrophysical effects (e.g. 3D convection etc.) become more apparent in the data (Gallagher et al., 2010). Modelling these effects with newer, more powerful synthetic codes is a relatively new concept and as such the codes are still in the development phase. Therefore there has been little to no analysis of isotopes in this manner using such codes. Below we see that the isotope structure and configuration of Ba currently make it the best element to work with for heavy element isotope studies.

2.5.1 Isotopic data

The relative s- and r-process contributions to nuclides used to determine the isotopic abundances of Ba, were calculated in Arlandini et al. (1999) for nuclides ranging from ^{63}Cu to ^{209}Bi. They used the hydrostatic LTE code FRANEC (Straniero et al., 1997; Gallino et al., 1998) to model two AGB stars with masses $1.5\,M_\odot$ and $3\,M_\odot$, at half solar metallicity ($Z = \frac{1}{2}\,Z_\odot = 0.01$). They assumed all the s-process yields to be the result of synthesis through the main s-process only. They say it is possible to model the weak s-process with the code, however the reaction rate of $^{22}\mathrm{Ne}(\alpha,\mathrm{n})^{25}\mathrm{Mg}$ has large uncertainties associated with it (Käppeler et al., 1994), which would have enhanced uncertainties in their results, so it was excluded. As such, the release of neutrons is determined by the rate of the $^{13}\mathrm{C}(\alpha,\mathrm{n})^{16}\mathrm{O}$ reaction, which is also rather uncertain at $kT = 8\,\mathrm{keV}$ ($T \approx 10^8\,\mathrm{K}$; He burning temperatures) as it is calculated using experimental data at higher energies (Denker et al., 1995). They state that no third dredge-up was found for lower mass ($M < 1.5\,M_\odot$) stars.

The code requires the input of a free parameter, the artificial "^{13}C pocket", as the precise physics of how ^{12}C and H are mixed before the $^{12}\mathrm{C}(\mathrm{p},\gamma)^{13}\mathrm{N}(\beta^+,\nu_\mathrm{e})^{13}\mathrm{C}$ reaction takes place, during H burning shell reignition, is still unknown. The ^{13}C pocket is located at the top of the convective He shell and below the H burning shell. Future generation hydrodynamic codes should be able to simulate the mixing processes in this

region of the star via time-dependent simulations, which would eliminate the need for the artificial ^{13}C pocket (Busso et al., 1999). The study presented by Herwig et al. (2006), who invested He-shell flash convection using multi-dimensional simulations, suggest that mixing occurs when convective motions cross the established convective boundaries, which is caused by high-velocity convection pockets bridging the two regions. The subsequent $^{13}\mathrm{C}(\mathrm{p},\gamma)^{14}\mathrm{N}$ reaction on the CN-cycle which is faster than the $^{13}\mathrm{C}(\alpha,\mathrm{n})^{16}\mathrm{O}$ reaction, and would prevent s-processing if H is plentiful, cannot consume large amounts of ^{13}C if the number of H nuclei available per ^{12}C nucleus is small (Gallino et al., 1998). The size of the ^{13}C pocket thus determines the neutron fluence in the model (Arlandini et al., 1999). The ^{13}C pocket is heated to $\sim 8\,\mathrm{keV}$ (Straniero et al., 1995) after subsequent thermal pulses, brought on by He shell instabilities. The $^{13}\mathrm{C}(\alpha,\mathrm{n})^{16}\mathrm{O}$ reaction takes place between thermal pulses, releasing free neutrons under radiative rather than convective conditions (Straniero et al., 1995). This means that the s-processing is extremely efficient in these zones; most of the free neutrons are consumed during s-process events (Arlandini et al., 1999).

The neutron-capture cross sections used for their stellar models were taken from a variety of sources, all of which are discussed in Arlandini et al. (1999). They find a satisfactory reproduction of the solar distribution of the s-process isotopes in the range $88 < A < 208$ (where A here represents the baryon number). Although not stated, one would assume this to be because the lighter elements calculated, $63 < A < 87$, are primarily synthesised via the weak s-process (Pignatari et al., 2010), which Arlandini et al. (1999) do not model. This is seen through large discrepancies that exist between solar-system measurements of isotope abundances (Anders & Grevesse, 1989) and the results produced by the Arlandini et al. (1999) stellar models.

Ba has five stable isotopes that can be synthesised via the two neutron-capture processes, all of which can be synthesised via the s-process. For ^{134,136}Ba, synthesis via the r-process path is blocked by the stable isotopes ^{134,136}Xe respectively. Therefore these two isotopes are s-process-only isotopes. The remaining three isotopes, ^{135,137,138}Ba, can be synthesised by both the s- and r-process. Table 2.1 presents details on the relative contributions of the s- and r-processes to the isotope abundances from the

Arlandini et al. (1999) calculations.

I use the ratio $f_{\rm odd}$ as a surrogate measure for the s- and r-process contributions, where

$$f_{\rm odd} = \frac{[N(^{135}{\rm Ba}) + N(^{137}{\rm Ba})]}{N({\rm Ba})}. \tag{2.28}$$

Limits on the s- and r-process values of $f_{\rm odd}$ can be set using the theoretical s-process and the r-process isotope abundances. Using the relationship in Eq. (2.28) with results presented in rows $(1)-(5)$ in Table 2.1 for an s-process or r-process-only isotope mix, we find $f_{{\rm odd},s} = 0.11 \pm 0.01$ and $f_{{\rm odd},r} = 0.46 \pm 0.06$ respectively. The r-process limit is expected to have a larger uncertainty associated with it, as $N_{\rm r}$ is taken to be the residual of $N_{\rm s}$ relative to solar ($N_{\rm r} = N_{\odot} - N_{\rm s}$).

Table 2.1: Isotopic abundances of Ba for the s- and r-process when normalised to ^{150}Sm (Arlandini et al., 1999), ^{134}Ba and ^{136}Ba. $N_{\rm r}$ is calculated as the residual of $N_s^{\rm main}$ relative to $N_{\odot}$. Errors on the isotope abundances presented in Arlandini et al. (1999) are given in rows $(1)-(5)$.

	Isotope	$N_{\odot}$	$N_{\rm s}^{\rm main}$	$N_{\rm r}$	contribution by the s-process	contribution by the r-process
	normalised to ^{150}Sm					
(1)	134	0.109	0.107 ± 0.008	···	98.2%	0.0%
(2)	135	0.296	0.078 ± 0.006	0.219 ± 0.019	26.4%	74.0%
(3)	136	0.353	0.354 ± 0.025	···	100.0%	0.0%
(4)	137	0.504	0.330 ± 0.024	0.174 ± 0.040	65.5%	34.5%
(5)	138	3.220	2.760 ± 0.179	0.459 ± 0.270	85.7%	14.2%
	normalised to ^{134}Ba					
(6)	134	0.109	0.109	···	100.0%	0.0%
(7)	135	0.296	0.079	0.217	26.7%	73.3%
(8)	136	0.353	0.361	···	102.3%	0.0%
(9)	137	0.504	0.336	0.168	66.7%	33.3%
(10)	138	3.220	2.810	0.408	87.3%	12.7%
	normalised to ^{136}Ba					
(11)	134	0.109	0.107	···	98.2%	0.0%
(12)	135	0.296	0.077	0.219	26.0%	74.0%
(13)	136	0.353	0.353	···	100.0%	0.0%
(14)	137	0.504	0.329	0.175	65.3%	34.7%
(15)	138	3.220	2.750	0.468	85.4%	14.5%

The isotope abundances presented in Arlandini et al. (1999) are normalised with respect to s-process-only isotope ^{150}Sm. Therefore discrepancies can occur in the relative isotopic abundances for other isotopes. This can be seen for ^{134}Ba, a main s-process-

only isotope, where the total contribution by the main s-process is reported as 98.2%, rather than 100%. To avoid unnecessary errors that could occur when propagating this normalisation to the Ba isotope abundances, we renormalised them to the Ba isotopes for two cases, ^{134}Ba and ^{136}Ba, both of which are s-process-only isotopes meaning the total measured solar abundance for them should originate from s-process nucleosynthesis only. This was used primarily as a test to check the rigidity of the limits on $f_{\rm odd}$ set by the s- and r-process-only isotopic abundances used during my analysis. When the isotopes were renormalised to ^{134}Ba, rows (6) − (10), Table 2.1, $f_{{\rm odd},s}$ remained unchanged at 0.11, however the r-process limit to $f_{\rm odd}$ was increased such that $f_{{\rm odd},r} = 0.49$. When the abundances were renormalised to ^{136}Ba, rows (11) − (15), Table 2.1, no change was found to either $f_{{\rm odd},s}$ or $f_{{\rm odd},r}$.

As little to no difference was found when renormalising the Ba isotopes, it seemed logical to use the values calculated in (Arlandini et al., 1999) to construct the line lists used for the work conducted in Chapters 3 & 4.

2.5.2 Hyperfine splitting

Fig. 2.9 shows various energy levels for several transitions of Ba II. The Ba II 4554 and 4934 Å resonance lines were used to determine $f_{\rm odd}$ in the present work. Other higher excitation lines were considered but subsequently rejected from any analysis as the hyperfine splitting in these lines is too small for us to detect the subtle changes in the line profile asymmetries due to different isotope mixtures to an acceptable degree of accuracy. The 4554 and 4934 Å lines have large hfs splitting patterns with $\sim$ 56 and 77 mÅ separating the bluest and reddest lines respectively, and are substantially larger than those found in higher excitation lines, e.g. the 4130, 5853 and 6141 Å lines have a total hfs split of $\sim$ 4.4, 10.3, and 12.2 mÅ, typical of the higher excitation lines. These transitions, as well as the 4554 and 4934 Å transitions can be seen in Fig. 2.9. In Chapter 4 I only analyse the Ba II 4554 Å line due to difficulties in the measurement of the 4934 Å line caused by Fe blends located within the blue wing, the details of which are discussed in §3.4.3.

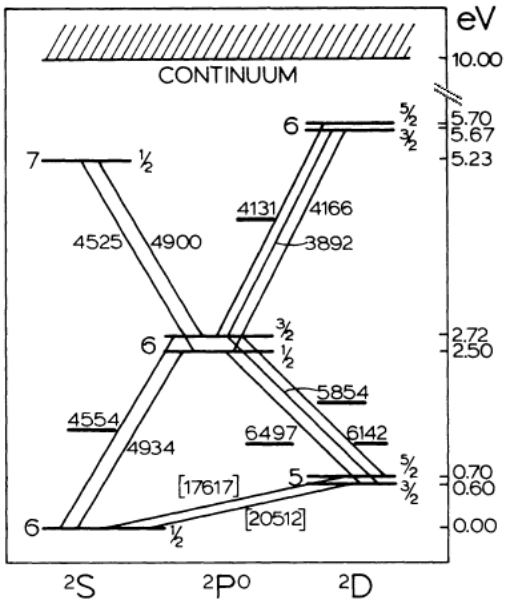

Fig. 2.9: The energy level diagram for several transitions of Ba II. The energies of each transition are displayed in eV on the right. No hfs is included in any transition. Image adopted from (Rutten, 1978).

For the purposes of the work conducted in this thesis I will only be discussing the $6S_{\frac{1}{2}} - 6P_{\frac{3}{2}}$ and $6S_{\frac{1}{2}} - 6P_{\frac{1}{2}}$ fine split transition (4554 and 4934 Å lines respectively).

Further splitting occurs in both transitions as each isotope has a slightly different transition energy that shifts the wavelength at which they absorb light ($\chi = hc/\lambda$), which is shown in the wavelength and relative isotope strength schematic in the bottom panel of Fig. 2.10. However the odd isotopes, where there is a non-zero net nuclear spin caused by an unpaired nucleon, experience further splitting due to hfs effects at the lower ($6S_{\frac{1}{2}}$) and upper ($6P_{\frac{1}{2}}$ and $6P_{\frac{3}{2}}$) energy levels. The schematic energy level diagrams in the top panel of Fig. 2.10 demonstrate the fragmentation at the lower and upper energy levels for both transitions.

We consider the 4554 Å line first. The hfs at the $6S_{\frac{1}{2}}$ energy level is large relative to the hfs at $6P_{\frac{3}{2}}$. This causes a larger wavelength split relative to the one seen in $6P_{\frac{3}{2}}$, which is represented by two large shifts either side of the central wavelength to the blue and the red (see Fig. 2.10, bottom left-hand panel). The $6P_{\frac{3}{2}}$ energy level, with a smaller difference in energies relative to those seen in $6S_{\frac{1}{2}}$, causes further splitting of the odd isotopes at both the red and the blue wavelengths relative to the even isotopes. In fact there are three odd isotope transitions at the blue and red of the even isotopes.

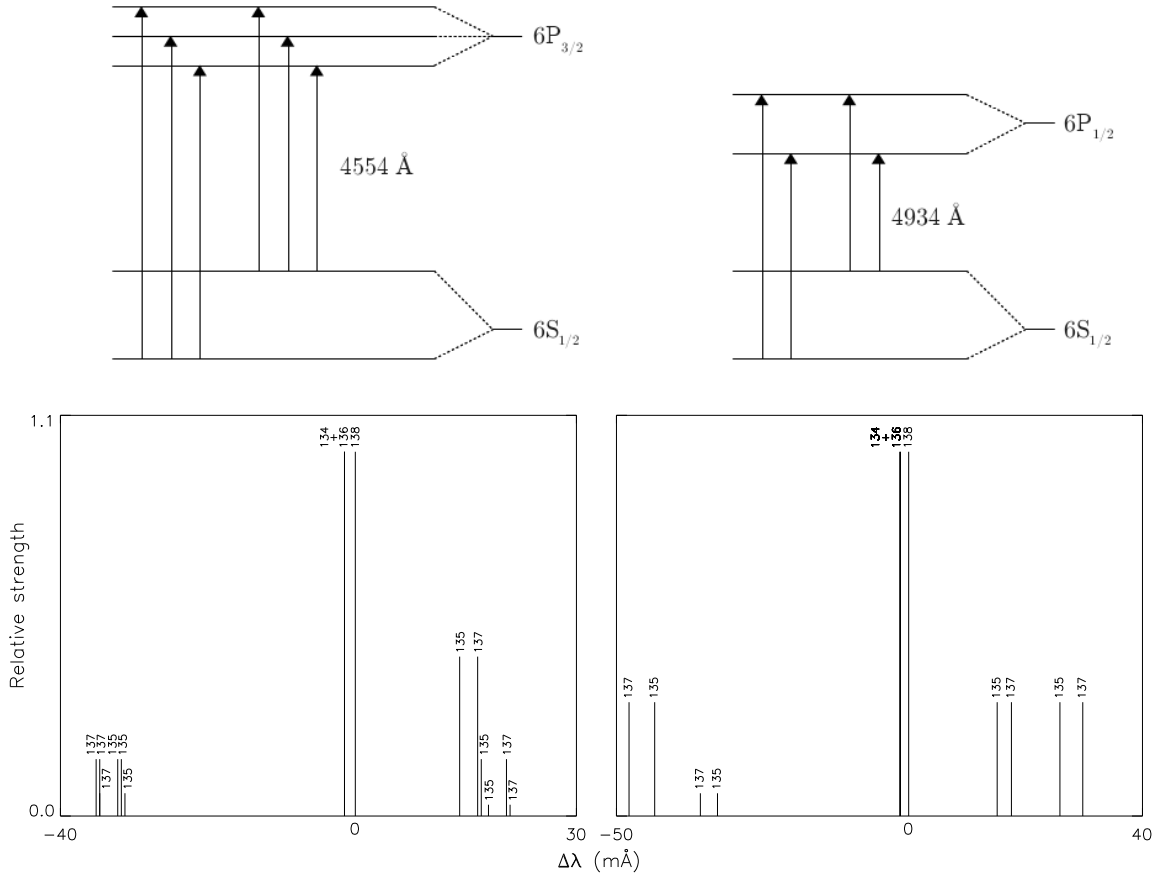

Fig. 2.10: *Top panel*: The schematic energy level diagram for the 4554 and 4934 Å lines showing hfs. The larger energy difference in the $6S_{\frac{1}{2}}$ level leads to the large wavelength shift, either side of the line's centre, shown in the bottom panel. *Bottom panel*: The hyperfine structure schematic for the 4554 Å line (*bottom left*) and the 4934 Å line (*bottom right*). Both have an odd isotope split essential for the work conducted in this thesis, however, the structure of the 4934 Å line shows a larger overall splitting of the isotopes than is found in the 4554 Å line. This is because the energy difference in the $6P_{\frac{1}{2}}$ transition is larger than that in the $6P_{\frac{3}{2}}$ transition.

The nature of the hfs in the odd isotopes in the 4934 Å line is in principle the same as in the 4554 Å line. However, Fig. 2.10 shows that there are only two hfs energy levels at $6P_{\frac{1}{2}}$. The effect of this causes two odd isotope splits either side of the even isotopes of 4934 Å rather than the three seen at 4554 Å, however, their wavelength shift relative to the even isotopes is larger than at 4554 Å due to a larger energy difference in the hfs of the $6P_{\frac{1}{2}}$ energy level relative to the $6P_{\frac{3}{2}}$ energy level.

The hfs information for Ba used throughout my work was adopted from Wendt et al. (1984) and Villemoes et al. (1993). Wendt et al. (1984) measured the isotope shifts of all seven stable Ba isotopes[6], and the hfs in the 4554 and 4934 Å lines. The even isotope

[6]The proton-capture isotopes ^{130,132}Ba and the neutron-capture series $^{134-138}$Ba.

wavelength information was adopted from this work. Villemoes et al. (1993) studied higher excitation lines with smaller hfs as a means of testing their subtle improvements to the Wendt et al. (1984) technique. They had made some improvements to the laser beam apparatus that had allowed them to constrain the hfs information with an improved accuracy. The odd isotope hfs information came from a combination of both studies, as Villemoes et al. (1993) only calculated the excited energy levels ($6P_{\frac{1}{2}}$ and $6P_{\frac{3}{2}}$) for each odd isotope. Table 2.2 displays the hyperfine magnetic dipole (A) and electric quadrupole (B) constants, which indicate the scale of the splittings of the energy levels. The relevant citation is also tabulated.

Table 2.2: The A and B constants taken from Wendt et al. (1984) and Villemoes et al. (1993) including their respective error estimates.

Level	135		137		Refs.
	A (MHz)	B (MHz)	A (MHz)	B (MHz)	
$6S_{\frac{1}{2}}$	3593.3 ± 2.2	$\cdots$	4020.3 ± 2.3	$\cdots$	(1)
$6P_{\frac{3}{2}}$	113.0 ± 0.1	59.0 ± 0.1	127.2 ± 0.2	92.5 ± 0.2	(2)
$6P_{\frac{1}{2}}$	664.6 ± 0.3	$\cdots$	743.7 ± 0.3	$\cdots$	(2)

(1) Wendt et al. (1984)
(2) Villemoes et al. (1993)

The A and B constants are processed via a simple Fortran code (written by Sean G. Ryan) that utilises the equations taken from McWilliam et al. (1995):

$$\Delta E = \frac{1}{2}AK + B\left[\frac{\frac{3}{2}K(K+1) - J(J+1)I(I+1)}{2I(2I-1)(2J-1)}\right], \tag{2.29}$$

where

$$K = [F(F+1) - I(I+1) - J(J+1)], \tag{2.30}$$

I is the nuclear spin quantum number (for both lines of interest and for both isotopes $I = 3/2$),

J is the total electronic angular momentum quantum number and

F is the total allowable angular momentum quantum number in a given level.

The Fortran code calculates the splittings ΔE using Eqs. (2.29) & (2.30) with the

constants from Table 2.2, over every allowable energy state, which is dependent on its quantum mechanical electronic angular momentum and nuclear spin. This gives the change in energy for each hfs split, which is displayed in Table 2.3 along with the even isotope energy differences, all with respect to the line centres.

Table 2.3: The Ba hfs wavelength information for the Ba II 4554 (λ_c = 4554.0332 Å) and 4934 Å (λ_c = 4934.0768 Å) lines relative to ^{138}Ba in both λ ($\Delta\lambda = \lambda_{\rm isotope} - \lambda_{138}$, where $\lambda_{138} = \lambda_c$) and ν space taken from the Wendt et al. (1984) and Villemoes et al. (1993) studies.

Isotope	4554 Å		4934 Å	
	$\delta\nu$ (MHz)	$\Delta\lambda$ (mÅ)	$\delta\nu$ (MHz)	$\Delta\lambda$ (mÅ)
134	233.9	−1.6	222.6	−1.8
135	4654.6	−32.2	5369.0	−43.6
	4582.3	−31.7	4051.4	−32.9
	4510.1	−31.2	−1847.1	15.0
	−2052.7	14.2	−3164.8	25.7
	−2471.9	17.1	···	···
	−2616.4	18.1	···	···
136	186.9	−1.3	179.4	−1.5
137	5088.3	−35.2	5910.9	−48.0
	5016.0	−34.7	4408.5	−35.8
	5016.6	−34.7	−2142.7	17.4
	−2399.6	17.1	−3645.0	29.6
	−2963.3	20.5	···	···
	−3035.6	21.0	···	···
138	0.0	0.0	0.0	0.0

Combined with the isotope information from Arlandini et al. (1999) I was able to create two Ba isotope lists; a fully s-process list and a fully r-process list. Copies of both lists are available in Appendix A.3. Gallagher et al. (2010) calculated, using their Fig. 1 (Fig. 3.1), a linear relationship between $f_{\rm odd}$ and the r-process percentage; $f_{\rm odd} = 3.5 \times 10^{-3}$ r-process (%)+0.11. Using the s- and r-process line lists and the equation from Gallagher et al. (2010), I could create hybrid lists by taking percentages of the s- and r-process lists' of gf values. They were then used as an input to the spectrum synthesis code ATLAS to create grids of Ba lines of varying $f_{\rm odd}$.

2.6 Observations

The synthetic spectra described above were used to analyse several dozen Fe lines and the Ba isotopes in six metal-poor stars. For each star I have high resolution

($R \equiv \lambda/\Delta\lambda = 90\,000 - 95\,000$), very high signal-to-noise ($S/N = 550 - 1100$) observed stellar spectra, which were obtained through observations using the High Dispersion Spectrograph (HDS) mounted on the Subaru 8.2 m optical-infrared telescope, located on the summit of Mouna Kea, Hawai'i.

The metal-poor subgiant star HD 140283 has the highest quality spectrum in my sample and is unique in its quality. This was obtained during the commissioning of the HDS by W. Aoki and reduced by S. Kawanomoto and first used in Aoki et al. (2004). As HD 140283 is a bright metal-poor star ($V = 7.21$ Cousins, 1984) a total of just 82 minutes spread over two nights (22$^{\rm nd}$ and 29$^{\rm th}$ July 2001) was required to obtain a spectrum with $R = 95\,000$ and $S/N = 1100$, about 4500 Å. The two giants in my sample, HD 122563 and HD 88609, were obtained over a number of nights between 2004 and 2005 and took 90 and 210 minutes to acquire spectra with $R = 90\,000$ and $S/N = 850$ and 750 about 4500 Å, respectively. They were obtained and reduced by S. Honda for work published in Honda et al. (2006) and Honda et al. (2007). The turn-off star, HD 84937, was obtained and reduced by A. Aoki for work with Li abundances in metal-poor turn-off stars (Aoki et al., 2009). The spectrum was obtained on the 22$^{\rm nd}$ March 2003 and took a total of 180 minutes of exposure time. The final two stars in my sample are the turn-off stars, BD-04° 3208 and BD-26° 3578. They were taken over three nights between the 17$^{\rm th}$ and 19$^{\rm th}$ of May 2005 and were obtained and reduced by A. García Pérez for work on Li isotopes (García Pérez et al., 2009).

As every spectrum in my sample is of the highest quality, which is needed for determining the Ba isotope ratios, it would have been difficult for me to obtain my own spectra for these stars of equal quality for the work conducted here because of the large amount of time required on an 8 m telescope to obtain even a single high quality spectrum. For further details of their acquisition I refer the reader to §3.2 and §4.2.

References

Allen, C. W. 1976, Astrophysical Quantities [ADS]

Anders, E. & Grevesse, N. 1989, Geochim. Cosmochim. Acta, 53, 197 [ADS]

Aoki, W., Barklem, P. S., Beers, T. C., Christlieb, N., Inoue, S., García Pérez, A. E., Norris, J. E., & Carollo, D. 2009, ApJ, 698, 1803 [ADS]

Aoki, W., Inoue, S., Kawanomoto, S., Ryan, S. G., Smith, I. M., Suzuki, T. K., & Takada-Hidai, M. 2004, A&A, 428, 579 [ADS]

Arlandini, C., Käppeler, F., Wisshak, K., Gallino, R., Lugaro, M., Busso, M., & Straniero, O. 1999, ApJ, 525, 886 [ADS]

Asplund, M., Carlsson, M., & Botnen, A. V. 2003, A&A, 399, L31 [ADS]

Bard, A., Kock, A., & Kock, M. 1991, A&A, 248, 315 [ADS]

Bard, A. & Kock, M. 1994, A&A, 282, 1014 [ADS]

Bell, R. A., Balachandran, S. C., & Bautista, M. 2001, ApJ, 546, L65 [ADS]

Blackwell, D. E., Ibbetson, P. A., Petford, A. D., & Shallis, M. J. 1979, MNRAS, 186, 633 [ADS]

Blackwell, D. E., Petford, A. D., Shallis, M. J., & Simmons, G. J. 1980, MNRAS, 191, 445 [ADS]

—. 1982, MNRAS, 199, 43 [ADS]

Böhm-Vitense, E. 1958, ZAp, 46, 108 [ADS]

—. 1989, Introduction to stellar astrophysics. Vol. 2. Stellar atmospheres. [ADS]

Busso, M., Gallino, R., & Wasserburg, G. J. 1999, ARA&A, 37, 239 [ADS]

Butler, R. P., Marcy, G. W., Williams, E., McCarthy, C., Dosanjh, P., & Vogt, S. S. 1996, PASP, 108, 500 [ADS]

Carlsson, M. 1986, Uppsala Astronomical Observatory Reports, 33 [ADS]

Cottrell, P. L. & Norris, J. 1978, ApJ, 221, 893 [ADS]

Cousins, A. W. J. 1984, South African Astronomical Observatory Circulars, Vol. 8, P. 59, 1984, 8, 59 [ADS]

Denker, A., Drotleff, H. W., Grosse, M., Knee, H., Kunz, R., Mayer, A., Seidel, R., Soiné, M., Wöohr, A., Wolf, G., & Hammer, J. W. 1995, in American Institute of Physics Conference Series, Vol. 327, Nuclei in the Cosmos III, 255 [ADS]

Freytag, B., Steffen, M., Wedemeyer-Böhm, S., Ludwig, H.-G., Leenaarts, J., Schaffenberger, W., Allard, F., Chiavassa, A., Höfner, S., Kamp, I., & Steiner, O. 2010, in Astrophysics Source Code Library, record ascl:1011.014, 11014 [ADS]

Fuhr, J. R., Martin, G. A., & Wiese, W. L. 1988, Journal of Physical and Chemical Reference Data, 17 [ADS]

Gallagher, A. J., Ryan, S. G., García Pérez, A. E., & Aoki, W. 2010, A&A, 523, A24 [ADS]

Gallagher, A. J., Ryan, S. G., Hosford, A., García Pérez, A. E., Aoki, W., & Honda, S. 2012, A&A, 538, A118 [ADS]

Gallino, R., Arlandini, C., Busso, M., Lugaro, M., Travaglio, C., Straniero, O., Chieffi, A., & Limongi, M. 1998, ApJ, 497, 388 [ADS]

García Pérez, A. E., Aoki, W., Inoue, S., Ryan, S. G., Suzuki, T. K., & Chiba, M. 2009, A&A, 504, 213 [ADS]

Gray, D. F. 2008, The Observation and Analysis of Stellar Photospheres (Cambridge: Cambridge University Press, 2008.) [ADS]

Herwig, F., Freytag, B., Hueckstaedt, R. M., & Timmes, F. X. 2006, ApJ, 642, 1057 [ADS]

Honda, S., Aoki, W., Ishimaru, Y., & Wanajo, S. 2007, ApJ, 666, 1189 [ADS]

Honda, S., Aoki, W., Ishimaru, Y., Wanajo, S., & Ryan, S. G. 2006, ApJ, 643, 1180 [ADS]

Käppeler, F., Wiescher, M., Giesen, U., Goerres, J., Baraffe, I., El Eid, M., Raiteri, C. M., Busso, M., Gallino, R., Limongi, M., & Chieffi, A. 1994, ApJ, 437, 396 [ADS]

Kromer, M., Sim, S. A., & Hillebrandt, W. 2009, in American Institute of Physics Conference Series, Vol. 1171, American Institute of Physics Conference Series, 207–214 [ADS]

Kurucz, R. L. 1970, SAO Special Report, 309 [ADS]

—. 1979, ApJS, 40, 1 [ADS]

Kurucz, R. L. & Peytremann, E. 1975, SAO Special Report, 362 [ADS]

Lester, J. B., Lane, M. C., & Kurucz, R. L. 1982, ApJ, 260, 272 [ADS]

McWilliam, A., Preston, G. W., Sneden, C., & Searle, L. 1995, AJ, 109, 2757 [ADS]

Nave, G., Johansson, S., Learner, R. C. M., Thorne, A. P., & Brault, J. W. 1994, ApJS, 94, 221 [ADS]

O'Brian, T. R., Wickliffe, M. E., Lawler, J. E., Whaling, W., & Brault, J. W. 1991, Journal of the Optical Society of America B Optical Physics, 8, 1185 [ADS]

Pignatari, M., Gallino, R., Heil, M., Wiescher, M., Käppeler, F., Herwig, F., & Bisterzo, S. 2010, ApJ, 710, 1557 [ADS]

Roederer, I. U., Lawler, J. E., Sneden, C., Cowan, J. J., Sobeck, J. S., & Pilachowski, C. A. 2008, ApJ, 675, 723 [ADS]

Rutten, R. J. 1978, Sol. Phys., 56, 237 [ADS]

—. 2003, Radiative Transfer in Stellar Atmospheres [ADS]

Ryan, S. G. 1998, A&A, 331, 1051 [ADS]

Steffen, M. 2007, in IAU Symposium, Vol. 239, IAU Symposium, 36–43 [ADS]

Steffen, M., Ludwig, H. G., & Wedemeyer-Böhm, S. 2010, LINFOR3D User Manual, Tech. rep. [LINK]

Stein, R. F. & Nordlund, A. 1998, ApJ, 499, 914 [ADS]

Straniero, O., Chieffi, A., Limongi, M., Busso, M., Gallino, R., & Arlandini, C. 1997, ApJ, 478, 332 [ADS]

Straniero, O., Gallino, R., Busso, M., Chiefei, A., Raiteri, C. M., Limongi, M., & Salaris, M. 1995, ApJ, 440, L85 [ADS]

Thévenin, F. & Idiart, T. P. 1999, ApJ, 521, 753 [ADS]

Villemoes, P., Arnesen, A., Heijkenskjold, F., & Wannstrom, A. 1993, Journal of Physics B Atomic Molecular Physics, 26, 4289 [ADS]

Wendt, K., Ahmad, S. A., Buchinger, F., Mueller, A. C., Neugart, R., & Otten, E.-W. 1984, Zeitschrift fur Physik, 318, 125 [ADS]

Chapter 3: The barium isotopic mixture for the metal-poor subgiant star HD 140283

The following chapter contains the unedited journal paper published by Gallagher, Ryan, García Pérez, & Aoki (2010), which was submitted and accepted for publication in Astronomy & Astrophysics. The associated online material for this article can be found in Appendix B.1. For analyses conducted after the publication of this paper please read Appendix C.

Abstract

Current theory regarding heavy element nucleosynthesis in metal-poor environments states that the r-process would be dominant. The star HD 140283 has been the subject of debate after it appeared in some studies to be dominated by the s-process. We provide an independent measure of the Ba isotope mixture using an extremely high quality spectrum and an extensive χ^2 analysis. We have acquired a very high resolution ($R \equiv \lambda/\Delta\lambda = 95\,000$), very high signal-to-noise ($S/N = 1110$ around 4554 Å, as calculated in IRAF) spectrum of HD 140283. We exploit hyperfine splitting of the Ba II 4554 Å and 4934 Å resonance lines in an effort to constrain the isotope ratio in 1D LTE. Using the code ATLAS in conjunction with KURUCZ06 model atmospheres we analyse 93 Fe lines to determine the star's macroturbulence. With this information we construct a grid of Ba synthetic spectra and, using a χ^2 code, fit these to our observed data to determine the isotopic ratio, $f_{\rm odd}$, which represents the ratio of odd to even isotopes. The odd isotopes and ^{138}Ba are synthesized by the r- and s-process while the other even isotopes (^{134,136}Ba) are synthesized purely by the s-process. We also analyse the Eu lines. We set a new upper limit of the rotation of HD 140283 at $v \sin i \leq 3.9\,\mathrm{km\,s^{-1}}$, a new upper limit on [Eu/H] < -2.80 and abundances [Fe/H] $= -2.59 \pm 0.09$, [Ba/H] $= -3.46 \pm 0.11$. This leads to a new lower limit on [Ba/Eu] > -0.66. We find that, in

the framework of a 1D LTE analysis, the isotopic ratios of Ba in HD 140283 indicate $f_{\rm odd} = 0.02 \pm 0.06$, a purely s-process signature. This implies that observations and analysis do not validate currently accepted theory. We speculate that a 1D code, due to simplifying assumptions, is not adequate when dealing with observations with high levels of resolution and signal-to-noise because of the turbulent motions associated with a 3D stellar atmosphere. New approaches to analysing isotopic ratios, in particular 3D hydrodynamics, need to be considered when dealing with the levels of detail required to properly determine them. However published 3D results exacerbate the disagreement between theory and observation.

3.1 Introduction

Heavy-element abundances are predominantly due to two classes of neutron-capture processes, the rapid (r-) process and the slow (s-) process. For the s-process the beta-decay lifetime is shorter than the time-scale for neutron-capture. These two classes can be sub-dived into the main, weak and strong s-process (Clayton & Rassbach, 1967; Busso et al., 2001; The et al., 2007; Sneden et al., 2008) and the main and weak r-process (Travaglio et al., 2004; Wanajo & Ishimaru, 2006; Izutani et al., 2009). Each neutron-capture process occurs in different environments. The main s-process occurs in late-type, low- to intermediate-mass stars ($1\ {\rm M}_{\odot} \lesssim M \lesssim 8\ {\rm M}_{\odot}$), during thermal pulsing on the asymptotic giant branch (AGB). An uncertain physical event or process is presumed to cause unprocessed H to mix with C-rich material in the He-burning shell to form ^{13}C (Busso et al., 2001). In this environment ^{13}C supplies the necessary neutrons via the reaction $^{13}{\rm C}(\alpha,{\rm n})^{16}{\rm O}$ (Burbidge et al., 1957). In the core He-burning phase of solar-metallicity massive stars, where temperatures are relatively high, the nuclear reaction $^{22}{\rm Ne}(\alpha,{\rm n})^{25}{\rm Mg}$ provides the main source of neutrons, however neutron-capture is mostly weak s-process (Pignatari & Gallino, 2008). The ^{22}Ne abundance is heavily dependent on the initial CNO abundance and the weak s-process produces little Ba relative to lighter species such as Sr (Gallino et al., 2000).

The astrophysical origin of the r-process is still relatively unknown. The most

widely proposed site for the r-process is when a massive star ($M > 8$ M$_\odot$) becomes a core-collapse supernova (Wheeler et al., 1998; Kajino et al., 2002). During a core-collapse supernova the neutron flux is believed to be so high that the neutron-capture time-scale is shorter than the beta decay lifetime. Other possible r-process sites have been considered such as neutron star mergers (Freiburghaus et al., 1999), however, these seem to have been ruled out as dominant sources for r-process material due to their low rates of occurrence (Argast et al., 2004). Several theoretical scenarios have been explored in an effort to understand this phenomenon (Wanajo & Ishimaru, 2006).

The relative importance of the r- and s-process throughout Galactic history depends on the evolutionary time-scales of the proposed sites and their elemental composition. The lifetimes for massive stars are much shorter than for low- to intermediate-mass stars. Typical lifetimes for 25 M$_\odot$, 8 M$_\odot$, 3 M$_\odot$ and 1 M$_\odot$ stars are $\sim 7 \times 10^{-3}$, 0.04, 0.4 and 10 Gyrs respectively (Romano et al., 2005). As such, the interstellar medium (ISM) at the time at which metal-poor (halo) stars were forming ($\sim$ 12 Gyr ago) should have been enriched by the supernovae of massive stars and hence, r-process material. Papers by Spite & Spite (1978) and Truran (1981) have been particularly influential in establishing this framework, as we now discuss.

Spite & Spite (1978) analysed 11 metal-poor halo stars that have a metal abundance less than 1/100 the solar metal abundance. They found that Ba and Y were overly deficient relative to Fe. Both elements can be formed via either neutron-capture process but are dominated by the s-process in the solar system where 81% of Ba and 92% of Y is formed via the s-process (Arlandini et al., 1999). The more metal-poor stars in Spite & Spite's sample had a greater [Ba/Fe][1] deficiency than [Y/Fe] deficiency meaning that as [Ba/Fe] decreases, [Ba/Y] decreases also. This is because a greater fluence of neutrons is needed to form Ba ($Z = 56$) than Y ($Z = 39$) so that [Ba/Y] gives a good indication of the number of neutrons captured (see Seeger et al., 1965). In contrast, Spite & Spite found that Eu, 94% of which is formed via the r-process in solar system material (Arlandini et al., 1999), has the same deficiency as Fe, such that [Eu/Fe] remains constant as [Fe/H] increases and is essentially solar at [Fe/H] $\geq$ -2.6.

[1] $[\mathrm{X/Y}] = \log_{10}\left(\frac{N(X)}{N(Y)}\right)_* - \log_{10}\left(\frac{N(X)}{N(Y)}\right)_\odot$

A consideration of the possible sites and seed requirements for neutron-capture led Truran (1981) to postulate that neutron-capture-element abundances in metal-poor stars should be dominated by those synthesized through the r-process. This expectation arises from the realisation that massive stars are capable of producing both the Fe-peak seed nuclei and the high neutron fluxes even from very low-metallicity gas, whereas intermediate-mass stars, while capable of producing neutrons, cannot produce the Fe-peak seeds necessary for the main s-process (see also Gallino et al., 1998). In Truran's interpretation, the variance of [Y/Fe] and [Ba/Fe] with [Fe/H] are exactly what one would find if the primary source for nuclei beyond the Fe-peak in metal-poor stars is due to r-process nucleosynthesis, while the s-process begins to contribute more significantly as [Fe/H] increases giving rise to the increase in [Y/Fe] and [Ba/Fe] seen by Spite & Spite (1978). He reasoned in addition that the enhancement of r-process nuclei would indicate that a prior generation of massive stars formed during or before the formation of the Galaxy. In a more quantitative calculation, Travaglio et al. (1999) examined the metallicity dependence of Ba synthesized in AGB stars via the s-process using the chemical evolution model, FRANEC (Straniero et al., 1997; Gallino et al., 1998). They found that Ba formed via the s-process has no significant contribution to the Ba abundance in the Galaxy until [Fe/H] $\gtrsim -1$. This supports Truran's hypothesis.

Different mixtures of odd and even Ba isotopes are produced by the r- and s-process. In particular, ^{134}Ba and ^{136}Ba are produced only by the s-process due to shielding by ^{134}Xe and ^{136}Xe in the r-process. Although the spectral lines of different Ba isotopes are not well resolved in stellar spectra, the profile core is dominated by the even isotopes while the odd isotopes, which experience hyperfine splitting (hfs), have more importance in the wings of the line profile, relative to the even isotopes. This means that the profiles of Ba II 4554 Å and 4934 Å are dependent on the contributions of the two processes. Hyperfine splitting arises from the coupling of nuclear spin with the angular momentum of its electrons. The nuclear spin is non-zero in nuclides with odd-N and/or odd-Z, i.e. where the nucleus has an unpaired nucleon. Hyperfine structure has been well documented in Ba (e.g. Rutten, 1978; Wendt et al., 1984; Cowley & Frey, 1989; Villemoes et al., 1993). As Ba has an even Z, only the two odd

isotopes, ^{135,137}Ba, experience hfs. Arlandini et al. (1999) calculate that the fraction of odd isotopes[2] of Ba is $f_{\mathrm{odd},s} = 0.11 \pm 0.01$ for a pure s-process mixture of Ba and infer $f_{\mathrm{odd},r} = 0.46 \pm 0.06$ for a pure r-process mixture. Their numbers are based on models which best reproduce the main s-process using an arithmetic average of 1.5 and 3 $\mathrm{M}_{\odot}$ AGB models at $Z = \frac{1}{2}\ \mathrm{Z}_{\odot}$. The errors stated here are our propagation of errors associated with individual isotope abundances for Ba. We show the linear relationship between r-process contributions (as a percentage) and f_{odd} in Fig. 3.1(a).

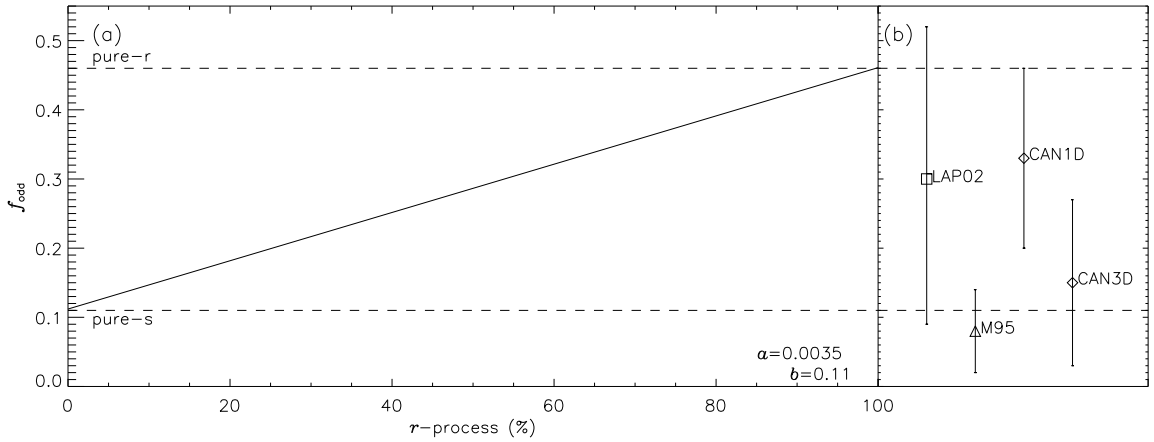

Fig. 3.1: (a) Relation between f_{odd} and the r-process contribution calculated from Arlandini et al. (1999). Coefficients are given where $f_{\mathrm{odd}} = a \times \text{r-process}\,(\%) + b$. (b) *LAP02*: the Lambert & Allende Prieto (2002) result for f_{odd}. *M95*: the Magain (1995) result for f_{odd}. *CAN1D*: the Collet et al. (2009) 1D LTE result for f_{odd}. *CAN3D*: the Collet et al. (2009) 3D hydrodynamical result for f_{odd}.

Magain (1995) attempted to verify Truran's proposal by measuring the odd fraction in HD 140283, a well studied metal-poor subgiant at [Fe/H] = -2.5 (Aoki et al., 2004), but found instead that theory and observations were not comparable. He used high-resolution ($R \equiv \lambda/\Delta\lambda = 100\,000$) high signal-to-noise ($S/N \approx 400$) data. Magain reported the fractional odd isotope ratio, f_{odd}, of Ba to be 0.08±0.06, implying that Ba production in HD 140283 is predominantly due to the s-process (see Fig. 3.1 (b)) despite [Fe/H] and [Ba/Fe] being very low, [Ba/Fe] = -0.8 (Spite & Spite, 1978). The code used to resolve the macroturbulence and analyse the Ba II 4554 Å line solves the equations of hydrostatic equilibrium under the assumption that the stellar atmosphere has a plane-parallel geometry (1D) and local thermodynamic equilibrium (LTE). In

[2] $f_{\mathrm{odd}} \equiv [N(^{135}\mathrm{Ba}) + N(^{137}\mathrm{Ba})]/N(\mathrm{Ba})$

contrast some more recent analyses, which we describe below, compute hydrodynamical 3D model atmospheres (3D) where the radiative transfer along multiple lines of sight is assessed.

The star was later reanalysed by Lambert & Allende Prieto (2002), again assuming 1D LTE. They obtained a very high-resolution ($R \equiv \lambda/\Delta\lambda = 200\,000$) high signal-to-noise ($S/N \approx 550$) spectrum about the Ba II 4554 Å line. They found a value for $f_{\rm odd} = 0.30 \pm 0.21$ and concluded that, contrary to Magain's result, the star is r-process dominated. A value for $f_{\rm odd} = 0.30 \pm 0.21$ would imply an r-process contribution of $54\% \pm 60\%$. We note, however, that the error in their measurement of $f_{\rm odd}$ means that their result covers the full range of possibilities from a pure s-process mix ($f_{{\rm odd},s} = 0.11$) to a pure r-process mix ($f_{{\rm odd},r} = 0.46$); see Fig. 3.1. This means that although they state that their result indicates that HD 140283 is r-process dominated, the range of $f_{\rm odd}$ is too broad to be conclusive. We consider that an r-process contribution of 54% does not substantially imply that the star's neutron-capture elements are dominated by those synthesised via the r-process.

Against this background, we sought to improve the determination of the s-process contribution to Ba in this star to help us understand the apparent conflicts.

While we conducted our study, Collet et al. (2009) reanalysed the Lambert & Allende Prieto (2002) spectrum in 1D LTE and, more significantly, also conducted a new 3D hydrodynamical analysis of the Ba isotopic fraction of HD 140283. In 1D LTE they found that $f_{\rm odd} = 0.33 \pm 0.13$, meaning that $64\% \pm 36\%$ of the Ba isotopes in HD 140283 are synthesized via the r-process. The central value (0.33) is little changed from that obtained by Lambert & Allende Prieto (2002) (0.30), which is not entirely surprising since they used the same spectrum, but Collet et al. (2009) quote smaller error bars. This is because Lambert & Allende Prieto (2002) adopted the standard deviation of macroturbulent broadening estimates as the main underlying measurement error. Collet et al. (2009) use the standard error $\sigma/\sqrt{N}$ (where N is the number of Fe lines used) as a measurement of error. The latter is a more reasonable estimate of the error as it is a measure of the uncertainty in the mean estimate of the broadening. Their analysis of the line using 3D hydrodynamics gives a value for $f_{\rm odd} = 0.15 \pm 0.12$

meaning only $11\% \pm 34\%$ of the isotopes are synthesized via the r-process. This value is in good agreement with the solar Ba isotopic mix ($f_{\mathrm{odd},ss} = 0.16$ implying that only 14% of isotopes formed via the r-process (Arlandini et al., 1999)) but is once more at odds with the high r-process fraction expected under Truran's hypothesis.

We have obtained a high resolution ($R \equiv \lambda/\Delta\lambda = 95\,000$) very high signal-to-noise ($S/N = 870 - 1110$) spectrum of HD 140283. During the course of this paper we discuss how we have constrained the macroturbulence by fitting synthetic spectra to Fe lines. In a detailed error analysis we show how we have improved constraining the macroturbulence, which was a major source of error that dominated previous studies that analyse the Ba II 4554 Å line in 1D LTE. The improvement is partly due to the higher quality spectrum we have used in this investigation. We also explore the impact of using radial-tangential macroturbulence, ζ_{RT}, and rotational broadening, $v \sin i$ (used by Collet et al. (2009)) to help constrain macroscopic broadening. We then move on to discuss the method used to re-evaluate the r- vs. s-process mix by analysing the Ba II 4554 Å line and, for the first time in this context, the Ba II 4934 Å line in 1D LTE. Furthermore we discuss the difficulties in analysing the Ba II 4934 Å line due to close blends with other lines. Also because of the exceptional quality of the data, we have been able to revise downward the Eu abundance limit for the star.

3.2 Observational data

Our stellar and ThAr calibration spectra were obtained over two nights during the commissioning of the High Dispersion Spectrograph (HDS) mounted on the Subaru Telescope. The stellar spectrum is the sum of 13 exposures totalling 82 minutes. This gives a $S/N = 1110$ per 12 mÅ wide pixel around the Ba II 4554 Å line and a $S/N = 870$ per 12 mÅ wide pixel around the Ba II 4934 Å line, as measured from the scatter in the continuum of the reduced spectrum. The typical resolution as measured from ThAr lines is $R \equiv \lambda/\Delta\lambda = 95\,000$. The spectrum was reduced using a ThAr spectrum to wavelength calibrate the stellar spectrum, with typical RMS errors of 1.5 mÅ (Aoki et al., 2004). We utilise the 4554 Å and 4934 Å lines as both arise from the ground state

where hyperfine structure is large. Although the 4934 Å line is weaker - we measure equivalent widths $W_{4554} = 20.1$ mÅ and $W_{4934} = 13.6$ mÅ - the hfs of the 4934 Å line is greater, which means both lines can be useful diagnostics. We do not attempt to analyse higher excitation lines of Ba which are weaker and have much smaller hfs.

3.3 Spectral profiles

To analyse the two Ba II line profiles in our spectrum we compared our observed profile to synthetic profiles produced by the 1D LTE code ATLAS (Cottrell & Norris, 1978). We describe below how Fe I and Fe II lines are used to constrain macroturbulence, and then proceed to analyse the Ba II lines. A 1D KURUCZ06 model atmosphere (`http://kurucz.harvard.edu/grids.html`) was used with parameters for the star $T_{\rm eff} = 5750$ K, [Fe/H] $= -2.5$ and microturbulence, $\xi = 1.4\,{\rm km\,s^{-1}}$ (Aoki et al., 2004) and $\log g = 3.7$ [cgs] (Collet et al., 2009).

3.3.1 Instrumental Profile

Two ThAr hollow-cathode-lamp spectra over the intervals $4102 - 5343$ Å and $5514 - 6868$ Å, taken during the observing run with the same instrumentation and set-up as the stellar exposures used in this study, were used to calculate the instrumental broadening. Using IRAF, the full-width at half-maximum ($FWHM$) and equivalent widths of 993 emission lines were measured. It was found that at a wavelength of 4554 Å the ThAr line $FWHM$ in velocity-space ($v_{\rm inst}$) was $3.31\,{\rm km\,s^{-1}}$, and at 4934 Å was $3.25\,{\rm km\,s^{-1}}$. The error in these measurements is taken as the standard error of the mean of the individual measurements, $\sigma/\sqrt{N}$, which is $0.01\,{\rm km\,s^{-1}}$, where σ is the standard deviation of the individual measurements, which is $0.22\,{\rm km\,s^{-1}}$. We assume here that the ThAr lines are unresolved and hence that the measured ThAr line width represents the instrumental broadening. The instrumental broadening could be slightly less than that stated, but the difference is immaterial since, in §3.3.2, we measure the combined instrumental and macroturbulent broadening without needing to distinguish between the two contributions precisely. Aoki et al. (2004) showed that the instrumental profile

is well approximated by a Gaussian.

3.3.2 Macroturbulence

Lambert & Allende Prieto (2002) established that one of the major limiting factors in their analysis was the accuracy with which macroturbulence could be measured. They found that $\delta f_{\rm odd}/\delta FWHM = -0.51$ (km s^{-1})$^{-1}$, and hence for $\sigma_{FWHM} = 0.33\,{\rm km\,s^{-1}}$ they achieved an accuracy in macroturbulence corresponding to $\sigma_{f_{\rm odd}} \sim 0.17$, dominating their total error of 0.21. It was clear that we would have to improve on this significantly to make progress.

We began to constrain macroturbulence by measuring the equivalent widths and the $FWHM$ (in velocity-space), $v_{\rm obs}$, of 257 apparently unblended Fe I and Fe II lines by fitting Gaussian profiles in IRAF. We used this information to produce Fig. 3.2. As $\Delta\lambda/\lambda$ remains constant with wavelength in an echelle spectrum (where $\Delta\lambda$ is the width of the pixel in wavelength units) it is possible to use Fig. 3.2 as a check of the quality of measurements.

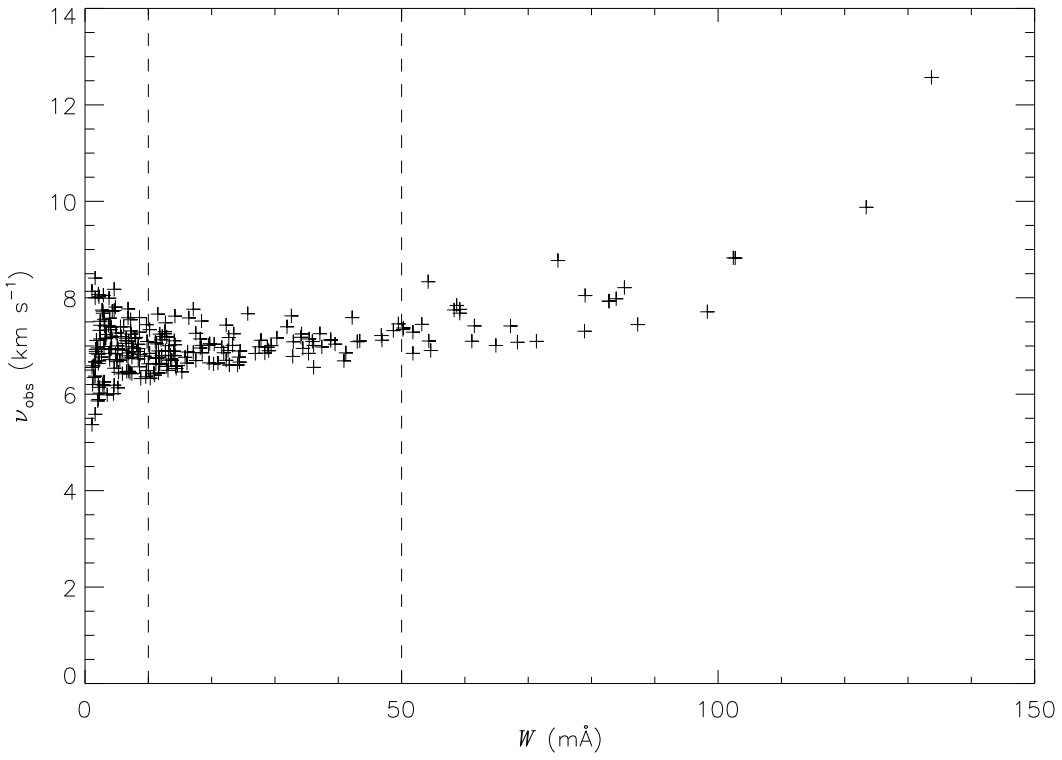

Fig. 3.2: $FWHM$ versus equivalent width for the 257 Fe I and Fe II lines measured for HD 140283. 93 lines fall into the range of $10 \leq W$ (mÅ) ≤ 50; the mean value for $v_{\rm obs}$ in this range is $6.9\,{\rm km\,s^{-1}}$.

From Fig. 3.2 we can see that weaker lines, $W \leq 50\,\mathrm{m\AA}$, almost form a plateau. Here, v_{obs} remains constant even as the Doppler core deepens in lines on the linear part of the curve of growth, where the Doppler broadening components are dominant. At $W > 50\,\mathrm{m\AA}$, pressure broadening become significant as the core of the line saturates, so the wings begin to broaden. Where $W < 10\,\mathrm{m\AA}$, the uncertainty produced by the finite signal-to-noise makes it difficult to measure the lines accurately, which is shown by the scatter in this region of Fig. 3.2.

Of the 257 Fe lines measured, 93 fell between $10\,\mathrm{m\AA} \leq W \leq 50\,\mathrm{m\AA}$ and were used to constrain macroturbulence (recall that $W_{4554} = 20.1\,\mathrm{m\AA}$ and $W_{4934} = 13.6$ mÅ). The average value for the observed velocity $FWHM$, v_{obs}, in this range is $6.9\,\mathrm{km\,s^{-1}}$. The full list of measurements can be found in Table B.1.

Gaussian macroturbulence

We convolve the synthetic flux spectrum of the star with a Gaussian of $FWHM$ v_{conv} which represents the convolution of the Gaussian instrumental profile with a Gaussian macroturbulent profile. For now we assume that the star has no significant rotation; we shall return to this point in §3.3.2. Current estimates of rotation of HD 140283 are $v \sin i = 5.0 \pm 2.0\,\mathrm{km\,s^{-1}}$ (de Medeiros et al., 2006). We create a grid of 385 convolved synthetic spectra for 11 values of macroturbulence $4.9\,\mathrm{km\,s^{-1}} \leq v_{\mathrm{conv}} \leq 6.9\,\mathrm{km\,s^{-1}}$ in steps $\Delta v_{\mathrm{conv}} = 0.1\,\mathrm{km\,s^{-1}}$ and 35 values for $A(\mathrm{Fe})$[3], $4.09 \leq A(\mathrm{Fe}) \leq 5.45$ with steps $\Delta A(\mathrm{Fe}) = 0.04$. Each synthetic spectrum covered the wavelength range $4100 - 6900$ Å in intervals of $\Delta\lambda = 0.01$ Å.

To determine the best fit for v_{conv} we compare our synthetic model grid to the observed spectrum employing a χ^2 test, $\chi^2 \equiv \sum (O_i - M_i)^2/\sigma_i^2$, where O_i is the observed continuum-normalised profile, M_i is the model profile of the line produced using ATLAS and σ_i^2 is the standard deviation of the observed points that define the continuum, i.e. $\sigma = (S/N)^{-1}$. All 93 Fe I and Fe II lines were individually fitted using a χ^2 code (García Pérez et al., 2009). This code allows small wavelength shifts, $\Delta\lambda$, which we discuss below and local renormalisation of the continuum of the observed profile for every line.

[3] $A(\mathrm{X}) \equiv \log_{10}\left(\frac{N(\mathrm{X})}{N(\mathrm{H})}\right) + 12$

It finds values for $\Delta\lambda$, A(Fe) and macroturbulence that minimize χ^2 for each Fe line analysed over a window 0.6 Å wide and with continuum windows typically 0.5 Å to 1.0 Å on each side of this, depending on neighbouring spectral features. Values of $v_{\rm conv}$ found by the χ^2 code for the 93 lines covering the wavelength range $4118 - 6253$ Å are shown in Fig. 3.3. The full table of results from the χ^2 code is found in Table B.1.

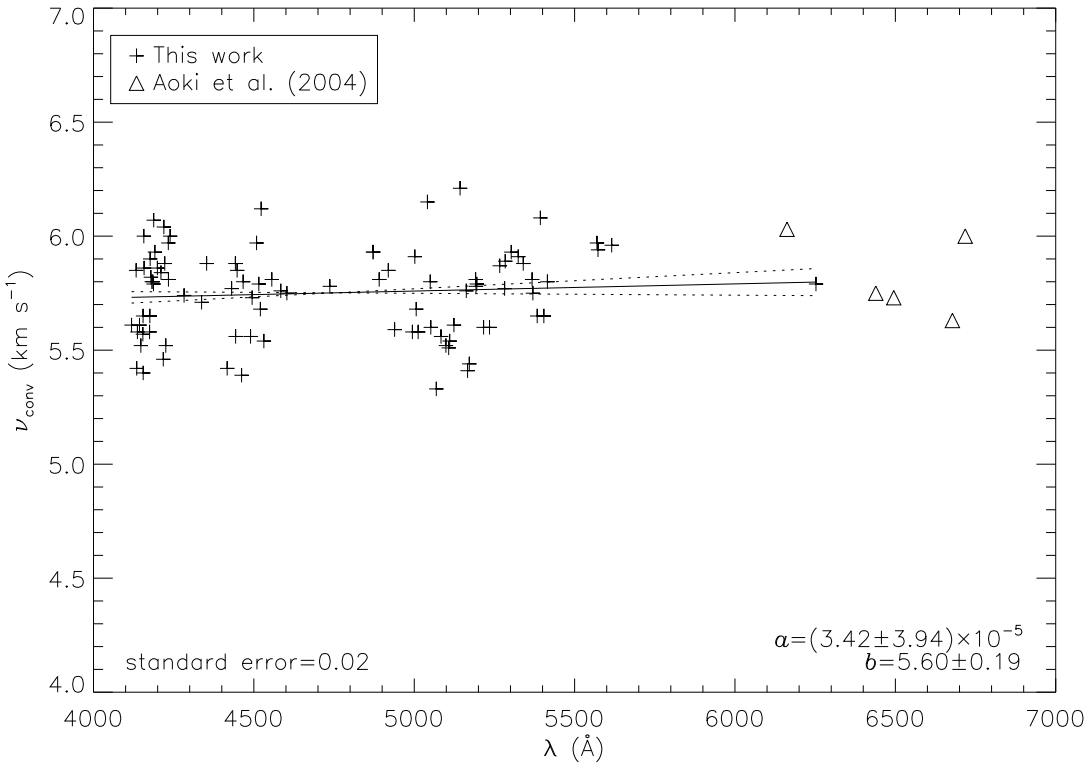

Fig. 3.3: Values of $v_{\rm conv}$ that satisfy the minimum value for χ^2 for the 93 lines (*plus symbols*). The standard error represents the scatter from the mean of each line ($\sigma/\sqrt{N}$) and a and b are coefficients of the least squared fit, $v_{\rm conv} = a\lambda + b$. The Ca I and Fe I lines used by Aoki et al. (2004) to constrain macroturbulence have been plotted (*triangles*) to show the consistency of our χ^2 fits with their results at red wavelengths.

We use an ordinary least squares (OLS) fit to determine $v_{\rm conv}$ at the wavelengths 4554 Å and 4934 Å. The OLS has the equation $v_{\rm conv} = a\lambda + b$, where a and b are coefficients of the OLS. We find that $v_{\rm conv} = 5.75\,{\rm km\,s^{-1}}$ and $v_{\rm conv} = 5.76\,{\rm km\,s^{-1}}$ at the Ba II 4554 Å and 4934 Å lines respectively. The error in these values, represented by the standard error, is $0.02\,{\rm km\,s^{-1}}$. As the uncertainty in these values is greater than the difference between them, we adopted one value for $v_{\rm conv}$ for both Ba II lines, $v_{\rm conv} = 5.75 \pm 0.02\,{\rm km\,s^{-1}}$. Subtracting the instrumental $FWHM$ at 4554 Å we find the macroturbulence, v_Γ, to be $v_\Gamma = \sqrt{5.75^2 - 3.31^2} = 4.70 \pm 0.02\,{\rm km\,s^{-1}}$. This value agrees

well with that found by Aoki et al. (2004). The error in v_Γ is given by $\sigma^2_{v_\Gamma} = \sigma^2_{v_{\rm conv}} + \sigma^2_{v_{\rm inst}}$, which is equal to $\pm 0.02\,{\rm km\,s^{-1}}$.

In using the Fe lines to determine the macroturbulence appropriate to Ba, it is important that we measure lines forming over a similar range of depths in the photosphere. This was achieved in the first instance by restricting the equivalent width range of the Fe lines to span the two Ba lines (see Fig. 3.2). In addition, we have regressed the $v_{\rm conv}$ measurements against equivalent width, W, and against excitation energy, χ, and find no statistically significant trend of $v_{\rm conv}$ with W, and a weak (2.5σ) trend with χ. This suggests that using a stricter restriction on the Fe line list would not materially alter the macroturbulent velocity. In the most extreme case, the value for $\chi = 0\,{\rm eV}$ would imply $v_{\rm conv} = 5.62 \pm 0.05\,{\rm km\,s^{-1}}$, which (as we show below) would increase $f_{\rm odd}$ by 0.09.

The χ^2 code also determined that $A({\rm Fe}) = 4.91 \pm 0.01$, where the error is taken as the standard error. Taking the solar Fe abundance to be $A({\rm Fe})_\odot = 7.50 \pm 0.05$ from Grevesse & Sauval (1998), we calculate the metallicity, $[{\rm Fe/H}] = -2.59 \pm 0.05$, where the error in [Fe/H] is the propagation of the statistical error in $A({\rm Fe})_*$ and $A({\rm Fe})_\odot$ but so far excludes the systematic errors associated with the imperfect choice of atmospheric parameters. That error, based on calculations we provide in §3.5, is around 0.07 dex, giving a total error of 0.09 dex. This is in good agreement with metallicity we adopted from Aoki et al. (2004). We note that there is an updated list of solar abundances given in Grevesse et al. (2007) calculated using 3D hydrodynamics, however we decided to use the 1D LTE results given in Grevesse & Sauval (1998) as we are working in 1D LTE.

We found that the mean wavelength shift, $\Delta\lambda$, was $-12.0\,{\rm m\AA}$ with a standard deviation $\sigma_{\Delta\lambda} = 3.8\,{\rm m\AA}$. There are several reasons why we would expect to find a wavelength shift between the observed and synthetic profiles. The most likely is an error in the approximate radial velocity correction of the star, but line-to-line differences require further comment. There could be inaccuracies in the assumed wavelengths in the Fe line list, however the Fe line list was produced using the most up to date data available through the IRON PROJECT and Nave et al. (1994), where wavelengths are

quoted to 1 mÅ, and are believed to be accurate to < 1 mÅ. The RMS error in the wavelength calibration was reported as only 1.5 mÅ (Aoki et al., 2004), so the line-to-line scatter $\sigma_{\Delta\lambda}$ exceeds that error. The excess could be due to the inability of 1D hydrostatic model atmospheres to model turbulent motions in a star's hydrodynamic atmosphere. Indeed, the residuals shifts were found to depend, at least partially, on the excitation potential, χ, and the equivalent width, W, suggesting an astrophysical cause.

Non-Gaussian symmetric broadening

So far we have adopted a Gaussian macroturbulent broadening mechanism. We looked at two other macro-scale broadening mechanisms, radial-tangential macroturbulence ($\zeta_{\rm rt}$) and rotation ($v \sin i$) (Gray, 2008, Chapter 18). Each broadening run was given the same atmospheric parameter set; $T_{\rm eff} = 5750$ K, $\log g = 3.7$, [Fe/H] $= -2.5$, $\xi = 1.4\,{\rm km\,s^{-1}}$. Table 3.1 shows the results from fitting the 93 Fe lines using the three broadening types, along with Gaussian instrumental broadening ($v_{\rm inst} = 3.31\,{\rm km\,s^{-1}}$). The third column indicates how many of the 93 lines were best fit by that broadening mechanism, as judged by the minimum χ^2 value for the three methods.

Table 3.1: Comparison of all three broadening types. Column two gives the broadening based on all 93 Fe lines for the wavelength 4554 Å, determined using the method described in §3.3.2. The errors given are the standard error ($\sigma/\sqrt{N}$). Column three shows how many of the Fe lines were statistically better fits with that particular broadening technique.

Broadening Parameter	Parameter ($\rm km\,s^{-1}$)	# of best fit lines
v_Γ	4.70 ± 0.02	32
$\zeta_{\rm rt}$	4.37 ± 0.02	58
$v \sin i$	3.89 ± 0.02	3

Only three of the 93 Fe lines were fit best by rotational broadening, and hence we concluded that using only rotational velocities to broaden the lines would be unsound. The derived value provides a firm upper limit on rotation, $v \sin i \leq 3.9\,{\rm km\,s^{-1}}$, in the case with no macroturbulent broadening. The fact that most lines are fit better by a macroturbulent profile emphasises that we have not detected true rotation of the star at this $3.9\,{\rm km\,s^{-1}}$ level.

The radial-tangential broadening function within the 1D LTE framework, provides a better fit than Gaussian macroturbulence to almost two thirds of the Fe lines. We present Ba results for both macroturbulent prescriptions in §3.4.4, but unless specified, our analysis is conducted using Gaussian fitting.

3.4 The Ba II resonance lines and the barium isotopic ratio

3.4.1 Ba II line structure

There are five principal, stable Ba isotopes that are formed via the two neutron-capture processes. The r- & s-process produce different mixes of odd and even isotopes. The r-process does not contribute to two even isotopes, ^{134,136}Ba, which are pure s-process isotopes. The two odd isotopes, ^{135,137}Ba, and even isotope ^{138}Ba are formed from both the s- & r-process. The odd isotopes broaden the line and make it asymmetric, whereas the even isotopes contribute to the centre of the Ba II line and make the core deeper.

We use the hfs information from Wendt et al. (1984) and Villemoes et al. (1993) to compute energy level splittings for the lower and upper levels of ^{135,137}Ba in the 4554 Å and 4934 Å lines, and incorporated the isotopic shifts relative to ^{138}Ba. Importantly, we note that the hfs splitting and isotope shift data in these papers is quite similar to that of some older studies (references can be found in Wendt et al., 1984; Villemoes et al., 1993), and hence we are confident that there is no significant uncertainty in the line structure. The line wavelength structure, relative to ^{138}Ba, is shown in Fig. 3.4, in which each isotope is shown with a total strength of 1.0. Using the s- and r-process contributions to the five isotopes from Arlandini et al. (1999), we construct line lists for pure s-process and pure r-process isotope mixes for the two Ba II lines, adopting total $\log gf$ values of +0.16 and -0.16 for 4554 Å and 4934 Å respectively, see Table 3.2. From these two lists we created a further 13 hybrid line lists. These covered a range for $f_{\rm odd}$ equal to $0.00 \leq f_{\rm odd} \leq 0.46$ where $\Delta f_{\rm odd} = 0.035$. We recognise that according to Arlandini et al. (1999), the cases with $f_{\rm odd} < 0.11$ are not achieved astrophysically

Table 3.2: The isotopic and hfs information for both Ba lines. The oscillator strengths relative to ^{138}Ba for each line are given in column 3 and the calculated gf-values are given in columns 4 and 5.

			gf-value	
λ (Å)	Isotope	Relative strength	s-process	r-process
4553.9980	137	0.1562	0.0210	0.0471
4553.9985	137	0.1562	0.0210	0.0471
4553.9985	137	0.0626	0.0084	0.0189
4554.0010	135	0.1562	0.0049	0.0594
4554.0015	135	0.1562	0.0049	0.0594
4554.0020	135	0.0626	0.0019	0.0238
4554.0316	134	1.0000	0.0429	0.0000
4554.0319	136	1.0000	0.1450	0.0000
4554.0332	138	1.0000	1.1256	0.7972
4554.0474	135	0.4376	0.0136	0.1663
4554.0498	137	0.4376	0.0589	0.1320
4554.0503	135	0.1562	0.0049	0.0594
4554.0513	135	0.0311	0.0010	0.0118
4554.0537	137	0.1562	0.0210	0.0471
4554.0542	137	0.0311	0.0042	0.0094
4934.0288	137	0.3125	0.0197	0.0441
4934.0332	135	0.3125	0.0045	0.0556
4934.0410	137	0.0625	0.0039	0.0088
4934.0439	135	0.0625	0.0009	0.0111
4934.0750	134	1.0000	0.0201	0.0000
4934.0753	136	1.0000	0.0678	0.0000
4934.0768	138	1.0000	0.5265	0.3729
4934.0918	135	0.3125	0.0045	0.0556
4934.0942	137	0.3125	0.0197	0.0441
4934.1025	135	0.3125	0.0045	0.0556
4934.1064	137	0.3125	0.0197	0.0441

because even a pure s-process mixture has a non-zero contribution of ^{135,137}Ba.

3.4.2 χ^2 test

The observed continuum was renormalised over a window of 1 Å either side of each of the two Ba lines. A new grid comprising 231 synthetic spectra around each of the two Ba II resonance lines was produced in ATLAS. Values for $v_{\rm conv}$ and A(Fe), constrained in the last section, were fixed. There were three free parameters in the new grid: A(Ba), $\Delta\lambda$ and the r- & s-process contributions. The χ^2 code allowed small changes

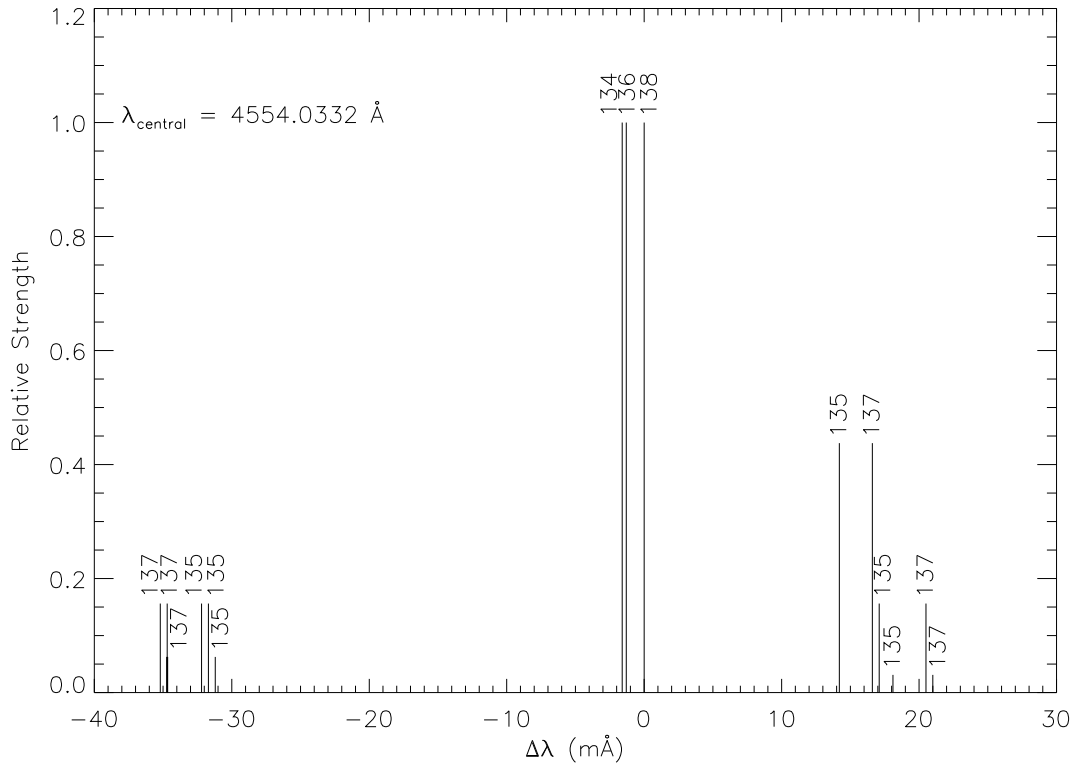

Fig. 3.4: The splitting patterns of the Ba II 4554 Å line relative to ^{138}Ba. The relative strengths of each isotope are normalised to 1 (Table 3.2, column (3)).

in these parameters exactly like the code described in §3.3.2. We used 21 values for $A(\mathrm{Ba})$, $-1.40 \leq A(\mathrm{Ba}) \leq -1.20$, where $\Delta A(\mathrm{Ba}) = 0.01$. Each synthetic spectrum covered the range $4550 - 4560$ Å (around 4554 Å), $4930 - 4940$ Å (around 4934 Å) and was computed every 0.01 Å. The windows in which both Ba lines were analysed was ± 0.25 Å from their centroid.

3.4.3 The iron blends at 4934 Å

It has been documented that the Ba II 4934 Å line has a known blend with a weak Fe I line (Cowley & Frey, 1989). We use the information for two Fe lines which are found in Nave et al. (1994, their table 2). The relevant data can be found in our Table 3.3.

When these wavelengths are compared with the wavelengths for the Ba 4934 Å line given in Table 3.2 it is clear that the two Fe lines would influence the r-process fraction found by analysis of the line. This is shown in Fig. 3.5 for pure s- and r-process isotope ratios. The analysis of the 4934 Å line is very sensitive to the characteristics of the Fe

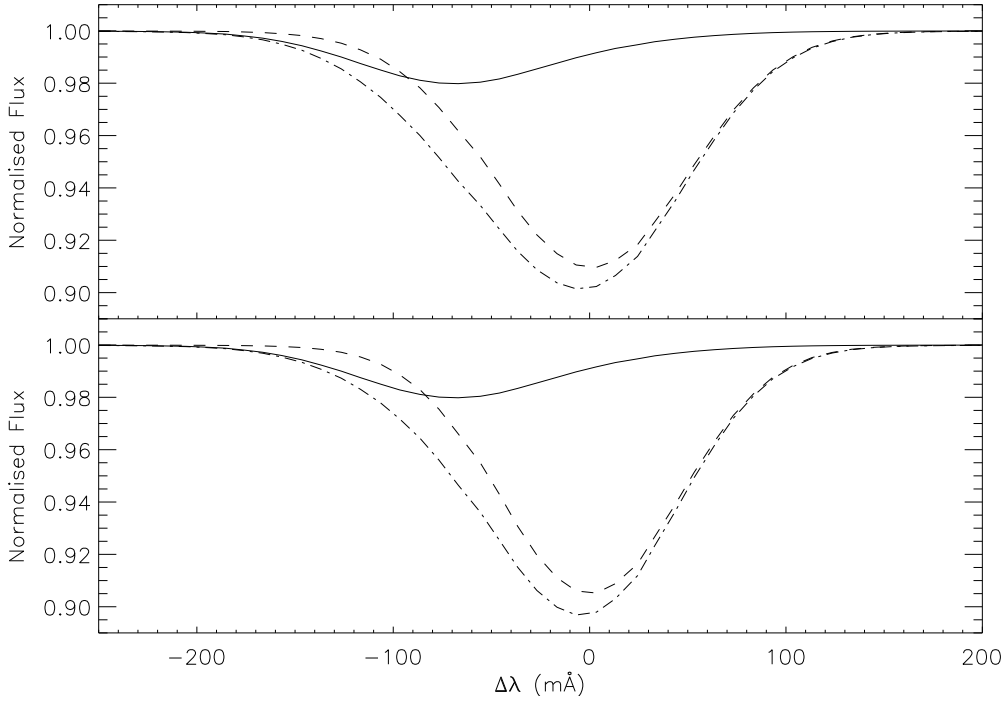

Fig. 3.5: Synthetic spectra showing the effect of the Fe I blends on the 4934 Å Ba II line. The top plot shows the r-process-only isotope fraction and the bottom shows the s-process-only isotope fraction. *Solid line*: the underlying Fe I blends. *Dashed line*: the uncontaminated Ba II line. *Dash-dot line*: the overall line profile.

Table 3.3: Spectroscopic information on the two weak Fe lines that are blended with the Ba II 4934 Å line as reported by Nave et al. (1994). The $\log gf$ values reported here were supplied by G. Nave (2009, private communication) but can be found using the Kurucz database http://www.cfa.harvard.edu/amp/ampdata/kurucz23/sekur.html.

λ (Å)	Ion	χ (eV)	$\log gf$
4934.0052	Fe I	4.15	-0.589
4934.0839	Fe I	3.30	-2.307

lines, as we show in §3.5.2. We include these Fe lines in our Ba 4934 Å line analysis.

3.4.4 The r-process contribution

The Ba abundances of the two lines are found to be $A(\mathrm{Ba})_{4554} = -1.28$ and $A(\mathrm{Ba})_{4934} = -1.30$. We take the implied Ba abundance as an average of the two, $A(\mathrm{Ba}) = -1.29 \pm 0.08$. Using the solar abundances calculated in Grevesse & Sauval (1998) we find that for HD 140283, $[\mathrm{Ba/H}] = -3.46 \pm 0.11$, and hence $[\mathrm{Ba/Fe}] = -0.87 \pm 0.14$. Errors stated here are calculated in §3.5. Results from other papers are given in Table 3.4. It

is shown that our result for [Ba/Fe] is in good agreement with previous results.

Table 3.4: Results from previous studies of HD 140283.

Paper	$T_{\rm eff}$ (K)	$\log g$ (cgs)	[Fe/H]	[Ba/H]	[Ba/Fe]
SS[a]	5727	3.30	-2.40	-3.20	-0.80
MMZ[b]	5640	3.10	-2.73	-3.86	-1.13
GS[c]	5690	3.58	-2.53	-3.17	-0.64
RNB[d]	5750	3.40	-2.54	-3.45	-0.91
MGB[e]	5640	3.65	-2.30	-3.10	-0.80
F[f]	5650	3.40	-2.40	-3.43	-1.03
MK[g]	5650	3.50	-2.50	-3.28	-0.78
LAP[h]	5777	3.74	-2.70	-3.79	-1.09
CAN[i]	5690	3.67	-2.50	...	...
GRPA[j]	5750	3.70	-2.59	-3.46	-0.87

[a] Spite & Spite (1978). [b] Magain (1989) and Zhao & Magain (1990). [c] Gratton & Sneden (1994). [d] Ryan et al. (1996). [e] Mashonkina et al. (1999). [f] Fulbright (2000). [g] Mishenina & Kovtyukh (2001). [h] Lambert & Allende Prieto (2002). [i] Collet et al. (2009). [j] This work.

Our χ^2 fitting procedure included a possible wavelength shift as a free parameter. The 4554 Å line has a wavelength shift $\Delta\lambda = -14.8$ mÅ. The 4934 Å line has a wavelength shift $\Delta\lambda = -21.5$ mÅ, possibly because of imperfect modelling of the Fe blend in the blue wing. Both lines fall within 3σ of the mean wavelength shift found in the Fe lines, -12.0 mÅ with $\sigma_{\Delta\lambda} = 3.8$ mÅ.

From the χ^2 analysis we find the best statistical fit for the 4554 Å line is $f_{\rm odd} = 0.01 \pm 0.06$. The best statistical fit for the 4934 Å line indicates a value of $f_{\rm odd} = 0.11 \pm 0.19$ (meaning an r-process contribution of $0\% \pm 54\%$). The 1σ errors stated here arise from uncertainties discussed in §3.5 and are larger for the 4934 Å line because of uncertainties associated with the underlying Fe blends. Our result is in good agreement with Magain (1995) who found that Ba II 4554 Å yielded $f_{\rm odd} = 0.08 \pm 0.06$, but seems to be at odds with values found by Lambert & Allende Prieto (2002) ($f_{\rm odd} = 0.30 \pm 0.21$) and the 1D result found for the same spectrum by Collet et al. (2009) ($f_{\rm odd} = 0.33 \pm 0.13$).

The reduced chi-squared values, χ^2_r, for the 4554 Å line and the 4934 Å line are 6.6 and 2.0 respectively. The two best statistical fits for both lines and their residuals (observed - synthetic profiles) are shown in Fig. 3.6. We also plot the synthetic profiles for the Ba lines with an r-process contribution of 100%, best fit A(Ba) $= -1.30$ for

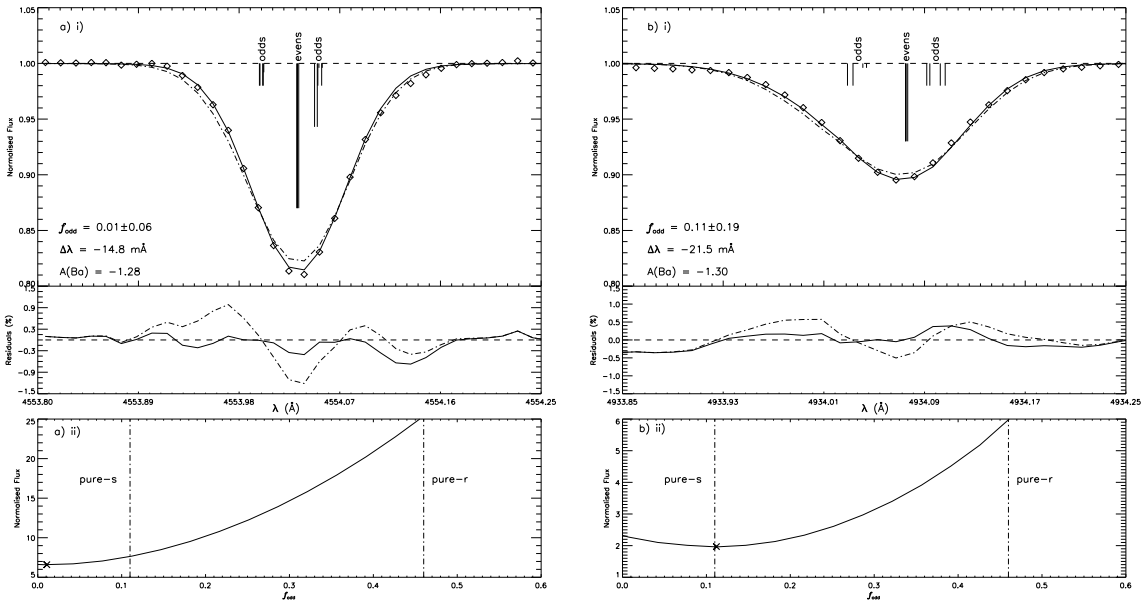

Fig. 3.6: *Panel a) i)*: The best statistical fit synthetic profile (*solid line*) for the observed Ba II 4554 Å line (*diamonds*) with the residual and χ^2 plots below. For comparison, a pure r-process line and residual has been plotted (*dash-dot line*). The value for A(Ba) has been optimised to one that minimises χ^2, values for A(Fe) and macroturbulence remain the same. *Panel a) ii)*: The χ^2 fit for the 4554 Å line, the cross shows where the minimum of the fit lies. Also plotted are the splitting patterns for Ba relative to Ba-138 (see Table 3.2). *Panels b) i)* and *ii)*: Show the same as *a) i)* and *ii)* for the 4934 Å line.

both lines. It can be seen in the residual plots for both lines that the pure r-process fits are very poor. In 4554 Å, χ^2_r changes faster with $f_{\rm odd}$ than for the 4934 Å line. This indicates that although the 4934 Å line is broader due to the effects of hyperfine structure, the 4554 Å line is more sensitive to changes in $f_{\rm odd}$. This could be both because the 4554 Å line is stronger ($W = 20.1$ mÅ) than the 4934 Å line ($W = 13.6$ mÅ), and because the latter has an Fe blend.

Based on the calculations by Arlandini et al. (1999), our 4554 Å result should not be achievable, and corresponds to an r-process contribution of -29% (i.e. the s-process contribution is equal to 129%). We have also plotted in Fig. 3.7 the fit and residual for the nearest physically possible value for $f_{\rm odd}$ (0.11). This fit has $\chi^2_r = 7.7$. We have also plotted the fit for $f_{\rm odd} = 0.01$, which is quite similar.

When we adopted radial-tangential macroturbulence, it was determined that $f_{\rm odd} = -0.02\pm0.06$ and -0.03 ± 0.19 for the 4554 Å and 4934 Å lines respectively, with $\chi^2_r = 6.1$ and 2.8. Errors stated here are assumed to be the same as those calculated using a Gaussian macroturbulence as only the broadening mechanism differs; the errors in the

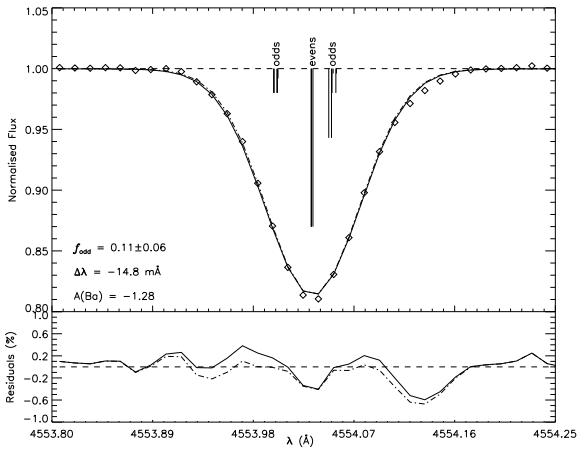

Fig. 3.7: Comparison between the nearest physical fit (*solid line*) where $f_{\rm odd} = 0.11$ and the best statistical fit (*dash-dot line*) where $f_{\rm odd} = 0.01$, for the 4554 Å line. Also plotted are the splitting patterns for Ba relative to Ba-138 (see Table 3.2).

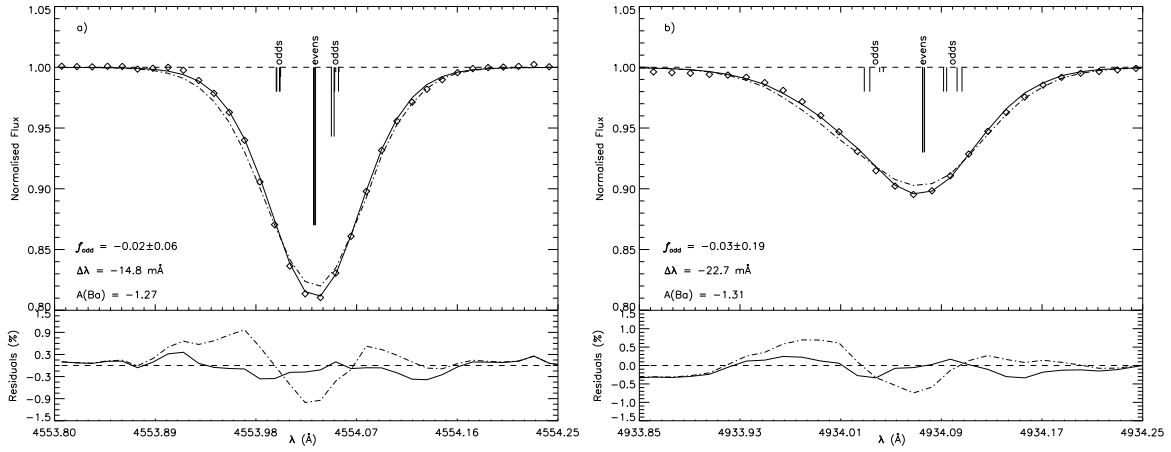

Fig. 3.8: *Panel a*): The best statistical fit for the 4554 Å line (*diamonds*) using a radial-tangential velocity profile (*solid line*). We have included a pure r-process, $f_{\rm odd} = 0.46$, synthetic profile for comparison(*dash-dot line*). Also plotted are the splitting patterns for Ba relative to Ba-138 (see Table 3.2). *Panel b*): Same as *panel a*) but for the 4934 Å line.

two broadening techniques have the same value. The best fits are shown in Fig. 3.8. So the radial-tangential fit for the 4554 Å line is a statistically better fit than the Gaussian macroturbulent fit, as seen by the residual plots (Figs. 3.6 (a)(i) & (b)(i) vs. Figs. 3.8 (a) & (b)). Both broadening mechanisms, which were analysed separately, yield similar values for $\Delta\lambda$, $f_{\rm odd}$ and [Ba/H]. Both indicate a strong s-process signature for Ba. Although these $f_{\rm odd}$ numbers are again beyond possible physical values, we inform the reader that due to the finite confidence in the χ^2_r test (discussed further in §3.7), the non-physical values $f_{\rm odd} \simeq 0.01$ are not greatly preferred over the physical value $f_{\rm odd} = 0.11$.

We have given values for $f_{\rm odd}$ for the two Ba lines and we have shown that the two lines are in agreement within the stated errors. We now discuss those uncertainties and what stellar parameters $f_{\rm odd}$ is sensitive to.

3.5 Uncertainties and sensitivity tests

In this section we scrutinise the analysis procedures and statistical tests employed in this study to determine the likely statistical and systematic errors. These include errors associated with the atmospheric parameters used in constructing the synthetic spectra, the calculated macroturbulence and the errors associated with the Fe lines used in conjunction with the Ba 4934 Å line.

Table 3.5 lists values found for [Ba/H] and $f_{\rm odd}$ by varying the temperature and $\log g$ of the model atmosphere. There are two cases. In case 1 we recalculate [Fe/H] and macroturbulence for every value of $T_{\rm eff}$ and $\log g$, whereas in case 2 we fix the macroturbulence and [Fe/H] to values calculated for $T_{\rm eff} = 5750\,{\rm K}$ and $\log g = 3.7$. Perhaps the first thing to note from this table is that altering temperature by $\pm 250\,{\rm K}$ and $\log g$ by ± 0.3 does not drive $f_{\rm odd}$ to an r-process dominated fraction. The errors quoted in this paper for HD 140283 are based on uncertainties in $T_{\rm eff}$ and $\log g$ of $\pm 100\,{\rm K}$ and ± 0.1 respectively.

Table 3.5: The sensitivity to [Fe/H], [Ba/H], $v_{\rm conv}$ and $f_{\rm odd}$ for different values of $T_{\rm eff}$ and $\log g$. *case 1*: The sensitivity of all atmospheric parameters used or calculated in this analysis to changes in temperature and $\log g$. *case 2*: The sensitivity of [Ba/Fe] and $f_{\rm odd}$ to temperature and $\log g$. Macroturbulence and [Fe/H] are fixed to values found for the model atmosphere used in this analysis ($T_{\rm eff} = 5750$, $\log g = 3.7$, $v_{\rm conv} = 5.75 {\rm km\,s^{-1}}$, [Fe/H] $= -2.59$). Columns (11) and (12) show the sensitivity of the blended 4934 Å line to changes in the stellar parameters.

								$f_{\rm odd}$			
								4554 Å		4934 Å	
$T_{\rm eff}$ (K)	$\log g$ (cgs)	$v_{\rm conv}$ (km s^{-1})		[Fe/H]		[Ba/H]					
(1)	(2)	(3)	(4)	(5)	(6)	(7)	(8)	(9)	(10)	(11)	(12)
		case 1	case 2	case 1	case 2	case 1	case 2	case 1	case 2	case 1	case 2
5500	3.4	5.79	...	−2.78	...	−3.69	−3.71	−0.01	0.02	0.15	−0.115
5500	3.7	5.67	...	−2.77	...	−3.59	−3.61	0.05	−0.01	0.20	−0.115
5500	4.0	5.52	...	−2.74	...	−3.50	−3.50	0.11	−0.07	0.24	−0.111
5750	3.4	5.82	...	−2.60	...	−3.50	−3.52	−0.02	0.04	0.09	0.113
5750	3.7	5.75	5.75	−2.59	−2.59	−3.42	−3.42	0.01	0.01	0.11	0.112
5750	4.0	5.60	...	−2.57	...	−3.33	−3.31	0.09	−0.03	0.15	0.112
6000	3.4	5.84	...	−2.43	...	−3.34	−3.34	−0.03	0.04	0.02	0.252
6000	3.7	5.77	...	−2.42	...	−3.24	−3.24	0.01	0.02	0.04	0.252
6000	4.0	5.69	...	−2.40	...	−3.15	−3.14	0.04	0.00	0.05	0.245

From Table 3.5 it is possible to calculate the error associated with [Fe/H], A(Ba), and hence [Ba/H] & [Ba/Fe], by examining how it is affected by the stellar parameters. We use case 1 to calculate these uncertainties. It is shown in Table 3.5 that gravity as very little affect on [Fe/H]. Temperature has a much greater affect on [Fe/H], altering the ratio by ± 0.07 dex for every 100 K. Therefore we find a total uncertainty in [Fe/H] of ± 0.07. We find that $\delta A(\mathrm{Ba})/\delta \log g = 0.35$. Therefore an error of 0.1 in $\log g$ implies an error $\sigma_{A(\mathrm{Ba}),\log g} = 0.04$. Similarly we find for temperature that $\delta A(\mathrm{Ba})/\delta T_{\mathrm{eff}} = 0.0007$ K^{-1}. Taking the uncertainty in temperature to be ± 100 K we find that $\sigma_{A(\mathrm{Ba}),T_{\mathrm{eff}}} = 0.07$. Macroturbulence affects the shape of lines but not the equivalent width. As such we do not include the uncertainties associated with macroturbulence here. Also [Fe/H] has very little affect on [Ba/H] when compared to temperature and gravity effects so this is not included in our error analysis of [Ba/H]. The solar Ba abundance is $A(\mathrm{Ba})_{\odot} = 2.17 \pm 0.07$ (Grevesse & Sauval, 1998). When these uncertainties are added in quadrature we find that [Ba/H] $= -3.46 \pm 0.11$. Therefore we find that [Ba/Fe] $= -0.87 \pm 0.14$.

3.5.1 The 4554 Å line

We have stated that potentially the most significant parameter that f_{odd} is sensitive to is macroturbulence. The difference between columns (9) and (10) in Table 3.5 show how f_{odd} is sensitive to macroturbulence. We find that on average, $\delta f_{\mathrm{odd}}/\delta v_{\mathrm{conv}} \backsimeq -0.7$ (km s^{-1})$^{-1}$ meaning that for $\sigma_{v_{\mathrm{conv}}} = 0.02$ km s^{-1}, calculated in §3.3.2, $\sigma_{f_{\mathrm{odd}}} \backsimeq 0.01$. That is, by using a large number of Fe lines to constrain v_{conv}, we have minimized the impact of this error.

Realistically, when you vary one parameter you alter all other parameters to compensate for this change. Increasing temperature increases the derived macroturbulence, which on its own decreases f_{odd}. For case 1 we see that an uncertainty in temperature of ± 100 K implies an uncertainty in macroturbulence of 0.01 km s^{-1} to 0.02 km s^{-1} with increasing gravity (see Table 3.5, column (3)). Using the relation we found between f_{odd} and macroturbulence we see that $\sigma_{f_{\mathrm{odd}}} = 0.02$ to 0.06. In case 2 (where we only

look at how $f_{\rm odd}$ is affected by one stellar parameter) we find that for an error in temperature of $\pm 100\,$K, $\sigma_{f_{\rm odd}} \approx \pm 0.004$ to 0.01 depending on $\log g$ (Table 3.5 column (10), case 2).

The uncertainty in $\log g$ for HD 140283 is quite small, $\lesssim 0.1$, due to its reliable Hipparcos parallax. As gravity affects line broadening, we find that $\log g$ influences the macroturbulence and $f_{\rm odd}$. Firstly we calculate the effect of $\log g$ on macroturbulence (case 1). We find $\delta v_{\rm conv}/\delta \log g \backsimeq 0.4\,{\rm km\,s^{-1}}$ depending on temperature. So for an uncertainty in $\log g = 0.1$, $\sigma_{v_{\rm conv}} \backsimeq 0.04\,{\rm km\,s^{-1}}$. Using the sensitivity we calculated for macroturbulence suggests an uncertainty in $f_{\rm odd} \backsimeq 0.03$. In comparison, the total case 1 sensitivity is $\delta f_{\rm odd}/\delta \log g \approx 0.2$ implying $\sigma_{f_{\rm odd}} = 0.02$. We can see from Table 3.5 the separate effect that $\log g$ has on $f_{\rm odd}$ when we fix macroturbulence (case 2). Here we find that $\delta f_{\rm odd}/\delta \log g \backsimeq -0.17$ meaning that an error in $\log g$ of 0.1 alters $f_{\rm odd}$ directly by 0.02. The implication is that some of the change in case 1 is driven by the revision of the macroturbulence, and some is driven more directly but in a way that partially compensates.

When examining the effect of microturbulence on $f_{\rm odd}$ one would expect to see two things. If we allow macroturbulence to compensate for the change in microturbulence (case 1) we would expect find that $f_{\rm odd}$ is essentially unchanged. If we fix macroturbulence and alter microturbulence, $f_{\rm odd}$ will change. Table 3.6 shows these two cases. As expected in case 1, the macroturbulence is driven up/down when the microturbulence is decreased/increased and $f_{\rm odd}$ is unaffected. In case 2 we see the sensitivity in $f_{\rm odd}$ as microturbulence is altered given by $\delta f_{\rm odd}/\delta \xi = -0.5\ ({\rm km\ s^{-1}})^{-1}$. Therefore an uncertainty in microturbulence of $0.1\,{\rm km\,s^{-1}}$ implies an error in $f_{\rm odd} = 0.05$. It is case 1 that is relevant to our Ba analysis.

In summary we can assign an uncertainty in $f_{\rm odd}$ for the 4554 Å line $\sigma^2_{f_{\rm odd}} = \sigma^2_{v_{\rm conv}} + \sigma^2_{T_{\rm eff}} + \sigma^2_{\log g} = \sqrt{0.01^2 + 0.02^2 + 0.03^2} = 0.04$ (case 1 - remember that $v_{\rm conv}$ compensates for any effect ξ has on $f_{\rm odd}$). In case 2, where we look at the separate effects the stellar parameters have on $f_{\rm odd}$, we find that for uncertainties in macroturbulence, temperature, $\log g$ and microturbulence $\sigma_{f_{\rm odd}} = \sqrt{0.01^2 + 0.01^2 + 0.02^2 + 0.05^2} = 0.06$. Case 1 is probably more applicable, but we adopt the larger error, case 2, as a pre-

Table 3.6: The sensitivity of $f_{\rm odd}$ to ξ. Temperature and $\log g$ are fixed at 5750 K and 3.7 respectively. *case 1*: The sensitivity of $f_{\rm odd}$ to microturbulence when macroturbulence is re-evaluated to compensate for the change to microturbulence. *case 2*: The sensitivity of $f_{\rm odd}$ to microturbulence when macroturbulence is fixed at the value calculated when $\xi = 1.4$.

ξ	$v_{\rm conv}$		$f_{\rm odd}$			
($\rm km\,s^{-1}$)	($\rm km\,s^{-1}$)		4554 Å		4934 Å	
	case 1	case 2	case 1	case 2	case 1	case 2
1.3	5.81	...	0.01	0.06	0.11	0.14
1.4	5.75	5.75	0.01	0.01	0.11	0.11
1.5	5.68	...	0.01	-0.04	0.11	0.07

caution, i.e. ± 0.06. We now move on to errors and uncertainties associated with the 4934 Å line.

3.5.2 The 4934 Å line

In order to assign an uncertainty in $f_{\rm odd}$ to the 4934 Å line we must also explore how uncertainties in the Fe blend (see Table 3.3) affect $f_{\rm odd}$.

We explored how the equivalent width of the Fe blend is affected by temperature and $\log g$. As in Tables 3.5 and 3.6, we computed two cases where we allow macroturbulence and [Fe/H] to vary with varying temperature and $\log g$ (case 1) and where we have fixed macroturbulence and [Fe/H] (case 2) - in Table 3.5.

The net result of an increase in $\log g$, decrease in macroturbulence, and increase in [Fe/H], is a small increase in synthesized $W_{\rm Fe}$, but these effects are minimal compared to the effects that macroturbulence has on $f_{\rm odd}$. Consequently we see a similar behaviour in $f_{\rm odd}$ (Table 3.5, column (11)) as that exhibited by the 4554 Å line (column (9)) (a roughly linear increase in $f_{\rm odd}$ with $\log g$ with $\Delta f_{\rm odd,4934}$ comparable to $\Delta f_{\rm odd,4554}$).

In case 2 an increasing temperature decreases the equivalent widths of the Fe lines. Unlike case 1, macroturbulence and A(Fe) are not compensating for the increasing ionisation fraction meaning that Fe I level populations are decreasing. This decreases the strength of the Fe lines, decreasing their equivalent widths.

As $\log g$ is driven up in case 2, we find that the equivalent widths are decreasing, recall that A(Fe) is fixed in case 2. Overall, however, we see little or no change in $f_{\rm odd}$ in column (12) in Table 3.5.

We also investigate how the $\log gf$ values, which are not well known for the two Fe lines, affect $f_{\rm odd}$. The 4934 Å line is driven to a pure r-process fraction if the Fe blend is eliminated from the line list, so we would expect that $f_{\rm odd}$ would be quite sensitive to $\log gf$. Table 3.3 shows the parameters of the two lines. We analyse the case that the $\log gf$ values have an error ± 0.15 as a heuristic estimate. Table 3.7 shows how $f_{\rm odd}$ for the 4934 Å line is affected by this increase/decrease in Fe strength. We have tabulated the results for $f_{\rm odd}$ for all values of temperature and $\log g$ we use in our sensitivity analysis. It can be seen for case 2 at a temperature of 5500 K and where the Fe blend strengths have been increased, that $f_{\rm odd}$ becomes so small and so non-physical that our χ^2 program cannot find a minimum solution. Similarly this is seen in case 1 at a temperature of 6000 K. It is clear from Table 3.7 that for 4934 Å, $f_{\rm odd}$ is more sensitive to the uncertainty in the strengths of the Fe lines than the atmospheric parameters. We see in case 1 that as we alter the Fe $\log gf$ by ± 0.15, $f_{\rm odd}$ is altered by ∓ 0.18. This means that when added in quadrature to the error discussed in §3.5.1, we find that for case 1, $f_{\rm odd} = 0.11 \pm 0.18$. For case 2, $f_{\rm odd} = 0.11 \pm 0.19$. We take the error to be the average of the two, so $f_{\rm odd} = 0.11 \pm 0.19$.

Table 3.7: Values of $f_{\rm odd}$ for the 4934 Å line found from altering the strength of the Fe lines. By changing the $\log gf$ values by ± 0.15 we find that $f_{\rm odd}$ alters to compensate for a weakening/strengthening of the Ba wing. We have also included an extra decimal place to show that there is a slight change in $f_{\rm odd}$ as we alter the temperature and gravity in case 2.

$T_{\rm eff}$ (K)	$\log g$ (cgs)	$v_{\rm conv}$ (km s^{-1})		[Fe/H]		[Ba/H]				$f_{\rm odd}$ (4934 Å)			
(1)	(2)	(3)	(4)	(5)	(6)	(7)	(8)	(9)	(10)	(11)	(12)	(13)	(14)
		case 1	case2	case1	case2	case 1		case 2		case 1		case 2	
						-0.15	+0.15	-0.15	+0.15	-0.15	+0.15	-0.15	+0.15
5500	3.4	5.79	...	−2.78	...	−3.67	−3.73	−3.71	−3.81	0.302	−0.046	0.126	...
5500	3.7	5.67	...	−2.77	...	−3.58	−3.63	−3.60	−3.69	0.342	−0.007	0.127	...
5500	4.0	5.52	...	−2.74	...	−3.48	−3.53	−3.49	−3.57	0.376	0.043	0.126	...
5750	3.4	5.82	...	−2.60	...	−3.51	−3.56	−3.51	−3.56	0.252	−0.150	0.275	−0.134
5750	3.7	5.75	5.75	−2.59	−2.59	−3.41	−3.47	−3.41	−3.47	0.273	−0.127	0.273	−0.127
5750	4.0	5.60	...	−2.57	...	−3.32	−3.37	−3.31	−3.36	0.316	−0.100	0.265	−0.115
6000	3.4	5.84	...	−2.43	...	−3.34	−3.39	−3.32	−3.36	0.200	...	0.373	0.083
6000	3.7	5.77	...	−2.42	...	−3.25	−3.31	−3.23	−3.27	0.221	...	0.369	0.084
6000	4.0	5.69	...	−2.40	...	−3.15	−3.21	−3.13	−3.17	0.235	...	0.362	0.083

3.5.3 Overall result

Inverse-variance-weighting the results for 4554 Å (0.01) and 4934 Å (0.11) give an overall result $f_{\rm odd} = 0.02 \pm 0.06$ when macroturbulence is modelled as a Gaussian. When a radial-tangential broadening mechanism is used we find that inverse-variance-weighting gives an overall result $f_{\rm odd} = -0.02 \pm 0.06$.

So far the uncertainties discussed in the section have been limited to errors in $T_{\rm eff}$, $\log g$, $v_{\rm conv}$ and $\log gf$. We have not yet quantified the impact of finite S/N and possible systematic errors associated with a 1D LTE analysis. We recall from §3.3.2 that systematic errors of order 0.09 may arise from using Fe lines to estimate, in 1D, the macroturbulent broadening of Ba. We discuss this further in §3.7. We shall now move on and discuss the Eu abundance and the various implications of the Ba and Eu results.

3.6 Europium abundance limit

Within our spectral range (4118−6253 Å) there are two Eu II resonance lines, 4129.70 Å and 4205.05 Å. Honda et al. (2006) report that the latter has a known blend with a V I line. Gilroy et al. (1988), Magain (1989) and Gratton & Sneden (1994) report [Eu/H] to be −2.31, −2.49 and −2.41 respectively. However, these lines do not appear strongly in our spectrum. This becomes clear when studying Fig. 3.9, which presents the observed data and several synthetic spectra. The Eu line lists were constructed using hyperfine splitting information from Krebs & Winkler (1960) and Becker et al. (1993). We acknowledge that more recent hyperfine splitting information is available from Lawler et al. (2001), which is in good agreement with Krebs & Winkler (1960) and Becker et al. (1993) but we do not use that data here. An isotopic ratio of 0.5:0.5 for Eu 151:153 was chosen for the r- and s-processes (the solar system isotopic ratio of Eu 151:153 is 0.48:0.52 (Arlandini et al., 1999)), and gf values from Biemont et al. (1982) and Karner et al. (1982) were used. The synthetic spectra were produced using KURUCZ06 model atmospheres in conjunction with the 1D LTE code ATLAS. The macroturbulence and [Fe/H] was set at values calculated in §3.3.2.

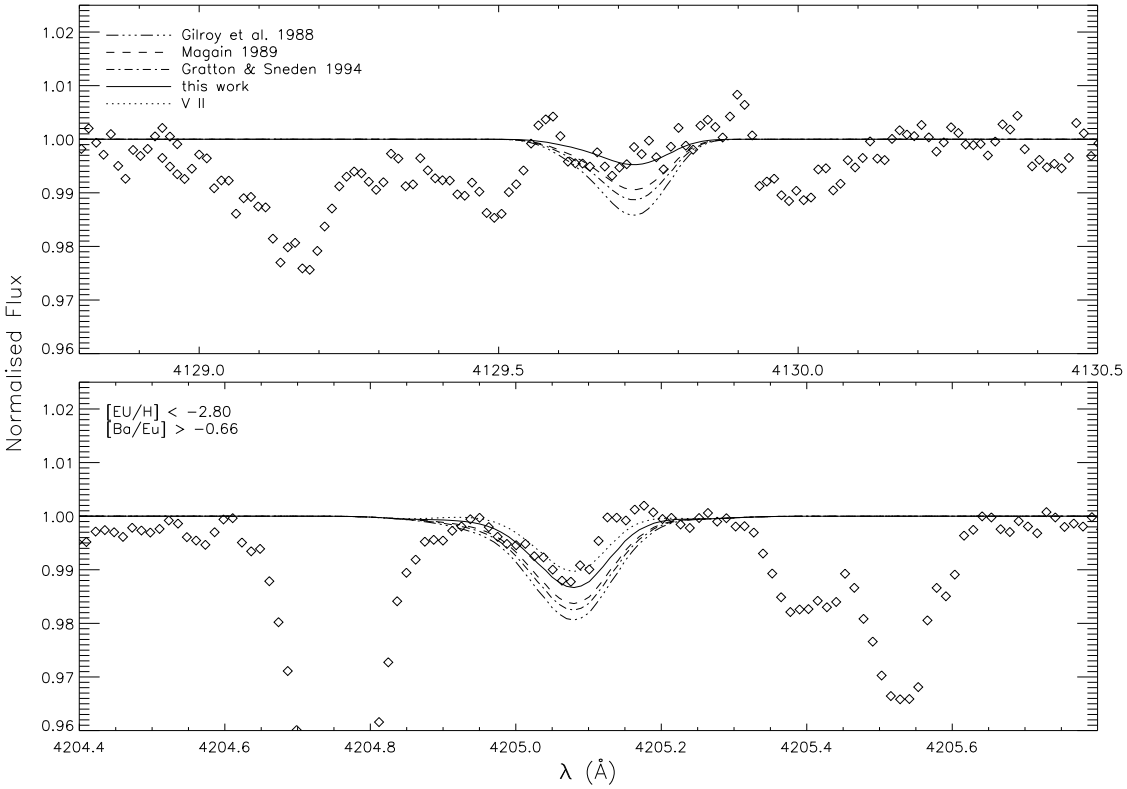

Fig. 3.9: Synthetic spectra for the Eu 4129 and 4205 Å lines for [Eu/H] = −2.80 and for the abundances calculated in three other studies of this star (see text). It is clear that they over estimate the strength of both lines. While the 4205 Å line includes several blends particularly V II 4205.09 Å, the 4129 Å has none. We show the V II line separately in the right-hand panel (*dot-line*).

The Eu 4205 Å synthesis includes several blends which we have adopted from the Kurucz theoretical database (http://www.cfa.harvard.edu/amp/ampdata/kurucz23/sekur.html). The dominant blend is a V II line at $\lambda = 4205.09$ Å, which has a gf value of 0.089 and $\chi = 2.04$ eV. The abundance of V was taken as the solar abundance scaled to the metallicity. We found no blends associated with the 4129 Å line. As these line blends are theoretical, we make no claim that the abundances we deduce from the Eu analysis are as accurate as the analysis conducted on the Ba lines. We interpret the absorption feature at 4205.1 Å as due to V II, not Eu, as it is much narrower than the synthesised, hfs-broadened Eu line. Moreover if it were Eu, not V, it would require an abundance inconsistent with the weakness of the Eu 4129 Å line. We find that a [Eu/H] abundance of −2.80 seems to be a generous upper limit on the Eu abundance, rather than a genuine detection and lower than the cited detections. Therefore we assign a lower limit [Ba/Eu] > −0.66. This marginally excludes an r-process ratio,

whether we assume an r-process limit set in Burris et al. (2000) (−0.81, which were calculated using the Anders & Grevesse (1989) isotopic abundances) or Arlandini et al. (1999) (−0.69). A pure s-process ratio (+1.45, (Burris et al., 2000) or +1.13, (Arlandini et al., 1999)) or a mixed s- and r-process regime, is compatible with the data. However, our [Ba/Eu] limit does agree well with observations found in François et al. (2007) for stars of similar metallicity to HD 140283.

We shall now move on and discuss the various implications of the results found in this paper and look at possible solutions to reduce systematic errors associated with a 1D LTE analysis.

3.7 Discussion

We have found that $f_{\rm odd} = 0.02 \pm 0.06$, and hence the r-process fraction implies a purely s-process signature of Ba in HD 140283. The [Ba/Eu] ratio, > -0.66, is also marginally inconsistent with a pure r-process regime. The isotope result does not entirely contradict previous work by Lambert & Allende Prieto (2002) and Collet et al. (2009) since, due to the size of their 1σ errors, an s- or r-process isotopic mixture was feasible (see Fig. 3.1). Although we find that $f_{\rm odd}$ for the 4554 Å line is non-physical (at the 1.8σ level) based on Arlandini et al. (1999), we must consider the possibility that the adopted s- and r-process isotope contributions may not be accurate, as they are based on our simplified understanding of nucleosynthesis, which could be flawed. For example, the Arlandini et al. (1999) calculations give a solar-system r-process isotopic ratio, and we cannot be certain that this applies in the Galactic halo. However, metal-poor stars with r-process enhancements do at least have similar neutron-capture abundance patterns to the Sun, e.g. CS 22892-052 (Sneden et al., 1996).

We also question whether the S/N ratio is high enough to measure these fractions accurately, and whether a 1D LTE analysis is an adequate tool in investigating isotopic ratios at these high levels of S/N, by looking at the confidence limits of the χ^2 minima, which we now discuss. The fact that our best fitting spectra have χ^2_r values significantly greater than 1 ($\chi^2_r = 6.6$ and 2.0 for the 4554 Å and 4934 Å line respectively) indicates

that the χ^2 denominator (σ_i) is not a good description of the deviation of the model spectrum from the data. We interpret the high χ^2_r values to indicate that systematic errors are present which exceed the random fluctuations in the signal. This influence is confirmed by inspection of Figs. 3.6, 3.7 & 3.8, where it can be seen that the residuals do not oscillate randomly from one pixel to the next but rather seem to meander over a cycle of a few pixels. In short, this tells us that the failure of the model profile to match to the data exceeds the error due to noise (mostly photon noise) in the spectrum, and hence σ_i as judged from the S/N underestimates the true residual. From Fig. 3.6 it can be seen that the best fit under-fits the core of the lines in order to fit the wings of the lines better. The r-process contributes more to the wings of the line, see Fig. 3.4 and Table 3.2. It is interesting to note that we under-fit the red wing of the 4554 Å line between 4554.11 Å and 4554.17 Å (see Figs. 3.6 & 3.7). Lambert & Allende Prieto (2002) and Collet et al. (2009) in 1D, see the same residual feature at this wavelength interval. When they reanalysed the line in 3D, Collet et al. (2009) appeared to remove the feature in the wing. This would suggest that it is a result of convection in a 3D atmosphere rather than a feature induced by inaccuracies when calculating the isotopic shifts. We suspect that the error arises due to the assumptions used in 1D LTE codes that are unable to correctly model physical conditions in a 3D atmosphere.

To explore this further, we have searched for evidence of asymmetries in the Fe line data. We have produced two Fe line plots by co-adding the residuals from all 93 lines to find an average residual, shown in Fig. 3.10 (*top panel*). The lower panel shows the average residual for the 82 Fe lines found to have no additional features or close non-Fe lines within the window over which the χ^2 analysis is calculated (0.6 Å). Lines marked with an asterisk in Table B.1 denote the 11 Fe lines that were rejected. For one plot (*dash-dot curve*) the average residuals (*obs-syn*) are based on synthetic spectra calculated using the average wavelength shift (-12.04 mÅ) and average macroturbulence (5.75 km s^{-1}) for all Fe lines. The average residual is very asymmetric, in that the blue wings are better fit than the red wings. The large residuals in the red wings, around $60-170$ mÅ from the line centre, are clearly not due to errors in the central wavelengths of the Fe lines, which are known to better than 1 mÅ (§3.3.2).

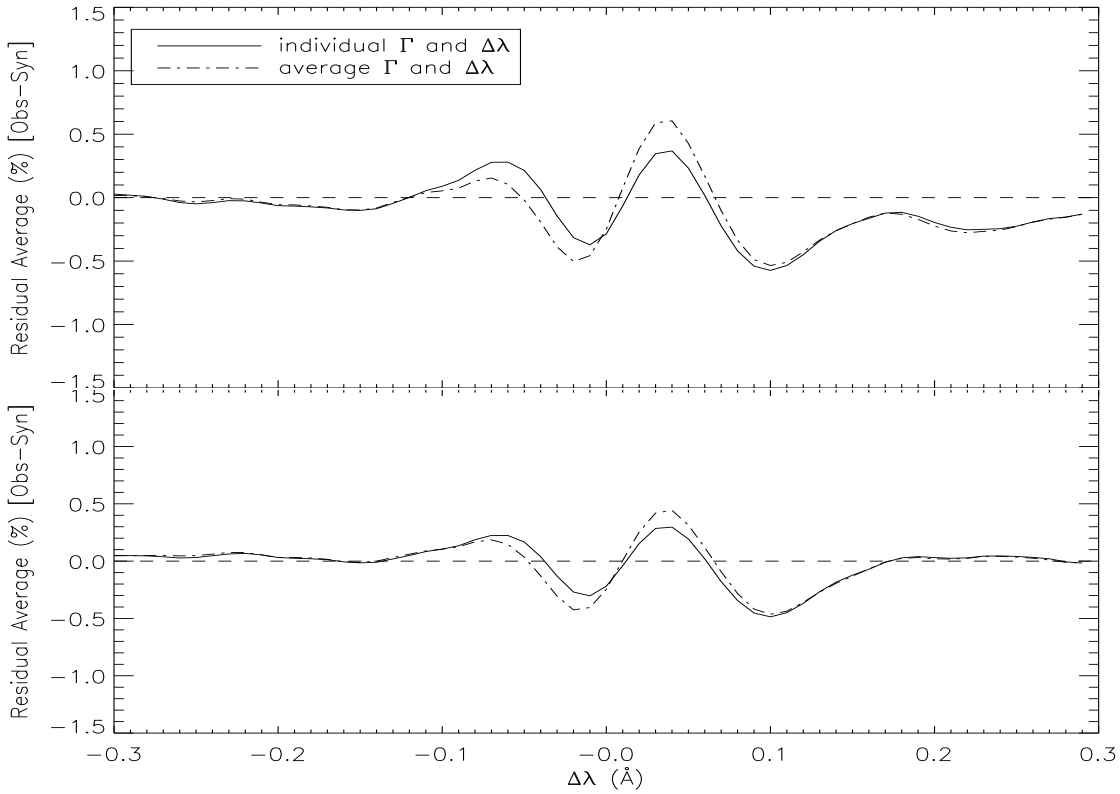

Fig. 3.10: Average residuals for fits to 93 Fe lines, for two cases. It is quite clear that assuming a constant wavelength shift and macroturbulence is adequate when working in 1D LTE but assuming 1D LTE when dealing with high quality data is not. *Top panel*: the reduced-noise residual plot for all 93 lines. *Bottom panel*: the reduced-noise residual plot for 82 lines without other close absorption features. Lines not included in lower panel are noted with an asterisk in Table B.1.

We also computed a new set of synthetic spectra using the optimised $v_{\rm conv}$ and $\Delta\lambda$ values belonging to each Fe line as found from the χ^2 analysis (see Table B.1), and recalculated the residuals (*obs-syn*) for these. These new residuals were coadded and averaged, and plotted in Fig. 3.10 (*solid curve*). These slightly reduce the overall amplitude of the residuals, as expected since we are optimising the fit to each Fe line. However, even after allowing each one to be optimised, the residuals are still quite asymmetric, with the red wings standing out as having larger residuals than the blue wings. From Fig. 3.10 we can see that a similar red feature to the one we see in Fig. 3.6 for Ba is present in both Fe residual plots, and appears at the same distance from the centroid of the Fe lines as the residuals for the Ba 4554 Å line (~ 100 mÅ). The feature remains whether we optimise $v_{\rm conv}$ and $\Delta\lambda$ or not. We suspect this feature may be the result of convection in the observed, dynamic atmosphere, similar to the feature seen

in the Ba spectrum, that underlying assumptions in 1D LTE do not compensate for.

Collet et al. (2009) conduct a 3D analysis of HD 140283. Our measurements of the residuals for the Fe lines provide a future test of whether 3D modelling produces similar residuals. We hope to explore this at a later date. As the 3D process calculates the velocity field ab initio, there is no concept of micro- or macroturbulence in that framework. Consequently, Collet et al. (2009) ascribe any excess broadening to stellar rotation, and for this they infer $v \sin i = 2.5\,\mathrm{km\,s^{-1}}$. We note that the upper limit on $v \sin i$ which we infer for zero macroturbulence is $3.9\,\mathrm{km\,s^{-1}}$. Their value is compatible with our limit. We note that Collet et al. (2009) find a lower r-process fraction for HD 140283 using a 3D analysis than they find for 1D. If our findings are similar, then this will further accentuate the difference between the analysis of HD 140283 and the expectations based on Truran's hypothesis.

One possible alternative explanation of the asymmetries is that we are seeing the combined spectra of more than one star, offset in velocity. It may be difficult to generate the observed levels of asymmetries for a realistic second star, and we have not attempted to do so, but note this possibility nonetheless. We also note that the radial velocity of HD 140283 has been steady to $\pm 0.35\,\mathrm{km\,s^{-1}}$ over long periods of time (Lucatello et al., 2005), decreasing the likelihood that it is a binary.

Finally we shall move on to discuss the conclusions we have drawn from our analysis of the isotopic ratio of Ba in HD 140283.

3.8 Conclusions

We have used very high quality data ($S/N = 870 - 1110$, $R \equiv \lambda/\Delta\lambda = 95\ 000$) to analyse the Ba isotopic fraction and the Eu abundance limit in the metal-poor subgiant HD 140283. We obtain $[\mathrm{Fe/H}] = -2.59 \pm 0.09$, $[\mathrm{Ba/Fe}] = -0.87 \pm 0.14$, and $[\mathrm{Eu/H}] < -2.80$. Using a 1D LTE analysis, we find $f_{\mathrm{odd}} = 0.02 \pm 0.06$, corresponding to a Ba isotopic fraction which indicates a 100% contribution by the s-process. This result contradicts the theory put forward by Truran (1981). The result published by Lambert & Allende Prieto (2002) has error bars which are too broad to allow one to

state conclusively that HD 140283 is r-process dominated. We have set a new lower limit to the [Ba/Eu] ratio, [Ba/Eu] > -0.66. This lower limit marginally rules out a pure r-process ratio in HD 140283, consistent with the isotopic fraction for Ba. A new high resolution spectrum with a greater S/N around the 4129 Å line is needed to constrain a genuine abundance for Eu.

We have also carried out a careful examination of the 4934 Å line, which is more sensitive to the effects of hyperfine-splitting. We found that, due to the lack of laboratory gf data surrounding the Fe blend affecting the wings of this line, it is less effective as a tool to analyse the isotopic mixture than Ba 4554 Å.

By examining the spectral residuals for 93 Fe lines and for Ba 4554, 4934 Å, we find strong line asymmetries in the red wing. These may show the shortcomings of using a 1D LTE analysis to explore isotope ratios; using a more sophisticated 3D analysis may be warranted. We are looking to take this work further in the future and analyse HD 140283 using a 3D code. We note that Collet et al. (2009) find a lower r-process fraction for HD 140283 using a 3D analysis than they find for 1D. If our findings are similar, then this will further accentuate the difference between the analysis of HD 140283 and the expectations based on Truran's hypothesis.

We set a new limit on the rotation of HD 140283: $v \sin i < 3.9\,\mathrm{km\,s^{-1}}$.

Acknowledgements

The authors would like to acknowledge Satoshi Kawanomoto for reducing the stellar spectrum used in this work. AJG and SGR would like to thank Gillian Nave and Juliet Pickering for kindly investigating Fe spectra to constrain spectroscopic information about a known Fe blend in the Ba 4934 Å line which was crucial for the present investigation. SGR wishes to acknowledge Ph.D. thesis work by Blake (2004) on a spectrum of HD 140283 which, while not having the benefit of a large number of Fe lines for the determination of macroturbulence, nevertheless gave a value $f_{\mathrm{odd}} = 0.08 \pm 0.11$.

References

Anders, E. & Grevesse, N. 1989, Geochim. Cosmochim. Acta, 53, 197 [ADS]

Aoki, W., Inoue, S., Kawanomoto, S., Ryan, S. G., Smith, I. M., Suzuki, T. K., & Takada-Hidai, M. 2004, A&A, 428, 579 [ADS]

Argast, D., Samland, M., Thielemann, F.-K., & Qian, Y.-Z. 2004, A&A, 416, 997 [ADS]

Arlandini, C., Käppeler, F., Wisshak, K., Gallino, R., Lugaro, M., Busso, M., & Straniero, O. 1999, ApJ, 525, 886 [ADS]

Becker, O., Enders, K., Werth, G., & Dembczynski, J. 1993, Phys. Rev. A, 48, 3546 [ADS]

Biemont, E., Karner, C., Meyer, G., Traeger, F., & Zu Putlitz, G. 1982, A&A, 107, 166 [ADS]

Blake, L. A. J. 2004, PhD thesis, Open University (United Kingdom) [ADS]

Burbidge, E. M., Burbidge, G. R., Fowler, W. A., & Hoyle, F. 1957, Reviews of Modern Physics, 29, 547 [ADS]

Burris, D. L., Pilachowski, C. A., Armandroff, T. E., Sneden, C., Cowan, J. J., & Roe, H. 2000, ApJ, 544, 302 [ADS]

Busso, M., Gallino, R., Lambert, D. L., Travaglio, C., & Smith, V. V. 2001, ApJ, 557, 802 [ADS]

Clayton, D. D. & Rassbach, M. E. 1967, ApJ, 148, 69 [ADS]

Collet, R., Asplund, M., & Nissen, P. E. 2009, Publications of the Astronomical Society of Australia, 26, 330 [ADS]

Cottrell, P. L. & Norris, J. 1978, ApJ, 221, 893 [ADS]

Cowley, C. R. & Frey, M. 1989, ApJ, 346, 1030 [ADS]

de Medeiros, J. R., Silva, J. R. P., Do Nascimento, Jr., J. D., Canto Martins, B. L., da Silva, L., Melo, C., & Burnet, M. 2006, A&A, 458, 895 [ADS]

François, P., Depagne, E., Hill, V., Spite, M., Spite, F., Plez, B., Beers, T. C., Andersen, J., James, G., Barbuy, B., Cayrel, R., Bonifacio, P., Molaro, P., Nordström, B., & Primas, F. 2007, A&A, 476, 935 [ADS]

Freiburghaus, C., Rosswog, S., & Thielemann, F. 1999, ApJ, 525, L121 [ADS]

Fulbright, J. P. 2000, AJ, 120, 1841 [ADS]

Gallagher, A. J., Ryan, S. G., García Pérez, A. E., & Aoki, W. 2010, A&A, 523, A24 [ADS]

Gallino, R., Arlandini, C., Busso, M., Lugaro, M., Travaglio, C., Straniero, O., Chieffi, A., & Limongi, M. 1998, ApJ, 497, 388 [ADS]

Gallino, R., Busso, M., Lugaro, M., Travaglio, C., & Straniero, O. 2000, in Liege International Astrophysical Colloquia, Vol. 35, Liege International Astrophysical Colloquia, 81 [ADS]

García Pérez, A. E., Aoki, W., Inoue, S., Ryan, S. G., Suzuki, T. K., & Chiba, M. 2009, A&A, 504, 213 [ADS]

Gilroy, K. K., Sneden, C., Pilachowski, C. A., & Cowan, J. J. 1988, ApJ, 327, 298 [ADS]

Gratton, R. G. & Sneden, C. 1994, A&A, 287, 927 [ADS]

Gray, D. F. 2008, The Observation and Analysis of Stellar Photospheres (Cambridge: Cambridge University Press, 2008.) [ADS]

Grevesse, N., Asplund, M., & Sauval, A. J. 2007, Space Science Reviews, 130, 105 [ADS]

Grevesse, N. & Sauval, A. J. 1998, Space Science Reviews, 85, 161 [ADS]

Honda, S., Aoki, W., Ishimaru, Y., Wanajo, S., & Ryan, S. G. 2006, ApJ, 643, 1180 [ADS]

Izutani, N., Umeda, H., & Tominaga, N. 2009, ApJ, 692, 1517 [ADS]

Kajino, T., Wanajo, S., & Mathews, G. J. 2002, Nuclear Physics A, 704, 165 [ADS]

Karner, C., Meyer, G., Traeger, F., & Zu Putlitz, G. 1982, A&A, 107, 161 [ADS]

Krebs, K. & Winkler, R. 1960, Zeitschrift fur Physik, 160, 320 [ADS]

Lambert, D. L. & Allende Prieto, C. 2002, MNRAS, 335, 325 [ADS]

Lawler, J. E., Wickliffe, M. E., den Hartog, E. A., & Sneden, C. 2001, ApJ, 563, 1075 [ADS]

Lucatello, S., Tsangarides, S., Beers, T. C., Carretta, E., Gratton, R. G., & Ryan, S. G. 2005, ApJ, 625, 825 [ADS]

Magain, P. 1989, A&A, 209, 211 [ADS]

—. 1995, A&A, 297, 686 [ADS]

Mashonkina, L., Gehren, T., & Bikmaev, I. 1999, A&A, 343, 519 [ADS]

Mishenina, T. V. & Kovtyukh, V. V. 2001, A&A, 370, 951 [ADS]

Nave, G., Johansson, S., Learner, R. C. M., Thorne, A. P., & Brault, J. W. 1994, ApJS, 94, 221 [ADS]

Pignatari, M. & Gallino, R. 2008, in American Institute of Physics Conference Series, Vol. 990, First Stars III, 336–338 [ADS]

Romano, D., Chiappini, C., Matteucci, F., & Tosi, M. 2005, A&A, 430, 491 [ADS]

Rutten, R. J. 1978, Sol. Phys., 56, 237 [ADS]

Ryan, S. G., Norris, J. E., & Beers, T. C. 1996, ApJ, 471, 254 [ADS]

Seeger, P. A., Fowler, W. A., & Clayton, D. D. 1965, ApJS, 11, 121 [ADS]

Sneden, C., Cowan, J. J., & Gallino, R. 2008, ARA&A, 46, 241 [ADS]

Sneden, C., McWilliam, A., Preston, G. W., Cowan, J. J., Burris, D. L., & Armosky, B. J. 1996, ApJ, 467, 819 [ADS]

Spite, M. & Spite, F. 1978, A&A, 67, 23 [ADS]

Straniero, O., Chieffi, A., Limongi, M., Busso, M., Gallino, R., & Arlandini, C. 1997, ApJ, 478, 332 [ADS]

The, L.-S., El Eid, M. F., & Meyer, B. S. 2007, ApJ, 655, 1058 [ADS]

Travaglio, C., Galli, D., Gallino, R., Busso, M., Ferrini, F., & Straniero, O. 1999, ApJ, 521, 691 [ADS]

Travaglio, C., Gallino, R., Arnone, E., Cowan, J., Jordan, F., & Sneden, C. 2004, ApJ, 601, 864 [ADS]

Truran, J. W. 1981, A&A, 97, 391 [ADS]

Villemoes, P., Arnesen, A., Heijkenskjold, F., & Wannstrom, A. 1993, Journal of Physics B Atomic Molecular Physics, 26, 4289 [ADS]

Wanajo, S. & Ishimaru, Y. 2006, Nuclear Physics A, 777, 676 [ADS]

Wendt, K., Ahmad, S. A., Buchinger, F., Mueller, A. C., Neugart, R., & Otten, E.-W. 1984, Zeitschrift fur Physik, 318, 125 [ADS]

Wheeler, J. C., Cowan, J. J., & Hillebrandt, W. 1998, ApJ, 493, L101 [ADS]

Zhao, G. & Magain, P. 1990, A&A, 238, 242 [ADS]

Chapter 4: The barium isotopic mixture in five metal-poor stars

The following chapter contains the unedited journal paper published by Gallagher, Ryan, Hosford, García Pérez, Aoki, & Honda (2012), which was submitted and accepted for publication in Astronomy & Astrophysics.

Abstract

Theory and observations of heavy element nucleosynthesis are in conflict with one-another. Theory states that in the most metal-poor stars, the rapid (r-) neutron-capture nucleosynthetic process would be dominant over the slow (s-) process. The most recent determinations of r- and s-process yields do not support this. We provide measurements of the Ba isotopic fractions for five metal-poor stars derived with a local thermodynamic equilibrium (LTE) analysis with 1D model stellar atmospheres. This increases the comparisons with heavy element nucleosynthesis theory. We use high resolution ($R \equiv \lambda/\Delta\lambda = 90\,000-95\,000$), very high signal-to-noise ($S/N > 500$) spectra to determine the fraction of odd Ba isotopes ($f_{\rm odd}$) by measuring subtle asymmetries in the profile of the Ba II line at 4554 Å. We also use two different macroturbulent broadening techniques, Gaussian and radial-tangential, to model the Fe lines of each star, and propagate each technique to model macroturbulent broadening in the Ba 4554 Å line. We conduct a 1D non-LTE (NLTE) treatment of the Fe lines in the red giant HD 122563 and the subgiant HD 140283 in an attempt to improve the fitting. We determine [Ba/Eu] ratios for the two giants in our study, HD 122563 and HD 88609, which can also be used to determine the relative contribution of the s- and r-processes to heavy-element nucleosynthesis, for comparison with $f_{\rm odd}$. We find mathematical solutions of $f_{\rm odd}$ for HD 122563, HD 88609 and HD 84937 of -0.12 ± 0.07, -0.02 ± 0.09, and -0.05 ± 0.11 respectively. BD+26° 3578 yielded a value for $f_{\rm odd} = 0.08 \pm 0.08$. Only BD−04° 3208 was found to have a physical $f_{\rm odd}$ ratio of 0.18 ± 0.08. This means that all stars examined here show isotopic fractions more compatible with an s-process

dominated composition. The [Ba/Eu] ratios in HD 122563 and HD 88609 are found to be -0.20 ± 0.15 and -0.47 ± 0.15 respectively, which indicate instead an r-process signature. We report a better statistical fit to the majority of Fe profiles in each star when employing a radial-tangential broadening technique during our 1D LTE investigation. With the increase of the number of stars for which the Ba isotope fraction $f_{\rm odd}$ has been measured, and the nature of their results, there is now a stronger argument to suggest that other synthesis codes that employ alternative approaches to radiative transfer (e.g. 3D hydrodynamics) have to be considered to tackle the high level of precision required for the determination of isotopic ratios. We have shown that, from a statistical point of view, one must consider using a radial-tangential broadening technique rather than a Gaussian one to model Fe line macroturbulences when working in 1D. No improvement to Fe line fitting is seen when employing a NLTE treatment of the Fe lines.

4.1 Introduction

Nuclei heavier than the Fe-peak are mainly synthesised via two neutron-capture processes, the slow (s-) and rapid (r-) process. For the s-process, neutron-capture rates are much lower than β-decay rates in unstable isotopes, whereas for the r-process, neutron-capture rates are higher than β-decay rates. Each n-capture process has a different site for nucleosynthesis (Burbidge et al., 1957). Low- to intermediate-mass stars ($1\,{\rm M}_{\odot} \lesssim M \lesssim 8\,{\rm M}_{\odot}$) evolving along the thermal pulsing asymptotic giant branch (TP-AGB) provide the necessary conditions for the "main" s-process, which is responsible for the majority of the s-process elements in the solar-system between $88 \leq A \leq 204$ (Sneden et al., 2008), releasing free neutrons via $^{12}{\rm C(p,\gamma)^{13}N}(\beta^{+}\nu_{\rm e})^{13}{\rm C}(\alpha,{\rm n})^{16}{\rm O}$ reaction occurring in the He-rich zone in radiative conditions (Straniero et al., 1997). Evidence of active s-processing in TP-AGB stars can be seen through absorption line detections of short lived ^{98}Tc and ^{99}Tc isotopes (Smith & Lambert, 1988, and references therein) visible at 4238, 4262 and 4297 Å.

There are many candidates for r-process sites including neutron star explosions

(Imshennik, 1992), neutron star surface explosions (Bisnovatyi-Kogan & Chechetkin, 1979) and neutron star winds (Panov & Janka, 2009; Wanajo et al., 2001), to name a few. However, presently the most favoured sites for the r-process are core-collapse supernovae (Wanajo & Ishimaru, 2006). Extreme temperatures and run away nuclear processes produce an extremely high fluence of free neutrons (Wanajo et al., 2003), which are necessary for r-process nucleosynthesis.

The presence of seed nuclei with high n-capture cross-sections (σ), such as Fe, is critical for n-capture nucleosynthesis. As low- to intermediate-mass stars cannot synthesise nuclides up to the Fe-peak, high-σ nuclei must be present at the time of the star's formation for the s-process to occur. High-mass supernova progenitors ($M > 8\mathrm{M}_{\odot}$) reach high enough temperatures at the very end of their evolution immediately before the supernova explosive phase to synthesise nuclides up to the Fe-peak. Unlike the s-process, the r-process does not need the presence of high-σ nuclei at the time of formation as they are produced in situ shortly before the end of the life of the star. Also, low- to intermediate-mass stars are long lived in comparison to high-mass stars. As such, r-process enrichment from supernovae explosions should dominate in the early universe, i.e. in metal-poor regimes, with the s-process signatures becoming increasingly dominant in more metal-rich regimes. This theory was set out by Truran (1981) and the chemical evolution of n-capture elements from Ba to Eu was quantified by Travaglio et al. (1999). Indications to support this theory can be seen in evidence presented in François et al. (2007, their Fig. 14).

As the Galaxy becomes more metal-rich over time, s-process signatures in stars begin to increase relative to the r-process for Ba (François et al., 2007). When one compares the [Ba/Eu] ratios from François et al. (2007) with those from Mashonkina et al. (2003), who study the metallicity at which the s-process begins to increase relative to the r-process for the halo and thick disk respectively, there are variations in star-to-star compositions which lead to different r- and s-process regimes for a given metallicity. In particular François et al. (2007) find that the s-process begins to increase relative to the r-process at $[\mathrm{Fe/H}] \gtrsim -2.6$, whereas Mashonkina et al. (2003) find this to occur at $[\mathrm{Fe/H}] \gtrsim -1.5$.

One potential way of detecting r- and s-process signatures in a star is to measure the isotopic fractions in heavy elements using the profile of their absorption lines. There are differences between pure s- and r-process isotope ratios in most heavy elements, which can be in principle detectable through minute changes in line asymmetry. Ba is an attractive heavy element for which to use of this method, as the hyperfine splitting (hfs) of its 4554 Å line from the singly-ionised stage is quite large (Rutten, 1978) and it offers the possibility of measuring the odd fraction ($f_{\rm odd}$[1]) via resolved asymmetric lines.

The r- and s-process are responsible for five of the seven stable isotopes of Ba (the lightest two, ^{130,132}Ba, arise in the so-called p-process (Burbidge et al., 1957)). Whereas the s-process can synthesise all five Ba n-capture isotopes, shielding by ^{134,136}Xe prevents the r-process from synthesising two of the even isotopes, ^{134,136}Ba.

Using nucleosynthesis calculations (Arlandini et al., 1999), the values of $f_{\rm odd}$ can be determined for the r- and s-process. For a fully s-process regime, $f_{{\rm odd},s} = 0.11 \pm 0.01$, and in a fully r-process regime, $f_{{\rm odd},r} = 0.46 \pm 0.06$. Gallagher et al. (2010) show a linear relationship between $f_{\rm odd}$ and r- and s-process contributions for Ba determined from Arlandini et al. (1999). Values of $0.0 \leq f_{\rm odd} < 0.11$ or $0.46 < f_{\rm odd} \leq 1.0$ are not physical in the context of the nucleosynthesis model but are achievable from more ad hoc isotopic mixes. However, we have assumed that the theory in Arlandini et al. (1999) is accurate and we state throughout our paper that any value of $f_{\rm odd}$ which lies outside the limits $0.11 \leq f_{\rm odd} \leq 0.46$ is non-physical.

From the point of view of spectroscopy, the even Ba isotopes contribute principally to the formation of the line centre in the Ba II 4554 Å line. The odd isotopes, which are hyperfine split, contribute to the spectral region closer to the wings of the line (see Fig. 4.1). The relative strength of the odd isotopes located toward the blue wing are smaller than those located toward the red wing and are further from the line core. As such, when the odd isotope contribution to the total line strength is increased, the asymmetry in the absorption line's profile is increased. When Ba is dominated by the s-process, more of the abundance is associated with the even isotopes, which contribute

[1] $f_{\rm odd} = [N(^{135}{\rm Ba}) + N(^{137}{\rm Ba})]/N({\rm Ba})$

to the line near its centre; the line profile has a deeper core with shallower wings and the line's asymmetry is reduced.

There are, however, difficulties in determining isotopic fractions in Ba, chief among which is the high precision required in the analysis of $f_{\rm odd}$, which demands the highest quality observations and radiative transfer models. Issues then arise when complex astrophysical behaviours, such as convection, start to become visible in the high quality stellar data. Basic assumptions used in conventional spectrum synthesis codes that assume a plane-parallel geometry (1D) and local thermodynamic equilibrium (LTE) cannot actually replicate the observed Ba II 4554 Å line profile (Gallagher et al., 2010).

The well studied metal-poor subgiant, HD 140283 illustrates the difficulties that are encountered when determining $f_{\rm odd}$, which has been attempted several times for this star. Gallagher et al. (2010) find [Fe/H] $= -2.59 \pm 0.09$ and a low [Ba/Fe] ratio $= -0.87 \pm 0.14$, which seemingly point to an r-process origin as Ba is mainly an s-process element in the solar system. Yet according to their isotopic analysis they find $f_{\rm odd} = 0.02 \pm 0.06$, which agrees with the result published by Magain (1995), who finds $f_{\rm odd} = 0.08 \pm 0.06$. Both isotope fractions indicate a fully s-process regime, contradicting the Truran (1981) model. However, measurements of $f_{\rm odd}$ in 1D LTE by Lambert & Allende Prieto (2002) and (for the same spectrum) Collet et al. (2009) show HD 140283 to be slightly r-process dominated with $f_{\rm odd} = 0.30 \pm 0.21$ and $f_{\rm odd} = 0.33 \pm 0.13$ respectively, which contradicts Magain (1995) and Gallagher et al. (2010). When Collet et al. (2009) reanalysed the same spectrum again using 3D hydrodynamic model stellar atmospheres they found $f_{\rm odd} = 0.15 \pm 0.12$, indicating an s-process signature and supporting results from Magain (1995) and Gallagher et al. (2010). If the three studies showing HD 140283 to have an s-process signature are correct, the contradiction with Truran's paradigm could be explained by how s- and r-processes vary with [Fe/H], or by the inhomogeneity of the interstellar medium (ISM) when this halo star formed, in which case star-to-star variations of n-capture signatures would be common. The cause of the discrepancy between the results of the various studies of HD 140283 is unclear.

Unlike Ba, Eu in the solar system has a predominantly r-process contribution, which Arlandini et al. (1999) calculates to be 94% of the total Eu. Both stable Eu

isotopes, ^{151,153}Eu, show significant r-process contributions relative to the s-process and these occur in almost equal amounts at a ratio of 0.48:0.52 for 151:153 (Arlandini et al., 1999). High abundances of Eu in metal-poor stars indicate a strong r-process signature (Spite & Spite, 1978; Sneden et al., 2008). Therefore it is common practice to use the [Ba/Eu] ratio as an indicator of a star's r- and s-process ratio (Burris et al., 2000; Honda et al., 2006, 2007; Sneden et al., 2008).

Limits on [Ba/Eu] abundance ratios can be set for pure s- and r-processes and are found to be +1.45 and −0.81 respectively (Burris et al., 2000), which were calculated using solar abundances in Anders & Grevesse (1989). Using the theoretical abundances in Arlandini et al. (1999), we find the [Ba/Eu] limits for the s- and r-processes to be +1.13 and −0.69 respectively.

Gallagher et al. (2010) highlighted the issues that arise when fitting Fe lines assuming 1D LTE, particularly in the wings of the line, and plotted the average residual for all the Fe lines analysed. They demonstrated the asymmetries that occur in line formation; 1D LTE radiative transfer codes cannot replicate asymmetries. Gallagher et al. (2010) speculated that a spectroscopic analysis based on 3D radiation-hydrodynamic model stellar atmospheres may resolve these problems. In addition they found irregularities between the observed and synthetic profiles in the Fe line's core.

In this paper we determine the isotopic fractions of Ba in a further five metal-poor stars under the assumption of 1D LTE. We describe the observations in §4.2, and the 1D LTE analysis of the Ba 4554 Å line in §4.3. Due to the lack of metals in metal-poor stars, i.e. stars with [Fe/H] < -2, electron number densities are low, which drives down opacities in the atmosphere of late-type stars. Therefore assuming LTE in line forming regions of the stellar atmosphere is no longer valid (Mashonkina et al., 2008). In §4.4 of the work presented here we test whether the irregularities seen in the Fe line residuals are due to LTE departures, using a non local thermodynamic equilibrium (NLTE) treatment for HD 140283 and HD 122563. We discuss the results in §4.5.

4.2 Target selection and observations

The stellar spectra used in this study are almost the highest quality spectra of very metal-poor stars obtained using the High Dispersion Spectrograph (HDS) (Noguchi et al., 2002) at the Subaru 8.2 m Telescope. All have high resolution ($R \equiv \lambda/\Delta\lambda = 90\,000 - 95\,000$, calculated from the widths of several hundred ThAr lines), and high signal-to-noise ($S/N > 500$ per pixel, as measured around 4500 Å). Such spectra are essential for an accurate measurement of $f_{\rm odd}$. Specifics of the observations can be found in Table 4.1.

Table 4.1: Details of the observations of the stellar spectra.

Star	Date	Exp. Time (min)	S/N	R
HD 140283	22/07/01	82	1100	95 000
HD 88609	20/04/04 19/10/05 20/10/05	210	750	90 000
HD 122563	30/04/04	90	850	90 000
HD 84937	22/03/03	180	630	95 000
BD+26° 3578	17/05/05	130	550	95 000
BD−04° 3208	18/05/05 19/05/05	180	580	95 000

Table 4.2 shows previous results on Ba published for four of the stars studied in this paper. It further illustrates the difficulties in determining $f_{\rm odd}$, in that for HD 122563, $f_{\rm odd}$ and [Ba/Eu] do not support each other[2], while for HD 140283 there are large discrepancies between $f_{\rm odd}$ determinations.

The two giants in our study, HD 122563 and HD 88609, and one of the turn-off stars, HD 84937, show a strong indication that Ba should be r-process dominated based upon [Ba/Eu] abundance ratios calculated in Honda et al. (2006), Honda et al. (2007) and Mashonkina et al. (2008). Mashonkina et al. (2008) complement the [Ba/Eu] determination nicely in HD 84937 calculating $f_{\rm odd} = 0.43 \pm 0.14$, indicating an almost

[2]One might take the view that these results are consistent with a mixed heavy element origin.

fully r-process regime. However they found $f_{\rm odd}$ in HD 122563 to be 0.22±0.15, a mostly s-process regime, which contradicts the [Ba/Eu] abundances found in their study and by Honda et al. (2006), see Table 4.2. We also calculate $f_{\rm odd}$ for two more turn-off stars, BD−04° 3208 and BD+26° 3578, neither of which have previous Ba and Eu analyses.

Table 4.2: Results from previous 1D LTE studies to determine [Ba/Eu] and/or $f_{\rm odd}$ for stars studied in this work.

Star	[Fe/H]	[Ba/Eu]	$f_{\rm odd}$	Reference
HD 140283	−2.59	> -0.66	0.01 ± 0.04	(1)
	−2.40	~ -1.05	0.30 ± 0.21	(2)
	−2.50	···	0.33 ± 0.13	(3)
	−2.70	···	0.08 ± 0.06	(4)
HD 122563	−2.77	−0.50	···	(5)
	−2.53	−0.41	0.22 ± 0.15	(6)
HD 84937	−2.15	−0.69	0.43 ± 0.14	(6)
HD 88609	−3.07	−0.48	···	(7)

(1) Gallagher et al. (2010), as measured by the 4554 Å line. (2) Lambert & Allende Prieto (2002). (3) Collet et al. (2009). (4) Magain (1995). (5) Honda et al. (2006). (6) Mashonkina et al. (2008). (7) Honda et al. (2007).

4.3 1D LTE analysis

In this section we briefly review the method used to determine the isotopic fractions, abundances and broadening values of the stars in our sample. All synthetic spectra in this section were created using the ATLAS (Cottrell & Norris, 1978) radiative transfer code with KURUCZ06 model atmospheres (`http://kurucz.harvard.edu/grids.html`). For a more extensive description of the processes involved in the following procedure, we refer the reader to Gallagher et al. (2010). Results are provided in Table 4.3.

4.3.1 Barium line lists

Line lists with all hfs components of the Ba line at 4554 Å, which is used to determine $f_{\rm odd}$, were constructed using isotopic information from Arlandini et al. (1999) and hfs information from Wendt et al. (1984) and Villemoes et al. (1993) for pure s- and pure r-process mixtures (corresponding to $f_{\rm odd} = 0.11$ and 0.46 respectively). Hybrid line

lists for $-0.24 \leq f_{\rm odd} \leq 0.46$ were created from these by adjusting the line strengths of the Ba isotopes. Further details on this can be found in Gallagher et al. (2010) but we remind the reader that $f_{\rm odd} = 0.11$ is the lowest value of $f_{\rm odd}$ achieved in the s-process of Arlandini et al. (1999); $f_{\rm odd} = 0.00$ is the lowest value of $f_{\rm odd}$ achievable in an even-only isotope mix, and that values of $f_{\rm odd} < 0.00$ are non-physical, mathematical solutions only.

Isotopic abundances presented in Arlandini et al. (1999) which we use to determine $f_{{\rm odd},r}$ and $f_{{\rm odd},s}$ were normalised (by Arlandini et al., 1999) to the s-process-only isotope ^{150}Sm. We explored a renormalisation to ^{134}Ba and ^{136}Ba, but found little to no change in $f_{{\rm odd},r}$: 0.49 (renormalised to ^{134}Ba) and 0.46 (renormalised to ^{136}Ba). The renormalisation does not affect $f_{{\rm odd},s}$, which remains $f_{{\rm odd},s} = 0.11$. This does not significantly alter the interpretation of the results presented here.

No attempt was made to determine $f_{\rm odd}$ for the 4934 Å line because, as showed by Gallagher et al. (2010), analysis of this line is extremely difficult and yields large errorbars due to Fe blends found in the wings of this line. Nor do we attempt to study higher excitation lines of Ba, as their hyperfine splitting is much smaller than that at 4554 Å.

4.3.2 Determination of the macroturbulence

To recap on Gallagher et al. (2010), we use a χ^2 code (derived from that of García Pérez et al. (2009)) to compare the observed and synthetic spectra of a number of Fe I and Fe II lines, computed for different abundances A(Fe)[3], wavelength shifts $\Delta\lambda$, and line broadening parameters. Two different broadening approaches are used, as described below. We derive, for each Fe line analysed, the best fitting abundance, wavelength shift and broadening. An ordinary least squares (OLS) fit is calculated through the wavelength-dependence of broadening and A(Fe) values to determine the best values at 4554 Å.

[3] $A(\mathrm{X}) = \log_{10}\left(\frac{N(\mathrm{X})}{N(\mathrm{H})}\right) + 12$.

Gaussian broadening

One approach to the macroscopic broadening is to adopt a Gaussian of $FWHM = v_{\rm conv}$, representing the convolution of a Gaussian instrumental profile with a Gaussian macroturbulent profile. As Lambert & Allende Prieto (2002) show, $f_{\rm odd}$ is extremely sensitive to $v_{\rm conv}$. They found $\delta f_{\rm odd}/\delta v_{\rm conv} = -0.51\,({\rm km\,s^{-1}})^{-1}$ for HD 140283. Gallagher et al. (2010) found an even larger sensitivity, $-0.7\,({\rm km\,s^{-1}})^{-1}$. The effects of this large sensitivity can be reduced by increasing the number of Fe lines, N, used to constrain $v_{\rm conv}$, as we take the error in $v_{\rm conv}$ as the standard error, $\sigma/\sqrt{N}$, where σ is the standard deviation of $v_{\rm conv}$ values. In our work, only Fe lines of comparable equivalent widths (W) to the Ba II line are selected, so they would have similar formation depths to the Ba line, implying that macroturbulent effects on Ba would be well described by Fe. We also do not analyse strong lines where uncertain pressure effects in the line broadening become significant.

The adopted atmospheric parameters for each star are listed in Table 4.3 (rows (1) to (5)) and the derived broadening is given in row (7).

Radial-tangential macroturbulent broadening

In Gallagher et al. (2010) we compared three different broadening techniques to find out which of them best fit the Fe lines. We found that using a rotational broadening mechanism, where the macroturbulent broadening of the star was represented by $v \sin i$ only (with the instrumental broadening still represented by a Gaussian), almost always gave a worse fit than when we employed a simple Gaussian. However we found that using a radial-tangential macroturbulent broadening technique ($\zeta_{\rm RT}$) allowed us to fit spectral lines slightly better than the Gaussian mechanism. As a result, we have continued to employ this broadening type in the current investigation for all five stars and again for HD 140283, as well as the simple Gaussian approach. The prescription we adopt for $\zeta_{\rm RT}$ assumes equal speeds in the radial and tangential flows, and equal temperatures (Gray, 2008).

The model spectra were synthesised with ATLAS using a grid of $\zeta_{\rm RT}$ values ranging

from 4.00 km s^{-1} to 9.00 km s^{-1} in steps of 0.2 km s^{-1}. The instrumental broadening, determined from ThAr lines, and represented as a Gaussian, was also included in the synthesis. Each line was fit using the same χ^2 code that was used in §4.3.2. Results for $\zeta_{\rm RT}$ can be found in Table 4.3 (rows (17) to (24)), where we have also listed the number of lines that are best fit by the $\zeta_{\rm RT}$ approach for each star.

4.3.3 The isotopic fraction of barium

Once $v_{\rm conv}$ and $\zeta_{\rm RT}$ were obtained for the two broadening mechanisms, the Ba II 4554 Å line was analysed using a χ^2 code very similar to the one described in §4.3.2 to find values for the free parameters $\Delta\lambda$, A(Ba) and $f_{\rm odd}$ that minimise χ^2 for the 4554 Å line in each star. Results for $f_{\rm odd}$ for Gaussian and radial-tangential broadening techniques can be found in Table 4.3. The best fit Ba profiles are shown in Fig. 4.1 (Gaussian) and in Fig. 4.2 (radial-tangential). From the Gaussian results we find for HD 122563, HD 88609, HD 84937, BD−04° 3208 and BD+26° 3578 that $f_{\rm odd} = -0.12\pm0.07$, -0.02 ± 0.09, -0.05 ± 0.11, 0.18 ± 0.08 and 0.08 ± 0.08 respectively. These results would suggest that all stars examined here show a high s-process fraction.

4.3.4 The [Ba/Eu] ratio

In our sample only the two giants had Eu line strengths adequate to conduct a Eu abundance analysis. This was done by examining the Eu II 4129 Å line. The Eu II 4205 Å line is not used in this study as it is blended with a V II line (Honda et al., 2006; Gallagher et al., 2010) that can affect abundance determinations. Also no attempt is made to analyse the isotopic splitting of ^{151,153}Eu; we assume a fixed 50:50 isotopic split of 151:153 when constructing the hfs-affected Eu 4129 Å line list. The Eu line list for the solar r- and s-process ratio was constructed using hfs information from Becker et al. (1993) and Krebs & Winkler (1960) with $\log gf$ values taken from Biemont et al. (1982). Abundances for Eu are taken as those that satisfy the χ^2 minimum. From these abundances, and those found by the Ba analysis, [Ba/Eu] was calculated and the results for both stars can be found in Table 4.3, row (10).

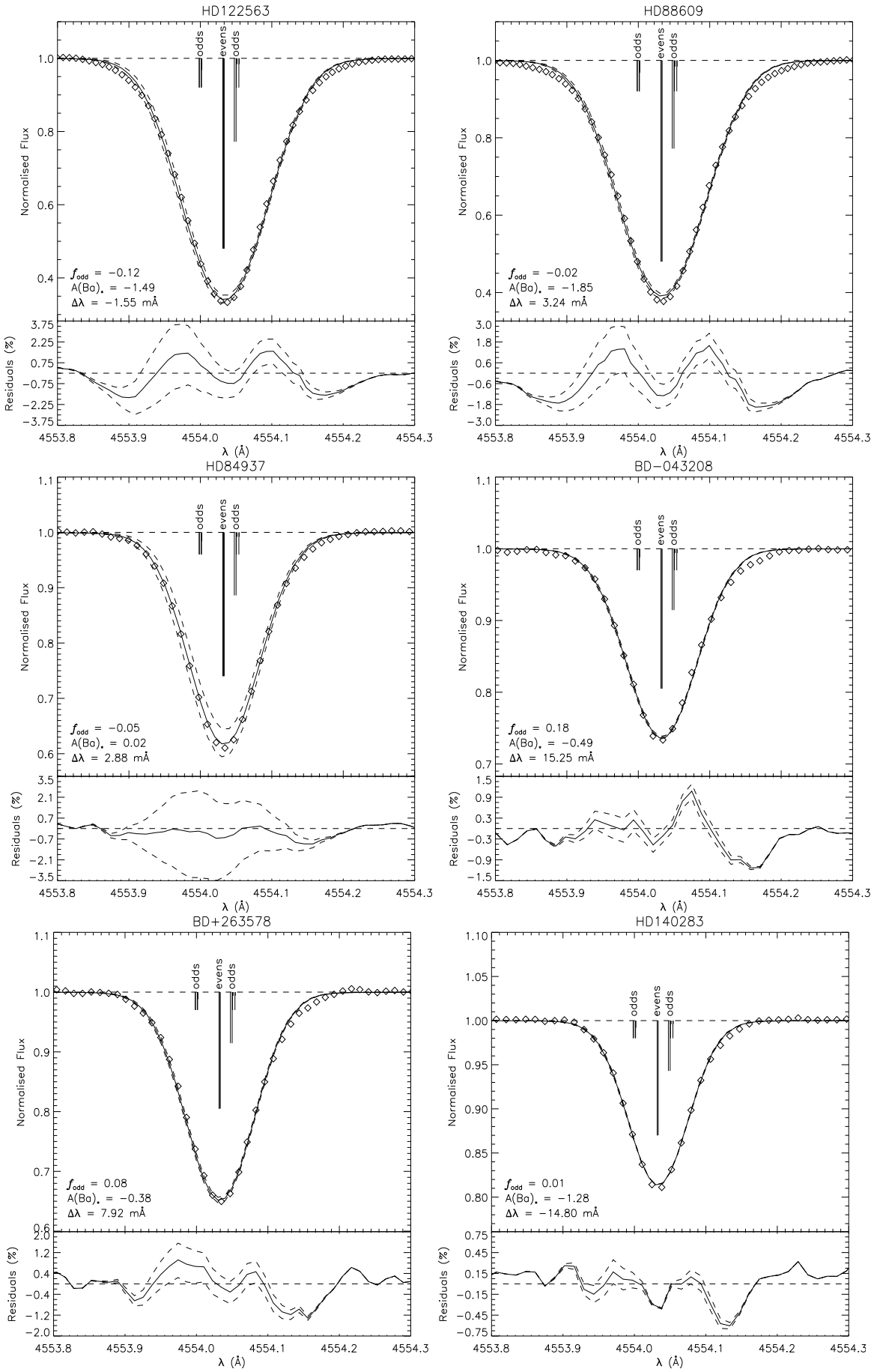

Fig. 4.1: The best fit Ba II 4554 Å lines for each star, using a Gaussian broadening technique. Each figure displays the observed Ba profile (diamonds) and the best fit synthetic profile (solid line), which includes the error on $f_{\rm odd}$ (dashed line). We have also included a schematic of the odd and even isotopes for reference. The lower panel of each figure shows the residuals (obs-syn) of each fit as a percentage. For reference we have included HD 140283, which was analysed in Gallagher et al. (2010).

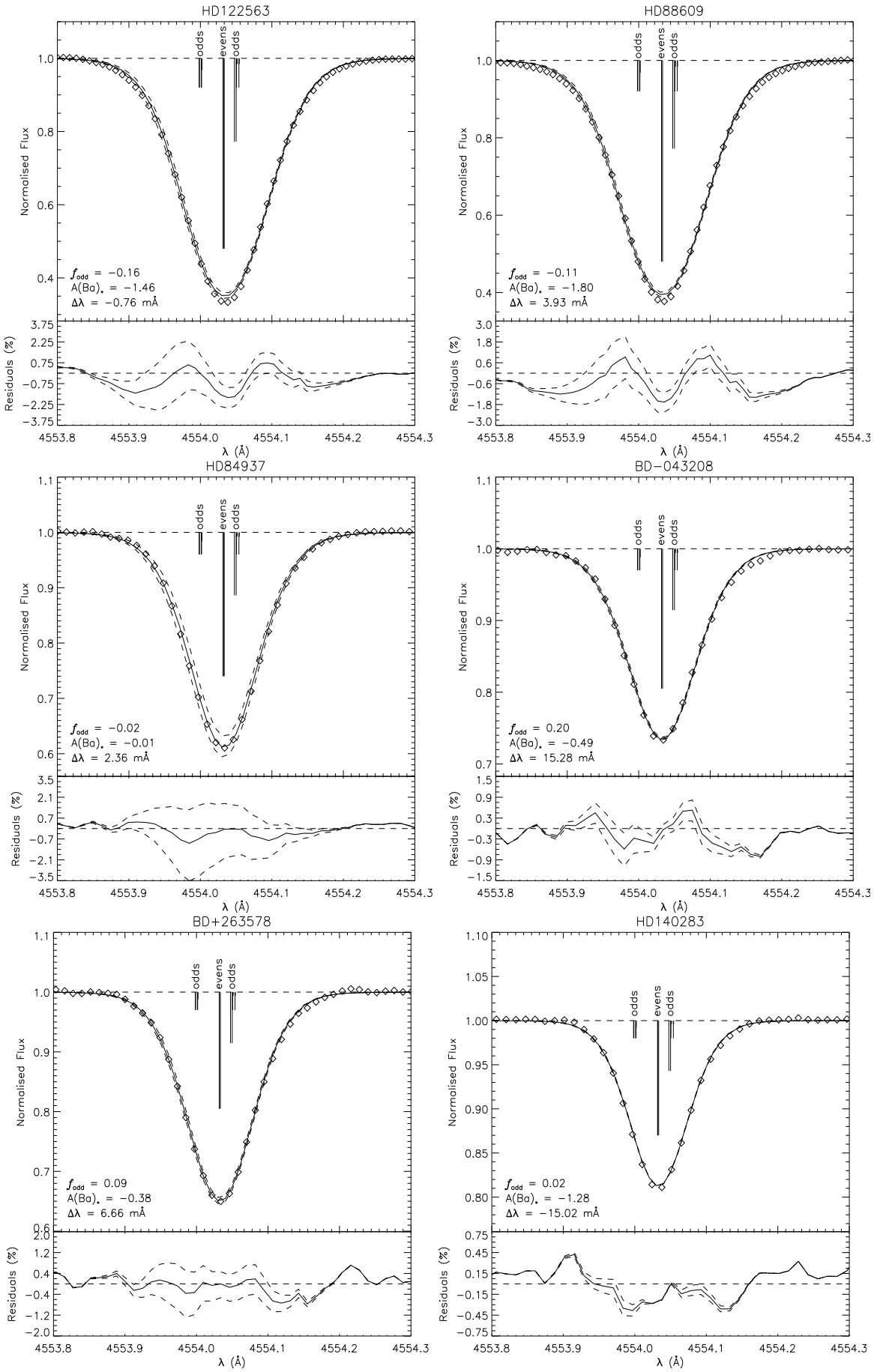

Fig. 4.2: The best fit Ba II 4554 Å lines for each star, using a radial-tangential broadening technique. Each figure displays the observed Ba profile (diamonds) and the best fit synthetic profile (solid line), which includes the error on $f_{\rm odd}$ (dashed line). We have also included a schematic of the odd and even isotopes for reference. The lower panel of each figure shows the residuals (obs-syn) of each fit as a percentage.

Table 4.3: Results of the 1D LTE analysis conducted on six metal-poor stars and the various parameters used in their analysis.

	Parameter	HD 122563	HD 88609	HD 84937	BD−04° 3208	BD+26° 3578	HD 140283
				Atmospheric Parameters			
(1)	$T_{\rm eff}$ (K)	4570 ± 100	4550 ± 100	6290 ± 100	6340 ± 100	6240 ± 100	5750 ± 100
(2)	$\log g$ (cm s^{-1})	1.1 ± 0.3	1.1 ± 0.3	3.9 ± 0.3	4.0 ± 0.2	3.9 ± 0.2	3.7 ± 0.1
(3)	[Fe/H]	-2.77 ± 0.19	-3.07 ± 0.20	-2.15 ± 0.30	-2.28 ± 0.20	-2.33 ± 0.20	-2.50 ± 0.20
(4)	ξ (km s^{-1})	2.2 ± 0.5	2.4 ± 0.5	1.2 ± 0.3	1.5 ± 0.2	1.5 ± 0.2	1.4 ± 0.1
(5)	Atmosphere Reference	(1)	(2)	(3)	(4)	(4)	(5)
				Gaussian broadening			
(6)	$f_{\rm odd}$	-0.12 ± 0.07	-0.02 ± 0.09	-0.05 ± 0.11	0.18 ± 0.08	0.08 ± 0.08	0.02 ± 0.06
(7)	$v_{\rm conv}$ (km s^{-1})	6.99 ± 0.07	7.03 ± 0.08	6.98 ± 0.06	6.62 ± 0.05	6.41 ± 0.06	5.75 ± 0.02
(8)	[Fe/H]	-2.90 ± 0.17	-3.17 ± 0.17	-2.24 ± 0.11	-2.42 ± 0.11	-2.45 ± 0.12	-2.59 ± 0.09
(9)	[Ba/Fe]	-0.85 ± 0.21	-0.91 ± 0.21	0.04 ± 0.15	-0.20 ± 0.15	-0.06 ± 0.16	-0.87 ± 0.14
(10)	[Ba/Eu]	-0.20 ± 0.15	-0.47 ± 0.15	···	···	···	> -0.66
(11)	$\langle \Delta\lambda \rangle$ (mÅ)	-15.86 ± 0.37	-14.70 ± 0.90	-14.69 ± 0.53	-11.47 ± 1.093	-13.29 ± 0.89	-12.67 ± 0.48
(12)	$\delta f_{\rm odd}/\delta v_{\rm conv}$ (km s^{-1})$^{-1}$	-0.57	-0.74	-0.89	-0.78	-0.77	-0.7
(13)	$\delta f_{\rm odd}/\delta \xi$ (km s^{-1})$^{-1}$	-0.08	-0.08	0.05	0.05	0.05	0.05
(14)	$\delta f_{\rm odd}/\delta T_{\rm eff}$ (100 K)$^{-1}$	-0.04	-0.05	-0.03	-0.02	-0.02	-0.02
(15)	$\delta f_{\rm odd}/\delta \log g$ (dex)$^{-1}$	0.02	0.02	-0.27	-0.23	-0.23	-0.28
(16)	$\delta f_{\rm odd}/\delta E_\gamma$ (0.7)$^{-1}$	-0.02	-0.02	-0.05	-0.04	-0.04	···
				Radial Tangential broadening			
(17)	$f_{\rm odd}$	-0.16 ± 0.05	-0.11 ± 0.07	-0.02 ± 0.10	0.20 ± 0.10	0.09 ± 0.10	0.02 ± 0.04
(18)	$\zeta_{\rm RT}$ (km s^{-1})	5.69 ± 0.09	5.74 ± 0.09	5.77 ± 0.08	5.36 ± 0.06	5.14 ± 0.07	4.30 ± 0.02
(19)	$v_{\rm inst}$ (km s^{-1})	3.32	3.32	3.20	3.20	3.20	3.32
(20)	number of best fit Fe lines	53	34	30	28	32	58
(21)	$\delta f_{\rm odd}/\delta \zeta_{\rm RT}$ (km s^{-1})$^{-1}$	-0.30	-0.64	-0.60	-0.73	-0.70	-0.63

continues on next page...

continued from previous page...

	Parameter	HD 122563	HD 88609	HD 84937	BD−04° 3208	BD+26° 3578	HD 140283
(22)	$\delta f_{\rm odd}/\delta\xi$ $(\mathrm{km\,s^{-1}})^{-1}$	−0.08	−0.08	0.05	0.05	0.05	0.00
(23)	$\delta f_{\rm odd}/\delta T_{\rm eff}$ $(100\ \mathrm{K})^{-1}$	−0.01	−0.001	−0.05	−0.07	−0.06	0.01
(24)	$\delta f_{\rm odd}/\delta\log g$ $(\mathrm{dex})^{-1}$	−0.01	−0.02	−0.18	−0.22	−0.21	−0.35
	Other spectral information						
(25)	Spectral range (Å)	3080 - 4780	3070 - 4780	4130 - 6860	4130 - 5340	4050 - 5250	4100 - 6900
(26)	Fe line sample size	54	35	44	36	37	93
(27)	$W_{\rm Ba}$ (m$\mathring{A}$)	99.1	93.2	49.7	34.7	42.7	20.1

(1) Honda et al. (2006).
(2) Honda et al. (2007).
(3) Aoki et al. (2009).
(4) García Pérez et al. (2009).
(5) Gallagher et al. (2010).

4.3.5 Error analysis

In Gallagher et al. (2010) we demonstrated how altering one stellar parameter can force other parameters, in particular $v_{\rm conv}$, to compensate for its effect on $f_{\rm odd}$. In that paper we called this case 1. The compensation by $v_{\rm conv}$ was well illustrated when one looked at the effects of changing the microturbulence (ξ). Once $v_{\rm conv}$ was recalculated from the Fe lines, the effect ξ had on $f_{\rm odd}$ was nullified. As $v_{\rm conv}$ partially compensates for other changes in the stellar parameters as well, i.e. $T_{\rm eff}$ and $\log g$, their effect on $f_{\rm odd}$ is also reduced.

To calculate the error in $f_{\rm odd}$ we look at five possible sources of error: $v_{\rm conv}$, ξ, $T_{\rm eff}$, $\log g$ and the Unsöld approximation enhancement factor, E_γ, which enhances the effect of $\gamma_{6,\rm vdW}$ in the Van Der Waals calculation, $\gamma_6 = \gamma_{6,\rm vdW} E_\gamma$. In our analysis we have used $E_\gamma = 2.2$. To test the effect it has on $v_{\rm conv}$ and $f_{\rm odd}$ we have decreased this to 1.5. The effect of uncertainties in [Fe/H] on $f_{\rm odd}$ is negligible and as such was ignored (Gallagher et al., 2010). It is expected that every star belonging to the same stage of evolution, i.e. giant, sub-giant and turn-off, would reproduce comparable sensitivities to each stellar parameter. As such we have run each test for two of the five stars: to test the sensitivity of $f_{\rm odd}$ in the giants we have used HD 88609, and for the turn-off stars we have chosen BD-04° 3208. However, we have run sensitivity tests of $v_{\rm conv}$ and $\zeta_{\rm RT}$ for all stars as these parameters have the largest effect on $f_{\rm odd}$. The results of the sensitivity of $f_{\rm odd}$ can be seen in Table 4.3, rows (12) to (16) and rows (21) to (24). The tests confirm that the $f_{\rm odd}$ determinations are essentially unaffected by the choice of E_γ, $T_{\rm eff}$ or ξ, but $\log g$ and the macroturbulent broadening effects are more important. It has been reported by Tajitsu et al. (2010) that the EEV 42-80 CCDs used in the HDS suffer from nonlinearity. By investigating the differences between the corrected and non-corrected spectra, we found that its effect on $f_{\rm odd}$ was negligible.

4.4 1D NLTE Fe line analysis

In Gallagher et al. (2010) we aimed to constrain the macroturbulence of HD 140283 through the use of the Fe lines. Using the same method, we have also done this for five

further stars in §4.3. This was done under the assumptions of LTE. However, it is well known that Fe I suffers from the effects of NLTE (Thévenin & Idiart, 1999; Shchukina et al., 2005) in metal-poor stars. We therefore sought to quantify NLTE effects for Fe on the preceding analysis, in particular on the determination of macroturbulence, and therefore the value of $f_{\rm odd}$. No attempt is made to determine NLTE corrections for Ba itself, either in $f_{\rm odd}$ or the [Ba/Eu] ratio. Mashonkina et al. (2008) demonstrated that corrections to the abundance ratio are not significant enough to change the inferred r- and s-process regime in a star. The determination of $f_{\rm odd}$ assuming NLTE goes beyond the scope of the work presented in this section.

To compute the Fe I profiles, a version of the NLTE code MULTI (Carlsson, 1986) was used with modifications to include the effects of line-blanketing, described in Collet et al. (2005). The code employs MARCS model atmospheres. The model atom used was that adopted by Hosford et al. (2010). For a longer discussion on the model atom, processes of NLTE radiative transfer and its impact on stars of this type, see Hosford et al. (2010). It is important, however, to mention the parameter $S_{\rm H}$, the scaling factor for the collisions due to H as described by the approximate Drawin formula (Drawin, 1968, 1969). Due to the uncertainties in the magnitude of the H collisions, the value of $S_{\rm H}$ is still uncertain and is treated differently by different works. Collet et al. (2005) treats it as a free parameter and tests values $S_{\rm H} = 1$ and 0.001. Korn et al. (2003) found a higher value, $S_{\rm H} = 3$, however in more recent work (Mashonkina et al., 2010) the same group has constrained it to 0.1 based on an improved Fe atom. Here we adopt the values 1 and 0.001; this gives us two sets of synthetic spectra, one with the Drawin ($S_{\rm H} = 1$) description of H collisions, and a second close to maximal NLTE effects ($S_{\rm H} = 0.001$). We also compute line profiles in LTE using MULTI.

NLTE calculations of Fe I line profiles were performed for two stars, the subgiant HD 140283 and the giant HD 122563. The first was analysed so a comparison could be made between this work and the LTE analysis of Gallagher et al. (2010). The second was analysed to understand the NLTE effects on Fe I in giants, where the atmospheres are more tenuous and also cooler, to act as a comparison to the LTE work in this paper.

Three sets of MULTI runs were completed for each star, one in LTE, and two in

NLTE with the $S_{\rm H}$ values mentioned above. A χ^2 analysis procedure similar to the one described in §4.3 has been used. Synthetic profiles were created over the parameter space shown in Table 4.4. The extrinsic broadening was represented by a Gaussian consolidating both macroturbulence and instrumental broadening, the values $FWHM_{\rm G}$ in Table 4.4 representing the $FWHM$ of the Gaussian.

Table 4.4: Ranges of parameters used to create the synthetic profiles in MULTI.

		χ^2 grid parameter ranges		
		A(Fe)	$FWHM_{\rm G}$	$\Delta\lambda$
Star	Run		(mÅ)	(mÅ)
HD 140283	$\rm LTE_{MULTI}$	$4.28 - 5.28$	$73 - 119$	±25
	$S_{\rm H} = 1$	$4.66 - 5.28$	$73 - 119$	±25
	$S_{\rm H} = 0.001$	$5.00 - 5.70$	$73 - 119$	±25
HD 122563	$\rm LTE_{MULTI}$	$4.00 - 5.58$	$74 - 114$	±25
	$S_{\rm H} = 1$	$4.00 - 5.58$	$74 - 114$	±25
	$S_{\rm H} = 0.001$	$4.68 - 5.50$	$74 - 114$	±25

The intention was to see if the observed Fe I profiles could be better fit by spectra computed in NLTE, in particular for the giants, where the cooler atmospheres result in larger line strengths (at fixed [Fe/H]). Here, the synthetic LTE core is too shallow and the wings too broad even at the minimum χ^2 value of the line. In switching to NLTE, we hoped we might model the Fe lines better, and hence obtain better values of macroturbulent broadening and, in later works, a more reliable value of $f_{\rm odd}$ for Ba.

Table 4.5 gives the results from the χ^2 analysis using MULTI, and the ATLAS LTE results for comparison. The MULTI values are the mean of 51 lines for HD 140283 and 31 lines for HD 122563; errors are the standard error. Fewer lines are used in the MULTI analysis than in the ATLAS LTE analysis due to the incompleteness of the adopted model atom which leads to several of the lines not being computable in MULTI. Also, after further scrutinizing the results, three lines from HD 140283 and three lines from HD 122563 were removed from the analysis. This was due to either a poorly defined continuum, or blending lines very close to the line of study.

A comparison of MULTI LTE and ATLAS LTE results shows that the abundances and extrinsic broadening value are comparable for both cases, the only exception be-

Table 4.5: Results from the NLTE analysis and the ATLAS LTE results for comparison.

Star	Run	$\langle A(\mathrm{Fe})\rangle$	$\langle v_{\mathrm{conv}}\rangle$ (km s^{-1})
HD 140283	$\mathrm{LTE_{MULTI}}$	4.96 ± 0.01	6.03 ± 0.04
	$S_{\mathrm{H}} = 1$	5.28 ± 0.01	5.98 ± 0.05
	$S_{\mathrm{H}} = 0.001$	5.53 ± 0.01	5.92 ± 0.04
	$\mathrm{LTE_{ATLAS}}$ (51 line subset)	4.92 ± 0.04	5.76 ± 0.09
	$\mathrm{LTE_{ATLAS}}$ (93 lines)	4.91 ± 0.01	5.75 ± 0.02
HD 122563	$\mathrm{LTE_{MULTI}}$	4.58 ± 0.03	7.02 ± 0.10
	$S_{\mathrm{H}} = 1$	4.98 ± 0.03	6.95 ± 0.09
	$S_{\mathrm{H}} = 0.001$	5.12 ± 0.03	6.91 ± 0.09
	$\mathrm{LTE_{ATLAS}}$ (31 line subset)	4.54 ± 0.11	7.06 ± 0.18
	$\mathrm{LTE_{ATLAS}}$ (54 lines)	4.51 ± 0.04	6.99 ± 0.07

ing the broadening values of HD 140283, which is the most important parameter as it directly affects f_{odd}. For HD 140283 we have larger values in NLTE than that of Gallagher et al. (2010). Table 4.5 shows that for HD 140283, choosing the same 51 line subset doesn't "fix" the discrepancy. For HD 122563 the difference is much smaller and is within the errors. One could naively ascribe this difference to be discrepancies in the MARCS and KURUCZ model atmospheres, e.g. different temperature gradients and density gradients. However, a comparison between the MARCS and KURUCZ model atmospheres can be found in Hosford (2010), who found little to no effect by these parameters. It is most likely that the differences arise from the different treatments of the broadening itself in MULTI and ATLAS. We see comparable wavelength shifts between the two analyses, and comparable profiles for each line. In NLTE we see an increase of abundance with decreasing S_{H} due to the overionisation effects becoming more pertinent; thus a larger positive abundance is needed for neutral lines to compensate. As a consistency check, NLTE abundances from the χ^2 analysis were compared to those from an equivalent width analysis and were found to be comparable at each S_{H} value.

An interesting thing to note here is the sensitivity of v_{conv} to the S_{H} value and the

difference between LTE and NLTE values. For both stars, $v_{\rm conv}$ decreases by 0.1 km s^{-1} in going from MULTI LTE to MULTI $S_{\rm H} = 0.001$. Naively, one might infer from Table 4.3 that this would increase $f_{\rm odd}$ from an LTE analysis of Ba 4554 Å between 0.06 and 0.09. However, some of this difference may not fully apply to Ba calculated in LTE, due to different broadening under NLTE. Nonetheless, it points to the importance of an accurate description of the radiative transfer if one is to be able to determine $f_{\rm odd}$.

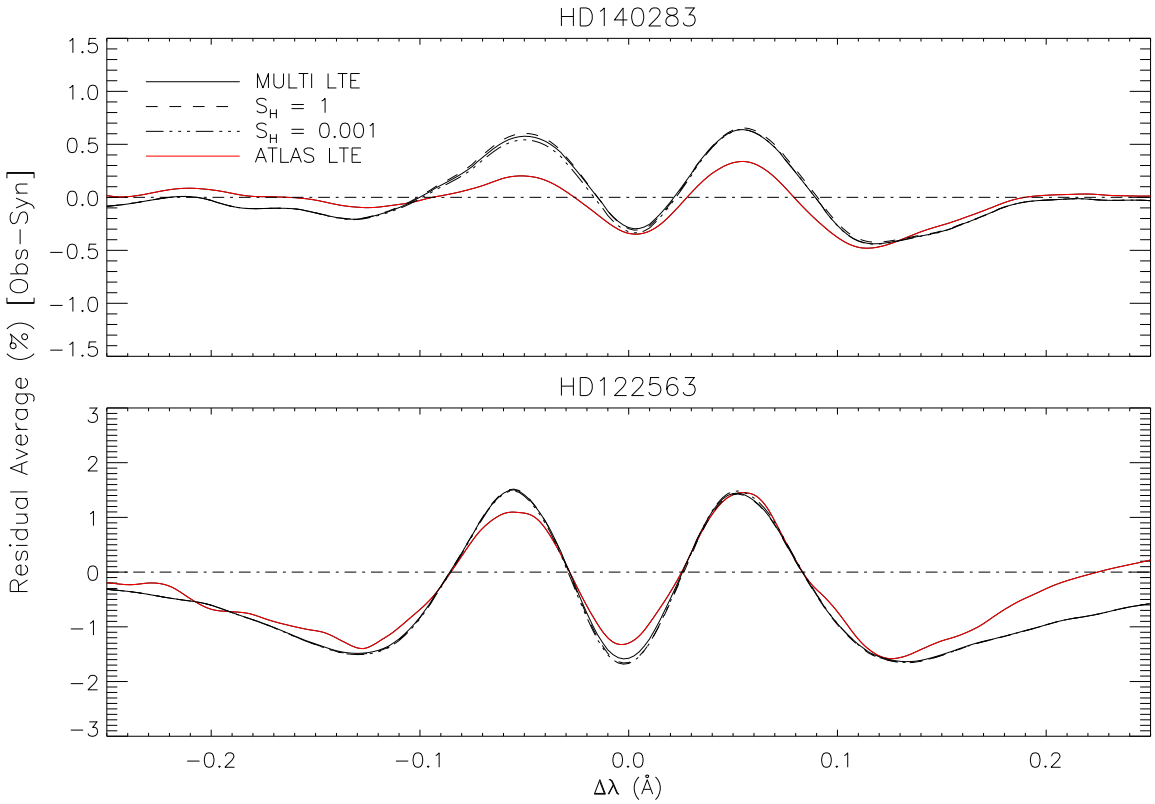

Fig. 4.3: Plots of average residuals from χ^2 analysis of Fe lines in HD 140283 and HD 122563, for $S_{\rm H} = 1$, 0.001 and LTE using MULTI. For comparison we have generated the same plot using ATLAS output data for the same subsets of lines.

One hope of the NLTE analysis was that it may aid in fitting the stronger Fe lines of the giant by producing more realistic line profiles, and hence reduce the residuals in the Fe analysis (see Gallagher et al., 2010, their Fig. 10). In Fig. 4.3 we regenerate the plot of average residuals for HD 140283 using a MULTI analysis of 51 Fe lines. We have co-added the residuals from each Fe line to smooth out any unique line defects. The residuals are of similar magnitude to those from Gallagher et al. (2010) and have similar features. Most importantly, the MULTI residuals for NLTE with different $S_{\rm H}$

values and for LTE are all very similar. There is in fact a very slight worsening of the core fit with increased NLTE effects. It is also seen that the residuals for HD 122563 are of a similar form, albeit with a greater magnitude. The lines analysed in HD 122563 are far stronger than those in HD 140283. As the lines become stronger, they become harder to fit precisely, but using NLTE profiles has no effect on improving this.

The fact that the MULTI NLTE analysis has led to no improvement over the MULTI LTE analysis in the fit of the Fe lines is not entirely surprising. In fact when compared to the ATLAS analysis for the same subset of Fe lines (seen in red) there is a considerable worsening of the residuals, particularly for HD 140283, although NLTE effects were still important to investigate. The effects of NLTE on Fe I in metal-poor stars are dominated by overionisation. To a first approximation, the populations of neutral Fe energy levels can be seen as following a Boltzmann distribution relative to one another, but with a shift in the ionization equilibrium. The results show that this does not affect the shape of the profiles, though for a given equivalent width the abundance needed to reproduce the line increases. The other main NLTE effect, a change in the line and continuum opacities with height in the atmospheres, apparently has little overall effect on the Fe I line profiles.

In summary, NLTE effects in Fe affect $v_{\rm conv}$ by up to $\sim 0.1\,{\rm km\,s^{-1}}$, and may affect $f_{\rm odd}$ for Ba up to 0.06 or 0.09, but NLTE does not result in a *better* fit to the Fe lines (Fig. 4.3). Other mechanisms may come into play, e.g. as represented by 3D model atmospheres. It would still be interesting to see, however, how a NLTE treatment of Ba affects the inferred $f_{\rm odd}$.

4.5 Discussion

With the exception of one star, BD-04° 3208, all of the stars analysed in this paper and HD 140283, which was studied in detail in Gallagher et al. (2010), show a non-physical isotope ratio ($f_{\rm odd} < 0.11$) close to the s-process-only composition. The non-physical results for $f_{\rm odd}$ suggest that applying a 1D LTE treatment to analyse the isotopic fraction of the Ba 4554 Å line does not appear to be very robust. There are several

possibilities why this might be the case, and a few possible solutions to the problem, which we now discuss.

Alternative broadening techniques

We have shown that $f_{\rm odd}$ has a high sensitivity to $v_{\rm conv}$, which we have determined by fitting synthetic 1D LTE (and in §4.4, NLTE) profiles to Fe lines. There are several reasons why we chose to use Fe lines. Firstly they are the most abundant species in a metal-poor spectrum and cover a considerable range in line strength. As mentioned above, these two attributes are useful because they allow us to use lines that form at similar depths to the Ba line. However, we revisit this argument and consider whether Fe is a sensible atomic species to use to determine the macroturbulence of another species.

To test this hypothesis, we analysed several Ca I lines in the star with the best quality stellar spectrum, HD 140283 (S/N = 1100), using the same techniques described in §4.3. Only seven lines were found to be unblended and to have similar strengths to the Ba line ($10 \leq W$ (m$\AA$) ≤ 50). This meant that the standard error in $v_{\rm conv}$ was much larger for this set of lines than was found for the 93 Fe lines we used in Gallagher et al. (2010). We found that $\langle v_{\rm conv} \rangle_{\rm Ca} = 5.63 \pm 0.13$ km s^{-1}. This is a smaller value than was determined using Fe lines (5.75 ± 0.02 km s^{-1}) but still within the 1σ error, and the statistics of using only seven lines meant that by using Ca we would greatly increase the uncertainty in $f_{\rm odd}$. Nevertheless it was found that $f_{\rm odd}$, which from the Fe analysis was found to be 0.01 ± 0.06 (in the 4554 Å line[4]), would move higher to 0.10 ± 0.11. We can not say whether Ca is a better atomic species to use than Fe as the spread in $v_{\rm conv}$ is too high.

To avoid using other elements to constrain the macroturbulent broadening of Ba, we experimented by treating $v_{\rm conv}$ as a free parameter whilst determining $f_{\rm odd}$, thus deriving it from the Ba line. This was done for all six stars in this study. Results are shown in Table 4.6. In Table 4.6 we also give the standard deviation (s.d.) of the Fe line measurements, as an indication of the uncertainty associated with the measurement of

[4]Table 4.3 lists $f_{\rm odd}$ as calculated by both the 4554 and 4934 Å lines for HD 140283.

Table 4.6: Values of $v_{\rm conv}$ (measured in km s^{-1}) as determined from Fe lines and directly by the Ba II 4554 Å line. Note that we cannot calculate $f_{\rm odd}$ in BD+26° 3578 when we employ $v_{\rm conv}$ (Ba).

Star	$v_{\rm conv}$ (Fe)	s.d. (Fe)	$f_{\rm odd}$ (Fe)	$v_{\rm conv}$ (Ba)	$f_{\rm odd}$ (Ba)
HD 122563	6.99	0.54	−0.12	6.82	−0.04
HD 88609	7.03	0.45	−0.02	6.98	0.01
HD 84937	6.98	0.41	−0.05	6.92	−0.03
BD−04° 3208	6.62	0.32	0.18	6.88	−0.01
BD+26° 3578	6.41	0.34	0.02	8.85	···
HD 140283	5.75	0.19	0.01	6.06	−0.23

just one line, e.g. Ba 4554 Å. As shown, $v_{\rm conv}$ is little changed (within 1 s.d.) in four stars when using just the Ba line, and within 2 s.d. in a fifth star, and therefore there is little change to $f_{\rm odd}$. It is interesting to note that two of the turn-off stars and the subgiant, HD 140283, are found to have higher $v_{\rm conv}$ values, driving smaller $f_{\rm odd}$ (more non-physical) ratios though in all cases the differences in $v_{\rm conv}$ are comparable to the uncertainty expected for one measurement. It is therefore still unclear whether the Fe analysis does describe the Doppler broadening for Ba well or not, but there is not strong evidence against it.

As well as testing whether Fe was an adequate species to use, we also considered whether a simple Gaussian adequately describes macroturbulent broadening. In Gallagher et al. (2010) we showed that a $\zeta_{\rm RT}$ macroturbulent broadening mechanism better fit several Fe lines than a Gaussian. Therefore we employed a $\zeta_{\rm RT}$ treatment for each star analysed in this investigation (§4.3.2, Fig. 4.2, and Table 4.3). It was found that for the giant stars, a radial-tangential fit the Fe lines better, with only one line in each spectrum better fit by a Gaussian. We found that for the three turn-off stars a $\zeta_{\rm RT}$ technique fit 68% − 86% of Fe lines better. This demonstrates a clear reason to consider using $\zeta_{\rm RT}$ when working in 1D LTE over a Gaussian broadening mechanism. This is particularly clear with the giant stars, whose Fe line cores are closer to saturation causing the wings to become more significant. Examination of the residual plots in Fig. 4.4 shows further the improvement to the fits when using $\zeta_{\rm RT}$. However we stress to the reader that whilst using such a technique under the assumptions of 1D LTE seems to

improve upon fitting errors associated with using a traditional Gaussian, both are still symmetric profiles and are unable to remedy the issue of asymmetries associated with absorption lines in real stellar spectra.

Fe line residuals

Fig. 4.4 shows the average residuals of the Fe lines used in determining $v_{\rm conv}$ and $\zeta_{\rm RT}$. It illustrates the difficulties in fitting absorption lines with 1D LTE synthetic profiles.

It is seen that the turn-off and subgiant stars have quite an asymmetric residual profile, with particular problems occurring in the red wings, 100 to 130 mÅ from line centre for all four stars. This seems to be caused by underlying assumptions adopted in 1D LTE radiative transfer codes; real absorption lines are not perfectly symmetric.

This investigation is an extension of the asymmetry analysis conducted in Gallagher et al. (2010); the asymmetry seems to occur in all four stars. Severe fitting issues occur in the giant stars, HD 122563 and HD 88609, where the Ba (and hence Fe) line equivalent widths are ~ 90 mÅ (Table 4.3, row (27)) and lines cores begin to saturate so pressure broadening becomes more significant in the wings, and this may explain the symmetric residuals seen at ± 0.14 Å.

New approaches to determine isotope mixtures

It is clear that there is still uncertainty over which atomic species to use to determine $v_{\rm conv}$. However it is more likely that the assumptions that a 1D LTE code adopts, in particular the symmetric broadening mechanisms used in replicating macroscopic turbulence in a star's atmosphere, is a more likely reason for the large residuals, illustrated in Fig. 4.4. In the previous paper we asked, but did not answer, whether 3D hydrodynamical codes could solve these issues. One major drawback of using 3D techniques is the time-scales involved with the both the model atmosphere production, which currently can take several months of computation, and the radiative transfer calculations, which currently take several hours per spectral line synthesis. In addition, 3D hydrodynamics is a rather new field of analysis, and as such there has been very little published to test the reliability of the codes currently available. However it appears

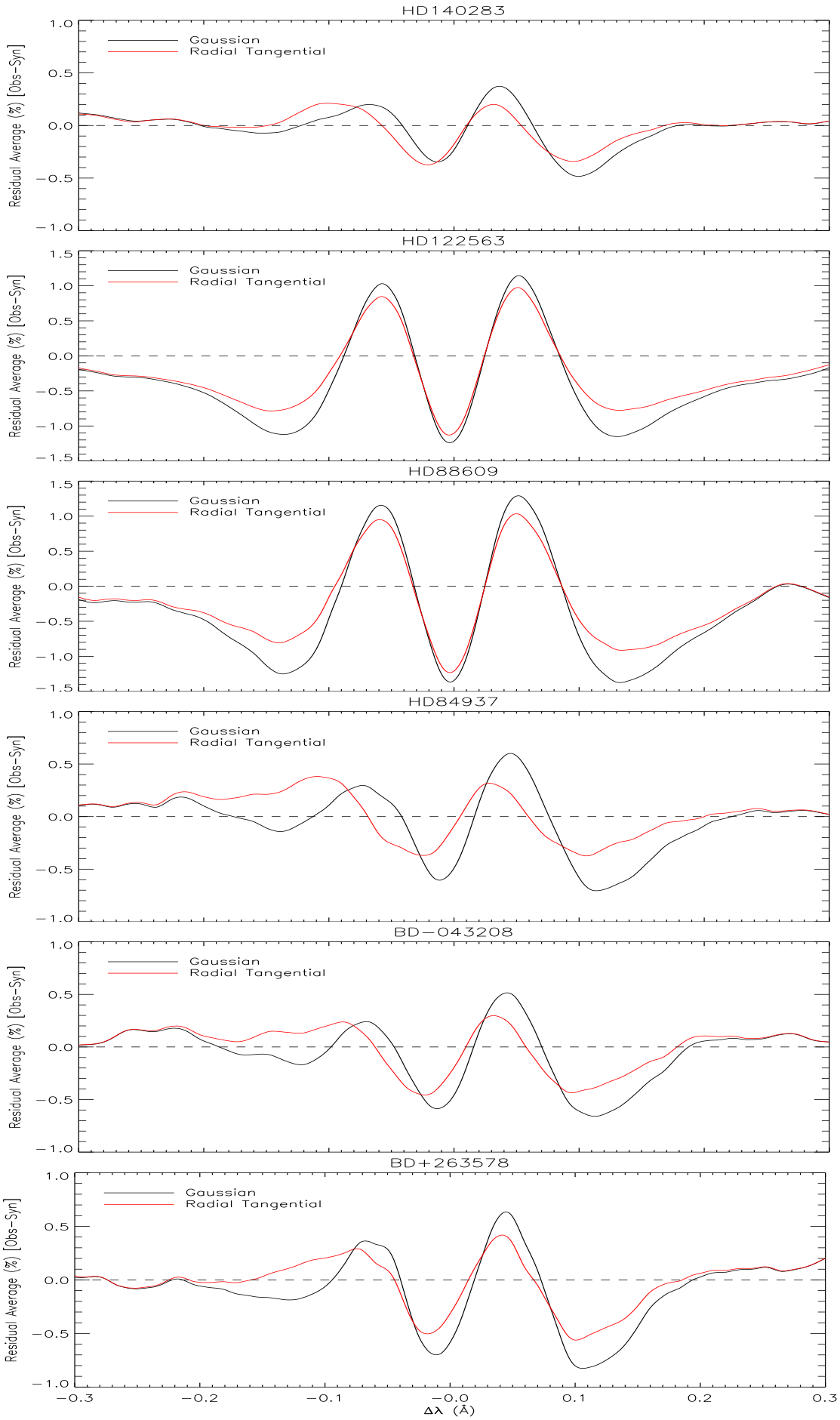

Fig. 4.4: The average residuals of the Fe lines used to constrain $v_{\rm conv}$ and $\zeta_{\rm RT}$.

that 3D hydrodynamics is the next logical step to take in this field (Collet et al., 2009; Ludwig & Kučinskas, 2005) in response to the asymmetric profiles. However, this may not solve the problem of $f_{\rm odd}$ since Collet et al. (2009) found that while the 3D model atmosphere did seem to improve upon asymmetries associated with the Ba 4554 Å absorption line, the result for $f_{\rm odd}$ increased the s-process contribution relative to the 1D LTE result. Therefore, even if adopting a spectral line synthesis code that employs 3D hydrodynamic model stellar atmospheres is the next step to better understanding the problems with fitting absorption lines, it does not yet appear to be able to reduce the high s-process fractions we have found, in fact it would appear using such a technique would enhance the s-process fraction further.

In addition to new approaches in the analysis of isotopic fractions, perhaps a new, more accurate observing technique is required to get the best possible data for this type of complex analysis. Astronomers using precise radial velocities to detect extrasolar planets via the parent star Doppler "wobble" are employing observing procedures to attain Doppler precisions $< 3\,{\rm ms}^{-1}$ by passing the starlight through an iodine (I_2) absorption cell. This allows them to measure very small wavelength shifts, which affect the instrumental profile (Butler et al., 1996). This can be calculated over all wavelength scales and in each short exposure, to determine the instrumental broadening profile at any time.

Aoki et al. (2004) have shown that there is a very slight asymmetry in the ThAr lines recorded with HDS, at least in the HD 140283 observing run, which were used to calculate $v_{\rm inst}$. Using the I_2 method described above, it is possible to deconvolve the instrumental profile from the stellar spectrum, leaving only real stellar broadening in the lines. This would remove most of the uncertainty surrounding the instrumental profile from any subsequent analysis. Issues with this method are the requirement for a stable I_2 cell and the large amount of time that would be required to complete such a complex reduction. In conjunction with a 3D hydrodynamical treatment this might require a lot of time and still may not explain the r- and s-process contributions any better than the method described in this paper. However, it is a method still favoured by astronomers looking for radial velocity fluctuations in stars, as it yields the smallest

error in the spectral data. The difficulty in modelling the Fe lines, let alone Ba, may justify the additional effort required.

4.6 Conclusions

We have carried out a careful examination of the Ba isotopic ratios for five metal-poor stars using a 1D LTE treatment in conjunction with high resolution ($R \equiv \lambda/\Delta\lambda \geq 90\,000$), high signal-to-noise ($S/N \geq 550$) spectra. We found that all stars show a high s-process signature, and only BD−04° 3208 had an $f_{\rm odd}$ value (0.18 ± 0.08) that was physical, $0.11 \geq f_{\rm odd} \geq 0.46$ according to the isotopic abundance determinations by Arlandini et al. (1999). According to these limits, all other stars yield a non-physical isotopic fraction, $f_{\rm odd} < 0.11$.

Using the radiative transfer code MULTI with MARCS 1D model atmospheres, we have also applied a 1D NLTE treatment to Fe lines in HD 122563 and HD 140283. We found that using NLTE did not fit the Fe line cores better, rather it increased the core residual in both stars, see Fig. 4.3. A large NLTE effect ($S_{\rm H} = 0.001$) did, however, reduce $v_{\rm conv}$ by $0.1\,{\rm km\,s^{-1}}$, and may imply an increase of $f_{\rm odd}$ by $\sim 0.06 - 0.09$, which would reduce the non-physicality of the results.

During the investigation we have shown how 1D LTE radiative transfer codes and model atmospheres seem to be inadequate to determine $f_{\rm odd}$. In particular we have shown that asymmetries in the red wings are observed in the Fe line residuals for all four turn-off and subgiant stars, while the two giants have larger, albeit symmetric, residuals. We speculate that spectral line synthesis with 3D hydrodynamic model stellar atmospheres would improve residuals in both the Fe and Ba lines, but we make no predictions as to whether it would improve upon the obvious problems with non-physical isotopic fractions we have encountered here. In addition we have asked, but not answered, whether taking the observations using an I_2 cell, designed to improve accuracy and quality of the data, would help to better constrain $f_{\rm odd}$. Certainly if one compares the error estimation of $f_{\rm odd}$ in HD 140283 (± 0.06, $S/N = 1100$) with HD 84937 (± 0.11, $S/N = 630$), there is almost double the uncertainty in HD 84937

than in HD 140283. We speculate that this could be due to the quality of the spectral data used, however, we acknowledge that this could also be a result of the difference in the number of Fe lines used to determine $v_{\rm conv}$, as we measure error by the standard error. However, $\sigma_{v_{\rm conv},\rm HD\,84937} = 0.06\,\rm km\,s^{-1}$ is fairly typical as an error estimate for these stars, yet $\sigma_{f_{\rm odd}}$ is larger in HD 84937 than in all other stars.

It was found that using a radial-tangential broadening technique rather than a traditional Gaussian improved upon fitting errors for both the Fe and Ba lines. Whilst using such a technique does not remove asymmetries seen in absorption lines for real stellar data, it appears that if one were to adopt a 1D LTE approach to resolve an absorption line, a radial-tangential profile should be used to model the macroturbulence of the star rather than a Gaussian, although a Gaussian could still be used to model the instrumental profile.

We have also conducted a study of Eu abundances in the two giants, HD 122563 and HD 88609. This was used to determine [Ba/Eu] ratios, which are used to assess the star's s- and r-process content. Both stars have [Ba/Eu] ratios that indicate a large r-process contribution, which agrees well with Honda et al. (2006) & Honda et al. (2007), but contradicts the isotope analysis conducted in this paper. This further justifies scepticism of the 1D LTE techniques employed in our Ba isotope analysis.

We have increased the number of stars that have undergone a Ba isotope analysis. However it is difficult to believe that all stars analysed have a significant s-process contribution, or s-process enhancement in contradiction of the (limited) [Ba/Eu] data and the strengths of the Truran (1981) theory and Travaglio et al. (1999) calculations. It is much more likely that the symmetric 1D LTE techniques used in this investigation are inadequate and improvements to isotopic ratio analysis need to be made.

References

Anders, E. & Grevesse, N. 1989, Geochim. Cosmochim. Acta, 53, 197 [ADS]

Aoki, W., Barklem, P. S., Beers, T. C., Christlieb, N., Inoue, S., García Pérez, A. E., Norris, J. E., & Carollo, D. 2009, ApJ, 698, 1803 [ADS]

Aoki, W., Inoue, S., Kawanomoto, S., Ryan, S. G., Smith, I. M., Suzuki, T. K., & Takada-Hidai, M. 2004, A&A, 428, 579 [ADS]

Arlandini, C., Käppeler, F., Wisshak, K., Gallino, R., Lugaro, M., Busso, M., & Straniero, O. 1999, ApJ, 525, 886 [ADS]

Becker, O., Enders, K., Werth, G., & Dembczynski, J. 1993, Phys. Rev. A, 48, 3546 [ADS]

Biemont, E., Karner, C., Meyer, G., Traeger, F., & Zu Putlitz, G. 1982, A&A, 107, 166 [ADS]

Bisnovatyi-Kogan, G. S. & Chechetkin, V. M. 1979, Soviet Physics Uspekhi, 127, 263 [ADS]

Burbidge, E. M., Burbidge, G. R., Fowler, W. A., & Hoyle, F. 1957, Reviews of Modern Physics, 29, 547 [ADS]

Burris, D. L., Pilachowski, C. A., Armandroff, T. E., Sneden, C., Cowan, J. J., & Roe, H. 2000, ApJ, 544, 302 [ADS]

Butler, R. P., Marcy, G. W., Williams, E., McCarthy, C., Dosanjh, P., & Vogt, S. S. 1996, PASP, 108, 500 [ADS]

Carlsson, M. 1986, Uppsala Astronomical Observatory Reports, 33 [ADS]

Collet, R., Asplund, M., & Nissen, P. E. 2009, Publications of the Astronomical Society of Australia, 26, 330 [ADS]

Collet, R., Asplund, M., & Thévenin, F. 2005, A&A, 442, 643 [ADS]

Cottrell, P. L. & Norris, J. 1978, ApJ, 221, 893 [ADS]

Drawin, H.-W. 1968, Zeitschrift fur Physik, 211, 404 [ADS]

Drawin, H. W. 1969, Zeitschrift fur Physik, 225, 483 [ADS]

François, P., Depagne, E., Hill, V., Spite, M., Spite, F., Plez, B., Beers, T. C., Andersen, J., James, G., Barbuy, B., Cayrel, R., Bonifacio, P., Molaro, P., Nordström, B., & Primas, F. 2007, A&A, 476, 935 [ADS]

Gallagher, A. J., Ryan, S. G., García Pérez, A. E., & Aoki, W. 2010, A&A, 523, A24 [ADS]

Gallagher, A. J., Ryan, S. G., Hosford, A., García Pérez, A. E., Aoki, W., & Honda, S. 2012, A&A, 538, A118 [ADS]

García Pérez, A. E., Aoki, W., Inoue, S., Ryan, S. G., Suzuki, T. K., & Chiba, M. 2009, A&A, 504, 213 [ADS]

Gray, D. F. 2008, The Observation and Analysis of Stellar Photospheres [ADS]

Honda, S., Aoki, W., Ishimaru, Y., & Wanajo, S. 2007, ApJ, 666, 1189 [ADS]

Honda, S., Aoki, W., Ishimaru, Y., Wanajo, S., & Ryan, S. G. 2006, ApJ, 643, 1180 [ADS]

Hosford, A. 2010, PhD thesis, University of Hertfordshire [LINK]

Hosford, A., García Pérez, A. E., Collet, R., Ryan, S. G., Norris, J. E., & Olive, K. A. 2010, A&A, 511, A47 [ADS]

Imshennik, V. S. 1992, Soviet Astronomy Letters, 18, 194 [ADS]

Korn, A. J., Shi, J., & Gehren, T. 2003, A&A, 407, 691 [ADS]

Krebs, K. & Winkler, R. 1960, Zeitschrift fur Physik, 160, 320 [ADS]

Lambert, D. L. & Allende Prieto, C. 2002, MNRAS, 335, 325 [ADS]

Ludwig, H.-G. & Kučinskas, A. 2005, in ESA Special Publication, Vol. 560, 13th Cambridge Workshop on Cool Stars, Stellar Systems and the Sun, 319 [ADS]

Magain, P. 1995, A&A, 297, 686 [ADS]

Mashonkina, L., Gehren, T., Shi, J., Korn, A., & Grupp, F. 2010, in IAU Symposium, Vol. 265, IAU Symposium, 197–200 [ADS]

Mashonkina, L., Gehren, T., Travaglio, C., & Borkova, T. 2003, A&A, 397, 275 [ADS]

Mashonkina, L., Zhao, G., Gehren, T., Aoki, W., Bergemann, M., Noguchi, K., Shi, J. R., Takada-Hidai, M., & Zhang, H. W. 2008, A&A, 478, 529 [ADS]

Noguchi, K., Aoki, W., Kawanomoto, S., Ando, H., Honda, S., Izumiura, H., Kambe, E., Okita, K., Sadakane, K., Sato, B., Tajitsu, A., Takada-Hidai, T., Tanaka, W., Watanabe, E., & Yoshida, M. 2002, PASJ, 54, 855 [ADS]

Panov, I. V. & Janka, H.-T. 2009, A&A, 494, 829 [ADS]

Rutten, R. J. 1978, Sol. Phys., 56, 237 [ADS]

Shchukina, N. G., Trujillo Bueno, J., & Asplund, M. 2005, ApJ, 618, 939 [ADS]

Smith, V. V. & Lambert, D. L. 1988, ApJ, 333, 219 [ADS]

Sneden, C., Cowan, J. J., & Gallino, R. 2008, ARA&A, 46, 241 [ADS]

Spite, M. & Spite, F. 1978, A&A, 67, 23 [ADS]

Straniero, O., Chieffi, A., Limongi, M., Busso, M., Gallino, R., & Arlandini, C. 1997, ApJ, 478, 332 [ADS]

Tajitsu, A., Aoki, W. Kawanomoto, S., & Narita, N. 2010, Publications of the National Astronomical Observatory of Japan, 13, 1

Thévenin, F. & Idiart, T. P. 1999, ApJ, 521, 753 [ADS]

Travaglio, C., Galli, D., Gallino, R., Busso, M., Ferrini, F., & Straniero, O. 1999, ApJ, 521, 691 [ADS]

Truran, J. W. 1981, A&A, 97, 391 [ADS]

Villemoes, P., Arnesen, A., Heijkenskjold, F., & Wannstrom, A. 1993, Journal of Physics B Atomic Molecular Physics, 26, 4289 [ADS]

Wanajo, S. & Ishimaru, Y. 2006, Nuclear Physics A, 777, 676 [ADS]

Wanajo, S., Kajino, T., Mathews, G. J., & Otsuki, K. 2001, ApJ, 554, 578 [ADS]

Wanajo, S., Tamamura, M., Itoh, N., Nomoto, K., Ishimaru, Y., Beers, T. C., & Nozawa, S. 2003, ApJ, 593, 968 [ADS]

Wendt, K., Ahmad, S. A., Buchinger, F., Mueller, A. C., Neugart, R., & Otten, E.-W. 1984, Zeitschrift fur Physik, 318, 125 [ADS]

Chapter 5: Modelling a stellar spectrum in 3-dimensions

Developing atmospheres and radiative transfer codes that model a stellar spectrum more accurately than classical 1-dimensional (1D) local thermodynamic equilibrium (LTE) radiative transfer codes and atmospheres (Chapter 2) has become necessary to attempt to explain intricate astrophysical effects, such as convection, which manifest themselves in high quality observed stellar spectra as asymmetric line profiles. I have shown through various methods (Chapters 3 & 4) that using 1D LTE in the face of such effects seen in high quality data is flawed due to the basic assumptions that such codes employ in their treatment of stellar atmospheres (§2.1).

Adam Hosford and I briefly examined the NLTE effects on the Fe lines, using his NLTE calculations in §4.4 and demonstrated that this had little to no effect on the overall Fe line profiles. This is not to say that such an effect should not be considered in Ba, especially when considering line core formation or the correct abundance, but rather it requires a detailed investigation including an equally detailed analysis of the full hfs in the Ba II line profile. However, a 1D NLTE analysis of this line using our approach in §4.4 would almost certainly find similar fitting errors found by the 1D LTE analysis in §3.4 & §4.3. This is because both the NLTE and LTE investigations were conducted assuming a 1D static atmosphere with symmetric line profiles, which is something I do not observe in my stellar spectra. I therefore speculated, but did not demonstrate, that these fitting problems may be removed using models that more closely replicate the various physical processes that occur in a stellar atmosphere, i.e. 3-dimensional (3D) convection, which through examination of two techniques and their imperfections in Chapters 3 & 4 I suspect may be the greatest shortcoming when determining $f_{\rm odd}$ for the Ba II lines. However, Collet et al. (2009) found that while their current 3D treatment of stellar atmospheres seems to model the Ba II line profile in HD 140283 more accurately, it appears that the technique enhances the s-process component for $f_{\rm odd}$, which exacerbates the disagreement with Truran's expectation of

an r-process origin of Ba in that star.

The issue of profile asymmetries appears to be important not only for my work on Ba and Fe. The Li line at 6707.80 Å consists of two Li isotopes, ^{6}Li and ^{7}Li, which are subject to fine and hyperfine structure splitting. However, the asymmetry caused by the isotope ratio is easy to model (García Pérez et al., 2009). In addition it is well known that departures from LTE exist in this absorption line (Lind et al., 2009; Osorio et al., 2011). Efforts to better fit the asymmetries associated with the isotope ratio of this line using 3D hydrodynamic model atmospheres as well as 3D NLTE radiative transfer calculations have been conducted (Asplund et al., 2003; Cayrel et al., 2007), with Cayrel et al. suggesting that part of the asymmetry associated with this line could be caused by 3D effects. We have seen through the 1D LTE analysis that Ba II lines suffer from similar issues, as isotope ratios are unable to correct for fitting errors seen in the red wing of the line, as shown in Figs. 3.6 & 4.1. Lind (2012 - in prep) has shown how very sensitive Li measurements are to assumptions about 3D/1D and LTE/NLTE.

In an attempt to improve in the modelling of the spectrum of HD 140283, a radiative transfer code that employs fully 3-dimensional, time-dependent model atmospheres was employed to model a selection of the Fe lines used in my 1D LTE analysis of the star. A list of the original 93 lines used for analysis in Chapter 3 can be found in Appendix B.1. HD 140283's spectrum is of the highest quality with high resolution ($R \equiv= \lambda/\Delta\lambda = 95\,000$) and very high signal-to-noise ($S/N = 1110$ about the 4554 Å line); it is the finest spectrum in my star sample. Therefore, random errors due to noise effects should be reduced, relative to the rest of my star sample. As the 3D models are very time consuming to compute, the scope of this investigation was limited and still leaves some unanswered questions to explore as the 3D computational framework matures, as I shall explain throughout this chapter.

In this chapter I discuss the positive and negative aspects to using a 3D LTE code through comparisons with results found during the 1D LTE investigation. The motive for choosing the Fe lines over the Ba line was four fold. First, weak and unblended Fe lines should be easier to model than the Ba II 4554 Å line as there are no extra concerns

such as hyperfine structure (hfs). Second, the fitting problems were seen in the Fe lines as well as the Ba line (Figs. 3.10 & 4.4). Third, if the 3D code couldn't fit the Fe line sample better, there would be no reason to assume that it would fit the Ba line better and improve on the current value of $f_{\rm odd}$ determined from the 1D LTE analysis. Fourth, there are many more Fe lines than Ba lines, so fitting residuals can be averaged to greatly reduce the impact of random errors, and thus make subtle effects clearer.

5.1 Modelling a stellar atmosphere with CO5BOLD

To model a stellar atmosphere in 3-dimensions, we use the code CO5BOLD, developed by B. Freytag and M. Steffen, which stands for "COnservative COde for the COmputation of COmpressible COnvection in a BOx of L Dimensions with L=2,3". (For details on CO5BOLD beyond the brief description given in this chapter see Freytag et al. 2002; Wedemeyer 2003; Wedemeyer et al. 2004; Freytag et al. 2010.) CO5BOLD is designed to model solar, stellar, and recently sub-stellar (e.g. brown dwarf) surface convection through time-dependent solutions to the equations of radiative transfer and hydrodynamics for a fully compressible, chemically homogeneous gas on a grid of Cartesian geometry in two or three spatial dimensions (Wedemeyer, 2003). This implies that CO5BOLD computes radiative transfer in a computational box of finite size rather than over the entire star, as computer technology is still not advanced enough to model an entire star with the necessary resolution used within the box.

Present limitations

The version of the code used for the present work does not include effects caused by magnetic fields, however, such additions to the code are available (Schaffenberger et al., 2005). The code also assumes strict LTE (i.e. $B_\nu = S_\nu$, Chapter 2), however, CO5BOLD is designed so that an NLTE "module" can eventually be incorporated, but the computational power required to run an NLTE formalism for hydrodynamic, multi-dimensional simulations would be enormous (Wedemeyer, 2003). Nevertheless studies that employ the NLTE formalism into the treatment of the line spectrum synthesis,

using the LTE CO^{5}BOLD model atmospheres, do exist (Cayrel et al., 2007). For the moment, however, solutions of a 3D NLTE atmosphere are beyond the capabilities of modern computing.

Stellar rotation is also ignored as the hydrodynamical time-scales of a model are short relative to the rotation of, for example, the Sun. This means that CO^{5}BOLD is currently not suitable for fast rotating stars, where the opposite would be true. The effect of rotation on line profiles is dealt with after line formation, in a similar fashion to the 1D LTE case. This is discussed further in §5.2.2. Inhomogeneous chemical compositions in the model can be included with the addition of a further module (Wedemeyer, 2003), but in the present work is not included. Despite these limitations and assumptions, photosphere and convective layer simulations are believed to be realistic through comparisons made between observed and synthetic granulation patterns (Wedemeyer, 2003). This point is further discussed later in this chapter.

Hydrodynamics and convection

In a hydrodynamic model, hydrostatic equilibrium is no longer fulfilled everywhere. This is because of the presence of large turbulences in the atmosphere of a star (Wedemeyer, 2003). In the hydrodynamic model, the continuity equation, the Eulerian equation of motion and the energy equation are solved. They are relations for the equations of the conservation of mass, momentum and energy, respectively. Additional terms which take into account the external gravity field and the change in the energy caused by the radiation field are also included in these equations. Definitions (and their derivations) of these equations, which are solved by CO^{5}BOLD, can be found in Wedemeyer (2003), his §4.2.1.

If we consider the basic energy transport in a star, various processes throughout the star transport energy from the fusing core (or shell) to the surface. Initially, this is done radiatively in the star. As the energy is transported to the convective region of a star, the turbulent motions contribute significantly to further transport of energy to the surface, while the radiative processes become less important. Convective transport of energy is an extremely important mechanism for the transport of energy in a star.

Convection occurs in gas with density differences, often due to temperature, relative to the surrounding gas. When the temperature of a cell of gas in a star is increased relative to its surroundings, the gas expands until pressure equilibrium is achieved. This causes the density of the gas to decrease and the force due to buoyancy causes it to rise adiabatically toward the surface until the relative densities of the gas cell and the surrounding gas are in equilibrium. When a gas cell is cooler than the surrounding gas the opposite is true and it sinks toward the centre of the star until the density of the gas cell is at equilibrium with its surroundings.

Line asymmetries

We have seen in §2.3.5 that the process of convection causes Doppler shifts of the absorbers within a convection cell and that classically, their velocity distributions are often modelled as a Gaussian. However, we know through observations of solar convection cells (de Boer et al., 1992; de Boer & Kneer, 1992) that they have velocities governed by gas interactions and convection that lead to a non Gaussian broadening of a spectral feature. Fig. 5.1 illustrates the granulation patterns seen in the Sun.

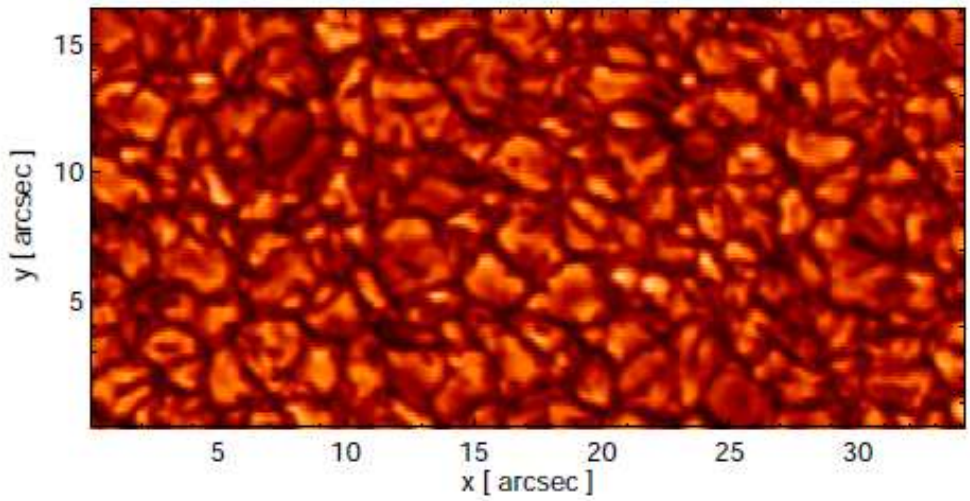

Fig. 5.1: Observed solar granulation pattern. Image taken from Wedemeyer (2003).

If we compare the line asymmetries with granulation patterns in a star (e.g. Fig. 5.1) we find that the brighter (hotter) granules correlate to a blue shift in a line and the darker (cooler) granules correlate to a red shift in a line so that the brighter granules

travel towards us and the darker granules travel away from us (Dravins et al., 1981).

However, I have previously mentioned that there is a larger depression of the flux in the red wing of a line than in a blue wing of a line, relative to its distance from the line's centre. This would indicate that on average, the gas in the darker regions has a higher velocity than the gas in the brighter parts of the granulation, which means that the width and shape of the line asymmetry is analogous to the behaviour of the convective motions in a star's atmosphere. When the photons from the hotter gas on the star's surface escape they remove both energy and entropy from the gas. This produces an over dense gas (relative to the hot gas), which is rapidly pulled down by gravity (Nordlund et al., 2009). As the hotter, less dense gas rises adiabatically to the surface its velocity will slow down as pressure equilibrium is almost fulfilled, whereas the cooler, denser gas will accelerate to a higher velocity and slow down deeper in the star when pressure equilibrium is achieved. The resultant difference in the two velocities leads to greater red shifts than blue shifts, which leads to asymmetries in a spectral line.

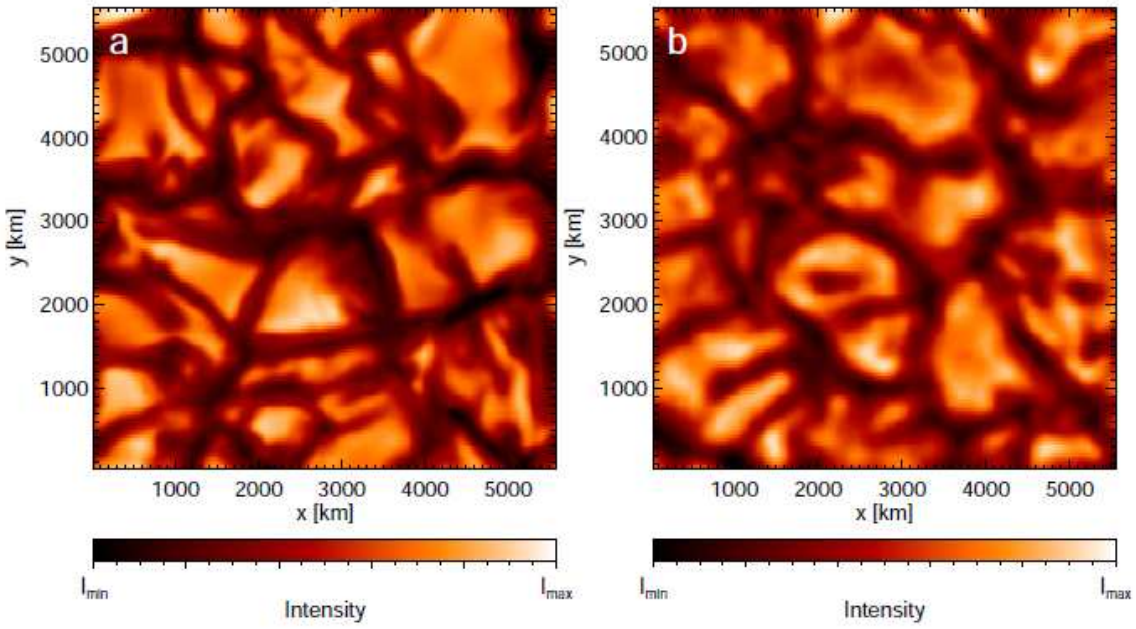

Fig. 5.2: A comparison of a CO5BOLD model atmosphere's granulation pattern with the observed granulation pattern for the Sun. a) The model granulation pattern at 5500 Å. b) The observed granulation pattern centred at 5576 Å. Image taken from Wedemeyer (2003).

It is therefore important that a 3D hydrodynamical model atmosphere can properly model the granulation patterns in a star's atmosphere so that asymmetries can be accurately replicated. When one compares a CO^{5}BOLD model atmosphere's granulation pattern with an observed granulation pattern, e.g. the solar granulation patterns seen in Fig. 5.2, one can see that the CO^{5}BOLD atmosphere models the granulation patterns very well.

Details of the model atmospheres

The model atmospheres used for this work were calculated for a star with $T_{\rm eff} = 5750\,\mathrm{K}$, $\log g = 3.7$ and for two metallicities [Fe/H] $= -2.0$ and [Fe/H] $= -3.0$. I later interpolate between the two models to [Fe/H] $= -2.5$ after the line synthesis is completed (see §5.2.2). It should be noted that the CO^{5}BOLD model atmosphere snap-shots used in the work presented here were computed by H.-G. Ludwig. The models were calculated in a computational box of geometrical dimensions $36.7 \times 36.7 \times 22.2\,\mathrm{Mm}$, with spatial sampling of $140 \times 140 \times 150$ voxels in x, y and z dimensions respectively, where z represents the dimension into the star.

A total of 20 snap-shots of the atmosphere are taken so that time variations can be traced. The time intervals between snap-shots are determined based on the sound speed of the gas. This depends on the densities in the box; the higher the density, the faster the sound speed and the less time between snap-shots. Choosing the time interval based on the sound speed allows for mixing of materials within the grid which means that pressures and densities, which affect line shapes, have had sufficient time to change. To show how the time-dependence affects the model atmosphere, Fig. 5.3 shows the temperature and average optical depth relationships for all 20 snap-shots and the time-averaged optical depth, which is calculated by taking the average temperature value for a given optical depth.

CO^{5}BOLD was written in Fortran90 and can be run using multiple CPUs in parallel using the OpenMP[1] directives for fast, efficient run times (Freytag et al., 2010).

[1]OpenMP is an application programming interface that supports shared memory multiprocessing in several languages including Fortran. Using such a directive allows the code to be run on a cluster machine. I refer the reader to the website `www.openmp.org`, for further information about OpenMP.

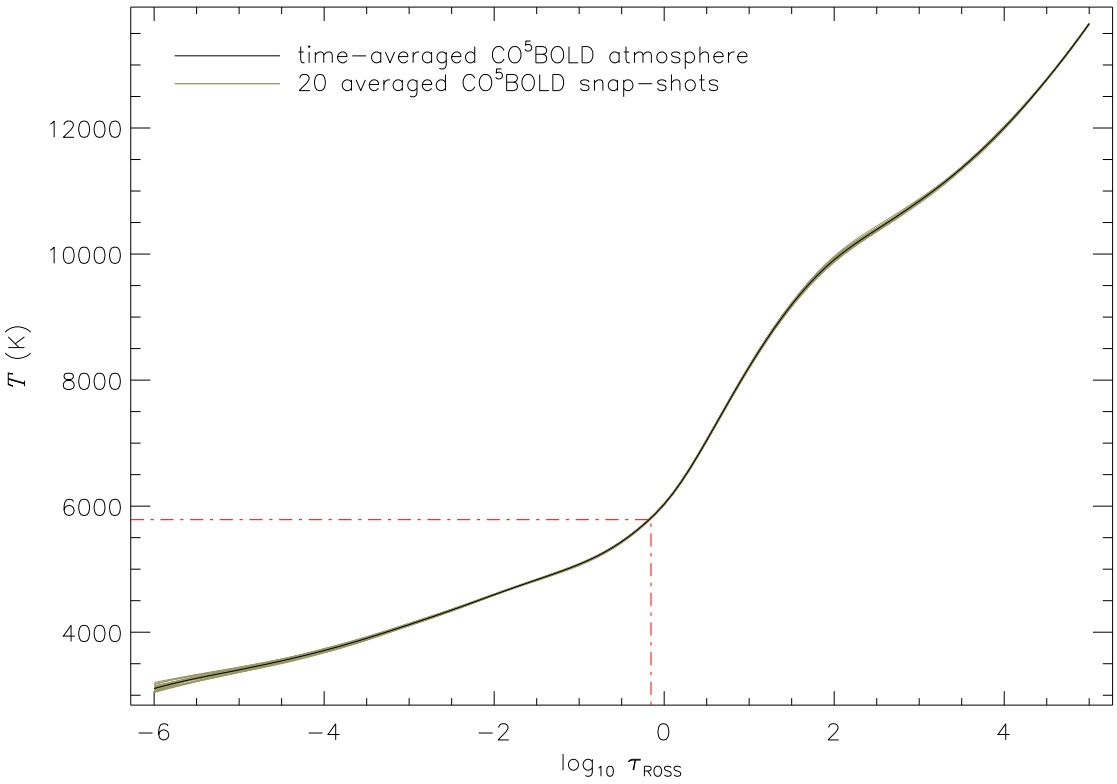

Fig. 5.3: The temperature profile as a function of the Rosseland mean optical depth in logarithmic space. The time-averaged result represents the average temperature profile over all 20 snap-shots. The average temperature profile for each snap-shot has been included to show the time-dependence. The red dash-dot line shows the temperature at which $\tau_{\mathrm{ROSS}} = \frac{2}{3}$ ($T = 5786$ K).

5.2 Synthesis of a stellar spectrum with LINFOR3D

Once H.-G. Ludwig provided me with the two CO5BOLD model atmospheres, I used the new radiative transfer code LINFOR3D, which is still under development, to calculate synthetic spectra. The code is being developed by M. Steffen, H.-G. Ludwig and S. Wedemeyer. It is a modified version of the LINFOR radiative transfer code, created by the Kiel group (Steffen et al., 1981). Every subroutine of the code has been written in IDL so that run time issues and bugs can be easily identified and resolved, although this means that the code runs very slowly. Once a subroutine has been fully tested it will then be rewritten in Fortran90 for better execution efficiency (Steffen et al., 2010). Eventually, the code will be parallelised with the OpenMP directives like CO5BOLD. As yet, there has been no effort to improve execution speed or remove redundant subroutines. This results in very long run times for each spectrum synthesis, in fact

computing a single absorption line (of 401 wavelength points) for a single abundance takes over $2\frac{1}{2}$ hours to complete on a single CPU[2]. An added disadvantage of the current version of LINFOR3D is that each synthesis run uses its own IDL license and these are usually limited on a particular system. The grid of lines used for this work, discussed in more detail below, took over two weeks to complete, because of the limited number of IDL licenses available. In this section I review the procedures followed to compute the Fe line grid used for analysis in §5.3.

5.2.1 The Fe line sample

To synthesise the Fe lines using LINFOR3D, line lists must first be created. These line lists contain all the relevant information relating to each Fe line. Several parameters, required by LINFOR3D, must be present in the line list (see Appendix A.4) including the central wavelength, λ_C, tabulated as "`alam`", the atomic or ionic species, tabulated as "`namj`", χ in eV, tabulated as "`ei`" and $\log gf$ tabulated as "`gflg`". These were also required in the 1D LTE synthesis (Chapters 3-4) and as such were set to the same values.

In addition to these basic line parameters, LINFOR3D requires details on the spectrum sample size or wavelength range, $\Delta\lambda$, tabulated as "`dlam`" and the wavelength spacing, $\delta\lambda$, tabulated as "`ddlam`". Both $\delta\lambda$ and $\Delta\lambda$ are measured in Ångstroms. Every line was calculated over the same wavelength range, $\Delta\lambda = \pm 0.4$ Å from the line's centre. Similarly, every line was calculated using the same wavelength spacing, $\delta\lambda = 2$ mÅ. Therefore every line was calculated over 401 wavelength points. The typical value of $\delta\lambda$ in the observed spectrum was 0.02 Å; this equates to just 60 wavelength points over the same $\Delta\lambda$ range.

LINFOR3D also requires details on the pressure broadening constants, in this case the van der Waals broadening, which is specified as the difference between mean square electron orbital radii of the upper and lower levels of each transition, $\Delta\overline{r^2}/a_0^2$, calculated

[2]The timing example given here was computed on a cluster machine using Intel® Xeon® processors with individual core speeds of 2.53 GHz. The time for completion of the synthesis will depend on the CPU clock speed.

as

$$\log\left(\Delta\overline{r^2}/a_0^2\right) = \log C_6 + 32.3867 \tag{5.1}$$

(Steffen et al., 2010), where a_0 is the Bohr radius and the constant, 32.3867, is the determined value of the constants in Eq. (2.17) when T is taken to be 10^4 K. This is tabulated as "`drrca1`" in the line lists. Also, there is an option to enhance the C_6 constant determined using the Unsöld/van der Waals approximation ($C_{6,\mathrm{vdW}}$) by including a $\Delta \log C_6$ term, tabulated as "`dlgC6`", where $\log C_6 = \log C_{6,\mathrm{vdW}} + \Delta \log C_6$. For consistency throughout my research, I calculated C_6 using the Unsöld approximation in Eq. (2.15) and included the γ_6 enhancement factor of 2.2, as in the 1D LTE work (Chapters 3 & 4), when calculating C_6 using the relationship in Eq. (2.17). In summary then, the C_6 terms in the LINFOR3D line lists include all the enhancement I required so that the pressure terms are dealt with in exactly the same way as they were in ATLAS. This meant that any differences in the comparisons made between the 1D and the 3D fits would not be due to differences in the pressure broadening calculations. Other alternatives to the Unsöld approximation of the van der Waals damping for collisional broadening in metal lines, such as the Anstee, Barklem and O'Mara (ABO) theory (Barklem et al., 1998) can be applied to the line synthesis. For other parameters that can be included in the line lists for synthesis, I refer the reader to Steffen et al. (2010).

A total of 90 individual Fe lines, taken from the 93 lines used for analysis in Chapter 3, were reproduced using LINFOR3D. Only 17 of the 90 lines synthesised were used for the analysis in §5.3; the reason for this is also discussed in §5.3. Each Fe line was synthesised for nine different values of A(Fe).

Unlike for the 1D calculations with ATLAS, the user cannot simply change the chemical abundance of the CO^{5}BOLD atmosphere so that more or fewer absorbers are synthesised within LINFOR3D for a particular species. Instead, one must manipulate the line strength through other means. The opacity associated with a particular absorption line can be doubled either by doubling the number of absorbers, N(X), or by

doubling their oscillator strength, f, or equivalently increasing gf. In LINFOR3D, an increase in abundance is simulated by increasing the gf, such that $\delta\log gf = \delta A(\mathrm{X})$. Appendix A.4 shows that for the Fe I 4282 Å line, nine values of $\delta\log gf$ were used, so that the abundance range is given by $-0.8 \leq \delta A(\mathrm{Fe}) \leq +0.8$, calculated at intervals $\Delta A(\mathrm{Fe}) = 0.2$. (For a more detailed interpretation of the relationship between $\log gf$, $A(\mathrm{X})$ and equivalent width, see Gray (2008), his Eq. (16.4).) The chemical abundances used in the CO^{5}BOLD model atmospheres are calculated as solar, scaled to the metallicity of the model, as in the Kurucz 1D LTE model atmospheres.

A final parameter that is not modelled by LINFOR3D, and hence needs attention before the line synthesis, is the microturbulence. Although this parameter is not essential to the 3D models, which was true for the 1D approach, at present this parameter is recommended.

Ideally, the microturbulence should have been replaced by the self-consistent hydrodynamical velocity field of the 3D simulations (Freytag et al., 2012). However, several parameters are key to the accuracy of these models (e.g. spacial resolution of the grid, formulation of boundary conditions, etc.), which are currently very time consuming to compute at high resolutions. Higher spacial resolutions coupled with improvements to other parameters that characterise the simulations should eliminate the need for this fudge factor. At present however, the microturbulence is required to compensate for the limitations in computing power that lower the accuracy of these parameters. The ultimate aim is to essentially eliminate the dependency the simulations have on these parameters so that low resolution models, like those presented in the present work, no longer require a fudge factor such as microturbulence (Freytag et al., 2012).

The microturbulence for HD 140283 was set to $1.50\,\mathrm{km\,s^{-1}}$, which is almost the identical value that was used in the 1D LTE analysis ($1.40\,\mathrm{km\,s^{-1}}$). This is not set in the line list but rather in the script used to run LINFOR3D when the command program used by IDL is created. An example of a run script can be found in Steffen et al. (2010).

5.2.2 Details of the LINFOR3D calculations

To minimise LINFOR3D run times, individual lines were synthesised over the width of ± 0.4 Å, rather than a complete spectrum. This meant the synthesis for several lines could be run in parallel and completed quicker. As previously stated, the code requires at least $2\frac{1}{2}$ hours of run time to complete a single line with one abundance. In order to run the synthesis for nine different abundances, which are completed in series, requires at least $22\frac{1}{2}$ hours. In fact, on average the run time was longer than this and took roughly 28 hours to compute. Up to 18 lines were completed in parallel by assigning each line synthesis to a separate CPU on a cluster. I originally synthesised 90 lines, but as each line requires a separate IDL license, which are limited, lines were submitted in five groups, each line to a different CPU. Once a group of 18 lines had completed for all 9 abundances, the next 18 lines were submitted and so on. This meant that to compute all 90 lines required 140 hours to complete, i.e. about one week.

As foreshadowed, the CO^{5}BOLD atmospheres cannot yet model stars with metallicities of -2.5 (the metallicity of HD 140283) because the grids are incomplete. Instead, two model atmospheres with metallicities [Fe/H] $= -3.0$ and [Fe/H] $= -2.0$ were run with LINFOR3D independently for every line. Both outputs are combined and interpolated to [Fe/H] $= -2.5$ at a later stage. This meant that the run time was doubled to two weeks, as each line had to be synthesised twice, once for each atmosphere.

5.2.3 LINFOR3D outputs

LINFOR3D outputs an IDL data file made up of several structures containing various aspects of line information, rather than a simple ASCII file containing wavelength points with the corresponding flux calibrated data points, as in the case of ATLAS output. I wrote a simple IDL code to extract the line information. This can be found in Appendix A.5.

There are several things the code does to process the LINFOR3D outputs so that each line is ready to be analysed. At this point, the LINFOR3D outputs contain no excess stellar broadening (which is modelled as rotational broadening) or instrumental

broadening and most importantly, each line consists of two synthesis outputs using two metallicities. After reading in both outputs for a specific line, the code calculates the time-averaged profile. As fully 3-dimensional, time-dependent atmospheres should be able to mimic the convective Doppler broadening in a star, it is assumed that any excess in the observed line broadening would be caused by the star's rotation, modelled as a $v \sin i$ profile, which is convolved with the line profile at this point. Stellar rotation is explained in §2.3.5.

The code then calculates the wavelength points of the profile from information submitted in the line list (λ_C, $\delta\lambda$ and $\Delta\lambda$), which is stored in the LINFOR3D output. Next, the code interpolates the flux between the two metallicities to [Fe/H] = −2.5 (the metallicity of HD 140283), and finally it convolves the instrumental profile, which is modelled as a Gaussian, with the line profiles. Once this process is complete, it formats the new output into a simple ASCII file comprised of wavelength and flux calibrated data points. This process took roughly two minutes to compute the output for a single line, or roughly three hours for the entire line sample.

5.3 Fe line analysis through χ^2 fitting

The Fe lines analysed in this chapter were fit using the same χ^2 routine used throughout the present work with the exception that in the 3D analysis a separate instrumental profile (Gaussian of $FWHM = 3.31\,\mathrm{km\,s^{-1}}$), as measured from 993 ThAr lines in Chapter 3, is adopted, and instead of fitting for the macroturbulence I fit for $v \sin i$. The code has a GUI interface for easy use and is designed to calculate the values of $v \sin i$, the wavelength shift[3] ($\Delta\lambda$) and A(Fe) that give the χ^2 minimum, and hence the best fit. This is achieved over several stages.

Firstly, the code calculates the value of $\Delta\lambda$ for the first value of A(Fe) in the grid at a given $v \sin i$. This is done by calculating χ^2 over a wavelength range of ±0.25 Å for 11 values of $\Delta\lambda$, set by the user (see Fig. 5.4, lower-right panel) and is unique for each line included for χ^2 analysis. The χ^2 minimum is calculated by fitting a spline

[3]Note that this is a different $\Delta\lambda$ to `dlam` in §5.2, but it is clear from the content which is which.

interpolation to the differential $\frac{\mathrm{d}(\chi^2)}{\mathrm{d}(\Delta\lambda)}$ and finding where $\frac{\mathrm{d}(\chi^2)}{\mathrm{d}(\Delta\lambda)} = 0$. Both the preferred $\Delta\lambda$ value and the corresponding χ^2 value are recorded. This shall be known as stage one, which is illustrated in Fig. 5.4.

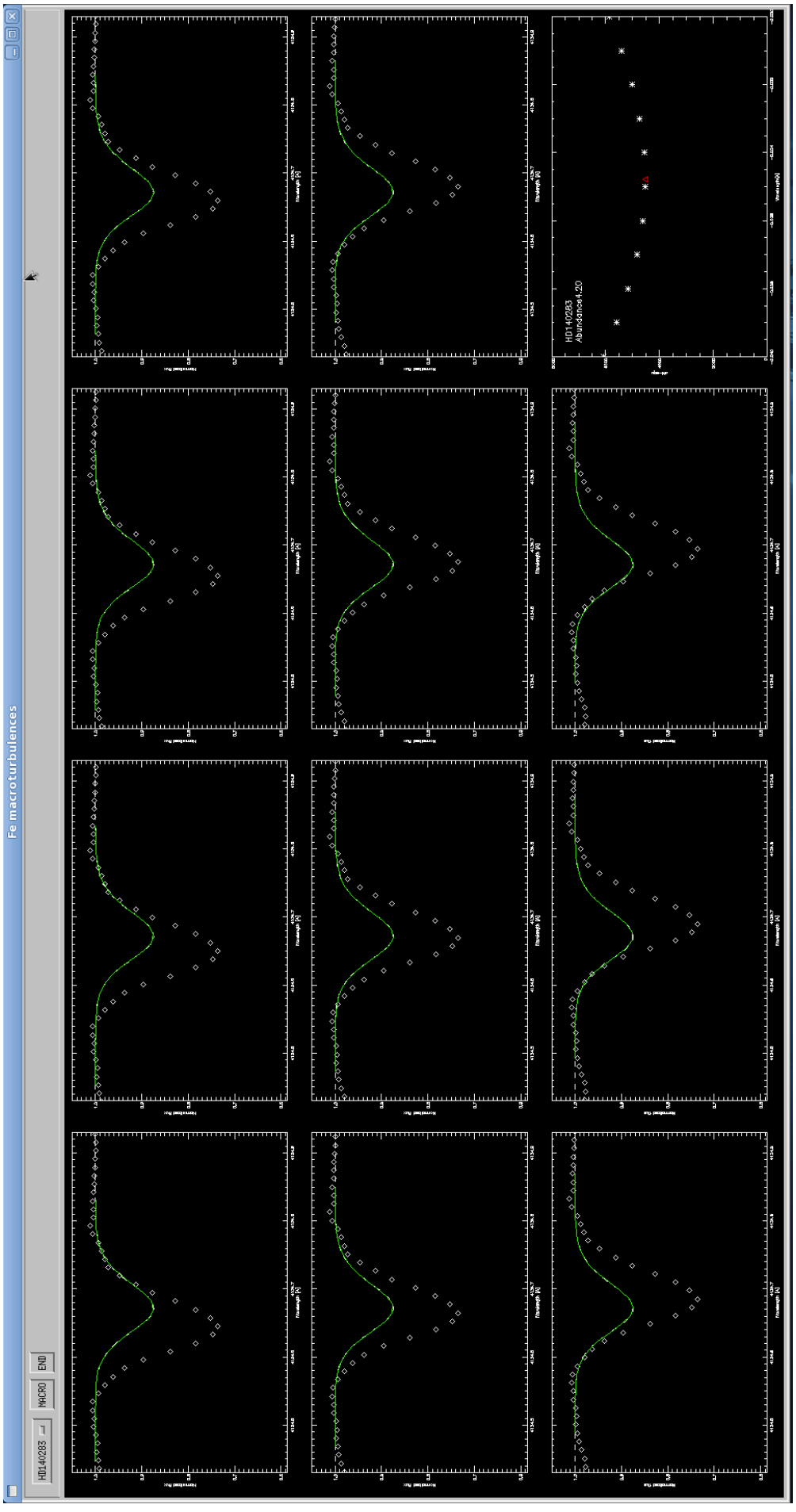

Fig. 5.4: A screen-shot of the χ^2 code plotting the wavelength shifts. The first 11 sub-plots in the figure show the observed profile (*diamonds*) being wavelength shifted by a small increment and over-plotted on the synthetic profile (*solid green line*). The code calculates the χ^2 value for each panel, i.e. for each value of $\Delta\lambda$. The final plot in the bottom right hand corner is a plot of χ^2 vs $\Delta\lambda$ for each of the 11 calculations and the red triangle shows where the calculations have determined the χ^2 minimum, and hence, the wavelength shift. This is repeated for every value of A(Fe) and for every $v \sin i$ value in the grid.

The code loops over all nine values of A(Fe) (see §5.2.1) and re-runs stage one for every A(Fe) value, for the first $v \sin i$ value. The spacing ΔA(Fe) is 0.2 dex. Once this is complete, the code then calculates the value of A(Fe) that corresponds to the χ^2 minimum, this time by calculating a spline interpolation of the differential $\frac{\mathrm{d}(\chi^2)}{\mathrm{d}(A(\mathrm{Fe}))}$ and finding where this equals zero. This shall be known as stage two and is illustrated by Fig. 5.5. The values of A(Fe) and χ^2 at the minimum are recorded.

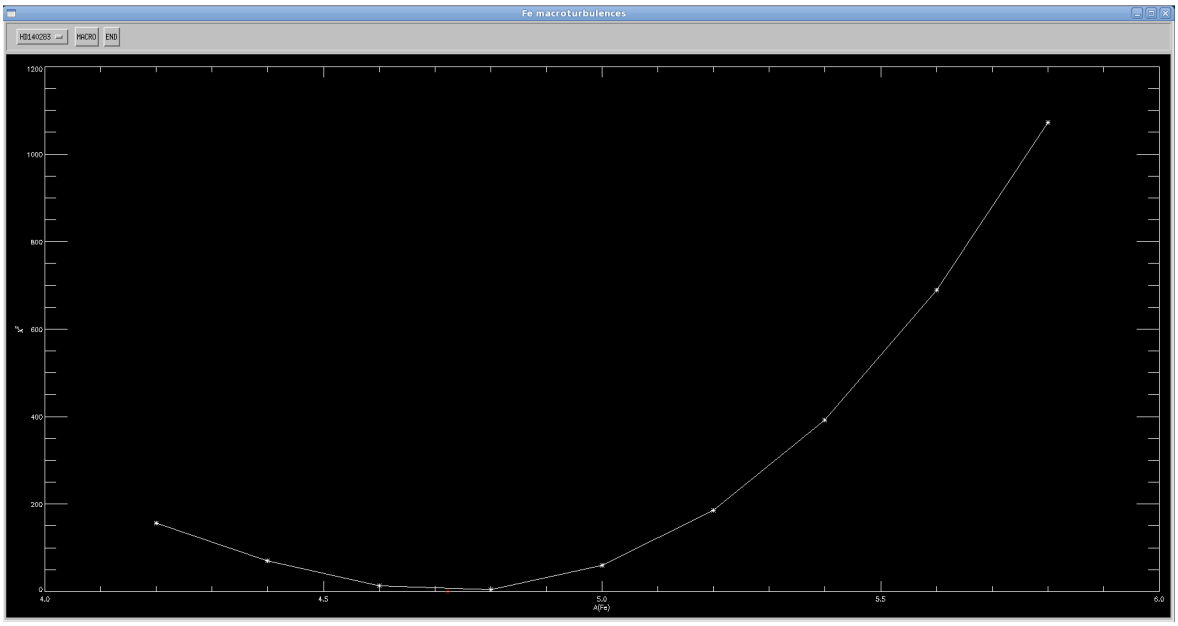

Fig. 5.5: A screen-shot of the χ^2 code plotting the χ^2 vs A(Fe) curve for a single value of $v \sin i$. Each point on the curve is the minimum χ^2 calculated at stage 1, and the red diamond represents the result of stage 2, i.e. the value of the spline interpolation that represents the minimum χ^2 for the adopted value of $v \sin i$. Stage two is repeated for each of the 11 values of $v \sin i$.

The code then loops over 11 values of $v \sin i$, and repeats stage one (11 times) and stage two each time. Once complete, the code calculates the $v \sin i$ value that corresponds to the χ^2 minimum. As above, this is calculated by fitting a spline interpolation to the differential $\frac{\mathrm{d}(\chi^2)}{\mathrm{d}(v \sin i)}$ and finding where the spline is equal to zero. We shall call this stage three, which is illustrated in Fig. 5.6. Finally, the code returns the values of $v \sin i$, A(Fe) and $\Delta\lambda$ that satisfy the χ^2 minimum. In total, a grid comprising $11 \times 9 \times 11$ χ^2 values (in $\Delta\lambda$, A(Fe) and $v \sin i$) has been computed.

The code then loops stages one, two and three for all 90 Fe lines for which synthetic spectra were calculated.

Each stage of χ^2 minimisation is completed using a spline interpolation routine,

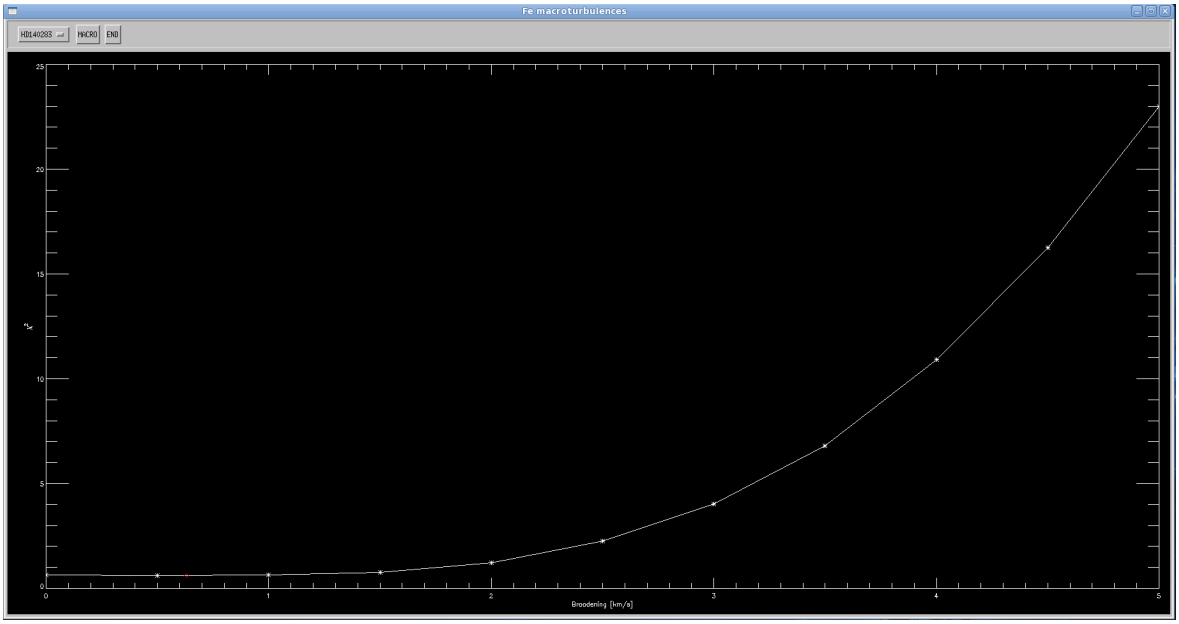

Fig. 5.6: A screen-shot of the χ^2 code plotting χ^2 vs $v \sin i$. The red diamond represents the χ^2 minimum calculated by the spline interpolation. The curve is asymmetric and illustrates that, in this case, the turbulence determined by the time-dependent 3D models almost completely accounts for the turbulent motions in HD 140283, i.e. $v \sin i$ is not significantly different from $0\,\mathrm{km\,s^{-1}}$ for this set of parameters and this spectral line.

which is found in the IDL routine library. By interpolating where the gradient of the χ^2 curve equals zero, the routine provides values of $\Delta\lambda$, A(Fe) and $v \sin i$ where their gradient, not the points within the grid sample, equal zero. For example, the interpolation may return a value for $v \sin i = 2.32\,\mathrm{km\,s^{-1}}$ even if the grid is defined discretely as $v \sin i = 0.0 + \Delta v \sin i \times j$ where the integer $j = 0$ to 10 and $\Delta v \sin i = 0.5\,\mathrm{km\,s^{-1}}$. This can be seen in Figs. 5.4, 5.5 & 5.6. However, the accuracy with which the spline interpolation determines these values diminishes as the grid spacing increases.

The 3D grid used for the work presented here included 11 values of $v \sin i$ in the range $0.0 \leq v \sin i\ (\mathrm{km\,s^{-1}}) \leq 5.0$, where $\Delta v \sin i = 0.5\,\mathrm{km\,s^{-1}}$, nine abundances with a range $4.20 \leq A(\mathrm{Fe}) \leq 5.80$, where $\Delta A(\mathrm{Fe}) = 0.2$, and 11 values of $\Delta\lambda$, unique to each line. When this is compared to the grids used in the 1D analysis ($4.9 \leq v_{\mathrm{conv}}\ (\mathrm{km\,s^{-1}}) \leq 6.9$ in steps $\Delta v_{\mathrm{conv}} = 0.1$; $4.09 \leq A(\mathrm{Fe}) \leq 5.45$ in steps $\Delta A(\mathrm{Fe}) = 0.04$) it is apparent that the 1D grid has a finer grid sampling than the 3D grid. This is because of the large time requirement in computing 3D synthetic spectra. Therefore the coarse grid spacing used for the analysis here for both A(Fe) and $v \sin i$ implies a larger uncertainty

than was found in the 1D analysis[4].

A direct consequence of this large uncertainty was the influence of numerical errors that propagated throughout the χ^2 code's various stages of calculations. Originally, 90 lines from the original Fe line list of 93 were synthesised. Three lines were dropped during the synthesis due to suspected blends with other Fe lines which contributed to the overall profile. When the remaining lines were processed using the χ^2 code, simple numerical interpolation errors in one of the three stages, which propagate through the remaining calculations, caused large deviations between the actual (visually inferred) best fit synthetic profile and the values calculated. This problem was discovered during the 1D investigations conducted in Chapters 3 & 4 and a simple fix was found.

The interpolation routine in IDL, which is employed to find the point at which the gradient of the χ^2 curve reaches zero, cannot accurately achieve this with large gradients, which can arise as a consequence of the grid size I use here ($\Delta A(\mathrm{Fe}) = 0.2$), unless the curve is either almost completely symmetric or has several more points with which it can determine an accurate polynomial. For the 1D analysis, using a finer grid sample ($\Delta A(\mathrm{Fe}) = 0.02$) fixed this issue. Also, creating extensive, finely sampled grids meant that I could change the abundances used by the χ^2 code to fit each individual spectral line to practically eliminate any asymmetry that arose. Therefore the spline interpolation could better determine where the gradient of the χ^2 curve equated to zero. However, to resolve this problem in the same way in the 3D analysis, with the same number of abundances for each line as used in 1D, would have meant many more hours of synthesis with LINFOR3D. As noted in §5.2.2, calculating the spectra at 0.2 dex spacing required over two weeks; switching to the 1D sampling of 0.02 dex over the same A(Fe) range would require five months. As time was limited at this part of my analysis, I elected to remove problem lines from my analysis, rather than compute a more finely sampled grid, so that only 17 lines remained in the analysis. Although I limit the scope of this first foray into 3D analyses, I intend to extend this analysis in future work (see §5.5).

[4]In fact, the grid spacing in the 1D analysis for both A(Fe) and $v \sin i$ was small enough that no uncertainty from the spline interpolation was detected.

The results of the χ^2 analysis for the remaining Fe lines can be seen in Table 5.1. If one compares the results of the 3D paradigm with the 1D (also tabulated in Table 5.1), it is shown that in general, the 3D fits produce smaller χ^2 values, despite the 3D grid having a much coarser abundance and broadening grid sampling.

Table 5.1: The Fe I line results found through analysis of 3D models calculated for HD 140283. For the reader's convenience, the corresponding χ^2_r and A(Fe) values found through the 1D analysis conducted in Chapter 3 have been included.

	3D analysis				1D analysis	
Wavelength (Å)	χ^2_r	$v \sin i$ (km s^{-1})	A(Fe)	$\Delta\lambda$ (mÅ)	χ^2_r	A(Fe)
4134.68	0.62	1.75	4.73	−14.56	1.61	4.91
4137.00	0.79	2.15	4.53	−12.98	0.88	4.79
4147.67	1.28	2.69	4.50	−15.82	1.88	4.92
4156.80	3.96	2.60	4.77	−16.84	5.27	4.98
4175.64	0.61	2.33	4.75	−12.63	4.40	4.97
4219.36	1.29	2.55	4.79	−17.65	2.35	4.92
4238.81	0.61	2.71	4.75	−17.86	6.52	4.91
4466.55	1.12	2.18	4.74	−24.32	2.98	4.88
4494.56	2.38	2.26	4.70	−22.79	4.27	4.94
4531.15	0.10	2.70	4.44	−14.68	0.66	4.90
4872.14	0.23	2.57	4.66	−17.26	10.91	4.87
4918.99	4.71	2.24	4.74	−22.93	15.34	4.88
5051.64	5.02	2.28	4.32	−11.82	5.42	4.97
5192.34	3.63	2.24	4.63	−28.88	29.32	4.84
5216.27	3.54	2.30	4.37	−25.56	4.69	4.89
5393.17	3.03	2.78	4.59	−20.87	4.10	4.88
5569.62	3.20	2.59	4.56	−22.06	4.20	4.84

In Fig. 5.7, the best fits to the 17 surviving Fe I lines are plotted for both the 3D and 1D analyses, complete with the corresponding residuals with respect to the observed data. Note that there are large systematic deviations between the 3D and 1D abundances. This is discussed in §5.4. The overall fit by the 3D profiles appears to be an improvement to the fit produced by the 1D profiles. In particular the red-wing residual asymmetries seen throughout the present work have been substantially reduced, or removed completely in all 17 Fe lines in the 3D analysis. In other words the 3D profiles are reproducing the observed asymmetries. However, it does appear that the 1D synthetic profiles better replicate the depth in the line cores. This could be due to the errors associated with the coarse grid sampling when fitting the 3D line profiles. This is discussed further in §5.4.

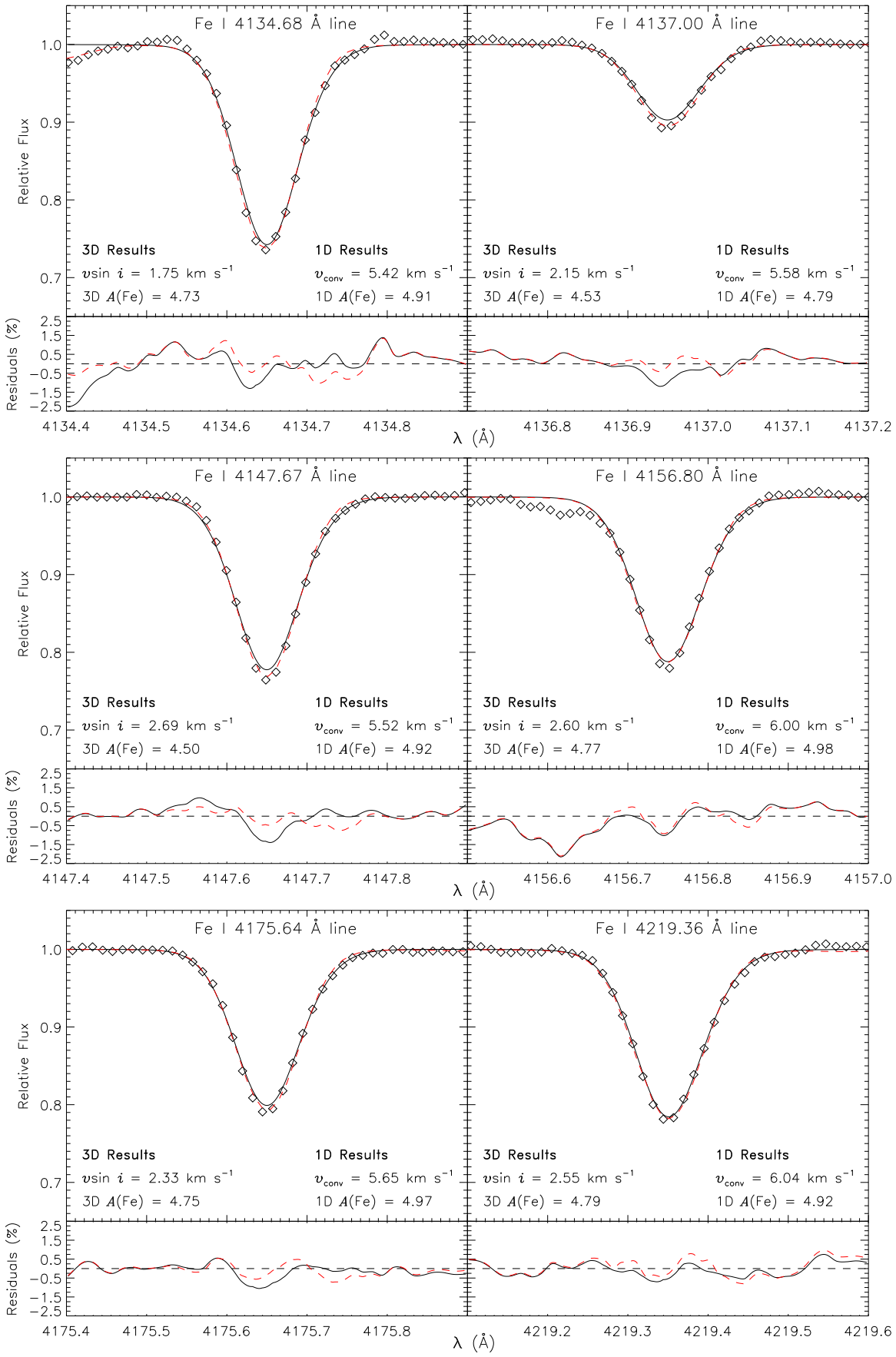

Fig. 5.7: The best fits to the 17 Fe lines using the 3D analysis and the corresponding best 1D fit. *Diamonds*: The observed Fe I line profile. *Solid black line*: The 3D synthetic profile. *Red dashed line*: The 1D synthetic profile. The lower portion in each panel shows the residuals, in the sense obs-syn.

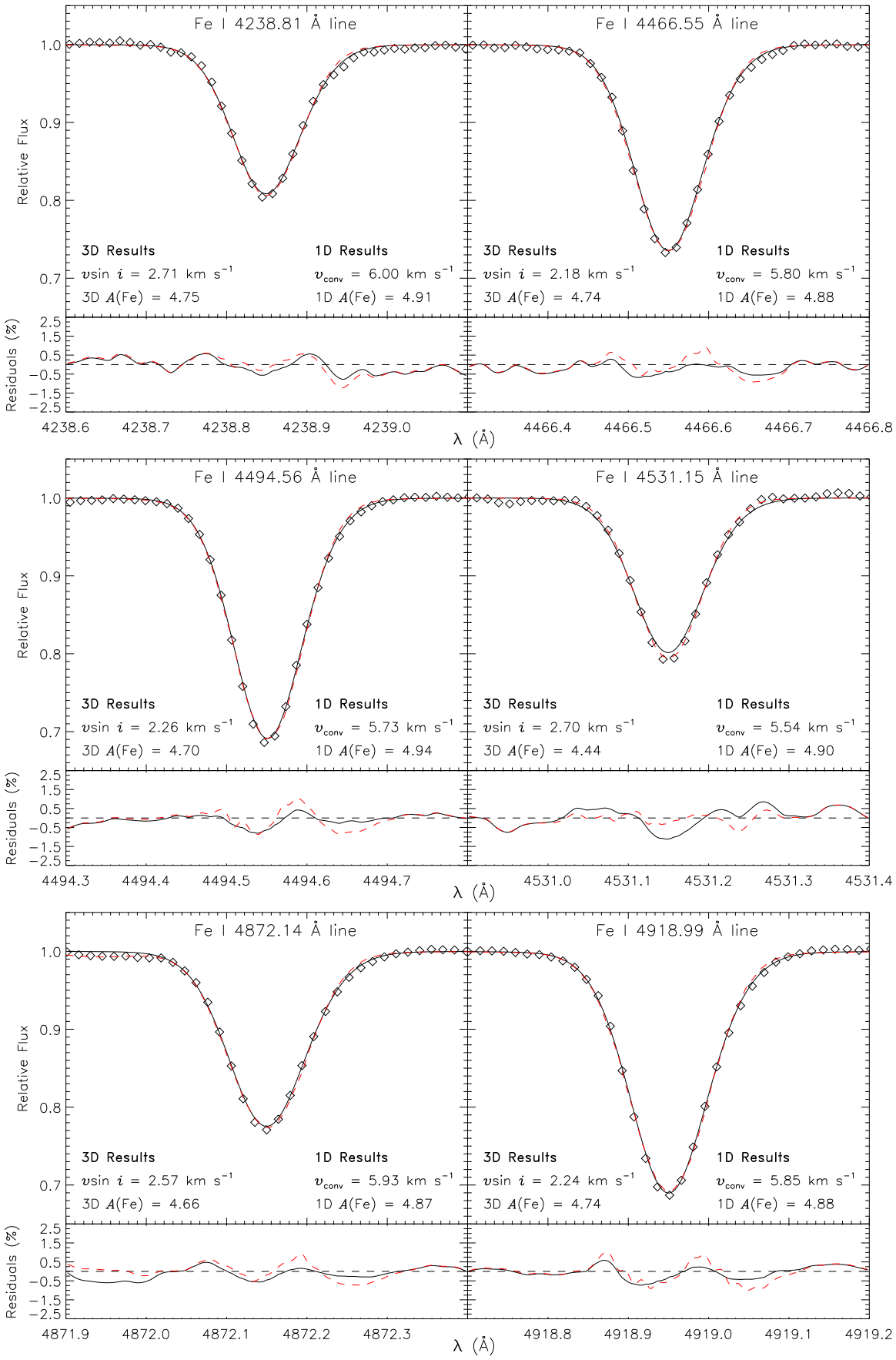

Fig. 5.7: continued from previous page...

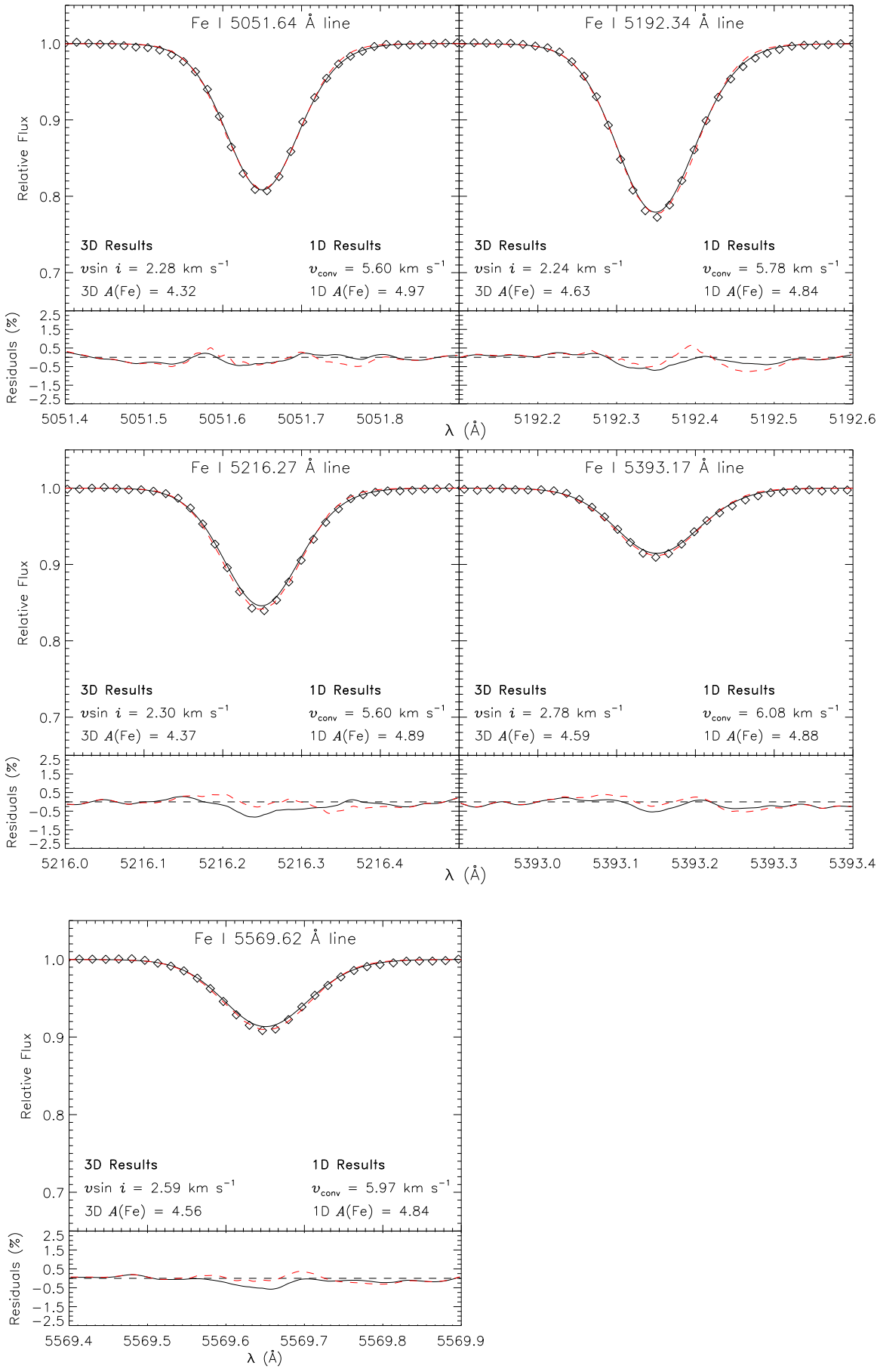

Fig. 5.7: continued from previous page...

To illustrate the improvements to the red-wing asymmetries, a reduced-noise average residual plot has been constructed by averaging all 17 Fe line residuals from Fig. 5.7 as was done for the 1D analysis in Chapter 3 (Fig. 3.10). This is shown in Fig. 5.8. Averaging the residual plots highlights fitting issues and improvements. We can see from Fig. 5.8 that the residual asymmetries in the red wing (at $\Delta\lambda \sim +0.1$ Å) have substantially diminished in 3D, but a worsening of the fit is seen in the line core when the 1D and 3D fits are compared.

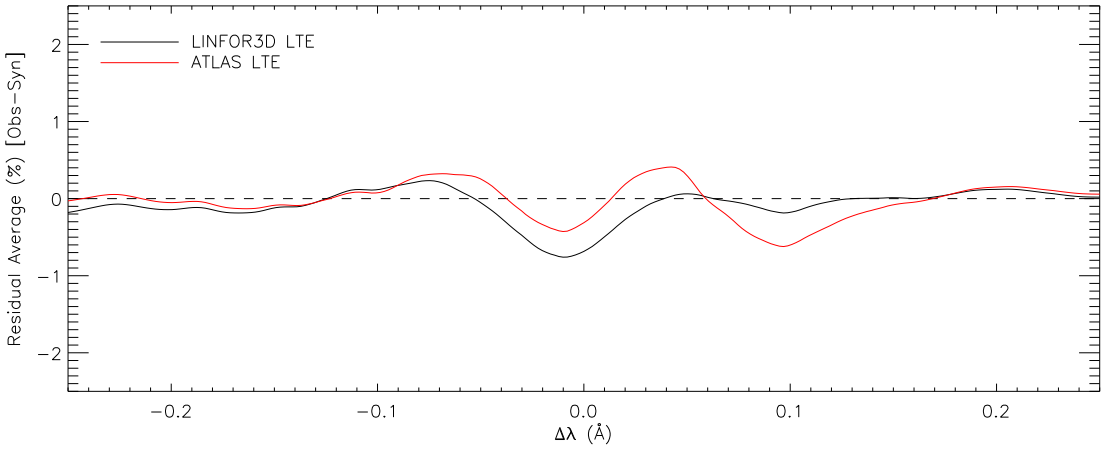

Fig. 5.8: The reduced noise average residual plot for all 17 Fe lines. The black line shows the 3D result and the red line shows the 1D result for this subset of Fe lines. A significant improvement to the red wing (at $\Delta\lambda \sim 0.1$ mÅ) is seen in the 3D treatment. However, the 1D synthesis better fits the line cores.

At $\Delta\lambda \sim -0.15$ Å, Fig. 5.8 shows the residual fit in the continuum. A slight improvement can be seen in the 1D residual over the 3D residual profile and hence, is fitting the observed continuum slightly better than the 3D. However, this is most likely because the 1D synthesis of the 4134.68 Å line includes another Fe line forming at a bluer wavelength. This is well illustrated by its best fit shown in Fig. 5.7. I remind the reader that the 1D synthesis was calculated over the entire observed spectrum, which has a wavelength range $4118 - 6253$ Å, as the computation of such a synthetic spectrum was extremely fast and more convenient than synthesising a single line. The 3D synthesis does not include any other line information other than the line of interest. Also the line synthesis was computed over a limited range (± 0.4 Å relative to line centre). LINFOR3D does have the capability of including blends, but they were not

included in the present investigation.

The positive result here means that further testing and analysis of the Fe lines with a larger line sample and smaller $v \sin i$ and A(Fe) grid sampling is fully justified.

Through this fitting process I am able to give an estimate to the rotational velocity of HD 140283. The mean $v \sin i$ value of the 17 lines is found to be $2.41 \pm 0.07\,\mathrm{km\,s^{-1}}$ where the error is taken as the standard error ($\sigma/\sqrt{N}$). This value agrees well with the upper limit set in Chapter 3, which was $v \sin i < 3.9\,\mathrm{km\,s^{-1}}$, and at the 1σ level with the $v \sin i$ value inferred by Collet et al. (2009) during their 3D investigation of f_{odd}: $v \sin i = 2.58\,\mathrm{km\,s^{-1}}$. There was no uncertainty stated by Collet et al..

5.4 Discussion and conclusions

In this chapter I began the first stages of a much larger investigation. The goal at this stage was to ascertain whether 3D synthetic profiles better fit their counterpart observed line profiles than the traditional 1D LTE approach. For this I chose the relatively uncomplicated Fe lines, used to determine the macroturbulence for HD 140283 in Chapter 3, rather than the much more complicated Ba II 4554 Å line. This was done by modelling 90 Fe lines from the original 93 lines, of which 17 were modelled successfully, and comparing their fits with the ones found during the 1D analysis. It would appear that pursuing a 3D analysis of HD 140283 is indeed warranted, as red-wing fitting problems found during the 1D analysis have been all but eliminated. However, several other issues arose during the 3D analysis. From Fig. 5.7, it is clear that there are inconsistencies in the best fit Fe abundances between the 1D and 3D synthesis, and, from Fig. 5.8, that the 1D analysis is, on average, better fitting the line cores.

Exploring the poor fit in the line cores by the 3D synthetic profiles would require further synthesis to create synthetic spectra with finer abundance sampling. This would improve the accuracy of the spline interpolation done during the χ^2 analysis and may fix this problem. This might slightly decrease the abundance differences between the 1D and 3D best fits, but probably not by as much as has been found since the lines' equivalent widths are well reproduced both in 1D and 3D. (Note that the χ^2

fitting does not force the equivalent widths of the observed and synthesised profiles to be identical.) However, the 3D profiles require a smaller Fe abundance. This could contribute partially to the worsening of the fits found in the line cores but the average abundance difference, $\langle A(\mathrm{Fe})_{\mathrm{3D-1D}} \rangle = -0.22$, would certainly not be explained by slight deviations between the best fit equivalent widths.

Rather, differences between the 1D and 3D atmospheres may explain the abundance differences. Fig. 5.9 shows the temperature and optical depth relationships for both atmospheres, as well as the temperature differences between them. There is clearly little consistency in the temperatures through the various layers in the two atmospheres. Asplund & García Pérez (2001) state that cooler temperatures associated with metal-poor 3D model atmospheres are the result of no longer fulfilling radiative equilibrium and instead solving the time-dependent energy equation, but they caution that the effect of radiative heating in 3D model atmospheres may currently be underestimated.

Frebel et al. (2008) and Collet et al. (2006) find $\langle A(\mathrm{Fe})_{\mathrm{3D-1D}} \rangle = -0.30$ and -0.24, respectively during their 3D investigations of the ultra metal-poor star HE 1327 − 2326, similar to the result found here for HD 140283. The deviation in 3D and 1D abundances is explained in Frebel et al. (2008) as the result of two things:

1. The cooler temperatures in the outer atmosphere of the 3D atmosphere allows for a significant fraction of Fe I opacity and hence lines to form in this region. This leads to much stronger line profiles in the 3D model than in 1D. This in turn leads to much smaller abundances being inferred in 3D than in 1D for the same equivalent widths. Fig. 5.9 shows almost identical temperature structures for HD 140283's 3D atmosphere as for HE 1327 − 2326 (Frebel et al. Fig. 1). Also, Frebel et al. illustrate the fraction of neutral Fe as a function of optical depth, which again shows an enhancement in the 3D Fe fraction at smaller values of optical depth.

2. Any given Fe I line forms at different depths in 1D than in 3D. This is illustrated by a contribution function diagram as a function of optical depth (their Fig. 5) for

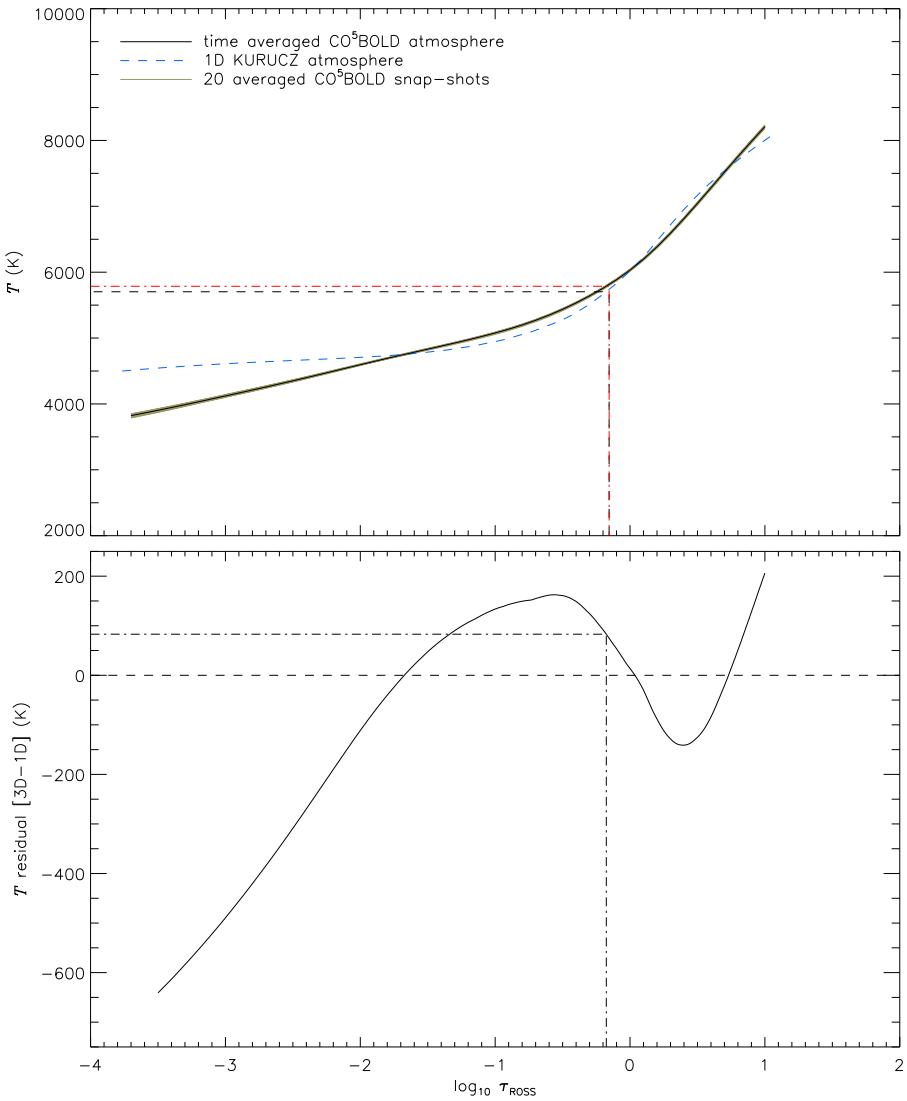

Fig. 5.9: Variations between the 1D KURUCZ06 (*blue dashed line*) and 3D CO^{5}BOLD (*solid black line*) model atmospheres for $T_{\rm eff} = 5750$, $\log g = 3.70$ and [Fe/H] $= -2.50$. *Top*: The two atmospheres over-plotted. The red dash-dot and black dashed lines show the temperature at which the 3D and 1D atmospheres reach $\tau_{\rm ROSS} = \frac{2}{3}$ respectively. In the Kurucz atmosphere this is found to be 5703 K and for the CO^{5}BOLD atmosphere the temperature is found to be 5786 K. *Bottom*: The residual temperature variation between the 3D and 1D atmospheres over the same optical depth range. The two atmospheres show large deviations in temperature for certain optical depths. The black dash-dot line shows that at $\tau_{\rm ROSS} = \frac{2}{3}$ the temperature residual is 83 K.

the Fe I 3859.9 Å line[5]. By comparing this with the temperature stratifications of the 1D and 3D models it shows that the majority of the absorption of the outgoing intensity of the Fe lines is found in higher layers of the atmosphere under 3D, where the temperature differences between the two models are larger.

[5]The contribution function in this particular instance is defined as the outgoing contribution intensity, following Magain (1986), rather than $\mathrm{d}\mathfrak{F}_\nu/\mathrm{d}\log\tau_0$ (Gray, 2008, his Fig. 13.2), where τ_0 is defined as the optical depth at a specific wavelength. The former is used, as calculating $\mathrm{d}\mathfrak{F}_\nu/\mathrm{d}\log\tau_0$ for the 3D synthetic line is highly non-trivial (Collet, 2012).

Similar departures in the Fe I abundance were found in Collet et al. (2006). It would appear likely that the abundance departures presented in this thesis are a result of the differences between the temperature profiles of the 1D and 3D LTE atmospheres. However, it would be naive to assume just that because similar results are found, they should have the same cause. Further investigation into this matter is required before this result is verified.

Fig. 5.10 shows how A(Fe) behaves as a function of equivalent width (*left panel*) and excitation potential (*right panel*). Looking at the left panel first, it is shown that both the 1D and 3D case have high levels of scatter as shown by the errors in the gradients associated with both ordinary least squares (OLS) plots, and their appears to be a trend on A(Fe) with equivalent width for both paradigms, more so in 3D. This could show a poor choice in microturbulence for the 3D synthesis, although the trend could equally be due to random scatter, which could be removed with a larger sample of Fe lines. Similarly the right panel seems to indicate that the four outliers, with the largest abundance departure, in the OLS (from the left panel) have the lowest excitation potentials. It appears that a large trend on A(Fe) exists with χ in 3D, indicating that larger departures in A(Fe) are expected in Fe lines with lower χ. This may signal problems with the temperatures. It could also be due to random scatter though it is a 4σ effect. A larger number of Fe lines is required to confirm this.

It would be difficult at this stage to predict how the differences in the 1D and 3D models would affect Ba. To assume that abundance determinations would yield similar departures as seen in Fe I would be naive. Unfortunately, Collet et al. (2009) did not report the Ba abundances found during their analysis of the Ba II 4554 Å line isotope configuration. They did, however, report that the application of 3D model atmospheres enhanced the s-process contribution to the line. When the 3D and 1D abundance limits for Ba are compared for HE 1327 − 2326 in Frebel et al. (2008), the 4554 Å abundance limits are $A(\mathrm{Ba})_{\mathrm{3D}} < -2.39$ and $A(\mathrm{Ba})_{\mathrm{1D}} < -2.14$. For the 4934 Å line they are $A(\mathrm{Ba})_{\mathrm{3D}} < -2.23$ and $A(\mathrm{Ba})_{\mathrm{1D}} < -2.04$. Therefore both lines show a decrease in their upper abundance limit, consistent with the observed behaviour of Fe I line abundances. The same values for the 4934 Å line abundance limits were also reported by Collet

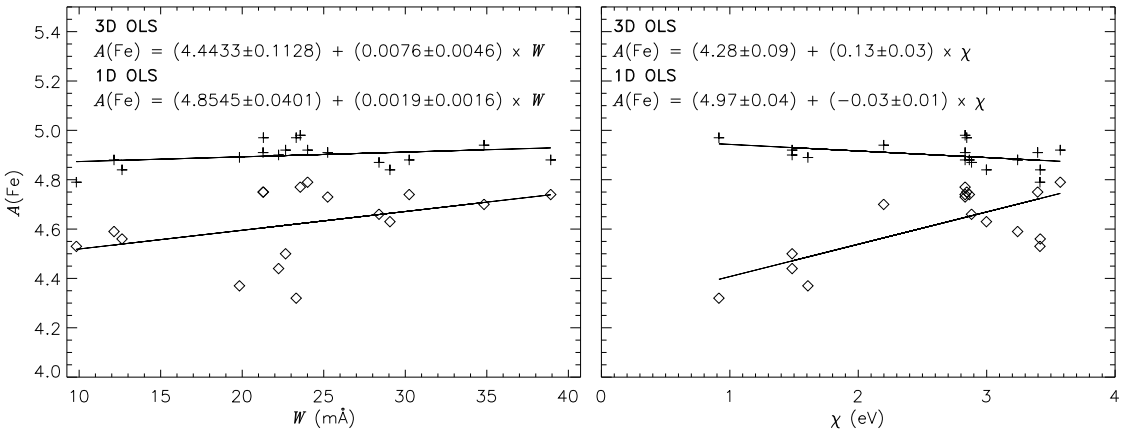

Fig. 5.10: *Left panel*: A(Fe) as a function of equivalent width for both the 1D (*crosses*) and 3D (*diamonds*) case. Equations of the best fit OLS are included for each case. It is shown that a slight trend exists in both cases, but particularly in the 3D. This could be an indication of a poorly chosen microturbulence. However, it is more likely that a bias caused by the small selection of lines exists when one considers the error estimate associated with the gradient of the OLS. *Right panel*: A(Fe) as a function of excitation potential (χ). It would appear that larger deviations in the 3D-1D abundances occur in lines with smaller values of χ. However, without a larger sample, this is difficult to determine.

et al. (2006). If one were to use the results shown in Fig. 5.10 (right panel), indicating that departures between the 1D and 3D abundances increase as excitation potential decreases, the Ba abundance would be expected to decrease given that the excitation potential of the line is 0 eV. I remind the reader that inferring this with the small Fe line sample presented here would be naive as such a trend maybe the result of scatter, which could be removed with a larger Fe line sample.

5.5 Future work

The project presented here represents the first stage in a much larger, much more detailed investigation. It was designed to test whether pursuing such a complex and time consuming analysis would improve on obvious shortcomings of the older, more traditional method of 1D LTE line synthesis. As it appears that using 3D models to fit absorption lines from high quality data does improve upon the traditional 1D LTE approach, there is cause to proceed with such an undertaking. A first step will be to resolve the fitting problems described in §5.3 by computing at finer grid spacings.

My intention is to complete a like-for-like re-investigation of Chapter 3, employing

3D hydrodynamic model atmospheres. Completion of the Fe line analysis will allow me to further understand CO^{5}BOLD and LINFOR3D, as work with them thus far has been limited.

Fully understanding and exploring the reasons behind the abundance departures seen in Fig. 5.7 would be useful. By completing that analysis for all 90 lines, I will also be able to assign a robust value to the rotational broadening of HD 140283. From the 1D analysis in Chapter 3, I can assume this to be $< 3.9\,\mathrm{km\,s^{-1}}$ and from the follow-up work on 17 Fe lines used in this chapter I have found this value to be $v \sin i = 2.41 \pm 0.07\,\mathrm{km\,s^{-1}}$, which agrees well with the limit set during the 1D investigation and also agrees at the 1σ level with the $v \sin i$ value used in the 3D Ba II synthesis by Collet et al. (2009). The final stage to this project will include the analysis of the Ba II 4554 Å line in 3D.

The new observational technique that passes the starlight through an I_2 absorption cell was mentioned in §4.5. The purpose was to improve upon errors in wavelength shifts, which affect the instrumental profile, thereby allowing calculation of the shape of the instrumental profile at any time (Butler et al., 1996). For the work presented in this chapter, I have used the traditional method of modelling the instrumental profile as a Gaussian (Aoki et al., 2004). This was to remove any avoidable inconsistencies between the 1D (Chapters 3 & 4) and 3D (Chapter 5) synthetic profiles so that any remaining deviations would be attributed to the synthesis. Astronomers working with the I_2 observational technique are able to achieve Doppler precisions $< 3\,\mathrm{ms^{-1}}$. We have already seen that even with the quality of spectroscopic data used in the present work, 1D models cannot replicate many of the astrophysical features that appear in line profiles. The same astrophysical effects, plus ones undetectable by traditional observations, would become even more dominant as systematic uncertainties such as instrumental effects are removed. Therefore the implementation of such a technique would be of little value if one continues to employ 1D spectrum synthesis to analyse this data. However, it seems from this initial investigation that the 3D technique employed here appears to improve upon these fitting issues. Perhaps then using 3D models in the future in conjunction with high quality spectra observed using the I_2 cell technique

will improve on errors currently associated with profile replication, and push current understanding of Galactic chemical evolution even further.

My research after this major project may take a slightly different direction to the one I have spent the last three years on. There are still many unexplored areas of spectrum synthesis yet to pursue with 3D model atmospheres, e.g. comparing them to high resolution data which have been obtained using the I_2 technique, so that improvements on instrumental and hence stellar line shape could be sought. Currently, the exploration and adoption of 3D atmospheres is still in its infancy and requires further development. In particular, I found the execution of LINFOR3D complex because it is still in its testing phase. Improvements to the interface would be useful, e.g. the addition of another module that calculates the relevant pressure broadening terms during the line synthesis so that the user can process new synthetic spectra quicker than is currently possible.

References

Aoki, W., Inoue, S., Kawanomoto, S., Ryan, S. G., Smith, I. M., Suzuki, T. K., & Takada-Hidai, M. 2004, A&A, 428, 579 [ADS]

Asplund, M., Carlsson, M., & Botnen, A. V. 2003, A&A, 399, L31 [ADS]

Asplund, M. & García Pérez, A. E. 2001, A&A, 372, 601 [ADS]

Barklem, P. S., Anstee, S. D., & O'Mara, B. J. 1998, PASA, 15, 336 [ADS]

Butler, R. P., Marcy, G. W., Williams, E., McCarthy, C., Dosanjh, P., & Vogt, S. S. 1996, PASP, 108, 500 [ADS]

Cayrel, R., Steffen, M., Chand, H., Bonifacio, P., Spite, M., Spite, F., Petitjean, P., Ludwig, H.-G., & Caffau, E. 2007, A&A, 473, L37 [ADS]

Collet, R. 2012, private Comminication, *Email correspondence*

Collet, R., Asplund, M., & Nissen, P. E. 2009, Publications of the Astronomical Society of Australia, 26, 330 [ADS]

Collet, R., Asplund, M., & Trampedach, R. 2006, ApJ, 644, L121 [ADS]

de Boer, C. R. & Kneer, F. 1992, A&A, 264, L24 [ADS]

de Boer, C. R., Kneer, F., & Nesis, A. 1992, A&A, 257, L4 [ADS]

Dravins, D., Lindegren, L., & Nordlund, A. 1981, A&A, 96, 345 [ADS]

Frebel, A., Collet, R., Eriksson, K., Christlieb, N., & Aoki, W. 2008, ApJ, 684, 588 [ADS]

Freytag, B., Steffen, M., & Dorch, B. 2002, Astronomische Nachrichten, 323, 213 [ADS]

Freytag, B., Steffen, M., Ludwig, H.-G., Wedemeyer-Böhm, S., Schaffenberger, W., & Steiner, O. 2012, Journal of Computational Physics, 231, 919 [ADS]

Freytag, B., Steffen, M., Wedemeyer-Böhm, S., Ludwig, H.-G., Leenaarts, J., Schaffenberger, W., Allard, F., Chiavassa, A., Höfner, S., Kamp, I., & Steiner, O. 2010, in Astrophysics Source Code Library, record ascl:1011.014, 11014 [ADS]

García Pérez, A. E., Aoki, W., Inoue, S., Ryan, S. G., Suzuki, T. K., & Chiba, M. 2009, A&A, 504, 213 [ADS]

Gray, D. F. 2008, The Observation and Analysis of Stellar Photospheres (Cambridge: Cambridge University Press, 2008.) [ADS]

Lind, K. 2012 - in prep, proc. IAP Conf. "Lithium in the Cosmos" [LINK]

Lind, K., Asplund, M., & Barklem, P. S. 2009, A&A, 503, 541 [ADS]

Magain, P. 1986, A&A, 163, 135 [ADS]

Nordlund, Å., Stein, R. F., & Asplund, M. 2009, Living Reviews in Solar Physics, 6, 2 [ADS]

Osorio, Y., Barklem, P. S., Lind, K., & Asplund, M. 2011, A&A, 529, A31 [ADS]

Schaffenberger, W., Wedemeyer-Böhm, S., Steiner, O., & Freytag, B. 2005, in ESA Special Publication, Vol. 596, Chromospheric and Coronal Magnetic Fields [ADS]

Steffen, M., Ludwig, H. G., & Wedemeyer-Böhm, S. 2010, LINFOR3D User Manual, Tech. rep. [LINK]

Steffen, M., Steenbock, W., Holweger, H., & Lemke, M. 1981, Program LINLTE.FOR (LINFOR) Fine analysis and spectrum synthesis of stellar spectra, Tech. rep., University of Kiel [LINK]

Wedemeyer, S. 2003, PhD thesis, University of Kiel [LINK]

Wedemeyer, S., Freytag, B., Steffen, M., Ludwig, H.-G., & Holweger, H. 2004, A&A, 414, 1121 [ADS]

Chapter 6: Conclusions and further work

The Ba isotope ratios have been measured in six metal-poor stars with the aim of determining the nucleosynthetic origin of the element in the early phases of the Galaxy. Currently prescribed theory (Truran, 1981) based on observations of metal-poor stars in the Galaxy (Spite & Spite, 1978) and observationally-constrained nucleosynthetic models (Arlandini et al., 1999) suggest that in the early phases of Galactic evolution, elements synthesised via the r-process would be more abundant than those synthesised via the s-process. When Magain (1995) attempted to measure the isotope ratios directly (in HD 140283) he found, contrary to expectations, that the s-process dominated. It could be argued that this conclusion is the result of the quality of the spectrum used for the analysis, which limits the accuracy with which the isotopes in the observed Ba II 4554 Å line can be measured, as the isotopic splitting of the line is barely resolvable due to the finite natural, thermal and pressure broadening of stellar spectral lines, made worse by additional turbulent and instrumental broadening.

For this reason, I embarked on a study of six metal-poor stars, one of which was HD 140283, using high resolution ($R \equiv \lambda/\Delta\lambda = 90\,000 - 95\,000$), very high signal-to-noise ($S/N = 500 - 1100$) stellar spectra obtained with the High Dispersion Spectrograph (HDS) on the Subaru 8.2 m telescope.

6.1 Conclusions

I have found that the six metal-poor stars ($-3.17 \leq$ [Fe/H] ≤ -2.24) analysed show a high s-process signature. This was found by fitting fully resolved synthetic 1D LTE line profiles (using a χ^2 routine) to observed Ba II 4554 Å lines in high resolution ($R = 90\,000 - 95\,000$), very high signal-to-noise ($S/N = 550 - 1100$) stellar spectra to determine the Ba isotope ratio, $f_{\rm odd}$, where $f_{\rm odd} = [N\,(^{135}{\rm Ba}) + N\,(^{137}{\rm Ba})]\,/N\,({\rm Ba})$. It was found that only one star, BD-04° 3208, had a physical $f_{\rm odd}$ value, as determined by

its χ^2 minimum, $f_{\rm odd} = 0.18 \pm 0.08$, which still indicates a high s-process contribution of $80 \pm 23\%$. A further two stars, HD 140283 and BD+26° 3578, had values of $f_{\rm odd}$ that lie beyond physical $f_{\rm odd}$ limits (as set in Arlandini et al., 1999) of $f_{\rm odd} = 0.02 \pm 0.06$ and $f_{\rm odd} = 0.08 \pm 0.08$, respectively. The last three stars in the sample, HD 122563, HD 88609 and HD 84937, were found to have purely mathematical solutions, as the Ba isotope ratios found are physically impossible, $f_{\rm odd} = -0.12 \pm 0.07$, -0.02 ± 0.09 and -0.05 ± 0.11, respectively. To confirm the isotope ratio in one star, HD 140283, the isotope ratio in the Ba II 4934 Å line was also measured. Fe line blends found in the blue wing of the Ba 4934 Å line made this line difficult to measure; if the blends were synthesised with inaccurate line information, they would affect the determination of $f_{\rm odd}$. Nevertheless, it was found that $f_{\rm odd} = 0.11 \pm 0.19$, which agrees well with $f_{\rm odd} = 0.01 \pm 0.06$ as measured from the 4554 Å line, although the 4934 Å result has a high level of inaccuracy ($\sigma_{f_{\rm odd}} = \pm 54\%$) caused by the Fe blends' uncertain line strengths. Results from both these lines were combined using inverse-variance-weighting which gave the overall Ba isotope ratio to be $f_{\rm odd} = 0.02 \pm 0.06$ (as listed above). No other stars in the sample were analysed using the 4934 Å line because of these uncertainties. The high s-process signatures found in these metal-poor stars conflict with current theory which states that the r-process should become dominant over the s-process as the Galaxy becomes more metal-poor (Truran, 1981).

The isotopic results are especially troubling when they are compared to their counterpart [Ba/Eu] detections. Such a ratio is often used to describe the ratio of the r- and s-process in a star. A low ratio (~ -0.69) would suggest an r-process origin and a high ratio ($\sim +1.13$) would suggest an s-process origin (Arlandini et al., 1999). The Eu II 4129 Å line could only be measured for three stars in my sample. For HD 140283 I assigned a lower limit of [Ba/Eu] > -0.66. For HD 122563 and HD 88609 I found this ratio to be [Ba/Eu] $= -0.20 \pm 0.15$ and -0.47 ± 0.15, respectively. Therefore each measurement of [Ba/Eu] for these two stars show a strong r-process regime, not the high s-process contribution, as the isotope ratios found in the Ba lines would suggest, whereas the limit found in HD 140283 would be consistent with everything. This would seem to indicate that there is a problem with the isotope ratio technique.

Lambert & Allende Prieto (2002) found that $f_{\rm odd}$ is extremely sensitive to the macroturbulent broadening of a star. Using a Gaussian to model the macroturbulence in HD 140283 it was found (in Chapter 3) that $\delta f_{\rm odd}/\delta FWHM = -0.7\,({\rm km\,s^{-1}})^{-1}$. Therefore, it was important to fully constrain macroturbulence with a high level of accuracy. The star's macroturbulence was found by fitting synthetic Fe lines, constructed using a 1D LTE radiative transfer code and 1D model atmospheres, to several dozen observed Fe line profiles for each star. Initially macroturbulent broadening was modelled using a Gaussian profile. Two other types of symmetric profile were also used to model HD 140283's macroturbulence; a radial-tangential and a $v \sin i$ profile. It was found that the $v \sin i$ profiles, which are used to model the effect of rotation on line broadening, fit the Fe lines poorly, relative to when they were fit with a Gaussian. This was not surprising as HD 140283 is a subgiant star, which should have at most a small rotational speed (Gray, 1989). Nevertheless, through this analysis an upper limit to the star's rotation was set at $v \sin i < 3.9\,{\rm km\,s^{-1}}$. It was found that the radial-tangential profiles better fit the majority of the Fe lines than the alternative Gaussian profiles. Therefore, the macroturbulence and $f_{\rm odd}$ values were determined for all six stars using both the radial-tangential and the Gaussian broadening profiles. It was found for all six stars that, while using a radial-tangential broadening profile fit the majority of the Fe lines and every Ba II line better, there was almost no difference in the $f_{\rm odd}$ value found using either profile.

An alternative conclusion

If the results found in the present study were confirmed in subsequent studies, and studies of other stars were found to further complement those results, they would have a severe impact on the Truran (1981) model of heavy-element production in the early universe. A possible alternative conclusion that could explain those results without dismissing the Truran scenario is discussed here by qualitatively addressing how s- and r-process material is distributed into the interstellar medium (ISM), by considering the effects their sites have on their surroundings.

It is fairly well established that the main s-process occurs in low- to intermediate-

mass asymptotic giant branch (AGB) stars while they evolve through a stage of periodic thermal pulses (TP-AGB). The r-process site(s) is only theoretical as it has never been directly observed. However, the most agreed upon location for the r-process is a supernova (SN) explosion. These sites are discussed at length in Chapter 1.

A SN has the following effects on the ISM. It quickly distributes stellar matter and it heats it up. The death of a low- to intermediate-mass star is far less energetic and distributes stellar matter slowly, which does not heat up the ISM to the same degree as the SN explosion. Nevertheless, there will be sporadic pockets of ISM that have been polluted with r-process material, and later other pockets of ISM that have been polluted with s-process material. These pockets of ISM will eventually become part of new star forming regions. The scenario suggested here questions the time-scales involved between heavy-element contamination of these two different ISM regions and the subsequent birth of new stars forming from the polluted gas.

The effect of heating the surrounding ISM by a SN temporarily prohibits further star formation until the temperature is reduced. Details on how star forming gas clouds lower their temperature by radiative cooling can be found in §1.1 and §1.2. As the heated ISM and potential star forming regions cool, the distribution of s-process material will increase through the deaths of evolved low- to intermediate-mass stars. The impact of their deaths is less severe on the surrounding ISM and subsequent star forming regions, polluted with s-process material, will continue to form without major hindrance to the time-scale of their collapse. Therefore future generations of stars containing s-process materials can form much sooner after the death of a low- to intermediate-mass star than stars that form following a SN event, which will contain r-process material.

A consequence of the s-process requires that Fe seed nuclei be present in the formation of the star, whereas Fe is not required in for a star that will r-process. Therefore this scenario would not affect the earliest generations of star formation, which would follow the violent deaths of super-massive, metal-free population III stars. Heating of the surrounding ISM will still halt new star formation but up until this point only the r-process will have been able to occur, as there were no Fe seed nuclei present in

the formation of any of the first stars for the s-process to occur. This means that for the first few generations of stars the r-process would most certainly dominate over the s-process.

However, this scenario might occur in later generations of stars that contain material from several generations of stars, such as those analysed in the present work and would explain why they seem to have a higher s-process fraction, relative to the r-process. A modification to the Truran scenario would be required if the s-process enhancement over the r-process is found observationally in the most metal-poor stars. However, this scenario is highly speculative at the present time. Also, other heavy-element studies of metal-poor stars that analyse their abundance patterns, particularly the [Ba/Eu] ratio (e.g. Sneden et al., 1996; Mashonkina & Zhao, 2006; Frebel et al., 2007; Mashonkina et al., 2010; Sitnova & Mashonkina, 2011, and references therein) seem to support the Truran scenario as they replicate metallicity scaled solar system r-process abundance distributions.

Further testing

In an attempt to better fit the Fe lines in HD 140283 and HD 122563, NLTE profiles were fit to a selection of lines used in the LTE investigations. The NLTE profiles were broadened using Gaussian profiles. A comparison with the LTE paradigm showed no improvement to the poor fits found using Gaussian profiles under LTE. Both these approaches use atmospheres that assume a 1D geometry and employ symmetric profiles to model line broadening. The high quality spectra used in this work show absorption line profiles with subtle asymmetries, particularly a depression of the flux $\sim 100\,\mathrm{m\AA}$ redward of the line centre. Therefore it was not surprising that the NLTE profiles showed no improvement over the LTE profiles to the fits of asymmetric observed lines. However, as I discuss in §6.2, using alternative approaches to determine the isotope ratio of Ba under NLTE are available.

By process of elimination, it seemed that the implementation of time-dependent 3D atmospheres to model real stellar dynamics, thought to be responsible for stellar absorption line asymmetries, was the next logical step to solve line profile fitting prob-

lems. Through fitting 3D synthetic Fe lines to 17 observed profiles in HD 140283, a clear improvement over the 1D LTE and NLTE fits was found. It would appear then that 1D/3D is a larger issue than LTE/NLTE. Lines synthesised under 3D LTE were able to completely model or at least partially compensate for line asymmetries found in the observed spectra of the 17 Fe I lines. However, the 3D synthetic spectra did not fit the line cores as well as the 1D spectra.

It was expected that 3D atmospheres would fully model complex motions in stellar atmospheres, partially responsible for the Doppler broadening of an absorption line. As such, any excess broadening seen between the observed and 3D synthetic profiles was assumed to be due to the star's rotation. The rotational broadening of HD 140283, set from the analysis of the 17 Fe lines, was found to be $v \sin i = 2.41 \pm 0.07\,\mathrm{km\,s^{-1}}$. This value agrees well with the upper limit, $v \sin i < 3.9\,\mathrm{km\,s^{-1}}$, set during the 1D LTE investigation and agrees at the 1σ level with the value inferred by Collet et al. (2009), $v \sin i = 2.58\,\mathrm{km\,s^{-1}}$, during their 3D analysis of the Ba isotopes for the same star.

Large abundance differences, $\langle A(\mathrm{Fe})_{\mathrm{3D-1D}} \rangle = -0.22$, were found between the 3D and equivalent 1D best fits. Frebel et al. (2008) found a similar result for HE 1327−2326 and explain that this is an effect of the lower temperatures in the outer atmospheres of 3D synthetic models, relative to their 1D counterparts, which Asplund & García Pérez (2001) state is an expected result when no longer fulfilling radiative equilibrium and instead solving the energy equation for time-dependent 3D models. By comparing the Fe abundances to the lines' equivalent widths (W) and excitation potentials (χ) I found a weak dependence of A(Fe) on W and a stronger dependence on χ. The small dependence on W could indicate a poorly chosen microturbulence, whereas the larger dependence on χ could be the result of problems with the 3D model's temperatures. However, these dependencies could be the result of scatter, which is exacerbated by the limited number of lines analysed. I also find that the 3D synthetic profiles under-fit the observed Fe line cores in all 17 lines. This could also indicate an issue with the 3D synthesis, or could simply be a result of fitting errors caused by the use of coarse A(Fe) grids synthesised under 3D LTE. Further investigation is required to confirm/disprove these suspicions.

6.2 An alternative approach to determine $f_{\rm odd}$

While I have cited the works of Magain (1995) and Lambert & Allende Prieto (2002) several times when comparing my results in Chapters 3 & 4 to other studies conducted in the same manor, I have neglected to mention any other studies that try to calculate the odd-to-even isotope ratio of Ba using methods other than the ones I use in the present work. In this section I will discuss some other methods for obtaining the isotope ratio of Ba conducted by other groups.

Most notably, Mashonkina & Zhao (2006) conducted an analysis of the Ba even-to-odd isotope ratios for 25 stars in the thin and thick disks using an intriguing NLTE technique first discussed in Mashonkina et al. (1999). The procedure relies on an NLTE analysis as very accurate abundance determinations need to be made that cannot be replicated under the assumption of LTE. This is especially evident in the subordinate Ba II lines, which are very sensitive to NLTE effects.

Mashonkina & Zhao used subordinate Ba II lines (the 5853 and 6496 Å lines) to determine the Ba abundance of each star. The difficulty here is accurately identifying and distinguishing between the Ba profiles and the well known blends that affect the 5853 and 6141 Å lines. As I found in Chapter 3 when I analysed the 4934 Å line, this can alter abundances, and for my work, severely change the isotope ratio. In fact the 6141 Å line was too strongly blended with the Fe I 6141.7 Å line to allow for accurate abundance determinations and was subsequently dropped from further analysis. However, they make no intention to calculate the isotope ratio at this stage.

Their method for determining the isotope ratio in the Ba II 4554 Å resonance line relies on the assumption that the larger the r-process fraction is, the larger the fraction of odd isotopes is, and hence the greater the total energy absorbed by the line, while the subordinate lines remain unchanged (Mashonkina et al., 1999). Therefore by forcing the abundances of all the Ba lines analysed to be the same, altering the isotope ratios of the 4554 Å line with constant abundance leads to stronger (r-process dominated) or weaker (s-process dominated) profiles. This has a notable advantage over the method used in the present work as one does not require extremely high resolution and signal-

to-noise spectra to determine the isotope fraction by measuring the change in line shape. All that is required is a measurement of the equivalent widths of each line.

However, there are a few disadvantages to using such a method, as I shall now discuss. Firstly to work with any atomic species under the assumption of NLTE requires the use of a model atom, the accuracy of which increases the more complete the level populations are, which should ideally include the transitions in both the previous and subsequent ionisation states. This is very time consuming. Improvements to the model atom complete with further transitions are constantly being published, e.g. the model atom used in Mashonkina & Zhao (2006) was greatly improved and closer to completion over the one used in Mashonkina et al. (1999). Another problem when using this method to analyse extremely metal-poor stars is that the subordinate 6496 and 5853 Å lines disappear from observed spectra at [Fe/H] < -2.3 and < -1.9 respectively (Mashonkina et al., 1999). This means that of the six stars in my sample, with $-3.17 \leq$ [Fe/H] ≤ -2.24, only one, HD 84937, could be analysed using this method. Finally, this method requires that the 4554 Å resonance line is saturated so that when one increases the fraction of the odd isotopes in the line, it works to cancel the saturation of the line and drive the line formation depth downwards. This means that small changes in abundance from the subordinate lines do not lead to large compensations of the fractional abundance of the odd isotopes so that the model and observed equivalent widths are equal (Mashonkina & Zhao, 2006). Therefore the types of stars that can be studied using this method are limited.

Overall, however, this is an interesting alternative approach, which has advantages and disadvantages compared to the line profile method applied in the present work. Both still require a correct treatment of the velocity field; the Mashonkina & Zhao method requires that the microturbulence is correctly established to avoid over or under saturation of the Ba lines and the technique presented in the current work requires a carefully calculated macroturbulence when fitting the Ba line(s) so that the broadening of the star does not affect the isotope ratio.

6.3 Future work

From the work conducted in this thesis, it would appear that radiative transfer codes that assume LTE and employ 1D atmospheres fail to produce trustworthy results when one is attempting to reproduce accurately the behaviours of absorption lines obtained with the latest high resolution, high signal-to-noise spectra. This was shown through their failure to model subtle asymmetric behaviours visible in high quality stellar spectra. The asymmetry is caused by complex motions of particles in dynamic stellar atmospheres, but is absent from the models because of the relatively simplistic assumptions made in their construction, as listed in §2.1.

It would seem that where these codes fail, codes that employ time-dependent, 3D hydrodynamics appear to be capable of modelling the intricate behaviours of a stellar atmosphere, and therefore could be considered more useful than the 1D LTE alternative when fitting synthetic profiles to high quality observed spectra. In fact, abundance calculations using such codes are becoming more frequent (Asplund, 2005) and are gradually replacing classical approaches that employ 1D atmospheres (Freytag et al., 2012). For example, new solar abundances calculated using such codes are available (Grevesse et al., 2007) and show deviations in the solar abundances previously determined using classical 1D atmospheres (Grevesse & Sauval, 1998).

However, the complexities of modelling 3D atmospheres and computing the radiative transfer for absorption lines is currently extremely computer intensive as these codes are still under development, as explained in §5.2. As such, modelling only a handful of lines, like those presented in this work, is extremely time consuming. However, the positive results found justify the extra time needed for a much more detailed investigation. Current 3D analyses of the Ba isotopes, however, indicate an enhancement of the s-process, relative to the equivalent 1D LTE analysis (Collet et al., 2009). If this was replicated in the present work, every star in the sample would show extremely high s-process enhancements, further exacerbating differences in observation and current theory (Truran, 1981).

I intend to conduct an investigation which will fully replicate all avenues considered

in Chapter 3 during the modelling of both the Fe lines, used to determine the star's macroturbulence under 1D, and the Ba II 4554 Å line to determine the isotope ratios and the s- and r-process fractions under 3D LTE. Such an undertaking will require time consuming computations of the synthetic Fe profiles for the large A(Fe) and $v \sin i$ grid parameters, discussed in §5.3. Also, the Ba II line will require many hours, weeks or months of construction to produce a similar grid of isotope ratios to that used during the 1D LTE work. Through analysis of the 90 Fe lines, a more precise value of $v \sin i$ can be set, which will be used to model the rotational broadening in the Ba II line, just like the macroturbulence found in the Fe lines during the 1D LTE work was used to model the broadening of the Ba II line. Also, the problems discovered in the present work, namely the 3D Fe abundance departures, must be fully investigated to eliminate any potential synthesis errors such as incorrect microturbulence or temperature determinations, which based on Fig. 5.10 and Frebel et al. (2008), appear to have some small contribution to the current abundance departures found.

To build a better understanding of neutron-capture nucleosynthesis at early times several more heavy elements, and indeed, other metal-poor stars should be examined. This would also test the modifications to the Truran scenario, proposed in §6.1, by increasing the number of metal-poor stars that either seem to confirm or disprove it. As discussed in §2.5, such an analysis is complex but it is hoped that with the use of new observational techniques, discussed in §4.5 & §5.5, which should improve the quality of stellar spectra, combined with a fully 3D treatment of their atmospheres, a more detailed analysis should be possible. As a precursor to such work, I intend to carry out this investigation using the highest quality spectrum currently available to me (i.e. HD 140283's spectrum). The results found with this spectrum should indicate whether the lengthy and complex process of obtaining new observed stellar spectra using the I_2 observational technique would help attain isotope fractions of other heavy elements to high enough degrees of accuracy, or whether determining such values produce spurious results, even with high quality observed spectra. It would also be useful to examine at least one star using the methods described in §6.2 and compare it with the results from an analysis conducted using the methods employed in the present work as a consistency

check between both methods.

The application of such codes is not limited to just abundance and isotope fraction determinations. As was mentioned in §5.5, other avenues of interest, such as stellar radial velocity measurements used to find extrasolar planets, could be explored using a fully 3D treatment of the synthetic profiles, as granulation and atmospheric turbulences, which 3D codes appear to model well (Freytag et al., 2012), plague accurate radial velocity measurements (Desort et al., 2009) and can lead to erroneous radial velocity measurements (Saar et al., 1998).

With the emergence of 3D codes, such as those discussed in this thesis, and their continued improvement, new avenues of investigation are emerging that should test current theories on Galactic chemical evolution (discussed in Chapter 1) to a higher level than previously seen. Coupled with new technologies that boast faster computational speeds, they will no doubt surface with greater frequency in the future.

References

Arlandini, C., Käppeler, F., Wisshak, K., Gallino, R., Lugaro, M., Busso, M., & Straniero, O. 1999, ApJ, 525, 886 [ADS]

Asplund, M. 2005, ARA&A, 43, 481 [ADS]

Asplund, M. & García Pérez, A. E. 2001, A&A, 372, 601 [ADS]

Collet, R., Asplund, M., & Nissen, P. E. 2009, Publications of the Astronomical Society of Australia, 26, 330 [ADS]

Desort, M., Lagrange, A.-M., Galland, F., Udry, S., Montagnier, G., Beust, H., Boisse, I., Bonfils, X., Bouchy, F., Delfosse, X., Eggenberger, A., Ehrenreich, D., Forveille, T., Hébrard, G., Loeillet, B., Lovis, C., Mayor, M., Meunier, N., Moutou, C., Pepe, F., Perrier, C., Pont, F., Queloz, D., Santos, N. C., Ségransan, D., & Vidal-Madjar, A. 2009, A&A, 506, 1469 [ADS]

Frebel, A., Christlieb, N., Norris, J. E., Thom, C., Beers, T. C., & Rhee, J. 2007, ApJ, 660, L117 [ADS]

Frebel, A., Collet, R., Eriksson, K., Christlieb, N., & Aoki, W. 2008, ApJ, 684, 588 [ADS]

Freytag, B., Steffen, M., Ludwig, H.-G., Wedemeyer-Böhm, S., Schaffenberger, W., & Steiner, O. 2012, Journal of Computational Physics, 231, 919 [ADS]

Gray, D. F. 1989, ApJ, 347, 1021 [ADS]

Grevesse, N., Asplund, M., & Sauval, A. J. 2007, Space Sci. Rev., 130, 105 [ADS]

Grevesse, N. & Sauval, A. J. 1998, Space Sci. Rev., 85, 161 [ADS]

Lambert, D. L. & Allende Prieto, C. 2002, MNRAS, 335, 325 [ADS]

Magain, P. 1995, A&A, 297, 686 [ADS]

Mashonkina, L., Christlieb, N., Barklem, P. S., Hill, V., Beers, T. C., & Velichko, A. 2010, A&A, 516, A46 [ADS]

Mashonkina, L., Gehren, T., & Bikmaev, I. 1999, A&A, 343, 519 [ADS]

Mashonkina, L. & Zhao, G. 2006, A&A, 456, 313 [ADS]

Saar, S. H., Butler, R. P., & Marcy, G. W. 1998, ApJ, 498, L153 [ADS]

Sitnova, T. M. & Mashonkina, L. I. 2011, Astronomy Letters, 37, 480 [ADS]

Sneden, C., McWilliam, A., Preston, G. W., Cowan, J. J., Burris, D. L., & Armosky, B. J. 1996, ApJ, 467, 819 [ADS]

Spite, M. & Spite, F. 1978, A&A, 67, 23 [ADS]

Truran, J. W. 1981, A&A, 97, 391 [ADS]

Appendix A:

Computer coding and input/output files

A.1 A KURUCZ06 model atmosphere

An example of a KURUCZ06 model atmosphere with parameters $T_{\rm eff}/\log g/[{\rm Fe/H}] = 5750\,{\rm K}/3.70\,{\rm dex}/-2.50$, the same parameters used for modelling HD 140283's atmosphere.

```
 TEFF  5750. GRAVITY  3.70 LTE
 TITLE K93 CDROM13 SDSC GRID, INTERPOLATED AND HEADER FUDGED
 OPACITY IFOP 1 1 1 1 1 0 1 1 1 0 0 1 1 0 0 0 1 0 1 1
 CONVECTION OFF 1.00 TURBULENCE OFF 2.00
 CORRECTION OFF
 PRESSURE OFF
 MOLECULES ON
 ITERATION 1
 PUNCH 5
 SURFACE FLUX
 ABUNDANCE SCALE 0.00316 ABUNDANCE CHANGE 1 0.911 2 0.089
 ABUNDANCE CHANGE  3 -11.45  4 -10.88  5  -9.25  6  -3.36  7  -4.04  8  -3.11
 ABUNDANCE CHANGE  9  -7.49 10  -4.60 11  -5.71 12  -4.41 13  -5.54 14  -4.40
 ABUNDANCE CHANGE 15  -6.58 16  -4.80 17  -6.40 18  -5.40 19  -6.91 20  -5.67
 ABUNDANCE CHANGE 21  -9.04 22  -7.04 23  -7.95 24  -6.36 25  -6.58 26  -4.53
 ABUNDANCE CHANGE 27  -7.11 28  -5.78 29  -7.60 30  -7.63 31  -9.21 32  -8.73
 ABUNDANCE CHANGE 33  -9.70 34  -8.80 35  -9.40 36  -8.80 37  -9.10 38  -9.10
 ABUNDANCE CHANGE 39  -9.79 40  -9.63 41  -9.75 42 -10.15 43 -20.00 44 -10.48
 ABUNDANCE CHANGE 45 -10.50 46 -10.48 47 -11.38 48 -10.08 49 -10.34 50 -10.34
 ABUNDANCE CHANGE 51 -10.40 52 -10.00 53 -10.60 54 -10.00 55 -10.90 56  -9.85
 ABUNDANCE CHANGE 57 -10.95 58 -10.39 59 -11.21 60 -10.55 61 -20.00 62 -11.06
 ABUNDANCE CHANGE 63 -11.52 64 -10.88 65 -11.60 66 -10.88 67 -11.50 68 -11.29
 ABUNDANCE CHANGE 69 -11.62 70 -11.24 71 -11.21 72 -11.40 73 -11.70 74  -9.48
 ABUNDANCE CHANGE 75 -11.40 76 -11.30 77  -9.84 78 -10.40 79 -11.73 80  -9.05
 ABUNDANCE CHANGE 81 -11.85 82 -10.18 83 -11.25 84 -20.00 85 -20.00 86 -20.00
 ABUNDANCE CHANGE 87 -20.00 88 -20.00 89 -20.00 90 -11.23 91 -20.00 92 -11.45
 ABUNDANCE CHANGE 93 -20.00 94 -20.00 95 -20.00 96 -20.00 97 -20.00 98 -20.00
 ABUNDANCE CHANGE 99 -20.00
 READ DECK 35 RHOX,T,P,XNE,ABROSS,PRAD,RHO
2.0434533E-03   4125.3 1.024E+01 5.147E+08 6.526E-05 6.718E-06 3.974E-11
1.9555026E-01   4499.6 9.800E+02 2.547E+10 8.883E-04 8.050E-04 3.487E-09
2.5616658E-01   4524.8 1.284E+03 3.221E+10 1.089E-03 1.119E-03 4.542E-09
3.3081833E-01   4548.3 1.658E+03 4.013E+10 1.319E-03 1.540E-03 5.836E-09
4.3298262E-01   4572.4 2.170E+03 5.041E+10 1.613E-03 2.175E-03 7.598E-09
5.6164247E-01   4595.6 2.815E+03 6.277E+10 1.957E-03 3.059E-03 9.804E-09
7.3234397E-01   4617.4 3.670E+03 7.792E+10 2.371E-03 4.364E-03 1.272E-08
9.5428640E-01   4636.8 4.783E+03 9.573E+10 2.850E-03 6.264E-03 1.651E-08
1.2502046E+00   4654.9 6.266E+03 1.174E+11 3.424E-03 9.123E-03 2.155E-08
1.6398417E+00   4672.4 8.219E+03 1.437E+11 4.110E-03 1.341E-02 2.816E-08
2.1536152E+00   4690.8 1.079E+04 1.764E+11 4.952E-03 1.991E-02 3.683E-08
2.8270702E+00   4711.6 1.417E+04 2.182E+11 6.008E-03 2.983E-02 4.813E-08
3.6990998E+00   4738.5 1.854E+04 2.751E+11 7.408E-03 4.501E-02 6.264E-08
4.8104167E+00   4773.4 2.411E+04 3.549E+11 9.316E-03 6.835E-02 8.084E-08
6.1913037E+00   4820.7 3.103E+04 4.738E+11 1.205E-02 1.042E-01 1.030E-07
7.8485451E+00   4885.8 3.934E+04 6.634E+11 1.622E-02 1.595E-01 1.289E-07
9.7691631E+00   4973.2 4.896E+04 9.823E+11 2.282E-02 2.451E-01 1.576E-07
1.1839594E+01   5095.9 5.934E+04 1.584E+12 3.434E-02 3.757E-01 1.864E-07
1.3969381E+01   5259.9 7.000E+04 2.794E+12 5.534E-02 5.805E-01 2.130E-07
1.5012367E+01   5360.5 7.523E+04 3.850E+12 7.224E-02 7.231E-01 2.247E-07
1.5975389E+01   5481.6 8.007E+04 5.512E+12 9.711E-02 8.959E-01 2.338E-07
1.6872589E+01   5623.7 8.456E+04 8.181E+12 1.342E-01 1.114E+00 2.407E-07
1.7689190E+01   5787.5 8.865E+04 1.253E+13 1.899E-01 1.390E+00 2.452E-07
```

```
1.8415186E+01   5973.6 9.230E+04 1.970E+13 2.749E-01 1.738E+00 2.473E-07
1.9046143E+01   6183.2 9.546E+04 3.166E+13 4.054E-01 2.175E+00 2.471E-07
1.9550453E+01   6423.8 9.798E+04 5.210E+13 6.138E-01 2.685E+00 2.440E-07
1.9978403E+01   6673.2 1.001E+05 8.406E+13 9.225E-01 3.303E+00 2.400E-07
2.0348253E+01   6910.7 1.020E+05 1.286E+14 1.337E+00 4.013E+00 2.359E-07
2.0677786E+01   7125.8 1.036E+05 1.845E+14 1.849E+00 4.778E+00 2.324E-07
2.0983185E+01   7319.9 1.052E+05 2.511E+14 2.457E+00 5.563E+00 2.294E-07
2.1275919E+01   7488.6 1.066E+05 3.238E+14 3.131E+00 6.332E+00 2.272E-07
2.1568996E+01   7648.1 1.081E+05 4.080E+14 3.919E+00 7.087E+00 2.253E-07
2.1866426E+01   7798.7 1.096E+05 5.036E+14 4.828E+00 7.828E+00 2.238E-07
2.2171928E+01   7941.5 1.111E+05 6.107E+14 5.868E+00 8.559E+00 2.226E-07
2.2489462E+01   8079.1 1.127E+05 7.311E+14 7.065E+00 9.288E+00 2.217E-07
 WAVELENGTH FL BY DL TO LL
 BEGIN                    1 COMPLETED
 END
```

A.2 A tc-shell script used to run ATLAS

An example of a tc-shell script used to automate the procedure of running ATLAS for many different parameters in order to create grids of stellar spectra for a single star.

```
#!/bin/csh
#-----------------Compile as runatlas_agFe_com filename.bmod----------------------
#
#--------------$1  is  model identifier, e.g. hd140283.cool.k89-----------------
if ( $#argv != 1) then                    # $#argv = # of arguments on command line
 echo ^G                                                  # leaves a line space
 echo Give model name on command line as e.g. hd140283.cool.bmod
 exit
endif
set star = $1:r                                    # Strips off trailing filename

#------------------------Setting user input parameters---------------------------
#
#--------------Gaussian microturbulence--------------
set TURB = 1.40
#--------------Gaussian macroturbulence--------------
foreach broad (5.00 5.20 5.40 5.60 5.80 6.00)          # Inc. instrumental profile
#---------Radial-tangential macroturbulence----------
#foreach zeta (4.00 4.20 4.40 4.60 4.80 5.00)          # Exc. instrumental profile
set zeta = 0.00
#------------If zeta not=0 then use this-------------
#set broad = 3.31                                       # The instrumental profile
#----AFE----
foreach AFe (-3.06 -3.16 -3.26 -3.36 -3.46 -3.56)
#-------------------------------------------------------------------------------
if (-w model.dat) mv model.dat model.dat.old
#----------------------Manipulating the atmosphere file-------------------------
sed \
-e '4s/TURBULENCE OFF 2.00/TURBULENCE OFF '$TURB'/' \            # microturbulence
-e 's/26  -4.53/26  '$AFe'/' \                                              # AFe
-e 's/FL BY DL TO LL/411.5 BY 0.001 TO 412.5/' \             # wavelength coverage
$1 > model.dat                                 # moving atmosphere into correct file
#-------------------------------------------------------------------------------
set num = "n_"$star"a"$AFe"M"$broad".out"
set flux = "syn."$star"a"$AFe"M"$broad".mdat.hdr"               # setting filename
\cp kurmol.ch mol.dat                                          # INPUT ATOMIC DATA
\cp linesnew2.dat lines.dat                                         # Input lines
echo Starting atlas_main ...
atlas_main.e                                        # Starting the main ATLAS program
#----------------------------checking the output--------------------------------
if ($status != 0) then
 echo ^G
 echo atlas_main.e failed!
 exit
endif
\mv flux.out fort.11                                  # OUTPUT WAVELENGTH,FLUX FILE
\mv numbers.out $num                                  # OUTPUT NUMBER DENSITIES ETC
if (-w fort.12) rm fort.12
echo Starting atlas_velbroaden ...
#--------------------Start the broadening of the synthesis-----------------------
atlas_velbroaden.e <<end_of_input                        # Input to "end_of_input"
$zeta                  ! zeta km/s
$vsini                 ! vsini km/s
```

```
$broad                  ! Gaussian FWHM km/s
0.0                     ! slope  per A
end_of_input
 if ($status != 0) then
     echo ^G
     echo atlas_velbroaden.e failed!
     exit
 endif
\mv fort.12 $flux                    # transfer final broadened output to filename
#------------------Strips header for compatibility with IDL-----------------------
set fluxtrim = $flux:r
if (-e $fluxtrim) \rm $fluxtrim
tail --lines=+4 $flux > $fluxtrim
#------------Housekeeping-move some files around to tidy work area up-------------
#
#-------------Note each file is over 15M check space to store them----------------
\mv $fluxtrim /data/agallagher/Project1/IDLwork/synthesis
\rm $num
\rm $flux
echo ^G
#--------------------------End of the Fe abundance loop---------------------------
end
#------------------------End of the radial-tangential loop-----------------------
#end
#--------------------------End the Gaussian macro loop----------------------------
end
exit
```

A.3 The Ba line lists

The 100% s- and 100% r-process line lists created using the procedures described in §2.5 that constructed the hybrid line lists of varying s- and r-process contribution used for the analysis in Chapters 3 & 4.

100% s-process:

```
4553.9980  56.01  137  0.00   0.021024  2.2
4553.9985  56.01  137  0.00   0.021024  2.2
4553.9985  56.01  137  0.00   0.008426  2.2
4554.0010  56.01  135  0.00   0.004852  2.2
4554.0015  56.01  135  0.00   0.004852  2.2
4554.0020  56.01  135  0.00   0.001944  2.2
4554.0316  56.01  134  0.00   0.042894  2.2
4554.0319  56.01  136  0.00   0.144952  2.2
4554.0332  56.01  138  0.00   1.125595  2.2
4554.0474  56.01  135  0.00   0.013592  2.2
4554.0498  56.01  137  0.00   0.058900  2.2
4554.0503  56.01  135  0.00   0.004852  2.2
4554.0513  56.01  135  0.00   0.000966  2.2
4554.0537  56.01  137  0.00   0.021024  2.2
4554.0542  56.01  137  0.00   0.004186  2.2

4934.0469  56.01  137  0.00   0.020754  2.2
4934.0503  56.01  135  0.00   0.003027  2.2
4934.0591  56.01  137  0.00   0.004151  2.2
4934.0610  56.01  135  0.00   0.000605  2.2
4934.0928  56.01  134  0.00   0.019370  2.2
4934.0930  56.01  136  0.00   0.058803  2.2
4934.0950  56.01  138  0.00   0.537529  2.2
4934.1104  56.01  135  0.00   0.003027  2.2
4934.1133  56.01  137  0.00   0.020754  2.2
4934.1211  56.01  135  0.00   0.003027  2.2
4934.1250  56.01  137  0.00   0.020754  2.2
```

100% r-process:

```
4553.9980  56.01  137  0.00   0.047131  2.2
4553.9985  56.01  137  0.00   0.047131  2.2
4553.9985  56.01  137  0.00   0.018889  2.2
4554.0010  56.01  135  0.00   0.059376  2.2
4554.0015  56.01  135  0.00   0.059376  2.2
4554.0020  56.01  135  0.00   0.023796  2.2
4554.0316  56.01  134  0.00   0.000000  2.2
4554.0319  56.01  136  0.00   0.000000  2.2
4554.0332  56.01  138  0.00   0.797235  2.2
4554.0474  56.01  135  0.00   0.166344  2.2
4554.0498  56.01  137  0.00   0.132040  2.2
4554.0503  56.01  135  0.00   0.059376  2.2
4554.0513  56.01  135  0.00   0.011822  2.2
4554.0537  56.01  137  0.00   0.047131  2.2
4554.0542  56.01  137  0.00   0.009384  2.2

4934.0469  56.01  137  0.00   0.025943  2.2
4934.0503  56.01  135  0.00   0.086907  2.2
4934.0591  56.01  137  0.00   0.005189  2.2
4934.0610  56.01  135  0.00   0.017381  2.2
```

```
4934.0928  56.01  134  0.00   0.000000  2.2
4934.0930  56.01  136  0.00   0.000000  2.2
4934.0950  56.01  138  0.00   0.330680  2.2
4934.1104  56.01  135  0.00   0.086907  2.2
4934.1133  56.01  137  0.00   0.025943  2.2
4934.1211  56.01  135  0.00   0.086907  2.2
4934.1250  56.01  137  0.00   0.025943  2.2
```

A.4 A LINFOR3D Fe line list

An example of the line list formatting that is used as the input into LINFOR3D.

```
Mult   namj    ei      alam     gflg     dlgC6   drrca1  dlam   ddlam
9   9
Fe I, 4282.400 A, 2.176 eV, -0.779 gflg -0.8
1   0
00     2600    2.176   4282.400 -1.579    0.0   49.466  4.D-1  2.D-3
Fe I, 4282.400 A, 2.176 eV, -0.779 gflg -0.6
1   0
00     2600    2.176   4282.400 -1.379    0.0   49.466  4.D-1  2.D-3
Fe I, 4282.400 A, 2.176 eV, -0.779 gflg -0.4
1   0
00     2600    2.176   4282.400 -1.179    0.0   49.466  4.D-1  2.D-3
Fe I, 4282.400 A, 2.176 eV, -0.779 gflg -0.2
1   0
00     2600    2.176   4282.400 -0.979    0.0   49.466  4.D-1  2.D-3
Fe I, 4282.400 A, 2.176 eV, -0.779 gflg 0.0
1   0
00     2600    2.176   4282.400 -0.779    0.0   49.466  4.D-1  2.D-3
Fe I, 4282.400 A, 2.176 eV, -0.779 gflg 0.2
1   0
00     2600    2.176   4282.400 -0.579    0.0   49.466  4.D-1  2.D-3
Fe I, 4282.400 A, 2.176 eV, -0.779 gflg 0.4
1   0
00     2600    2.176   4282.400 -0.379    0.0   49.466  4.D-1  2.D-3
Fe I, 4282.400 A, 2.176 eV, -0.779 gflg 0.6
1   0
00     2600    2.176   4282.400 -0.179    0.0   49.466  4.D-1  2.D-3
Fe I, 4282.400 A, 2.176 eV, -0.779 gflg 0.8
1   0
00     2600    2.176   4282.400 0.021    0.0   49.466  4.D-1  2.D-3
clam        gfscale
4282.400    1.0
```

A.5 The linfor_grid.pro IDL code

This code was used in Chapter 5 to extract the relevant data from the LINFOR3D output so that the 3D synthetic spectra could be compared to the HD 140283 stellar spectrum.

```
PRO linfor_grid

;----------------------------Asking for the user's input----------------------------
press=''
whichmet=''
type=''
read,prompt='Enter which van der Waals approximation to use (VALD/Unsold): ',press
read,prompt='Enter desired metallicity to interpolate to (e.g. -2.1): ',whichmet
read,prompt='Enter which synthetic run to use (m2m3 or mm25): ',type
;----------------------------------User input end-----------------------------------

;-------------------------Defining variables and constants-------------------------
AFe=[4.20,4.40,4.60,4.80,5.00,5.20,5.40,5.60,5.80] ;A(Fe)_sol values scaled to
;[Fe/H]=-2.5
wav=read_table('/data/agallagher/linfor/wrk/analysis/linelist_'+press,ncol=2)
ion=reform(wav(1,*))
wav=reform(wav(0,*))
swav=strcompress(string((wav),format='(I4)'),/remove_all)
npts=n_elements(swav)
met=['20','30']
vsini=(findgen(11))/2. ;vsini ranging from 0 to 5 km/s in steps of 0.5
flux=dblarr(n_elements(met),401,(size(AFe))(1),n_elements(vsini))
intflux=dblarr(n_elements(swav),401,(size(AFe))(1),n_elements(vsini))
convflux=dblarr(n_elements(swav),401,(size(AFe))(1),n_elements(vsini))
percent=(whichmet-(-3.0))/((-2.0)-(-3.0))*100 ;calculates the percentage of
;[Fe/H]=-3.0 to -2.0 for required [Fe/H] (default value=-2.5)
lambda=dblarr(npts,401)
band=dblarr(n_elements(swav))
c=2.9979D5 ;speed of light in km/s
v=3.31 ;velocity-spaced instrumental broadening from ThAr lines
;---------------------End of variable and constant definitions---------------------

obs=read_table('/data/agallagher/Project1/IDLwork/synthesis/obs.HD140283.dat'$
,ncol=2)

;---------------------------------line loop-----------------------------------------
for i=0,npts-1 do begin

;---------------------------------vsini loop----------------------------------------
   for m=0,n_elements(vsini)-1 do begin

;---------------------------------A(Fe) loop----------------------------------------
      for l=0,(size(AFe))(1)-1 do begin

;-----------------------metallicity interpolation loop-------------------------------
         for j=0,(size(met))(1)-1 do begin

            if ion(i) eq 2601 then fei='FeII' else fei='FeI'
            restore,'/data/agallagher/linfor/wrk/'+press+'/'+type+'/d3t57g37mm'+$
             met(j)+'n01.20ss-'+fei+swav(i)+'.idlsave'
            flux(j,*,l,m)=linfor_rotate(imuphi,-1,l,vsini(m),/normalize)
         endfor
;---------------------metallicity interpolation loop end---------------------------
```

```
        band(i)=v*line.clam/c
        band(i)=band(i)/2*sqrt(2*alog(2)) ;converting FWHM to sigma
        lambda(i,*)=(line.clam-line.dlam(0))+dindgen(1+2*line.dlam(0)/$
         line.ddlam(0))*line.ddlam(0) ;calculates lambda points for given line
        for k=0,400 do intflux(i,k,l,m)=flux(1,k,l,m)+(((flux(0,k,l,m)-$
         flux(1,k,l,m))/100)*percent) ;interpolates between [Fe/H]=-3.0 to -2.0
        f=reform(intflux(i,*,l,m)) ;1D array required for next routine
        linfor_convol,lambda(i,*),f,cf,band(i) ;convolution routine
        convflux(i,*,l,m)=cf
      endfor
;--------------------------------A(Fe) loop end-------------------------------------

      print,'Extracting flux data for the '+swav(i)+' line for vsini='$
       +strcompress(string(vsini(m),format='(F3.1)'),/remove_all)+' km/s...'
   endfor
;--------------------------------vsini loop end-------------------------------------

endfor
;--------------------------------line loop end--------------------------------------

print,'saving data in 3D_grid.idlsave...'

save,convflux,lambda,vsini,AFe,wav,obs,file=$
'/data/agallagher/Project2/linfor_grids/3D_grid_'+press+'-'+type+'.idlsave'

end
```

Appendix B:

Paper I: Online material

B.1

The following table contains data calculated by the analysis of 93 Fe I and Fe II lines used to determine $v_{\rm conv}$ for HD 140283, and was published online for use with Gallagher et al. (2010) (i.e. Chapter 3). For a select number of lines, measured equivalent widths from Hosford et al. (2009) & Lambert & Allende Prieto (2002) are tabulated in column 3. Wavelengths with asterisks denote lines that were excluded from the lower panel of Fig. 3.10.

Table B.1: Fe line observations and results used to constrain macroturbulence for HD 140283.

Measured data from observed spectrum					Results from χ^2 code			
Wavelength[a] (Å)	W^b (mÅ)	W^c (mÅ)	$v_{\rm obs}$ (km s^{-1})	Ion	Γ (km s^{-1})	A(Fe)	$\Delta\lambda$ (mÅ)	χ^2_r
4118.54*	28.8	32.2	6.97	Fe II	5.61	4.83	-8.2	3.3
4132.90	14.6	14.6	6.59	Fe I	5.85	4.99	-9.6	4.6
4134.68	26.9	28.1	6.84	Fe I	5.42	4.91	-8.8	1.6
4137.00	11.1	11.7	7.07	Fe I	5.58	4.79	-6.9	0.9
4143.41	34.2	33.7	7.25	Fe I	5.61	4.83	-8.3	5.4
4147.67	22.8	23.5	6.61	Fe I	5.52	4.92	-11.4	1.9
4153.90	18.2	19.2	6.96	Fe I	5.57	4.91	-8.5	0.7
4154.50	21.0	22.2	6.65	Fe I	5.65	4.84	-8.6	2.1
4154.81	16.1	15.9	6.65	Fe I	5.40	4.90	-9.1	0.9
4156.80*	22.7	24.6	7.18	Fe I	6.00	4.98	-8.9	5.3
4157.78	13.7	13.2	6.71	Fe I	5.86	4.90	-10.7	1.4
4174.91*	14.3	14.7	6.58	Fe I	5.58	4.96	-11.5	8.7
4175.64	20.3	19.9	6.63	Fe I	5.65	4.97	-8.9	4.4
4176.57	11.6	11.9	6.90	Fe I	5.90	5.06	-9.6	2.5
4178.86	18.5	...	6.86	Fe II	5.82	4.95	-4.7	3.2
4181.76*	38.8	39.7	7.13	Fe I	5.80	4.91	-9.2	3.4
4184.89	17.1	17.1	6.86	Fe I	5.80	4.89	-10.5	1.8
4187.04	46.8	46.4	7.22	Fe I	5.79	4.84	-11.1	4.7
4187.80*	49.5	50.2	7.46	Fe I	6.07	4.87	-12.1	11.7
4191.43	39.5	38.8	7.04	Fe I	5.93	4.87	-7.8	7.2
4199.09	48.7	49.0	7.32	Fe I	5.86	4.80	-8.7	14.1
4210.34	31.9	32.2	7.40	Fe I	5.84	4.89	-9.8	2.0
4217.54	12.0	13.9	7.13	Fe I	5.46	4.85	-9.5	1.2
4219.36	23.5	23.5	7.25	Fe I	6.04	4.92	-8.6	2.4
4222.21	29.0	28.5	6.90	Fe I	5.88	4.88	-8.9	6.8
4225.45	13.2	14.4	6.70	Fe I	5.52	4.95	-7.7	0.9

continued from previous page...

Measured data from observed spectrum					Results from χ^2 code			
Wavelength[a] (Å)	W^b (mÅ)	W^c (mÅ)	$v_{\rm obs}$ (km s^{-1})	Ion	Γ (km s^{-1})	A(Fe)	$\Delta\lambda$ (mÅ)	χ^2_r
4233.17*	43.0	43.2	7.09	Fe II	5.97	4.87	-3.8	9.5
4233.60	43.4	43.7	7.10	Fe I	5.81	4.87	-10.0	7.2
4238.81	20.4	21.6	7.04	Fe I	6.00	4.91	-9.3	6.5
4282.40	46.9	45.7	7.12	Fe I	5.74	4.84	-8.8	10.0
4337.05	36.1	41.9	7.01	Fe I	5.71	4.90	-14.3	3.9
4352.73*	24.3	24.4	6.77	Fe I	5.88	4.91	-10.2	22.3
4416.82	10.9	11.8	6.43	Fe II	5.42	4.97	-9.1	0.4
4430.61	13.5	13.2	6.73	Fe I	5.77	5.00	-9.7	1.8
4442.34	30.3	31.2	7.17	Fe I	5.88	4.92	-9.8	4.1
4443.19	11.7	9.9	6.64	Fe I	5.56	4.85	-9.6	0.3
4447.72	24.5	24.0	6.90	Fe I	5.85	4.94	-10.9	4.2
4461.65	40.9	42.4	6.69	Fe I	5.39	5.01	-13.7	6.4
4466.55	29.4	30.3	7.01	Fe I	5.80	4.88	-12.7	3.0
4489.74	11.7	11.6	6.76	Fe I	5.56	4.97	-14.9	1.3
4494.56	34.4	34.6	6.95	Fe I	5.73	4.94	-13.1	4.3
4508.28	16.2	17.2	6.88	Fe II	5.97	5.01	-10.2	4.7
4515.33	11.8	13.5	6.61	Fe II	5.79	4.96	-6.0	1.2
4520.22	11.2	12.8	6.63	Fe II	5.68	4.98	-10.9	1.3
4522.63*	23.3	24.7	7.01	Fe II	6.12	4.88	-10.8	52.4
4531.15	22.3	22.6	6.70	Fe I	5.54	4.90	-10.6	0.7
4555.89*	15.8	18.3	6.76	Fe II	5.81	4.89	-12.6	4.3
4583.83	37.4	38.6	6.98	Fe II	5.76	5.13	-11.3	2.6
4602.94	21.6	21.9	6.97	Fe I	5.75	4.97	-11.0	2.9
4736.77	14.0	14.6	6.89	Fe I	5.78	4.99	-14.2	1.7
4871.33	37.1	...	7.25	Fe I	5.93	4.84	-12.2	5.5
4872.14	27.8	...	7.12	Fe I	5.93	4.87	-11.6	10.9
4890.76	35.9	...	7.09	Fe I	5.81	4.86	-15.1	10.3

continued from previous page...

Measured data from observed spectrum					Results from χ^2 code			
Wavelength[a] (Å)	W^b (mÅ)	W^c (mÅ)	$v_{\rm obs}$ (km s^{-1})	Ion	Γ (km s^{-1})	A(Fe)	$\Delta\lambda$ (mÅ)	χ^2_r
4918.99	38.8	...	7.11	Fe I	5.85	4.88	-11.0	15.3
4938.81	12.1	...	6.80	Fe I	5.59	4.89	-15.0	2.3
4994.13	13.1	14.0	6.50	Fe I	5.58	4.88	-12.4	0.8
5001.86	13.3	...	7.01	Fe I	5.91	4.87	-11.1	2.2
5006.12	27.5	...	6.98	Fe I	5.68	4.84	-13.1	1.4
5012.07	32.8	32.0	6.78	Fe I	5.58	4.98	-17.9	8.8
5041.07	13.2	...	6.89	Fe I	6.15	5.07	-12.5	19.1
5049.82	22.6	...	6.90	Fe I	5.80	4.92	-15.6	3.6
5051.64	22.8	...	6.61	Fe I	5.60	4.97	-15.6	5.4
5068.77	11.2	...	6.76	Fe I	5.33	4.85	-17.4	0.7
5083.34	15.3	16.0	6.46	Fe I	5.56	4.88	-14.6	3.8
5098.70	10.2	...	7.34	Fe I	5.52	5.03	-15.9	0.6
5107.45*	11.6	12.0	6.44	Fe I	5.51	5.01	-20.3	5.1
5110.41	24.1	25.0	6.61	Fe I	5.54	5.06	-18.8	4.3
5123.72	11.0	12.0	6.40	Fe I	5.61	4.99	-15.1	2.7
5142.93*	11.8	...	7.25	Fe I	6.20	4.95	-14.5	46.7
5162.27	12.6	...	7.25	Fe I	5.76	5.06	-10.3	0.6
5166.28	10.3	...	6.33	Fe I	5.41	4.97	-15.4	0.9
5171.60	41.2	...	6.86	Fe I	5.44	4.67	0.3	18.0
5191.46	21.9	...	6.86	Fe I	5.81	4.86	-16.5	10.5
5192.34	28.4	...	6.85	Fe I	5.78	4.84	-16.9	29.3
5194.94	24.4	26.0	6.67	Fe I	5.79	4.93	-19.2	7.2
5216.27	19.6	...	6.65	Fe I	5.60	4.89	-14.9	4.7
5234.64	12.9	13.0	6.57	Fe II	5.60	4.89	-15.8	1.9
5266.56	32.9	...	7.09	Fe I	5.87	4.85	-14.0	8.6
5281.79	13.5	...	6.81	Fe I	5.77	4.86	-17.4	5.1
5283.62	19.5	...	7.02	Fe I	5.89	4.94	-17.1	12.1

continued from previous page...

Measured data from observed spectrum					Results from χ^2 code			
Wavelength[a] (Å)	W^b (mÅ)	W^c (mÅ)	$v_{\rm obs}$ (km s^{-1})	Ion	Γ (km s^{-1})	A(Fe)	$\Delta\lambda$ (mÅ)	χ^2_r
5302.31	10.2	...	6.85	Fe I	5.93	4.86	-13.8	2.8
5324.19	35.4	...	7.15	Fe I	5.91	5.10	-15.2	21.5
5339.93	12.7	...	6.90	Fe I	5.88	4.95	-18.5	4.7
5367.47	11.3	...	7.04	Fe I	5.81	4.84	-12.5	5.0
5369.96	14.1	...	7.11	Fe I	5.75	4.81	-13.0	5.1
5383.37	18.4	...	7.01	Fe I	5.65	4.78	-15.3	10.0
5393.17	12.2	...	7.20	Fe I	6.08	4.88	-14.2	4.1
5404.15	18.4	...	7.52	Fe I	5.65	4.93	-4.3	4.6
5415.20	17.5	...	7.26	Fe I	5.80	5.28	-13.6	2.3
5569.62	12.9	...	7.19	Fe I	5.97	4.84	-15.2	4.2
5572.85	19.7	...	7.05	Fe I	5.94	4.29	-16.0	4.1
5615.66	34.1	...	7.18	Fe I	5.96	4.80	-15.4	5.6
6252.56	11.3	14.0	6.74	Fe I	5.79	5.00	-21.1	2.6

[a] Lines marked with an asterisk denote those excluded from the lower panel of Fig. 3.10 due to contamination with other lines found ±0.3 Å from the Fe line centre.

[b] Equivalent widths of Fe II and Fe II lines measured in this work.

[c] Equivalent widths of Fe II and Fe II lines measured by Hosford et al. (2009) and Lambert & Allende Prieto (2002).

References

Gallagher, A. J., Ryan, S. G., García Pérez, A. E., & Aoki, W. 2010, A&A, 523, A24 [ADS]

Hosford, A., Ryan, S. G., García Pérez, A. E., Norris, J. E., & Olive, K. A. 2009, A&A, 493, 601 [ADS]

Lambert, D. L. & Allende Prieto, C. 2002, MNRAS, 335, 325 [ADS]

Appendix C:

Paper 1: Extra analyses

C.1 Re-examination of the χ^2_r results

The χ^2_r analysis conducted in Chapter 3 to determine which broadening mechanism best describes the Fe line's broadening has been extended. The individual χ^2_r results for a given broadening profile can be co-added so that the best overall result can be determined as judged by the total χ^2_r value. In this section I conduct such an analysis for the three broadening types used to describe the broadening profiles of the Fe lines. In Chapter 3 I found that the best broadening profile was a radial-tangential (ζ_{RT}) profile, with most Fe lines better fit by the mechanism, followed closely by the Gaussian technique. Finally the $v \sin i$ profile, which is used to approximate the effect a star's rotation has on line broadening, was the poorest broadening approximation with fewest lines better fit by the profile.

In Chapter 3, the same 93 Fe lines were used to determine the macroturbulent broadening of HD 140283 for each broadening mechanism. The table below tabulates the results of the total χ^2_r value for each broadening mechanism.

Table C.1: Total χ^2_r values for the three types of broadening profile used in Chapter 3

Broadening Mechanism	$\Sigma\chi^2_r$
ζ_{RT}	584.91
Gaussian	598.94
$v \sin i$	912.16

As one can see, the above result nicely confirms the result found in Chapter 3, which showed that the best broadening mechanism approximation to use in HD 140283 is a ζ_{RT} profile. However, the co-addition of the χ^2_r values for each broadening type have shown that there is not a large statistical significance to separate the ζ_{RT} and Gaussian profiles, meaning that use of either would have little effect in improving the overall best fit. It also shows that using the $v \sin i$ profiles are still statistically unsound when compared to the other two broadening techniques. However, further work can be done to compare the ζ_{RT} and Gaussian profiles. One can still change the ratios of the radial and tangential broadening as a comparison with the Gaussian profiles to determine whether the resultant profiles better fit the Fe lines or worsen the total χ^2_r value when compared to the Gaussian and current ζ_{RT} results.